JETP Letters, Vol. 82, No. 8, 2005, pp. 463–466. Translated from Pis'ma v Zhurnal Éksperimental'noĭ i Teoreticheskoĭ Fiziki, Vol. 82, No. 8, 2005, pp. 519–523.

Discovery of a *P*-Odd Effect in Triton Emission from the Reaction ^{6}Li(n, α)^{3}H

V. A. Vesna[a], Yu. M. Gledenov[b], V. V. Nesvizhevsky[c], A. K. Petukhov[c], P. V. Sedyshev[b], T. Soldner[c], O. Zimmer[d], and E. V. Shulgina[a]

[a] *Petersburg Nuclear Physics Institute, Russian Academy of Sciences, Gatchina, Leningrad region, 188300 Russia*
e-mail: vvesna@pnpi.spb.ru
[b] *Joint Institute for Nuclear Research, Dubna, Moscow region, 141980 Russia*
[c] *Institut Max von Laue–Paul Langevin, BP 156, F-38042 Grenoble Cedex 9, France*
[d] *Technische Universität München, D-85748 Garching, Germany*
Received September 9, 2005

The results of measuring the *P*-odd asymmetry ($\mathbf{S}_n \cdot \mathbf{P}_t$) for triton emission from the reaction ^{6}Li(n, α)^{3}H are presented. Here, $\mathbf{S}_n$ is the neutron spin and $\mathbf{P}_t$ is the triton momentum. Three series of measurements were performed, one at the Petersburg Nuclear Physics Institute (Gatchina, Russia) in a vertical neutron beam from the PWR reactor and two in the PF1B beam from the reactor at the Institute Laue–Langevin (Grenoble, France). On the basis of all three experiments, the *P*-odd asymmetry coefficient was found to be $\alpha_{PN} = -(8.6 \pm 2.0) \times 10^{-8}$. The results of zero experiments and calculations give every reason to believe that the above *P*-odd asymmetry is due to the reaction being studied. © *2005 Pleiades Publishing, Inc.*

PACS numbers: 13.75.Cs, 23.20.En

The standard model of electroweak interaction predicts the existence of weak neutral currents. Such currents were unambiguously discovered in lepton–nucleon interactions, the predictions of the theory being in good agreement with the experimental data. Parity violation in nucleon–nucleon interactions, which was observed in various processes involving few-nucleon systems and nuclei, must be due both to charged and to neutral currents. The presence of a charged current was revealed in proton–proton scattering at various proton energies, and the experimental results there are in agreement with the respective theoretical predictions [1, 2]. However, a weak neutral current has not yet been discovered in nucleon–nucleon interactions.

For the neutral-current constant, processes in which an attempt was made to estimate a neutral current yielded the constraint $f_\pi < 1.2 \times 10^{-7}$ at a 90% confidence level [3].

It should be noted that *P*-odd effects were discovered in heavy nuclei [4], where these effects are much stronger owing to enhancement mechanisms. At the same time, the question of whether it is possible in principle to extract the parameters of weak nucleon–nucleon interaction from measurements of this type is still the subject of lively discussions. Therefore, a reliable observation of a significant effect of *P*-odd asymmetry in an extremely light nucleus, where one can perform relevant calculations in terms of weak coupling constants, is one of the important problems.

In our opinion, investigation of the *P*-odd asymmetry ($\mathbf{S}_n \cdot \mathbf{P}_t$) in the reaction ^{6}Li(n, α)^{3}H through observing the *P*-odd asymmetry in the ^{3}H channel is the most optimal and promising. Here, $\mathbf{S}_n$ is the neutron spin and $\mathbf{P}_t$ is the triton momentum.

The ^{6,7}Li nuclei are well described within cluster and multicluster models.

Theoretical models predict a 70% clustering of the ^{6}Li nucleus in the form of an alpha particle and a deuteron d' that is deformed in the alpha-particle field. Therefore, we propose considering the reaction in question on the basis of the respective cluster model of the nucleus—that is, as the three-body pickup reaction

$$n + \{\alpha d'\} \longrightarrow \{nd\} + \alpha.$$

The total energy release in the reaction is 4.78 MeV, this value being distributed among the reaction products as follows: $E_\alpha = 2.05$ MeV and $E_t = 2.73$ MeV. Since the specific energy loss of the alpha particle is much greater than that of the triton (the triton free path is approximately five times longer than the alpha-particle free path), one can employ ionization gas chambers to detect tritons and separate the tritium component without an alpha-particle admixture. The separation of a specific reaction component by means of a chamber makes it possible to apply the integral detection method and to obtain unambiguous results. In order to compensate for fluctuations of the reactor power, one can readily construct a system of two chambers where *P*-odd effects differ in sign.

0021-3640/05/8208-0463$26.00

The first measurements of *P*-odd asymmetry in the reaction ^{6}Li(n, α)^{3}H revealed a rather large spurious effect, which, in further dedicated experiments, where the neutron spin $\mathbf{S}_n$ was orthogonal to the triton momentum $\mathbf{P}_t$ and the neutron momentum $\mathbf{P}_n$, was determined as the effect of left–right asymmetry of the form $\alpha_{LR} \sim \mathbf{S}_n \cdot [\mathbf{P}_n \times \mathbf{P}_t]$. In the reaction being considered, this coefficient proved to be $\alpha_{LR} = (1.06 \pm 0.04) \times 10^{-4}$ [5].

In order to remove the effect of left–right asymmetry on the measured *P*-odd asymmetry, we performed an experiment where the observed vectors $\mathbf{S}_n$, $\mathbf{P}_n$, and $\mathbf{P}_t$ are parallel: $\mathbf{S}_n \parallel \mathbf{P}_n \parallel \mathbf{P}_t$. The alignment of these three vectors to within $\varepsilon \sim 10^{-2}$ can readily be achieved in our experiment. As a result, the contribution of the left–right asymmetry to the *P*-odd asymmetry decreases in proportion to ε^2, falling below a value of about 1×10^{-8}.

We performed three series of measurements, one at the Petersburg Nuclear Physics Institute (PNPI, Gatchina, Russia) in a vertical neutron beam from a PWR reactor and two in the PF1B beam from the reactor of the Institute Laue–Langevin (Grenoble, France), which is commonly abbreviated as ILL.

Twenty-four targets and detecting chambers, one on each side in the vicinity of each target, were arranged in an ionization gas chamber along the beam axis. One half of a double chamber detected tritons emitted along the beam-propagation direction—that is, along the neutron momentum (forward direction)—while the other half of this chamber recorded tritons traveling in the opposite (backward) direction. Since one observed *P*-odd asymmetry of the form $W(\Theta) \sim 1 + \alpha_{PN}(\mathbf{S}_n \cdot \mathbf{P}_t)$, the effects arising in detecting tritons that travel in the forward and backward directions were opposite in sign. Here, α_{PN} is the *P*-odd-asymmetry coefficient. All forward (backward) halves of the double chambers were connected electrically in order to employ one preamplifier of signals. For the targets, we took ^{6}LiF layers 400 μg/cm^2 thick sputtered onto an aluminum foil 14 μm thick. The calculated degree of neutron-beam absorption was about 60%.

An aluminum foil 14 μm thick was additionally glued to each target in order to ensure alpha-particle absorption and to create the required solid angle of triton emission. Therefore, tritons whose momenta were parallel or antiparallel to the neutron momentum traversed a 14-μm-thick aluminum layer, with the result that there arose a specific solid angle at which the detector was seen from a target. The mean cosine of the triton emission angle was calculated by the Monte Carlo method. The result was $\langle\cos(\mathbf{S}_n \cdot \mathbf{P}_t)\rangle = 0.75$.

In order to detect charged reaction products, we employed gaseous argon at an excess pressure of P = 1.4 atm in the first ILL experiment and at an excess pressure of P = 0.9 atm in the second ILL experiment. At these pressure values and a sensitive-gap thickness of 21 mm, the free path of tritons emitted from a target was fully within the volume of the sensitive gas gap adjacent to the target. The pressure was taken to be different for the different experiments in order to change the conditions of observation.

As a rule, experiments aimed at reaching extremely high accuracies of about 10^{-8} require test measurements for revealing asymmetries that owe their existence to imperfections of the equipment used. In order to remove spurious asymmetries in the measurements with chambers, the direction of the magnetic field guiding the neutron spin was reversed at regular time intervals. This was done in an automated mode every hour and every four minutes in the first and last experiments, respectively.

Since *P*-odd effects are proportional to the scalar product $(\mathbf{S}_n \cdot \mathbf{P}_t)$, the reversal of the magnetic field leads to the reversal of the sign of the effect. Accumulating the identical numbers of series for the two directions of the magnetic field that guides the neutron spin and taking the difference of the effect magnitudes calculated for series that correspond to opposite magnetic-field directions, we ultimately arrive at the doubled true effect. All spurious effects that have nothing to do with neutron polarization are canceled.

Such experiments include a test measurement with a polarized beam but without the target being studied. The procedure outlined above takes fully into account all possible spurious effects.

The uncompensated magnetic field of the Earth and the time-independent magnetic fields of the other operating physics facilities are present in the experiment. These magnetic fields may increase the contribution of the left–right asymmetry to the *P*-odd asymmetry. The effect of the left–right asymmetry due to such fields does not change sign upon the reversal of the main guiding magnetic field. If identical numbers of series are accumulated for opposite directions of this field, the contribution of the spurious effect being considered to the results of the measurements is canceled upon taking the difference of the experimental results for opposite field directions.

Fluctuations of the reactor power were compensated by subtracting the product of the voltages across the backward integrator and a compensation factor from voltages across the forward integrator and finding the compensation factor such that the variance $D(\alpha)$ of the resulting difference α was minimal for one series of the measurements. Concurrently, we determined the absolute effect as $\alpha \pm \delta\alpha(\min)$ with $\delta\alpha = \sqrt{D(\alpha)}$.

The relative effect was calculated by the formulas [6]

$$\delta = \frac{\alpha}{L(U_f + U_b)}, \quad D_\delta = \frac{D(\alpha)}{(L(U_f + U_b))^2},$$

$$\sigma_\delta = \sqrt{D_\delta}, \quad L = \frac{L_f + L_b}{2},$$

where δ is the relative effect; σ_δ is the statistical error in measuring the relative effect; L_f and L_b are the amplification factors in the forward and backward channels, respectively; and U_f and U_b are the constant components of the forward and backward signals, respectively.

In order to assess the contribution of the left–right asymmetry to the *P*-odd effect, we changed the configuration of the magnetic field guiding the neutron spin—the magnetic field was chosen to be orthogonal to the plane of the Earth and the neutron-beam axis. It was possible to rotate the chamber through small angles about the neutron-beam axis in the plane of the Earth. The figure shows the left–right asymmetry as a function of the angle between the neutron momentum and the chamber axis. The angle in the figure is reckoned from the chamber position corresponding to the minimum value of the magnitude of the left–right asymmetry factor. One can see that the zero of the left–right asymmetry and the maximum value of the intensity do not coincide.

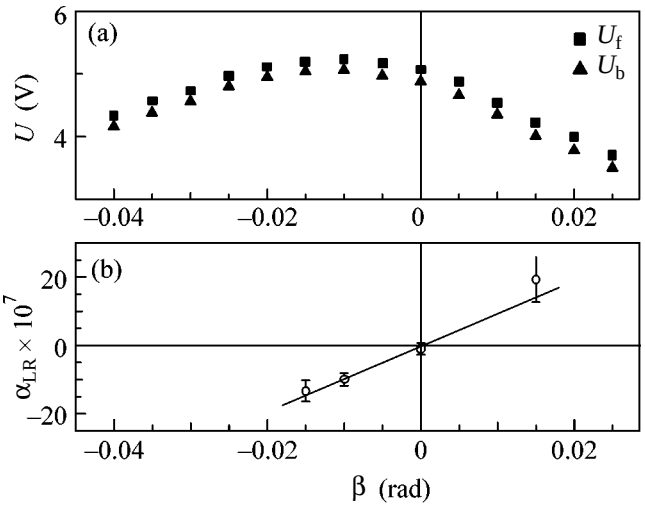

(a) Constant components U_f and U_b and (b) left–right asymmetry factor α_{LR} versus the angle β between the neutron and triton momenta.

If, using these data, one calculates the maximum value of the left–right asymmetry factor for the case where the vectors $\mathbf{S}_n$, $\mathbf{P}_n$, and $\mathbf{P}_t$ are mutually orthogonal, the result would agree, within the errors, with that which was measured previously [5]. This indicates that the ionization chamber used functions properly and has a reasonably high sensitivity.

In addition, we measured the left–right asymmetry in a different plane, where the magnetic field guiding the neutron spin is parallel to the plane of the Earth and is orthogonal to the neutron momentum. For the operating geometry of the chamber position, we tested the contribution of the left–right asymmetry due to the possible vertical deviation of the chamber. In this geometry, the measured left–right asymmetry factor was $\alpha_{LR} = (4.9 \pm 1.9) \times 10^{-7}$.

If the field is applied in the direction parallel to the beam-propagation direction, the contribution of the left–right asymmetry to the *P*-odd effect must decrease by two orders of magnitude and must not exceed 1×10^{-8} since the direction of the guiding magnetic field is specified to within 10^{-2} by the solenoid wound round the chamber casing. In order to experimentally test this statement, the *P*-odd asymmetry coefficient was measured in the most recent experiment at three values of the angle between the neutron momentum and the chamber axis for the neutron spin nearly parallel to the average triton momentum. From our calculations, it follows that, at any small value used here for the angle of deviation, the contribution of the left–right asymmetry to the effect being studied must not exceed $(1–1.5) \times 10^{-8}$. This means that, for $\alpha_{PN} \gg \alpha_{LR}$, the measured *P*-odd effect must be virtually identical at small angles of deviation of the neutron momentum from the chamber axis if this is indeed a *P*-odd effect. However, if the result of the measurements at zero angle is due exclusively to left–right asymmetry, it must vary at different angles in just the same way as in the figure.

Table 1 gives the *P*-odd-asymmetry coefficient α_{PN} at various values of the angle β between the neutron and triton momenta.

A modest decrease in the magnitude of the effect with increasing angle may be due to an increase in the contribution of the left–right asymmetry with a plus sign, but this statement is not statistically significant. Therefore, we can state that the contribution of the left–right asymmetry to the *P*-odd effect, if any, is much less than the error in measuring the effect.

Table 2 presents the *P*-odd asymmetry coefficient in the reaction $^6\mathrm{Li}(n, \alpha)^3\mathrm{H}$ according to our measurements performed in different experiments, these results being corrected for the neutron polarization *P* and for the detector solid angle Ω.

In order to perform a zero experiment involving a complete absorption of the tritium component, the targets were additionally covered with an aluminum foil 20 μm thick. The zero-test result normalized to the constant components in the operating mode and corrected for the solid angles and neutron polarization is $\alpha_{backgr} = (2.0 \pm 1.7) \times 10^{-8}$ [6].

Table 1

β [rad]	α_{PN}
~0	$-(10.8 \pm 4.4) \times 10^{-8}$
−0.01	$-(9.9 \pm 4.1) \times 10^{-8}$
−0.015	$-(7.4 \pm 4.2) \times 10^{-8}$
Average value	$\alpha_{PN} = -(9.3 \pm 2.5) \times 10^{-8}$

Table 2

	$P\Omega$	α_{PN}
PNPI, vertical channel	0.66	$-(5.4 \pm 6.0) \times 10^{-8}$ [6]
ILL, PF1B channel	0.66	$-(8.1 \pm 3.9) \times 10^{-8}$ [7]
ILL, PF1B channel	0.70	$-(9.3 \pm 2.5) \times 10^{-8}$
Average value $\alpha_{PN} = -(8.6 \pm 2.0) \times 10^{-8}$		

Since the design of the chamber used was identical to that described in [6], the zero-test result remains valid for the later experiments in the beam of the Institute Laue–Langevin; however, the need for performing yet another zero experiment with a higher statistical accuracy can clearly be seen.

In order to estimate the effect of electromagnetic noise, we measured the *P*-odd asymmetry without a neutron beam. The result obtained from the measurements in the last series and normalized to the constant components of the main experiment is

$$\alpha_{\text{noise}} = -(0.6 \pm 0.5) \times 10^{-8}.$$

Thus, the effect of noise is at least ten times smaller than the effect value.

We performed some approximate calculations in order to determine the possible contribution of competing processes that include

(i) β^- radiation in admixed ^{8}Li decay, in which case the asymmetry is about 8% [8];

(ii) admixed gamma radiation from isotopes, in which case *P*-odd effects associated with photons were found at a level of 10^{-5};

(iii) the possible admixture of the *P*-odd effect in the reaction $^{35}\text{Cl}(n, p)^{35}\text{S}$, with the *P*-odd-asymmetry coefficient for protons being about 1.5×10^{-5}.

The results of the calculations show that, in the reaction $^6\text{Li}(n, \alpha)^3\text{H}$, the possible admixed-reaction-induced contribution α_{PN} (admixed) to the *P*-odd effect does not exceed $(2–5) \times 10^{-9}$ in the worst case, this being much less than the observed effect of *P*-odd asymmetry. Thus, we can state that the effect found here is due to the reaction $^6\text{Li}(n, \alpha)^3\text{H}$.

At the present time, there is only one study devoted to calculating the *P*-odd effect in this reaction in terms of the weak coupling constants [9]. The result of that calculation is

$$\alpha_{PN} \approx (0.06 h_\rho - 0.45 f_\pi) \approx -1.6 \times 10^{-7},$$

where $h_\rho = -11.4 \times 10^{-7}$ and $f_\pi = 2 \times 10^{-7}$ are the most commonly used weak coupling constants associated with ρ and π exchanges, respectively. The constant f_π is responsible for a neutral current.

Assuming that the charged-current constant is known precisely and that $h_\rho = -11.4 \times 10^{-7}$ and relying on the model considered here and on our experimental result, we can estimate the neutral constant itself and the range of its variation as

$$f_\pi \approx (0.4 \pm 0.4) \times 10^{-7}.$$

At the 90% confidence level, we have

$$-0.3 \times 10^{-7} \le f_\pi \le 1.1 \times 10^{-7}.$$

At the present time, this is likely to be one of the most stringent constraints on the neutral-current constant in nucleon–nucleon interaction. It should be borne in mind, however, that this constraint is based on a theoretical study that provides no information about the accuracy of the calculations performed there.

This work was supported by the Russian Foundation for Basic Research (project no. 03-02-17338).

REFERENCES

1. R. Balzer, R. Hennek, Ch. Jachquemart, *et al.*, Phys. Rev. C **30**, 1409 (1984).
2. V. Yuan, H. Fraunfelder, R. W. Harper, *et al.*, Phys. Rev. Lett. **57**, 1680 (1986).
3. S. A. Page, Phys. Rev. C **35**, 1119 (1987).
4. Yu. G. Abov, P. A. Krupchitsky, and Yu. A. Oratovsky, Phys. Lett. **12**, 25 (1964).
5. N. V. Borovikova, V. A. Vesna, A. I. Egorov, *et al.*, Pis'ma Zh. Éksp. Teor. Fiz. **30**, 527 (1979) [JETP Lett. **30**, 495 (1979)].
6. V. A. Vesna, Yu. M. Gledenov, I. S. Okunev, *et al.*, Yad. Fiz. **59**, 23 (1996) [Phys. At. Nucl. **59**, 19 (1996)].
7. V. A. Vesna, Yu. M. Gledenov, V. V. Nesvizhevsky, *et al.*, Preprint No. 2479, PIYaF RAN (St. Petersburg Inst. of Nuclear Physics, Russian Academy of Sciences, Gatchina, 2002).
8. Y. G. Abov, O. N. Yermakov, A. D. Gulko, *et al.*, Nucl. Phys. **34**, 505 (1962).
9. N. N. Nesterov and I. S. Okunev, Pis'ma Zh. Éksp. Teor. Fiz. **48**, 573 (1988) [JETP Lett. **48**, 621 (1988)].

Translated by A. Isaakyan

JETP Letters, Vol. 82, No. 8, 2005, pp. 467–471. From Pis'ma v Zhurnal Éksperimental'noĭ i Teoreticheskoĭ Fiziki, Vol. 82, No. 8, 2005, pp. 524–528.

Heavily-Chirped Solitary Pulses in the Normal Dispersion Region: New Solutions of the Cubic–Quintic Complex Ginzburg–Landau Equation¶

E. Podivilov[a] and V. L. Kalashnikov[b]

[a] *Institute for Automation and Electrometry, Russian Academy of Sciences, Novosibirsk, 630090 Russia*
e-mail: Podivilov@iae.nsk.su

[b] *Institut für Photonik, TU Wien, A-1040 Vienna, Austria*

Received July 11, 2005

A new type of the heavily-chirped solitary pulse solutions of the nonlinear cubic–quintic complex Ginzburg–Landau equation has been found. The methodology developed provides for a systematic way to find the approximate but highly accurate analytical solutions of this equation with the generalized nonlinearities within the normal dispersion region. It is demonstrated that these solitary pulses have the extra-broadened parabolic-top or fingerlike spectra and allow compressing with more than a hundredfold growth of the pulse peak power. The obtained solutions explain the energy scalable regimes in the fiber and solid-state oscillators operating within the normal dispersion region and promise to achieve microjoules femtosecond pulses at MHz repetition rates.

PACS numbers: 05.45.Yv, 42.65.Tg, 42.65.Re, 42.81.Dp

The complex nonlinear Ginzburg–Landau equation (CGLE) is a basic nonlinear equation taking into account linear and nonlinear dispersion as well as linear and nonlinear dissipation that allows describing a variety of phenomena from nonlinear optical waves to Bose–Einstein condensation and field theory [1]. In a nondissipative limit, the cubic CGLE gives the nonlinear Schrödinger equation (NLSE), which is completely integrable in one dimension [2]. An isolated solitary-wave solution of NLSE is called a soliton and is of interest for telecommunication, nonlinear, and laser optics. The solitary pulse solutions of CGLE have been found, as well [3]. However, in the case of more general nonlinearity within the normal dispersion region (NDR), where there exists no bright soliton of NLSE and the solitary pulse solutions of the cubic CGLE can suffer an explosive instability, the exact or approximated solitary-wave partial solutions of CGLE are known only for some restrictions imposed on the pulse phase [4, 5].

Numerical simulations have also revealed a variety of the pulsing solutions of CGLE in NDR [6, 7]. Such breatherlike regimes have, as a counterpart, the so-called self-similar pulses (SSP) propagating under the group-delay dispersion and the nonlinearity varying along propagation axis [8]. As it was demonstrated, SSP in NDR tolerates the strong nonlinearities that allow the compressible high-energy pulses from a fiber laser [9, 10]. This regime offers producing the high-energy femtosecond pulses directly from fiber [9] as well as solid-state [11–13] oscillators. Such oscillators are required for both scientific (e.g., high harmonics generation in gases) and technological (e.g., effective material modification at MHz pulse repetition rate) purposes.

Here, we report on a new type of approximated but high-accuracy heavily-chirped solitary pulse (CSP) solution of the cubic–quintic CGLE. A closed analytical form of such a solution allows tracing all the basic characteristics of CSP in dependence on variation of the CGLE parameters. One can suppose that CSP is highly interesting for laser and fiber optics. This results from its energy scalability in NDR and the possibility of compression down to femtosecond pulse duration. An energy scalability of the compressible CSP is based on a simple physical ground. The pulse energy can increase with both its peak power and duration. However, the peak power growth is restricted from above by the nonlinear processes such as self-focusing, optical damage, etc. A single way to the higher energy is to increase the pulse duration T. For the soliton propagating in the anomalous dispersion region, this means an inevitable decrease of its spectral width $\Delta \simeq 1/T$. On the contrary, it is possible to increase the CSP duration without loss of its spectral width in NDR: $\Delta \simeq 4f/T$, where $f \gg 1$ is the chirp. Then, the CSP can be compressed down to $\simeq 1/\Delta$, which results in its peak power growth ($\simeq f$ times). In contrast to the compressible chirped SSP [14], which is disrupted in a spectrally dissipative system [15], CSP propagates under the spectral filtering. This suits perfectly an oscillator generating the spectrally wide (≈100 nm) pulses in NDR [12].

¶ The text was submitted by the authors in English.

0021-3640/05/8208-0467$26.00 © 2005 Pleiades Publishing, Inc.

We base an analysis on the (1 + 1)-dimensional cubic–quintic CGLE [3]:

$$\frac{dA}{dz} = \left(-\sigma + (\alpha + i\beta)\frac{d^2}{dt^2} + (\kappa - i\gamma)P - \kappa\zeta P^2\right)A, \quad (1)$$

where t and z are the local time and the propagation distance, respectively; $A(t, z)$ is the slowly varying field amplitude, so that $|A|^2$ means the power P. Parameter σ is the net-loss, which in an oscillator equals the difference of the net-passive loss and the saturated gain. Parameters α and β are the square of the spectral filter bandwidth and the group-delay dispersion (GDD) coefficient, respectively. Parameters κ and γ are the self-amplitude modulation (SAM) and the self-phase modulation (SPM) coefficients, respectively. And at last, parameter ζ describes the saturation of SAM and confines the maximum power.

We shall search for approximated solutions of Eq. (1) for positive parameters and in the limit of $\alpha/\beta < \kappa/\gamma \ll 1$. This limit is well grounded for an oscillator operating in NDR. As an example, $\alpha < 5$ fs^2 and $\beta \approx 100$ fs^2 for a Ti : sapphire oscillator of [12, 13, 16]. Simultaneously, $\kappa/\gamma \approx 0.04$ is a typical value for the so-called Kerr-lens mode-locking regime [16, 17].

To find a stationary solution of Eq. (1), we use ansatz $A(t, z) = \sqrt{P(t)}\exp(i\phi(t) - iqz)$, which results in

$$\gamma P(t) = q - \beta\Omega^2(t),$$
$$\beta\left(\frac{d\Omega}{dt} + \frac{\Omega(t)}{P(t)}\frac{dP}{dt}\right) = \kappa P(t)(1 - \zeta P(t)) - \sigma - \alpha\Omega^2(t). \quad (2)$$

Here, $\Omega(t) \equiv d\phi(t)/dt$ is the instant frequency. In Eqs. (2), the terms $\propto d^2\sqrt{P(t)}/dt^2$ are omitted in the framework of the adiabatic approximation ($\beta \simeq 10^{-4}$ ps^2, whereas $T \simeq 1$ ps for CSP [12]). In the first Eq. (2), a smallness of the terms $\propto\alpha/\beta$ is used.

Since the power $P(t)$ is a positive defined value, Eqs. (2) give $\Omega(t)^2 < \Delta^2 \equiv q/\beta$ and the peak power $P_0 \equiv P(0) = q/\gamma = \beta\Delta^2/\gamma$. The regularity of the desired solution demands $d\Omega/dt < \infty$ that imposes a restriction on P_0:

$$\gamma P_0 = \beta\Delta^2 = \frac{3\gamma}{4\zeta}(1 - c/2 \mp \sqrt{(1 - c/2)^2 - 4\sigma\zeta/\kappa}). \quad (3)$$

The parameter $c = \alpha\gamma/\beta\kappa$ means a contribution of spectral dissipation (dispersion) relative to that of SAM (SPM). It is confined from above: $c < c_{\max} = 2 - 4\sqrt{\sigma\zeta/\kappa}$. This defines the maximum peak power: $P_0^{\max} = (3/4\zeta)(1 - c_{\max}/2) = (3/2)\sqrt{\sigma/\kappa\zeta}$. For a given c, the parameter σ is also confined from above: $\sigma < (\kappa/4\zeta)(1 - c/2)^2$.

One can see from Eq. (3) that the solution for P_0 with a "+" sign before a square root does not have a finite asymptotic for $\zeta \longrightarrow 0$. Hence, this solution does not have a counterpart among the solutions of the cubic CGLE, and, therefore, we shall not consider it henceforth.

The regularity condition also simplifies Eqs. (2):

$$\frac{d\Omega}{dt} = \frac{\beta\zeta\kappa}{3\gamma^2}(\Delta^2 - \Omega^2)(\Omega^2 + \Omega_L^2),$$
$$\beta\Omega_L^2 = \frac{\gamma}{\zeta}(1 + c) - \frac{5}{3}\gamma P_0. \quad (4)$$

The implicit solution of differential Eq. (4) with a zero asymptotic of the local power $P(t)$ at $t \longrightarrow \pm\infty$ is

$$t = \tau\left[\operatorname{arctanh}\left(\frac{\Omega}{\Delta}\right) + \frac{\Delta}{\Omega_L}\arctan\left(\frac{\Omega}{\Omega_L}\right)\right], \quad (5)$$

where $\tau = 3\gamma^2/(\zeta\beta\kappa\Delta(\Delta^2 + \Omega_L^2))$. Equation (5) gives a time profile of the instant frequency $\Omega(t)$ and, as a result of Eq. (2), a time profile of the power $P(t)$. In the limit of the cubic CGLE ($\zeta \longrightarrow 0$), this solution turns into the well-known solitary pulse solution $A \propto \cosh(t/\tau)^{if-1}$ [3]. The duration $T = 1.76\tau$ and the chirp f are close to the exact ones to an accuracy $\approx\alpha/\beta$, $\kappa/\gamma \ll 1$.

The spectral amplitude is $E(\omega) = \int dt\sqrt{P(t)}\exp(i\phi(t))\exp(-i\omega t)$. For CSP, one can assume in the limit of $\gamma/\kappa \gg 1$ that the phase $\phi(t)$ is a rapidly varying function. Then, $E(\omega)$ can be calculated by the method of stationary phase [18]. The resulting spectral power is

$$p(\omega) \equiv |E(\omega)|^2 \simeq \frac{6\pi\gamma}{\zeta\kappa}\frac{\theta(\Delta^2 - \omega^2)}{\omega^2 + \Omega_L^2}, \quad (6)$$

where $\theta(x)$ is the Heaviside function. Equation (6) allows finding the pulse energy:

$$\mathscr{E} = \int_{-\infty}^{\infty} dtP(t) = \int_{-\Delta}^{\Delta}\frac{d\omega}{2\pi}p(\omega) = \frac{6\gamma}{\zeta\kappa\Omega_L}\arctan\left(\frac{\Delta}{\Omega_L}\right). \quad (7)$$

One can see from Eqs. (3)–(5) and (7) that the dimensionless values $\Delta' = \Delta\sqrt{\beta\zeta/\gamma}$, $\Omega_L' = \Omega_L\sqrt{\beta\zeta/\gamma}$, $\tau' = \tau\kappa/\sqrt{\beta\zeta\gamma}$, and $\mathscr{E}' = \mathscr{E}\kappa\sqrt{\zeta/\gamma\beta}$ completely define the CSP spectral and time profiles as well as its energy. These values depend on only two dimensionless parameters c and $b = \sigma\zeta/\kappa$.

A typical example of the variations of Δ', Ω_L' and the normalized pulse width T' with c are shown in Fig. 1 for $b = 11/64$. One can see that the spectrum half-width Δ' (thick curve) increases monotonically with c. In particular, this can be interpreted as the spectrum broadening with GDD approaching zero in agreement

with the experimental data of [13]. The Lorentzian half-width reaches a maximum and then shortens with the c growth (thin curve). As a result, a main part of $p(\omega)$ concentrates within the interval of $|\omega| < \Omega_L$ that provides a higher peak power P_0 close to the boundary of CSP existence. In agreement with [13], the CSP duration decreases with c except for the narrow region close to $c_{\max}$ (dashed curve).

The importance of the parameter b is explained by the fact that σ affects the CSP stability against the noise excitation. From Eq. (1), the minimum requirement for the pulse stability is $\sigma > 0$. The numerical simulations [16] have demonstrated that the chirped pulse in NDR is stable except for the narrow regions close to the edges of the CSP existence region. In an oscillator, parameter σ is not quite an independent value because it depends on the pulse energy due to the effect of the gain saturation [19]. In this case, the energy dependence of b can noticeably change the variation of CSP parameters with c.

A distinguishing feature of CSP is its spectral profile. Figure 2 shows the normalized powers $p' = p\kappa/\beta$ in dependence on the normalized frequency $\omega' = \omega\sqrt{\beta\zeta/\gamma}$. From Eq. (6), it is the Lorentzian function truncated at $\pm\Delta$. In fact, such truncation is slightly smoothed as the stationary phase approximation losses its validity close to $\pm\Delta$. Nevertheless, the spectral intensity vanishes very rapidly at the spectrum edges in the experiment as well [9, 12, 13].

For a small b ($\sigma < 9\kappa/64\zeta$, $c_{\max} > 1/2$), the Lorentzian spectral half-width Ω_L is larger than Δ. As a result, the spectrum has a flat-top profile (thick curve) and a comparatively small area (energy). Also, this case corresponds to $\zeta \longrightarrow 0$ (the limit of the cubic CGLE). Within the region of a large b ($\sigma > 3\kappa/16\zeta$, $c_{\max} < 2 - \sqrt{3}$), $\Omega_L < \Delta$ and the spectrum has a fingerlike profile and a maximum energy (dashed curve). In the intermediate region $9\kappa/64\zeta < \sigma < 3\kappa/16\zeta$, there exists some $c^* \equiv c = \sqrt{1 - 16b/3}$ providing $\Omega_L = \Delta$ (Fig. 1) and forming a transitional parabolic-top spectrum (thin curve). As such spectrum is the most distant from the boundaries of the CSP existence, it possesses maximum stability.

The chirp $Q(\omega)$ is defined as

$$Q(\omega) = (1/2)\frac{d^2\psi(\omega)}{d\omega^2} \simeq \frac{3\gamma^2}{2\beta\kappa\zeta} \times \frac{1}{(\Delta^2 - \omega^2)(\Omega_L^2 + \omega^2)}, \quad (8)$$

where $\psi(\omega) = -\phi(t^*(\omega)) + \omega t^*(\omega)$ is the phase in spectral representation, and the stationary point $t^*(\omega)$ is defined as the right-hand side of Eq. (5) with Ω replaced with ω. Figure 3 shows the dependence of the normalized chirp $Q' = Q\kappa/\beta\zeta$ on ω'. The flat-top and

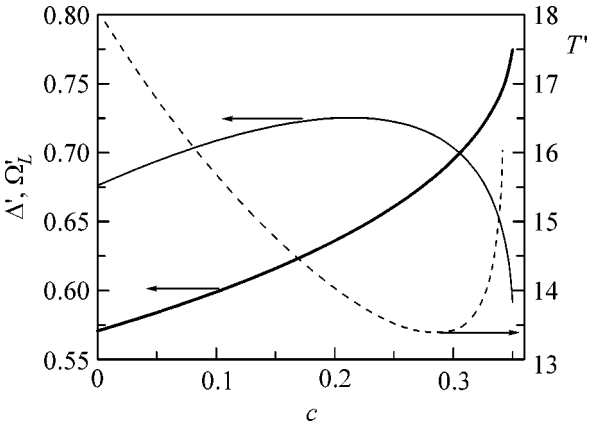

Fig. 1. Variation of dimensionless spectral (Δ', solid thick curve) and Lorentzian (Ω'_L, thin curve) half-widths as well as CSP duration (T', dashed curve) with $c = \alpha\gamma/\beta\kappa$; $b = 11/64$.

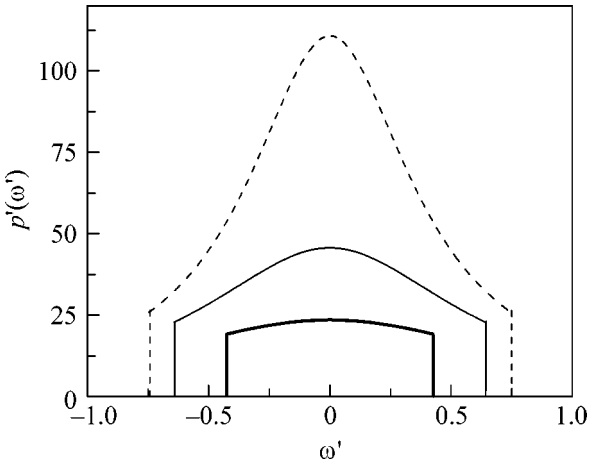

Fig. 2. Normalized spectral powers of CSP. $b = 0.1$ (thick), 0.186 (thin), and 0.215 (dashed); $c = 0.1$.

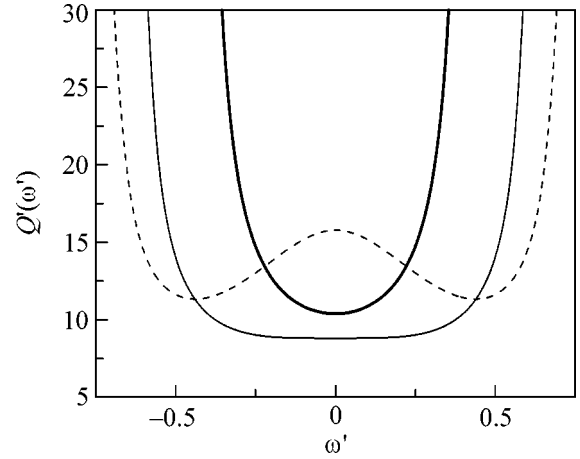

Fig. 3. Normalized chirps $Q'(\omega')$ corresponding to the spectra in Fig. 2.

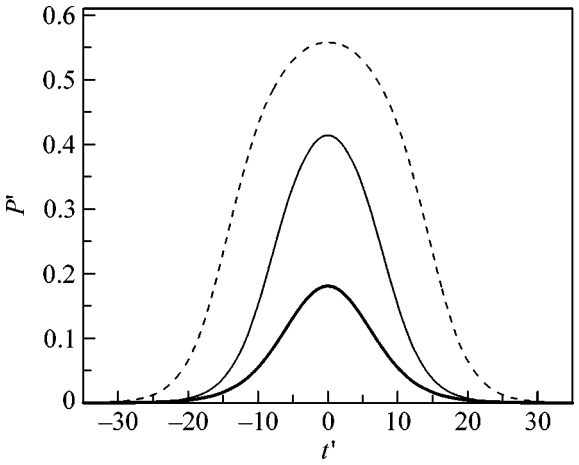

Fig. 4. Normalized time profiles of CSP corresponding to the spectra in Fig. 2.

parabolic-top spectra have a chirp minimum in the center (solid curves). At $c = c^*$ (or $b = 3(1 - c^2)/16$ for a fixed c), where the parabolic-top spectrum exists, the chirp varies most slowly with ω near the central frequency (thin curve). In contrast to the flat-top spectrum, this results from the disappearance of the squared dependence on ω:

$$Q(\omega) \simeq \frac{3\gamma^2}{2\beta\kappa\zeta}\frac{1}{\Delta^4 - \omega^4}.$$

At this point, the CSP peak power and its spectral half-width are

$$\gamma P_0 = \beta\Delta^2 = \frac{3\gamma}{8\zeta}(1 + c^*).$$

In contrast to the flat-top and parabolic-top spectra, the fingerlike one has a local chirp maximum in the spectrum center (dashed curve).

For all the spectral types of CSP, the chirp increases rapidly at the spectrum edges. The frequency dependence of the chirp limits its compressibility. A compressor with the dispersion $\simeq -Q(0)$ will produce an almost chirp-free pulse with the duration $\simeq 2/\Delta^* > 2/\Delta$. Here, the reduced spectral half-width $\Delta^* < \Delta$ corresponds to the spectral region around $\omega = 0$, where the frequency dependence of the chirp is weak. Therefore, the parabolic-top spectrum possessing a most weak frequency dependence of the chirp is most compressible. In agreement with the experiment [12, 13], CSP with the picosecond duration can be compressed by the factor $T\Delta \simeq 3\gamma/\kappa \simeq 100$, which allows producing femtosecond pulses with over-10 MW peak power at the MHz repetition rate.

The normalized time profiles are shown in Fig. 4. CSP with a flat-top spectrum has the solitonic-like time profile (thick curve). It is reasonable, because the limit of $\zeta \longrightarrow 0$ (i.e., $b \longrightarrow 0$) corresponds to the exact solitonic solution of the cubic CGLE. The fingerlike spectrum close to the boundary of the CSP existence corresponds to the parabolic-like (or even flat-top) time profile (dashed curve). Such a profile agrees with the numerical results of [4, 9] and is caused by the saturation of SAM around the pulse peak. The parabolic-top spectrum corresponds to the transitional time profile (thin curve).

The above-described method of the approximate integration of the cubic–quintic CGLE can be applied successfully to the various modifications of CGLE. For example, CGLE with the SAM term $\kappa P/(1 + \zeta P)$ is also integrable in the considered limits. The spectra in this case are also parabolic-top with the profiles:

$$p(\omega) \propto (\Delta^2 + A - \omega^2)/(\Delta^2 + B - \omega^2),$$

where $|\omega| < \Delta$; A, B, and Δ are the positive-definite functions of the CGLE parameters.

In conclusion, the new method of integration of the nonlinear CGLE was proposed in the limits of domination of GDD over the spectral dissipation as well as SPM over SAM. These limits are valid for both fiber and solid-state oscillators operating within NDR. The proposed method was realized for the cubic–quintic CGLE, but it is applicable also to CGLE with a more general nonlinearity. The approximated but highly accurate heavily-chirped solitary pulse solution of CGLE was obtained. It was found that CSPs have the flat-top, parabolic-top, and fingerlike spectra, which agree with the latest experimental data obtained from the high-energy oscillators. The parabolic-top spectrum corresponds to the most stable and compressible CSP. The wide spectrum of CSP in combination with its strong chirp allow compressing the pulse from picosecond down to femtosecond duration. As the microjoule energy is reachable for CSP, the over-10 MW peak power is available from an oscillator operating at the MHz repetition rate.

We are grateful to Drs. A. Apolonski and A. Chernykh for valuable discussions concerning both experimental and theoretical aspects of the NDR regime. V.L.K. acknowledges support from the Max-Planck Gesellschaft.

REFERENCES

1. I. S. Aranson and L. Kramer, Rev. Mod. Phys. **74**, 99 (2002).
2. M. J. Ablowitz and P. A. Clarkson, *Solitons, Nonlinear Evolution Equations and Inverse Scattering* (Cambridge Univ. Press, Cambridge, 1991).
3. N. N. Akhmediev and A. Ankiewicz, *Solitons, Nonlinear Pulses and Beams* (Chapman and Hall, London, 1997).
4. J. M. Soto-Crespo, N. N. Akhmediev, V. V. Afanasjev, and S. Wabnitz, Phys. Rev. E **55**, 4783 (1997).
5. J. M. Soto-Grespo and L. Pesquera, Phys. Rev. E **56**, 7288 (1997).

6. R. J. Deissler and H. R. Brand, Phys. Rev. Lett. **72**, 478 (1994).
7. J. M. Soto-Crespo, N. Akhmediev, and A. Ankiewicz, Phys. Rev. Lett. **85**, 2937 (2000).
8. D. Anderson, M. Desaix, M. Karlsson, *et al.*, J. Opt. Soc. Am. B **10**, 1185 (1993).
9. F. Ö. Ilday, J. R. Buckley, W. G. Clark, and F. W. Wise, Phys. Rev. Lett. **92**, 213902 (2004).
10. Sh. Chen and L. Yi, Phys. Rev. E **71**, 016606 (2005).
11. F. Ö. Ilday, F. W. Wise, and F. X. Kaertner, Opt. Express **12**, 2731 (2004).
12. A. Fernandez, T. Fuji, A. Poppe, *et al.*, Opt. Lett. **29**, 1366 (2004).
13. S. Naumov, A. Fernandez, R. Graf, *et al.*, New J. Phys. **7**, 216 (2005).
14. M. E. Fermann, V. I. Kruglov, B. C. Thomsen, *et al.*, Phys. Rev. Lett. **84**, 6010 (2000).
15. A. C. Peacock, R. J. Kruhlak, J. D. Harvey, and J. M. Dudley, Opt. Commun. **206**, 171 (2002).
16. V. L. Kalashnikov, E. Podivilov, A. Chernykh, *et al.*, New J. Phys. **7**, 217 (2005).
17. J. Herrmann, J. Opt. Soc. Am. B **11**, 498 (1994).
18. F. W. J. Olver, *Asymptotics and Special Functions* (Academic, New York, 1974; Nauka, Moscow, 1990).
19. H. A. Haus, J. Appl. Phys. **46**, 3049 (1975).

JETP Letters, Vol. 82, No. 8, 2005, pp. 472–476. Translated from Pis'ma v Zhurnal Éksperimental'noĭ i Teoreticheskoĭ Fiziki, Vol. 82, No. 8, 2005, pp. 529–533.

Induced Absorption Resonance on the Open $F_g = 1 \longrightarrow F_e = 2$ Transition of the D_1 Line of the ^{87}Rb Atom

A. S. Zibrov[a, b] and A. B. Matsko[c]

[a] *Lebedev Physical Institute, Russian Academy of Sciences, Leninskiĭ pr. 53, Moscow, 117924 Russia*

[b] *Department of Physics, Harvard University, Cambridge, Massachusetts 02138, USA*

e-mail: azibrov@cfa.harvard.edu

[c] *Jet Propulsion Laboratory, California Institute of Technology, 4800 Oak Grove Drive, Pasadena, California 91109-8099, USA*

Received August 1, 2005

Induced absorption resonance on the open $F_g = 1 \longrightarrow F_e = 2$ transition of the D_1 line of the ^{87}Rb atom has been observed. The effect of atomic motion on the formation of the resonance has been revealed. The numerical calculations are in good agreement with experiment. © *2005 Pleiades Publishing, Inc.*

PACS numbers: 42.50.Gy, 42.65.–k

Narrow atomic resonances are always important in spectroscopy, particularly in metrology. A new type of resonances was recently discovered in a degenerate two-level system and was called induced absorption resonance [1]. Rautian [2] pointed out that spontaneous coherence transfer plays an important and universal role in the formation of spectra. If transitions with approximately equal frequencies $\nu_{(m_1 - n_1)}$ and $\nu_{(m-n)}$, where m_i and n_i are the upper and lower levels, respectively, are coupled through spontaneous relaxation, it transfers coherence between the states $|m_i\rangle$ and $|n_i\rangle$. Rautian thought that the importance of this process is comparable with the importance of the spontaneous and stimulated emission processes introduced by Einstein. In the spectroscopy of a coherently prepared medium, coherence spontaneous transfer is clearly manifested when induced absorption resonance is observed. Its name appeared by analogy with induced transparency resonance. In the case of induced absorption resonance, absorption increases due to constructive interference between the quantum states of the system. Coherence is transferred between Zeeman sublevels due to a spontaneous process [3, 4].[1] As was recently predicted in [5], spontaneous coherence transfer could be efficiently used in the γ radiation range to control Mössbauer spectra. Analysis of spontaneous coherence transfer seems to be important, because this effect is the same in microwave and optical ranges, as well as in γ optics. This motivation stimulated us to analyze induced absorption resonance in the rubidium vapor and to present the results in this paper.

[1] Among other mechanisms of the formation of the induced absorption resonance, Goren *et al.* [4] analyzed population transfer between Zeeman sublevels.

Induced absorption resonance was first detected on the closed transition of the D_2 line of the Rb atom that absorbs two in-phase copropagating light waves [1]. It was pointed out that induced absorption resonance was observed when the degeneracy factor of the excited state exceeded the degeneracy factor of the ground state, i.e., $0 < F_g \le F_e = F_g + 1$ [6]. This effect was theoretically described in [7] for various intensities of the pump field, magnetic moments, and polarizations.

Signals associated with induced absorption resonance were also observed in experiment [8], where the Hanle configuration was used (laser light propagated along the magnetic-field direction). In that experiment, the atomic Rb vapor was pumped by a single linearly polarized wave. In the case of the degeneracy of the lower level of the ground state, bright resonances were detected in fluorescence with a concomitant increase in absorption. Those experimental results were theoretically analyzed in [9]. In the more recent work [10], it was shown that an increase in absorption in the Hanle configuration should also be expected when a laser beam is perpendicular to the magnetic field.

As was mentioned above, induced absorption resonance was observed on the closed transition of the degenerate ground state. The weak induced absorption resonance was also observed on the open $F_g = 2 \longrightarrow F_e = 2.3$ transition in the ^{85}Rb atom [8]. However, on the other open transition $F_g = 1 \longrightarrow F_e = 2$ of the D_1 line of the ^{87}Rb atom, the effect was not detected [11, 12]. It was assumed that this was due to optical pumping and the low degeneracy factor of the corresponding atomic states.

In this paper, we present the results of the experimental investigation of induced absorption resonance on the open $F_g = 1 \longrightarrow F_e = 2$ transition of the D_1 line

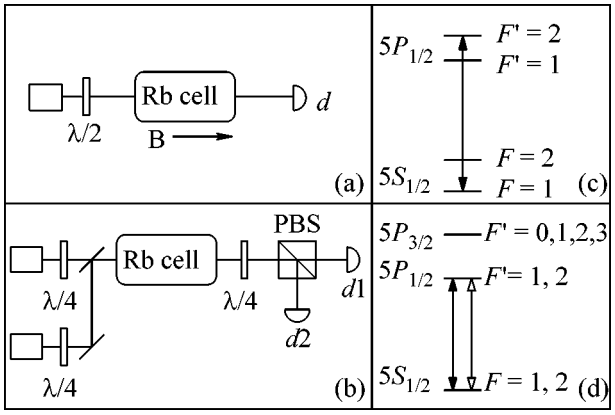

Fig. 1. Layouts of the experiments and the scheme of levels for observing induced absorption resonance. (a) The Hanle-configuration experiment, where the transmittance of the linearly polarized coherent light is detected as a function of the magnetic field *B*. (b) The experiment that involves a pump laser inducing atomic coherence and the probe laser. The transmission of a weak circularly polarized probe field is measured as a function of the frequency. The frequency of the pump laser is fixed. The rotation of the polarization of the pump field is opposite to the rotation of the polarization of the probe field. (c) The scheme of the levels of the D_1 line of the ^{87}Rb atom. (d) The scheme of the levels of the D_1 and D_2 lines of the ^{87}Rb atom.

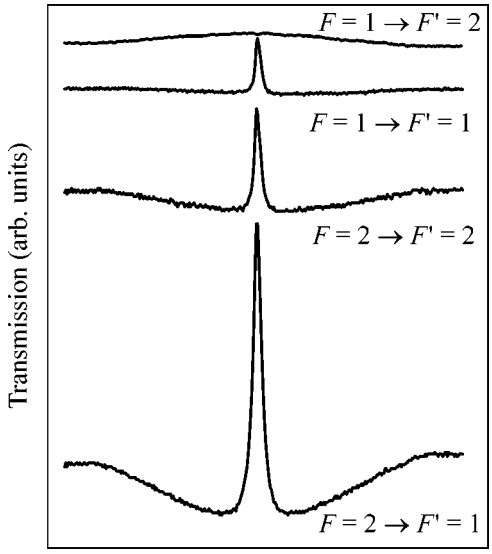

Fig. 2. Transmission of laser radiation vs. the longitudinal-field magnitude (see the layout in Fig. 1a). The laser frequency is tuned to the D_1 line of the ^{87}Rb atom. Transmission increases at zero magnetic field for all the transitions except for the $F = 1 \longrightarrow F' = 2$ transition (see Fig. 1c). The relative amplitudes of the resonances are not changed. The magnitude of the induced absorption resonance on the $F = 1 \longrightarrow F' = 2$ transition is very small and is equal to 0.2% of the total 60% absorption. The shape of the resonance is shown in Fig. 3.

of the ^{87}Rb atom that were obtained in the double-beam scheme [1] and in the Hanle configuration [8]. The observed effect appeared to be weak (0.2% of the total absorption due to the optical-pumping-induced depletion of the population). Optical pumping does not completely destroy spontaneous coherence transfer, which is responsible for the formation of induced absorption resonance, because the atoms interact with light for a finite time. Thus, this experiment corroborates that induced absorption resonance occurs on all $F_g \longrightarrow F_e = F_g + 1$ transitions both closed and open. The numerical calculation confirms the conclusions drawn using those experimental results.

We describe both experiments. The first experiment is the same as in [11]. Figure 1a shows the layout of the setup. An external-cavity laser was tuned to the D_1 or D_2 line of the ^{87}Rb atom (see Figs. 1c, 1d). A laser beam passed through a half-wave plate and a cell 3.0 cm in length that contained isotopically pure ^{87}Rb. The vapor density was controlled by the cell temperature. The transmission was detected by a photodiode *d*. The cell was placed in a three-shell magnetic screen. The longitudinal magnetic field is produced by a solenoid placed inside the screen. The static magnetic field gives rise to the appearance of Zeeman sublevels. The splitting was equal to the splitting $\mu_B B/\hbar$ between the neighboring Zeeman sublevels, where μ_B is the Bohr magneton. In the case of the ^{87}Rb atom, the splitting is equal to $0.7B$ MHz/G.

In the second experiment, two external-cavity lasers were used. The frequency of the laser creating coherence remained unchanged, whereas the frequency of the probe laser was scanned. The radiation of the strong laser after the passage through a quarter-wave plate became circularly polarized in the direction σ^+, whereas the radiation of the probe laser was polarized in the opposite direction σ^-. Downstream of the cell, beams were split by a quarter-wave plate and polarization cube (PBS) and were detected by photodetectors d_1 and d_2.

The magnetic-field dependence of the light transmission at four frequencies in the Hanle experiment was shown in Fig. 2. The cell temperature was equal to 50°C, the light power was 0.1 mW, and the beam diameter was equal to 1.5 mm. The transmission increases near the region where the magnetic field is zero for all transitions except for the $F = 1 \longrightarrow F' = 2$ transition. The absorption resonance with the subnatural width of the optical transition is almost unseen in the curve. This behavior was observed in [11].

After an increase in sensitivity, we detected this increase in absorption (see Fig. 3). The induced absorption resonance is broadened as the intensity of light increases and disappears at intensities above 20 mW/cm^2. The total increase in absorption is a con-

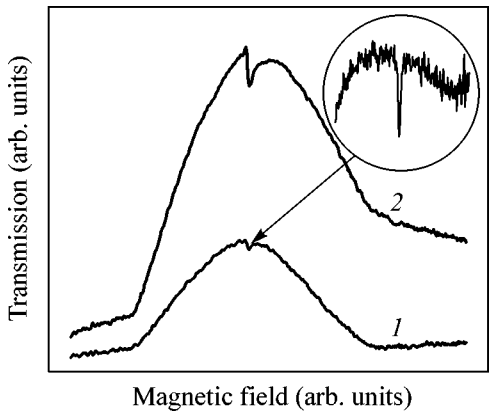

Fig. 3. Transmission of laser radiation vs. the magnetic field B in the experiment whose layout is shown in Fig. 1a. The laser is tuned to the open $F = 1 \longrightarrow F' = 2$ transition (of the D_1 line). Transmission increases at zero magnetic field. Lines *1* and *2* correspond to the laser-field intensities 1.5 and 3 mW/cm^2, respectively. A decrease in absorption on line *1* is equal to 3% of the total 60% absorption. The inset shows the fine structures of induced absorption resonance.

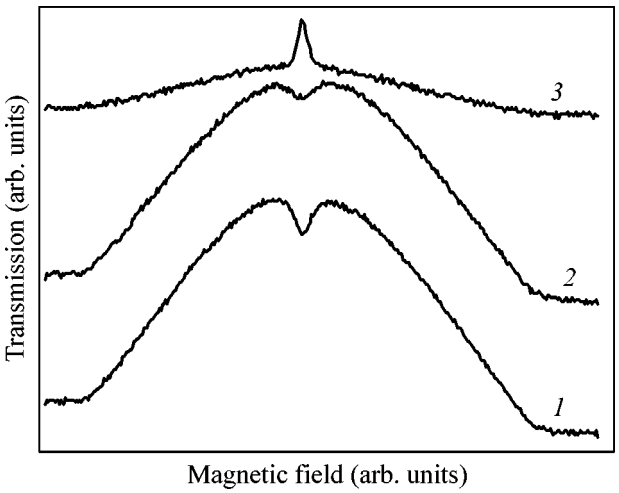

Fig. 4. Transmission of laser radiation vs. the magnetic field B in the experiment whose layout is shown in Fig. 1a (Hanle configuration). The laser is tuned near the transition $5S_{1/2}$, $F = 1 \longrightarrow 5P_{3/2}$, $F' = 0, 1, 2$ of the D_2 line of the rubidium atom: (*1*) the laser frequency is shifted by 250 MHz from the center of the Doppler profile toward the blue end, (*2*) the laser frequency is turned to the center of the Doppler profile, and (*3*) the laser frequency is shifted by 250 MHz from the center of the Doppler profile toward the red end. A decrease of absorption at the center of line *1* is equal to 2%, whereas the total absorption is equal to about 60%.

sequence of the depopulation of levels due to optical pumping.

An increase in absorption was also observed on the transition $5S_{1/2}$; $F = 1 \longrightarrow 5P_{3/2}$; $F' = 0, 1, 2$ of the D_2 line of rubidium. Unfortunately, the Doppler broadening prevents the resolution of all the transitions interacting with light in this transition. We measured the transmission for three different tunings of the laser frequency (see Fig. 4). An increase in absorption is easily seen with tuning to the high-frequency part of the Doppler profile. We emphasize that interaction with the $F = 1 \longrightarrow F' = 2$ transition is stronger at these frequencies, whereas interaction with the $F = 1 \longrightarrow F' = 0$ transition is stronger in the low-frequency range.

We studied induced absorption resonance in the "standard scheme" of experiments with induced absorption, where two lasers were used. The frequency dependence of the transmission of the radiation of the probe laser is shown in Fig. 5. The frequency of the laser creating coherence was tuned to the center of the Doppler profile of the $F_g = 1 \longrightarrow F' = 2$ transition. The power of this laser was equal to 3 mW, whereas the power of the probe laser was equal to 0.1 mW. The beams of both lasers had a diameter of 1.5 mm. Induced absorption resonance was located at the peak of the bell-shaped transparency resonance associated with optical pumping.

In order to explain the experimental results, numerical calculations based on the Maxwell–Bloch equations describing the propagation of the electromagnetic field in the cell are performed with the inclusion of all the Zeeman sublevels of the D_1 line of the ^{87}Rb atom. We studied the interaction with linearly polarized light tuned to the frequency of the $F_g = 1 \longrightarrow F_e = 2$ transition of the D_1 line. Light in the model propagates in the direction coinciding with the direction of the external magnetic field. The model also takes into account that atoms are continuously refreshed in the region of inter-

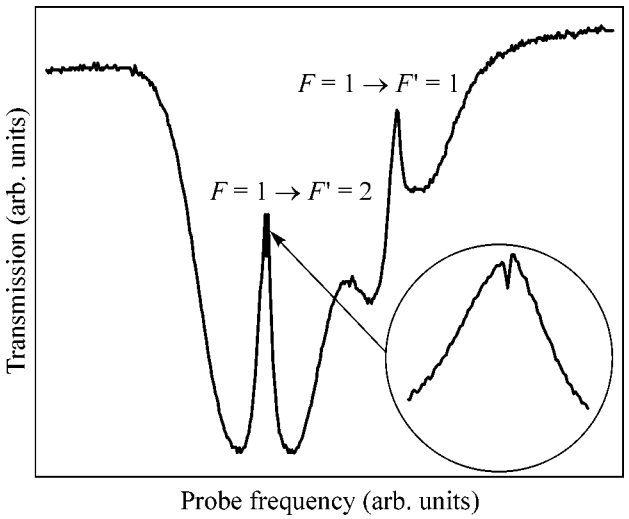

Fig. 5. Transmission I_{out}/I_{in} of the probe beam in the experiment whose layout is shown in Fig. 1b. The frequency of the laser inducing coherence is tuned to the open transition $5S_{1/2}$, $F = 1 \longrightarrow 5P_{1/2}$, $F' = 2$ (see Fig. 1d). The inset shows the resonance peak at an increased scale.

action with light due to influx from other regions of the cell. The rate γ_0 of this process is determined by the time of flight of atoms through the laser beam. The Bloch equations are the same as in [9]. The calculations were performed with $\gamma_0 = 0.0004\gamma$, where γ is the rate of the natural decay of the excited state, and the Rabi frequency $\Omega = 0.04\gamma$, which corresponds to the field intensity $I_{in} = 0.025$ mW/cm^2. The normalized magnetic-field dependence of the transmission of the incident radiation is shown in Fig. 6. Induced absorption resonance is seen near zero magnetic field. We emphasize that induced absorption resonance on this transition was not observed in the theoretical work [9].

As the intensity of the laser field increases, the contrast of induced absorption resonance decreases. Moreover, we observe in experiments that induced absorption resonance completely disappears at intensities of several milliwatts per centimeter squared. To understand this observation, we performed numerical simulation along the Doppler profile with $\gamma_0 = 0.003\gamma$ and $\Omega = 0.34\gamma$, which corresponds to an intensity of $I_{in} = 1.5$ mW/cm^2. The width of the velocity distribution was taken to be 100γ. The result of the numerical simulation is shown by the right line in Fig. 6, where it is seen that the behavior of the calculated line coincides with the experimentally observed dependence given by line *1* in Fig. 3.

The resulting differences shown in Figs. 6a and 6b are obviously caused by the motion of atoms. In order to ensure this conclusion, we calculated the population of the $F_e = 2$ excited state for the inhomogeneously broadened transition with various detunings Δ of the laser frequency (in other words, for groups of atoms with various velocities). The calculations were performed with the same Rabi frequencies and coherence decay rates as in the calculations presented in Fig. 6b and in the experiment (see Fig. 3). As is seen in Fig. 7, induced absorption resonance on the homogeneously broadened transition is not observed at zero detuning and only atoms with nonzero velocity contribute to the formation of the resonance. Such a behavior is due to the fact that atoms with lower velocities more rapidly leave the process of the formation of induced absorption resonance on the inhomogeneously broadened transition. Under the action of optical pumping, atoms efficiently decay into another level of the ground state and thereby the effect of spontaneous coherence transfer, which determines the formation of induced absorption resonance, is small.

Spontaneous coherence transfer is substantial for the $F_g \longrightarrow F_e = F_g + 1$ transition, because the population of the magnetic sublevels of the excited state exceeds the population of the sublevels of the states of the $F_g \longrightarrow F_e = F_g$ or $F_g \longrightarrow F_e = F_g - 1$ transitions under the same conditions. Atoms in these states are trapped in dark states due to coherent population trapping [13], whereas this is not the case for the $F_g \longrightarrow F_e = F_g + 1$ transition.

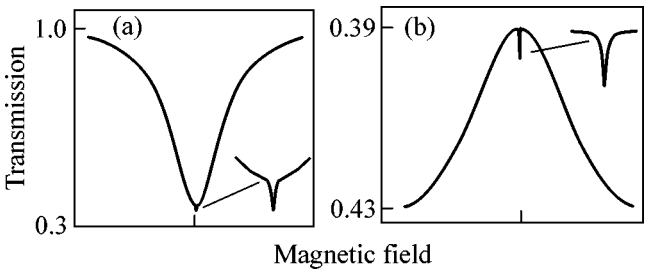

Fig. 6. Transmission I_{out}/I_{in} on the open $F = 1 \longrightarrow F' = 2$ transition vs. the magnetic field as obtained in the numerical calculation for (a) *homogeneously broadened* and (b) *Doppler broadened* rubidium vapor. The calculation was performed for the case shown in Fig. 1a.

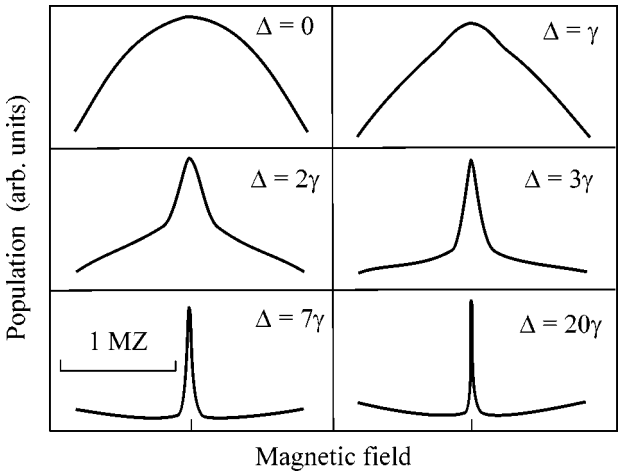

Fig. 7. Magnetic-field dependence of the population of the excited state for various detunings Δ for the homogeneously broadened $F = 1 \longrightarrow F' = 2$ transition. As the detuning Δ increases, the population decreases. The maximum population at $B = \Delta = 0$ is equal to 0.002. The maximum population for the detuning $\Delta = \gamma$, 2γ, 3γ, 7γ, and 20γ is equal to 0.98, 0.95, 0.89, 0.59, and 0.15, respectively. The intensity of the laser field and field–atom interaction are the same as in Fig. 6b. No subnatural width of resonance is observed for atoms with zero velocity.

It is also easy to explain why absorption on the induced absorption resonance near the open transition is small in our experiment. Near the open transition, atoms efficiently decay into another level of the ground state and thereby the effect of spontaneous coherence transfer, which determines the formation of induced absorption resonance, is small.

Thus, induced absorption resonance on the open $F_g = 1 \longrightarrow F_e' = 2$ transition of the D_1 line of rubidium has been observed in the experiment. Experiments show that induced absorption resonance is observed even in the presence of strong optical pumping on the

transition. Therefore, the previous statement made in [1] that a closed transition is necessary for observing induced absorption resonance should be revised. This study also shows that the intensity range for observing induced absorption resonance in a Doppler broadened medium is wider than that in a homogeneously broadened medium.

In conclusion, we try to explain why the induced absorption resonance on the open transition under investigation was not observed in the previous theoretical and experimental works cited above. The population of the open transition is equal to zero in the steady state. In a real experiment, fresh atoms from other regions of the cell enter the region of atom–light interaction. This process maintains a nonzero population of the state. The shorter the interaction time, the larger the number of atoms in the excited state. However, when the interaction time is too short, coherence degrades. It is necessary to search for the optimum interaction time. The interaction time is determined by the laser-beam radius. An increase in the radius increases the interaction time. In our experiment, we chose the beam radius according to the available intensities. We think that optimization determined the success in the observation of the induced absorption resonance in this experiment.

We are grateful to V.L. Velichanskiĭ and V.P. Yakovlev for interest in this work and stimulating discussions.

REFERENCES

1. A. M. Akulshin, S. Barreiro, and A. Lezama, Phys. Rev. A **57**, 2996 (1998).
2. S. G. Rautian, Zh. Éksp. Teor. Fiz. **108**, 1186 (1995) [JETP **81**, 651 (1995)]; Zh. Éksp**.** Teor. Fiz. **115**, 12 (1999) [JETP **88**, 6 (1999)].
3. A. V. Taichenachev, A. M. Tumaikin, and V. I. Yudin, JETP Lett. **69**, 819 (1999); Phys. Rev. A **61**, 011802 (2000).
4. C. Goren, A. D. Wilson-Gordon, M. Rosenbluh, and H. Friedmann, Phys. Rev. A **70**, 043814 (2004).
5. R. Coussement, Y. Rostovtsev, J. Odeurs, *et al.*, Phys. Rev. Lett. **89**, 107601 (2002).
6. A. Lezama, S. Barreiro, and A. M. Akulshin, Phys. Rev. A **59**, 4732 (1999).
7. A. Lipsich, S. Barreiro, A. M. Akulshin, and A. Lezama, Phys. Rev. A **61**, 053803 (2000); A. Lipsich, S. Bareiro, P. Valente, and A. Lezama, Opt. Commun. **190**, 185 (2001).
8. Y. Dancheva, G. Alzetta, S. Cartaleva, *et al.*, Opt. Commun. **178**, 103 (2000).
9. F. Renzoni, C. Zimmermann, P. Verkerk, and E. Arimondo, J. Opt. B: Quantum Semiclassic. Opt. **3**, S7 (2001).
10. F. Renzoni, S. Cartaleva, G. Alzetta, and E. Arimondo, Phys. Rev. A **63**, 065401 (2001).
11. F. Renzoni, W. Maichen, L. Windholz, and E. Arimondo, Phys. Rev. A **55**, 3710 (1997).
12. G. Alzetta, S. Cartaleva, Y. Dancheva, *et al.*, J. Opt. B: Quantum Semiclassic. Opt. **3**, 181 (2001).
13. E. Arimondo, in *Fundamentals of Quantum Optics III*, Ed. by F. Ehlotz (Springer, Berlin, 1993); Lect. Notes Phys. **420**, 170 (1994); in *Progress in Optics*, Ed. by E. Wolf (Elsevier, Amsterdam, 1996), p. 257.

Translated by R. Tyapaev

JETP Letters, Vol. 82, No. 8, 2005, pp. 477–481. Translated from Pis'ma v Zhurnal Éksperimental'noĭ i Teoreticheskoĭ Fiziki, Vol. 82, No. 8, 2005, pp. 534–538.

Experimental Investigation of the Dark Pseudoresonance on the *D*1 Line of the ^{87}Rb Atom Excited by a Linearly Polarized Field

S. A. Zibrov[a, b], V. L. Velichansky[a, b], A. S. Zibrov[a, e], A. V. Taĭchenachev[c, d], and V. I. Yudin[c, d]

[a] *Lebedev Physical Institute, Russian Academy of Sciences, Leninskiĭ pr. 53, Moscow, 117924 Russia*

[b] *Moscow Engineering Physics Institute (State University), Kashirskoe sh. 31, Moscow, 115409 Russia*

e-mail: szibrov@yandex.ru

[c] *Institute of Laser Physics, Siberian Division, Russian Academy of Sciences, pr. Lavrent'eva 13/3, Novosibirsk, 630090 Russia*

[d] *Novosibirsk State University, ul. Pirogova 2, Novosibirsk, 630090 Russia*

[e] *Department of Physics, Harvard University, Cambridge, Massachusetts 02138, USA; Harvard–Smithsonian Center for Astrophysics, Cambridge, Massachusetts 02138, USA*

Received August 22, 2005

The measurements of the metrological characteristics (amplitude, width, and shift in the magnetic field) of the dark pseudoresonance, which was proposed by Kazakov *et al.* [quant-ph/0506167] as the reference resonance for an atomic frequency standard, are reported. It has been shown that the characteristics of the pseudoresonance are worse than those of the unsplit electromagnetically induced transparency resonance for the excitation scheme with the lin||lin polarization on the *D*1 line of the ^{87}Rb atom. © *2005 Pleiades Publishing, Inc.*

PACS numbers: 42.50.Gy, 42.65.–k, 42.65.Ky

Since the 1970s, two-photon resonances free of Doppler broadening have been successfully used as a reference for quantum frequency standards [1, 2]. In 1993, the effect of coherent population trapping was proposed to be used to create a microwave frequency standard based exclusively on optical elements without a UHF cavity [3]. In recent years, the possibility of creating an atomic clock based on this effect is actively analyzed [4–7]. Two copropagating laser fields acting on the allowed electric dipole transitions in the Λ configuration create a long-lived superposition of states in hyperfine sublevels of alkali-metal atoms. When the difference between the frequencies varies near the hyperfine splitting frequency Δ_{hfs}, the transmission resonance is observed (coherent population trapping resonance or Λ resonance). The resonance width in the limit of low intensities is determined by the coherence lifetime in the ground state. To date, a frequency stability of 6.4×10^{-13} (τ = 2000 s) is reached in such a UHF standard [6]. Moreover, the possibility of a radical decrease in the volume of quantum discriminators of the coherent population trapping clock on Cs and Rb (to about 10 mm^3) was demonstrated [8, 9]. Investigations in this direction are actively continued.

It is known that the stability of quantum frequency standards increases with increasing the amplitude A of the resonance and with decreasing its width W [5, Eq. (8)]:

$$\sigma(\tau) \sim \sqrt{\eta I_{bg}}\frac{1}{\Delta_{hfs}}\frac{W}{A}\tau^{-1/2}, \qquad (1)$$

where $\sigma(\tau)$ is the Allan parameter, Δ_{hfs} is the standard frequency, and I_{bg} is the background caused by radiation that is not absorbed by the medium. For this reason, the search for schemes for the excitation of the coherent population trapping resonance with high contrast (>5%), minimum width, and light shift is of current interest for an increase in the stability of the clock.

A "push–pull" pumping scheme that allows the production of a pure coherent state was proposed in [9]. Atoms in such a state do not interact with the field; i.e., the atom–field interaction operator is equal to zero: $-(\hat{\mathbf{d}}\,\mathbf{E})|\mathrm{Dark}\rangle = 0$, where $|\mathrm{Dark}\rangle$ is the coherent superposition of the wave functions of the Zeeman sublevels of the ground state. In that work, a contrast of about 30% was experimentally achieved. The pure dark state prepared by means of a standing wave was also demonstrated in [10]. In [11], it is shown that, when the red detuning of the frequency of the pump field is equal to the hyperfine splitting Δ_{hfs} of the ground state, a contrast of about 20% is reached with almost zero shifts. We note that, although that work does not involve the coherent population trapping effect, it is close to the subject under discussion in its aim, the use of the

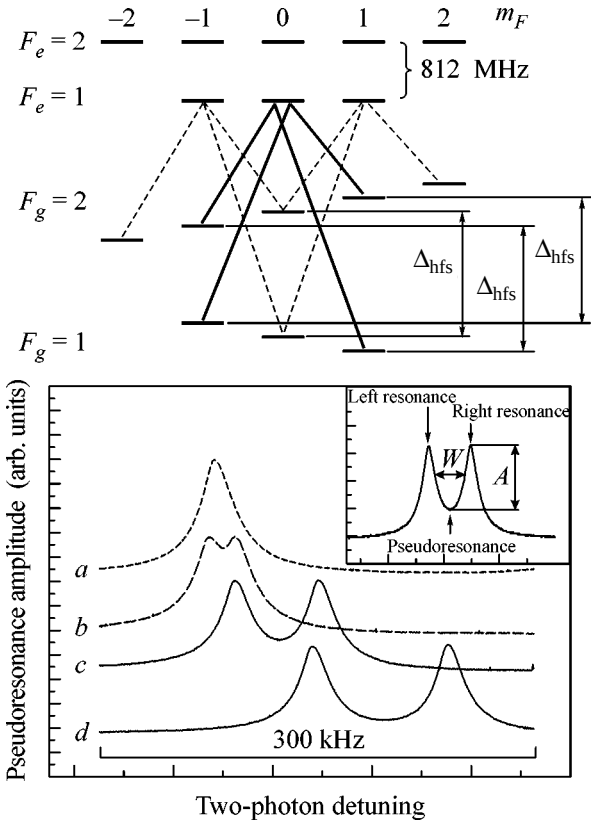

Fig. 1. (Upper panel) The scheme of the lin||lin excitation of the two-photon transition ($F = 1 \longleftrightarrow F = 2$) $5S_{1/2}$ of the $D1$ line of the ^{87}Rb atom. The lower panel illustrates the appearance of the pseudoresonance as the longitudinal magnetic field increases: (*a*) 0.35, (*b*) 3.0, (*c*) 9.0, and (*d*) 15 G; *A* and *W* are the amplitude and width of the resonance, respectively. The total power of the laser radiation was equal to 2 mW and the beam diameter was equal to 4 mm.

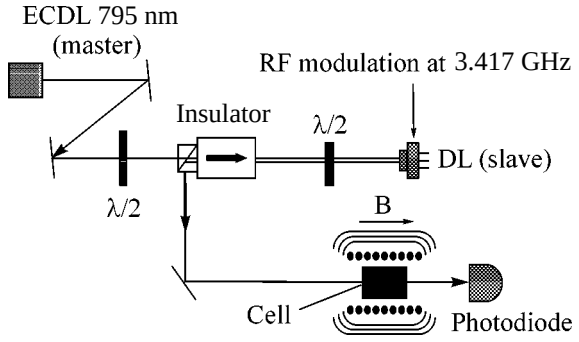

Fig. 2. Layout of the setup: the ECDL is the external-cavity injection laser, the DL is the diode laser, the Insulator is the insulator with a reflection suppression factor of 60 dB. The cell temperature was equal to 50°C.

bichromatic field, and the Λ configuration of the involved processes. In order to improve the metrological characteristics of the coherent population trapping resonance, the pulse scheme of detecting the resonance was studied by the Ramsey method [12]. A unique possibility was pointed out in [13] for forming the pure coherent population trapping resonance (free of trap states) due to the interaction between the bichromatic field with lin||lin polarized components and the $5P_{1/2}$ state of ^{87}Rb atoms. In that case, a pure dark state appeared under the action of the linearly polarized bichromatic field under the condition of the spectral resolution of the hyperfine structure of the excited state (Fig. 1). The achievement of a contrast of about 50% was reported in that work. It was pointed out that the magnetic field sensitivity (quadratic Zeeman shift) of the proposed resonance should be 1/1.33 of the shift of the resonance formed due to excitation by the circularly polarized bichromatic field (σ^+–σ^+ scheme). In that work, it was also noted that the resonance was split into two resonances in high magnetic fields. This splitting arises because the *g* factors of two hyperfine sublevels of the ground state are slightly different due to the nuclear-spin contribution.

In [14], it was proposed to use a dip arising due to such a splitting of the resonance as the reference for the UHF standard (see Fig. 1). The authors of [14] referred to the dip as pseudoresonance, because it appeared due to the splitting of the coherent population trapping resonance in the magnetic field. The estimates made in that work showed the possibility of reaching a frequency stability of $10^{-14}/\sqrt{\tau}$. Such a high stability would enable one to consider the pseudoresonance as a high-priority and promising tool for creating atomic frequency standards based on the coherent population trapping effect. For this reason, theoretical and experimental investigation of the pseudoresonance, as well as comparison with the unsplit coherent population trapping resonance, seems to be of interest.

In this paper, the experimental results on certain metrological characteristics of the pseudoresonance are reported. It is shown that they are worse than those of the initial (unsplit) coherent population trapping resonance.

Figure 2 shows the layout of the experimental setup that consists of a laser system, a cell filled with ^{87}Rb vapor, and a detection system. The experiment was conducted with a Pyrex cylindrical cell (40 mm in length and 25 mm in diameter) containing Ne at a pressure of 4 Torr and isotopically pure ^{87}Rb. The cell was placed inside a solenoid, which provided variation in the longitudinal magnetic field. To screen the external laboratory field, the cell was placed inside three cylindrical magnetic screens. The heating of the cell was performed by means of a bifilar nichrome wire coiled around the inner magnetic screen. The cell temperature was equal to 50°C. The bichromatic resonance field was produced by modulating the current of a laser ("slave") whose frequency was optically matched by the frequency of a single-mode external-cavity injec-

tion laser (ECLD, "master"). To this end, the radiation of the latter laser was injected through a diplexer into the active region of the driven laser (DL). In this case, the modulation did not violate the regime of the maser laser (ECLD). The injection current of the driven laser (DL) was modulated at a frequency of $\Delta_{hfs}/2 = 3.417$ GHz by means of an Agilent E8257D-502 UHF generator, which was connected to the driven laser through a Minicircuits ZFBT-6G T bias. Such a procedure ensured the generation of resonant optical fields with a high correlation degree of phase noises. The ratio of the intensities of these fields could be changed by slightly varying the current of the driven laser. The resonant fields carried approximately 50% of the total power of the radiation (2 mW). The ratio of the intensities of the resonant fields was equal to 1.4. In this case, the amplitude of the coherent population trapping resonance was maximal. The remaining power was contained in the carrying and higher order side frequencies. The laser beam in the cell had a diameter of 4 mm. The coherent population trapping resonance was excited by the linearly polarized first-order components, which were tuned to the $F_g = 1 \longleftrightarrow F_e = 1$ and $F_g = 2 \longleftrightarrow F_e = 1$ transitions. The intensity of the radiation passed through the cell was measured by a photodiode. In order to study the pseudoresonance, the modulation frequency $\Delta_{hfs}/2$ was linearly scanned in a narrow range (~150 kHz) for various magnetic fields. The amplitude and width (Fig. 3) of the resonance, as well as its amplitude-to-width ratio and its position (Fig. 4), were studied as functions of the magnetic field.

In the absence of the magnetic field, the amplitude of the coherent population trapping resonance is one order of magnitude less than the amplitudes of the resonances observed in the presence of the magnetic field. In the presence of the magnetic field, this resonance is split into three resonances: the magnetically independent central resonance at the transition frequency Δ_{hfs} and two magnetically dependent resonances. The central resonance is formed by two Λ transitions: $\{|F_g = 1, m_F = -1\rangle \longleftrightarrow |F_e = 1, m_F = 0\rangle \longleftrightarrow |F_g = 2, m_F = 1\rangle\}$ and $\{|F_g = 2, m_F = -1\rangle \longleftrightarrow |F_e = 1, m_F = 0\rangle \longleftrightarrow |F_g = 1, m_F = 1\rangle\}$. The main contribution to the magnetically dependent resonances comes from the following Λ transitions: $\{|F_g = 2, m_F = -1\rangle \longleftrightarrow |F_e = 1, m_F = 0\rangle \longleftrightarrow |F_g = 1, m_F = -1\rangle\}$ and $\{|F_g = 2, m_F = +1\rangle \longleftrightarrow |F_e = 1, m_F = 0\rangle \longleftrightarrow |F_g = 1, m_F = 1\rangle\}$. Immediately after the appearance of the magnetic field, the amplitude of the central resonance increases and its contrast reaches 40%. The amplitude of the magnetically dependent resonances also increases to 12%. The resonances grow upon the appearance of the magnetic field, because the removal of degeneration destroys dark trap states on the Zeeman sublevels that belong to the same hyperfine level and on which atoms "are hidden." To destroy these traps, a magnetic field whose magnitude is higher than the width of the resonance is necessary. In not too strong fields, the width of the resonance is determined

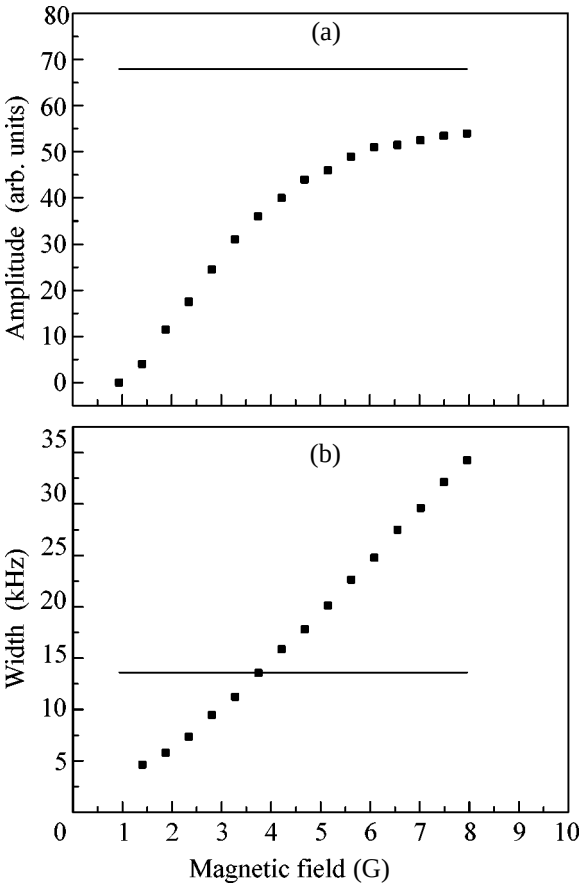

Fig. 3. Magnetic-field dependence of the (a) amplitude A and (b) width W of pseudoresonance, where the horizontal straight lines show the respective values of the unsplit coherent population trapping resonance in the presence of a magnetic field of 0.2 G.

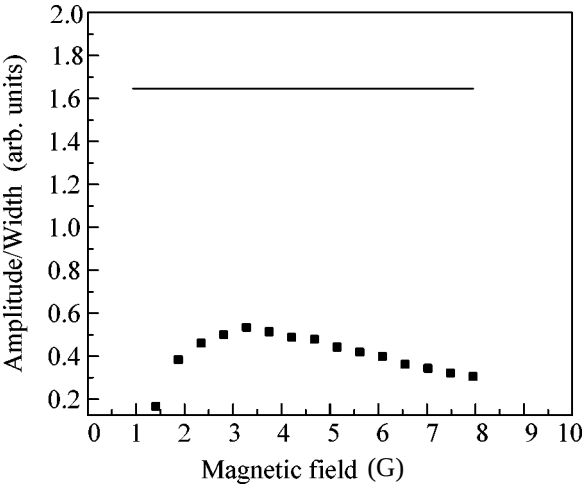

Fig. 4. Magnetic-field dependence of the amplitude-to-width ratio for the pseudoresonance, where the horizontal straight line shows the ratio for the unsplit coherent population trapping resonance in the presence of a magnetic field of 0.2 G.

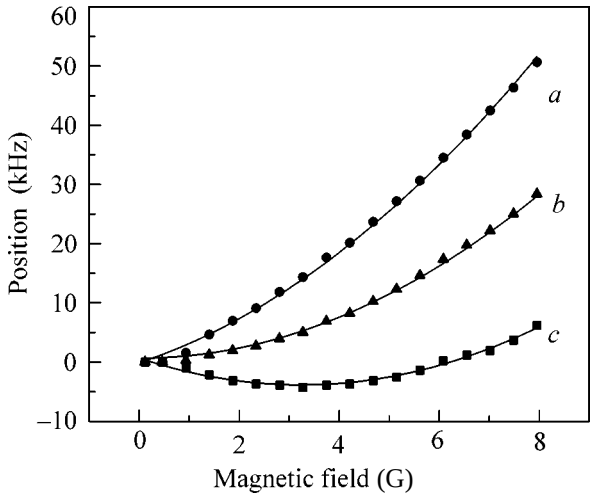

Fig. 5. Magnetic-field dependence of the position of the (*a*) right resonance, (*b*) pseudoresonance, and (*c*) left resonance. The origin of the abscissa axis corresponds to the position of the unsplit coherent population trapping resonance. The points are experimental data and lines are approximations.

by the optical pumping rate for the ground state [15]. A further increase in the magnetic field (to 0.5 G, see Fig. 5) results in a new splitting of the central resonance. In this way, the pseudoresonance appears. The amplitude of the pseudoresonance is saturated at a magnetic field exceeding 7.0 G but does not reach the amplitude of the initial coherent population trapping resonance, see Fig. 3a. The width of the pseudoresonance becomes less than the width of the initial resonance at a magnetic field of less than 4.0 G, for which the amplitude of the pseudoresonance is very small.

It is seen in Fig. 4 that the maximum A/W ratio is reached at a magnetic field of about 3.4 G. For this field, both the width and amplitude of the pseudoresonance are less than the respective values of the initial resonance. The ratio A/W for the pseudoresonance is worse at any magnetic field. It is worth noting that, for matching the quartz-oscillator frequency in the atomic clock, resonances with a sharp peak (with a larger slope of the first derivative) are preferable over those with a smooth peak, as in the case of the pseudoresonance.

We point to one more feature of the behavior of the split resonance. Figure 5 shows the shift of (lines *a* and *c*) two true coherent population trapping resonances and (line *b*) the pseudoresonance as the longitudinal field varies. This dependence for the coherent population trapping resonances has the form (see, e.g., [14])

$$\Delta = \Delta_{\rm hfs} \pm \frac{2g_I\mu_{\rm N}}{\hbar}H + \frac{3g_J^2\mu_{\rm B}^2}{8\omega_{\rm hfs}\hbar^2}H^2, \qquad (2)$$

where $\mu_{\rm B}$ is the Bohr magneton, $\mu_{\rm N}$ is the nuclear magneton, and g_I and g_J are the nuclear and electron Lande factors, respectively. It is seen that the shift of the coherent population trapping resonances are the sum of the linear and quadratic contributions from both transitions $m_F = -1 \longleftrightarrow m_F = +1$ (left resonance) and $m_F = +1 \longleftrightarrow m_F = -1$ (right resonance) involved in the formation of the reference resonance. For low magnetic fields, the left resonance is shifted from the right resonance (and from the pseudoresonance) according to the linear law. However, as the field increases, the left resonance changes the direction of its shift and begins to move in the same direction as the right resonance, because the quadratic term begins to dominate in Eq. (2). From experimental line *b*, the quadratic dependence of the position of the dark resonance on the magnetic field is found with a coefficient of about 0.43 ± 0.04 kHz/G^2 [see Eq. (2)]. As was predicted in [13], this coefficient is less than the corresponding coefficient for the standard atomic clock by a factor of 1.33 [16].

In this work, certain metrological characteristics of the dark pseudoresonance have been experimentally studied. The results provide the conclusion that these characteristics are noticeably worse than the respective characteristics of the initial (unsplit) coherent population trapping resonance from which the pseudoresonance appears. Thus, we think that the use of the pseudoresonance as the reference for the atomic clock is not an optimum solution when using the lin||lin excitation scheme on the $D1$ line of the ^{87}Rb atom. At least more detailed theoretical investigation is required for determining the experimental conditions (cell sizes, buffer-gas pressure, etc.) under which the pseudoresonance could be preferable over the unsplit coherent population trapping resonance.

We are grateful to Tamara Zibrova for the high-quality blooming of the mirrors of the laser diodes. The work of A.V.T. and V.I.Yu. was supported by INTAS (grant no. 01-0855) and the Russian Foundation for Basic Research (project nos. 05-02-17086 and 04-02-16488).

REFERENCES

1. V. S. Letokhov and V. P. Chebotayev, *Nonlinear Laser Spectroscopy* (Nauka, Moscow, 1975; Springer, Berlin, 1977).
2. W. Demtroder, *Laser Spectroscopy: Basic Concepts and Instrumentation*, 3rd ed. (Springer, Berlin, 2002; Nauka, Moscow, 1985).
3. N. Cyr, M. Têtu, and M. Breton, IEEE Trans. Instrum. Meas. **42**, 640 (1993).
4. S. Knappe, R. Wynands, J. Kitching, *et al.*, J. Opt. Soc. Am. B **18**, 1545 (2001).
5. J. Vanier, M. W. Levine, D. Janssen, and M. J. Delaney, IEEE Trans. Instrum. Meas. **52**, 822 (2003).
6. M. Merimaa, T. Lindwall, I. Tittonen, and E. Ikonen, J. Opt. Soc. Am. B **20**, 273 (2003).
7. J. Vanier, A. Godone, and F. Levi, Phys. Rev. A **58**, 2345 (1998).
8. Li-Anne Liew, S. Knappe, J. Moreland, *et al.*, Appl. Phys. Lett. **84**, 2694 (2004).

9. Y.-Y. Jau, E. Miron, A. B. Post, *et al.*, Phys. Rev. Lett. **93**, 160802 (2004).
10. A. V. Taichenachev, V. I. Yudin, V. L. Velichansky, *et al.*, Pis'ma Zh. Éksp. Teor. Fiz. **80**, 265 (2004) [JETP Lett. **80**, 236 (2004)].
11. S. Zibrov, I. Novikova, D. F. Phillips, *et al.*, Phys. Rev. A **72**, 011801(R) (2005).
12. T. Zanon, S. Guerandel, E. de Clercq, *et al.*, Phys. Rev. Lett. **94**, 193002 (2005).
13. S. A. Zibrov, Y. O. Dudin, V. L. Velichansky, *et al.*, in *Abstract Book of ICONO'05* (St. Petersburg, Russia, 2005); A. V. Taichenachev, V. I. Yudin, V. L. Velichansky, and S. A. Zibrov, Pis'ma Zh. Éksp. Teor. Fiz. **82**, 449 (2005) [JETP Lett. **82**, 398 (2005)].
14. G. Kazakov, B. Matisov, I. Mazets, *et al.*, quant-ph/0506167.
15. E. Arimondo, in *Progress in Optics*, Ed. by E. Wolf (Elsevier, Amsterdam, 1996), p. 257; M. Erhard and H. Helm, Phys. Rev. A **63**, 043813 (2001).
16. J. Vanier and C. Audoin, *The Quantum Physics of Atomic Frequency Standards* (Adam Hilger, New York, 1989).

Translated by R. Tyapaev

JETP Letters, Vol. 82, No. 8, 2005, pp. 482–486. From Pis'ma v Zhurnal Éksperimental'noĭ i Teoreticheskoĭ Fiziki, Vol. 82, No. 8, 2005, pp. 539–543.

Quantum Limits of Feedback Cooling in Optical Lattices¶

T. Yu. Ivanova and D. A. Ivanov

Laser Research Institute, St. Petersburg State University, St. Petersburg, 198504 Russia

e-mail: tanya@home.rclph.spbu.ru

Received July 4, 2005; in final form, September 29, 2005

A quantum-mechanical analysis of feedback cooling [see Phys. Rev. Lett. **94**, 153002 (2005)] of atoms trapped in a far-off-resonant optical lattice is presented. The model considered is valid for ultralow energies of atoms, thus, allowing for the study of an ultimate cooling limit. The influence of the measurement-induced noise and feedback-induced atom–atom correlations on the cooling efficiency is discussed. It is shown that there are regimes where the quantum noise can be effectively compensated for. © *2005 Pleiades Publishing, Inc.*

PACS numbers: 32.80.Pj, 42.50.Lc

At present, manipulation and control of single atoms and atomic ensembles represent important challenges for experimentalists and theoreticians. A widely used strategy for manipulating atoms is based on the resonant interaction of atoms with laser fields [1]. However, application of resonant fields considerably restricts the controllability due to the noise induced by spontaneous emission. Moreover, only atomic species possessing specific cyclic transitions resonant with available lasers can be addressed in this case.

On the other hand, the range of accessible atomic species can be extended and the spontaneous-emission noise can be diminished if one could use far-off-resonant laser fields to control atoms. In this case, the mechanism of manipulation would be the nonresonant interaction of the induced atomic dipole moment with laser light (ac Stark effect), which results in a dipole force acting on atoms. This mechanism can be conveniently realized in far-off-resonant optical lattices. An optical lattice is a periodic light-shift potential seen by neutral atoms located inside an interference pattern formed by laser beams tuned far from the atomic transition. Adjusting the wavelength, polarization, and intensity of the lasers forming the optical lattice, one can flexibly control the motion of cold atoms [2–5].

In particular, some years ago, the possibility of using feedback to control the motion of cold atoms in a one-dimensional optical lattice was experimentally demonstrated [6]. As is also proposed in [6], the concept of feedback can be applied to cool atoms in a manner similar to stochastic cooling [7, 8]. In a recent paper [9], the realization of such a feedback cooling (termed as "optical shaking") was elaborated in more detail, and the operation of this cooling technique has been studied in the classical limit. The classical approach developed in [9] can be successfully applied to describe cooling in the case of sufficiently high energies of atoms. However, it does not apply in the limit of low energies when quantum effects start to play a significant role. In this case, the noise introduced into the system due to the measurement can strongly restrict the cooling efficiency and therefore should not be ignored. Furthermore, as will be shown below, the cooling efficiency is also influenced by atom–atom correlations, which appear due to the feedback process itself. The effect of these correlations is not evident from the discussions in [9].

In this letter, the feedback cooling of atoms in optical lattices is studied on the basis of the quantum theory. Such an approach will allow us to study the effect of both feedback-induced noise and atom–atom correlations on the cooling efficiency at low temperatures and estimate the cooling limit as well.

We restrict our consideration to the case of a one-dimensional optical lattice. In the limit of low temperatures, the optical lattice potential can be approximated by the array of harmonic potential wells with each well containing only one atom. The tunneling of atoms between neighboring potential wells can be neglected, which allows us to distinguish atoms according to the specific potential well they belong to. Consequently, the quantum statistics of atoms is not of relevance in the considered model. Furthermore, being trapped in separate potential wells, the atoms interact weakly with each other, which does not affect the evolution of the system considerably and can be also neglected. In this case, as will be shown below, a rather complete analysis of the evolution of the system's state is possible.

The feedback loop is organized as follows. The first step is the measurement of the collective coordinate of atoms, which is the position of atoms with respect to the

¶ The text was submitted by the authors in English.

center x_i of their wells averaged over all wells or, equivalently, over all atoms

$$\hat{Q} = \frac{1}{N}\sum_{i=1}^{N}(\hat{q}_i - x_i). \quad (1)$$

Here, N is the total number of atoms, which is assumed to be fixed, and $\hat{q}_i$ is the coordinate of the ith atom. The constant c number

$$\frac{1}{N}\sum_{i=1}^{N}x_i \quad (2)$$

can be ignored.

The average coordinate (1) is obtained experimentally by measuring the imbalance in the intensities of laser beams forming the lattice, which appears due to the interaction with atoms (see [6] for experimental details).

Then, the measurement outcome Q of the observable $\hat{Q}$ is used to perform the spatial translation of the optical-lattice potential to compensate for the measured coordinate. The compensation of this coordinate leads to the decrease of the total potential energy of atoms and, hence, to cooling of the gas.

The time duration of the measurement and the lattice shift is assumed to be negligibly small compared with the characteristic time of the free evolution of atoms in the lattice potential [6]. Therefore, the oscillations of atoms in the lattice potential during the feedback operation will be neglected.

The quantum state of the system after a single feedback step is given by the density operator $\hat{\rho}_+$:

$$\hat{\rho}_+ = \int dQ\hat{U}(Q)\hat{M}(Q)\hat{\rho}_-\hat{M}^+(Q)\hat{U}^+(Q). \quad (3)$$

Here, $\hat{\rho}_-$ is the many-atom density operator before the feedback, the operator $\hat{M}(Q)$ describes the effect of the measurement on the system conditioned on the measurement outcome Q, and $\hat{U}(Q)$ is the unitary shift of the collective coordinate $\hat{Q}$ to zero. In general, the feedback is an automatic process requiring no intervention of an experimentalist. Thus, the quantum state of the system after the feedback is obtained averaging over all the possible measurement outcomes Q.

To include imprecision, measurements are described in terms of operators constituting a positive operator-valued measure (POVM) [10]. Thus, the operators $\hat{M}(Q)$ appearing in Eq. (3) are the measurement resolution amplitudes constituting POVM. The simplest choice for these operators is a Gaussian operator

$$\hat{M}(Q) = \left(\frac{1}{2\pi\sigma^2}\right)^{1/4}\exp\left[-\frac{(\hat{Q}-Q)^2}{4\sigma^2}\right], \quad (4)$$

where σ is the resolution of a measurement device.

The shift of the collective coordinate of atoms to zero being actually a one-parametric shift transformation is described by the unitary operator

$$\hat{U}(Q) = \exp(iQ\hat{P}), \quad (5)$$

where the generator

$$\hat{P} = \sum_{i=1}^{N}\hat{p}_i \quad (6)$$

is the total momentum of the atoms. The operator $\hat{p}_i$ in this equation is the momentum of the ith atom. The operator $\hat{P}$ is the canonical conjugate to $\hat{Q}$ with the standard commutator $[\hat{Q}, \hat{P}] = i$.[1] It may be shown using this commutator that the operator $\hat{U}(Q)$ acts on the observable $\hat{Q}$ as

$$e^{-iQ\hat{P}}\hat{Q}e^{iQ\hat{P}} = \hat{Q} - iQ[\hat{P}, \hat{Q}] = \hat{Q} - Q \quad (7)$$

resulting in the required shift of $\hat{Q}$ by $-Q$.

It is advantageous to use a phase-space representation of the quantum state of the system introducing the many-atom Wigner function defined as

$$W(\mathbf{p}, \mathbf{q}) = \frac{1}{\pi^N}\int d^N y e^{-2i\mathbf{yp}}\langle \mathbf{q}+\mathbf{y}|\hat{\rho}|\mathbf{q}-\mathbf{y}\rangle. \quad (8)$$

Here, $\mathbf{q} = \{q_1, q_2, \ldots, q_N\}$ and $\mathbf{p} = \{p_1, p_2, \ldots, p_N\}$ denote the vectors with components being the single-atom coordinates and momenta, respectively. The many-atom basis in Eq. (8) is the product of the single-atom basis vectors, so that

$$|\mathbf{q}-\mathbf{y}\rangle = |q_1 - y_1\rangle|q_2 - y_2\rangle\ldots|q_N - y_N\rangle. \quad (9)$$

Using definition (8) and Eq. (3), the Wigner function after a single feedback step can be written as

$$W_+^{(1)}(\mathbf{p}, \mathbf{q}) = \pi^{-N}\int dQ d^N y du du' \mathcal{M}(u)\mathcal{M}^*(u')$$

$$\times \exp\left[-\frac{i(u-u')}{N}\sum_{i=1}^{N}q_i - \frac{i(u+u')}{N}\sum_{i=1}^{N}y_i\right] \quad (10)$$

$$\times \exp(-2i\mathbf{yp})\langle \mathbf{q}+\mathbf{y}+Q\mathbf{e}|\hat{\rho}_-|\mathbf{q}-\mathbf{y}+Q\mathbf{e}\rangle,$$

where $\mathbf{e}$ is the vector with N unit components: $\mathbf{e} = \{1, 1, \ldots, 1\}$. Here, the Fourier representation of the measurement resolution amplitudes $\hat{M}(Q)$,

$$\hat{M}(Q) = \int du \mathcal{M}(u)\exp[i\nu(Q-\hat{Q})], \quad (11)$$

with c-functions $\mathcal{M}(u)$,

[1] We use $\hbar = 1$ throughout the paper.

$$\mathcal{M}(u) = \left(\frac{\sigma_1^2}{2\pi^3}\right)^{1/4} \exp(-\sigma_1^2 u^2) \quad (12)$$

has been used. Changing the variables now to $u + u' = v$ and $u - u' = v'$ in Eq. (10) and integrating then over v', the Wigner function after the feedback operation reads

$$W_+^{(1)}(\mathbf{p}, \mathbf{q}) = \frac{1}{2\pi}\exp\left(-\frac{1}{2\sigma_1^2 N^2}\sum_{i,j=1}^{N} q_i q_j\right) \times \int dQ dv \exp\left(-\frac{\sigma_1^2 v^2}{2}\right) W_-\left(\mathbf{p} + \frac{v}{2N}\mathbf{e}, \mathbf{q} + Q\mathbf{e}\right), \quad (13)$$

where W_- denotes the Wigner function before the feedback. This result can be rewritten in a compact form introducing the following integral kernel

$$\mathcal{F}^{(1)}(\mathbf{p}, \mathbf{q}; \mathbf{p}', \mathbf{q}') = \frac{1}{2\pi}\exp\left(-\frac{1}{2\sigma_1^2 N^2}\sum_{i,j=1}^{N} q_i q_j\right) \times \int dQ dv \exp\left(-\frac{\sigma_1^2 v^2}{2}\right) \times \delta\left(\mathbf{p}' - \mathbf{p} - \frac{v}{2N}\mathbf{e}\right)\delta(\mathbf{q}' - \mathbf{q} - Q\mathbf{e}), \quad (14)$$

which gives

$$W_+^{(1)}(\mathbf{p}, \mathbf{q}) = \int d^N p' d^N q' \mathcal{F}^{(1)}(\mathbf{p}, \mathbf{q}; \mathbf{p}', \mathbf{q}') W_-(\mathbf{p}', \mathbf{q}'). \quad (15)$$

The integral transformation (15) with the kernel (14) represents the core component of the solution to the feedback problem and will be used below to study the dynamics of the system due to a number of feedback steps.

To do this, the transformation of the Wigner function due to the free evolution of atoms between feedbacks should be included. Assuming that the time interval between two successive feedbacks is small enough so that the noise does not affect the system considerably, the evolution of atoms between the feedbacks is governed by the free Hamiltonian

$$\hat{H} = \sum_{i=1}^{N}\left(\frac{\hat{p}_i^2}{2m} + \frac{m\omega^2}{2}\hat{q}_i^2\right), \quad (16)$$

and results in a simple rotation of the Wigner function

$$W(\mathbf{p}, \mathbf{q}, t + \Delta t) = W(\mathbf{p}', \mathbf{q}', t),$$
$$\mathbf{p}' = m\omega\mathbf{q}\sin(\omega\Delta t) + \mathbf{p}\cos(\omega\Delta t), \quad (17)$$
$$\mathbf{q}' = \mathbf{q}\cos(\omega\Delta t) - (1/m\omega)\mathbf{p}\sin(\omega\Delta t),$$

where Δt denotes the time interval after the last feedback step, m is the atomic mass, and ω is the vibrational trap frequency. Now, the resulting Wigner function after an arbitrary number of feedbacks and an arbitrary duration of free evolution between them can be found applying Eqs. (15) and (17) in an appropriate sequence.

Aiming to effectively compensate for the collective coordinate of atoms, one can try to find an optimal time interval between feedbacks. This optimal interval can be fixed considering the collective motion of the atoms in the harmonic potential classically. It is easily seen that taking the time interval between feedback steps equal to one fourth of the oscillation period $\Delta t = \tau/4$, the collective motion is completely damped after two feedback steps. Given another time of free evolution, this would normally take more operations.

Using Eqs. (15) and (17) with $\Delta t = \tau/4$, the Wigner function of the system immediately after the kth feedback step ($k \geq 2$) is expressed as

$$W_+^{(k)}(\mathbf{p}, \mathbf{q}) = \int d\mathbf{p}' d\mathbf{q}' \mathcal{F}^{(k)}(\mathbf{p}, \mathbf{q}; \mathbf{p}', \mathbf{q}') W_-(\mathbf{p}', \mathbf{q}') \quad (18)$$

with the feedback kernel given by

$$\mathcal{F}^{(k)}(\mathbf{p}, \mathbf{q}; \mathbf{p}', \mathbf{q}') = \frac{1}{2\pi}(4\sigma_k^4 N^2 + 1)^{-1/2} \times \exp\left(-\frac{1}{2\sigma_k^2 N^2}\sum_{i,j=1}^{N} q_i q_j\right) \times \exp\left(-\frac{2\sigma_k^2}{4\sigma_k^4 N^2 + 1}\sum_{i,j=1}^{N} p_i p_j\right) \times \int dQ dv \delta\left[\mathbf{q}' + \cos\left(\pi\frac{k+1}{2}\right)\mathbf{q} - \sin\left(\pi\frac{k+1}{2}\right)\mathbf{p} + Q\mathbf{e}\right] \times \delta\left[\mathbf{p}' + \sin\left(\pi\frac{k+1}{2}\right)\mathbf{q} + \cos\left(\pi\frac{k+1}{2}\right)\mathbf{p} - \frac{v}{2N}\mathbf{e}\right]. \quad (19)$$

Given the measurement resolution being the same at each feedback step, because of the 2π periodicity of the feedback kernel (Eq. (19)), the state of the system will reach a quasi-stationary regime where the state after the second step will be revealed with the four-step periodicity. In the case of the symmetric initial Wigner function, the period of oscillations can be shorter. For example, given a thermal equilibrium state or a Fock state, the Wigner function after the second feedback step is not affected by the next feedback operations. This represents certain limitations of the cooling scheme.

To study the operation of feedback cooling in more detail, let us now specify the initial state of the atoms. In most cases, the initial state of the atoms can be represented by a thermal equilibrium state. Given distinguishable atoms in a thermal equilibrium state, the atom–atom correlations are absent. Thus, the initial state of the many-atom system is then the tensor product of the states of single atoms $\hat{\rho}_- = \hat{\rho}_1^{\text{th}} \otimes \hat{\rho}_2^{\text{th}} \otimes \ldots \otimes$

$\hat{\rho}_N^{\text{th}}$. Consequently, the Wigner function is the product of the thermal Wigner functions of N single atoms. It is given by

$$W_-(\mathbf{p}, \mathbf{q}) = \left[\frac{\tanh(1/\xi)}{\pi}\right]^N \exp\left[-\frac{\tanh(1/\xi)}{2}\sum_{i=1}^{N}(q_i^2 + p_i^2)\right], \quad (20)$$

where q_i and p_i are expressed in units of the ground-state position and momentum uncertainty in the trap potential $\Delta q_0 = \sqrt{1/(2m\omega)}$ and $\Delta p_0 = \sqrt{m\omega/2}$, respectively. The parameter $\xi = k_B T/(\omega/2)$ denotes the single-atom energy in units of the ground-state energy in the trap. k_B is the Boltzmann constant.

From Eq. (15), after the evaluation of corresponding integrals, the Wigner function after a single feedback is found in the form

$$\begin{aligned} W_+^{(1)}(\mathbf{p}, \mathbf{q}) &= \left[\frac{\tanh(1/\xi)}{\pi}\right]^N \left[\frac{\coth(1/\xi)}{N\sigma_1^2 + \tanh(1/\xi)}\right]^{1/2} \\ &\times \exp\left[-\frac{1 + N\sigma_1^2(N-1)\tanh(1/\xi)}{2N^2\sigma_1^2}\sum_{i=1}^{N} q_i^2\right. \\ &\left. - \frac{1 - N\sigma_1^2\tanh(1/\xi)}{2N^2\sigma_1^2}\sum_{i\neq j=1}^{N} q_i q_j\right] \\ &\times \exp\left[-\frac{(N-1)\tanh(1/\xi) + N^2\sigma_1^2}{2N[1 + N\sigma_1^2\coth(1/\xi)]}\sum_{i=1}^{N} p_i^2\right. \\ &\left. + \frac{\tanh(1/\xi)}{2N[1 + N\sigma_1^2\coth(1/\xi)]}\sum_{i\neq j=1}^{N} p_i p_j\right], \end{aligned} \quad (21)$$

where σ_1 is now also measured in units of Δq_0. From this equation, one can readily see the appearance of correlations between coordinates (the second term in the first exponent) and momenta (the second term in the second exponent) of different atoms. The factor in front of the double sum over coordinates can be either negative or positive depending on the values of the number of atoms, the measurement resolution, and the parameter ξ. This means that the coordinates after a single feedback can be either anticorrelated or correlated. It is worth noting that the momenta of atoms in contrast are always correlated, which is the result of the measurement back-action on the center of mass.

Using Eq. (21), let us now address the efficiency of a single feedback step. It can be determined by calculating the average energy change due to the feedback process: $\Delta E = \langle \hat{H} \rangle_+ - \langle \hat{H} \rangle_-$, where $\langle \hat{H} \rangle_\pm$ is the average energy of atoms after/before the feedback step.

Given that the average energy of the system before the feedback equals $\langle \hat{H} \rangle_- = (N\omega/2)\coth(1/\xi)$, the total energy change due to the single feedback in units of the ground-state energy becomes

$$\Delta E^{(1)} = \frac{1}{2}\left(N\sigma_1^2 + \frac{1}{N\sigma_1^2}\right) - \frac{1}{2}\coth(1/\xi). \quad (22)$$

The positive contribution in this expression is the measurement-induced noise resulting in the energy increase. The first term arises from the imprecision of the coordinate measurement, and the second term is the back-action noise. The negative contribution in Eq. (22) represents the energy subtracted from the system due to the shift of the collective coordinate and, thus, represents the sought cooling effect. It is worth noting that the noise due to the measurement can be minimized by choosing the optimal measurement resolution

$$\sigma_{\text{opt}} = \frac{1}{\sqrt{N}}. \quad (23)$$

Now consider the effect of the second feedback step. The Wigner function of the system after the second step is obtained from the general result (Eq. (18)), taking there $k = 2$. The average energy change after two subsequent feedback steps with the free evolution between them during $\tau/4$ is given by

$$\Delta E^{(2)} = \frac{1}{2}\left(N\sigma_1^2 + N\sigma_2^2 + \frac{1}{N\sigma_2^2}\right) - \coth(1/\xi), \quad (24)$$

where $\sigma_{1,2}$ denotes the measurement resolution for the first and the second step, respectively. From this equation, one can see that the energy removed from the system after two steps appears to be equal to the average energy of a single atom being in a thermal equilibrium state.

The noise introduced into the system contains contributions due to the measurement imprecision at both steps and the measurement back-action at the second feedback step. It is remarkable that the back-action noise due to the first step is completely compensated for by the second feedback step. This is, however, true only for the specific time intervals between two feedbacks equal to $\Delta t = \tau(1 + 2k)/4$.

Thus, to minimize the noise, it would be optimal to perform the absolutely precise measurement of the coordinate at the first step and then take the measurement resolution given by Eq. (23) at the second step. Taking this into account, let us find a theoretical limit for the cooling, i.e., the temperature where the feedback does not subtract the energy from the gas. In other words, at this temperature, the average energy change would be zero, $\Delta E = 0$. If we let $\Delta E = 0$ in Eq. (24), then

the minimal energy in units of the energy of the ground state where the feedback still works is

$$E_{\lim} = \coth(1/\xi_{\lim}) = 1. \quad (25)$$

That is, ideally, the energy can be subtracted from the gas always until all the atoms are not at the ground state or, in other words, the method exhibits no theoretical cooling limits. This important result shows that the measurement back-action noise could be, in principle, overcome in an appropriately designed feedback scheme.

However, this theoretical limit can hardly be reached, since the absolutely precise measurement at the first feedback step would introduce an infinite amount of energy into the system (see the term corresponding to the back-action noise in Eq. (22)). Thus, in order to keep the atoms in a laboratory until the next feedback, the atoms have to be trapped inside infinitely deep potential wells, which would require in turn infinitely large intensities of the lasers forming the lattice.

Therefore, the limit energy of the gas where the feedback still works is given by

$$E_{\lim} = 1 + \frac{N\sigma_1^2}{2}, \quad (26)$$

where the finite accuracy of the measurement at the first feedback is taken into account.

It is worth noting that the considered feedback-cooling method, contrary to the standard laser cooling techniques, does not rely on resonant interactions of atoms with laser fields. Therefore, its operation is not restricted to the photon recoil limit as is the case in Doppler and Sisyphus cooling, for example. As it can be seen from Eq. (26), the minimal energy where the feedback loop still provides the cooling effect is limited only by the measurement accuracy. Except for the problems mentioned above, there are no fundamental constrains forbidding the measurement resolution σ_1 to be very small. Thus, one can expect that the recoil limit can be overcome for any particular sort of atoms and laser frequencies used to cool them.

Using Eqs. (18) and (19), one can show that, for the initial thermal state, the phase-space volume occupied by the atoms does not change after the third feedback step. Therefore, the only energy change is the energy change due to that described above the first and the second steps. Such a behavior may be understood as a result of the appearance of feedback-generated atom–atom correlations (see discussion of Eq. (21)).

Thus, aiming the practical use of the considered cooling scheme at very low temperatures, one should provide a mechanism destroying the atom–atom correlations.

To conclude, the scheme of feedback cooling of atoms trapped in a one-dimensional far-off-resonant optical lattice has been considered in the limit of low temperatures. The evolution of the Wigner function of the atoms due to a series of feedbacks with the free harmonic rotation between them has been analytically derived. It has been shown that, in spite of the presence of quantum noise, the feedback scheme subtracts energy from the gas at any temperature at least in principle. In a realistic situation, the limiting temperature, where the feedback does not work, is determined by the classical-type noise due to an imprecision of measurements. In any case, the performance of the cooling scheme at low temperatures is limited by the feedback-induced atom–atom correlations. These correlations should be gradually destroyed in order to cool atoms to the ground state of the lattice potential.

The authors would like to thank S. Wallentowitz for helpful discussions.

REFERENCES

1. S. Chu, Rev. Mod. Phys. **70**, 685 (1998); C. N. Cohen-Tannoudji, Rev. Mod. Phys. **70**, 707 (1998); W. D. Phillips, Rev. Mod. Phys. **70**, 721 (1998).
2. M. B. Dahan, E. Peik, J. Reichel, *et al.*, Phys. Rev. Lett. **76**, 4508 (1996).
3. S. R. Wilkinson, C. F. Bharucha, K. W. Madison, *et al.*, Phys. Rev. Lett. **76**, 4512 (1996).
4. Qian Niu, Xian-Geng Zhao, G. A. Georgakis, and M. G. Raizen, Phys. Rev. Lett. **76**, 4504 (1996).
5. M. Greiner, O. Mandel, T. Esslinger, *et al.*, Nature **415**, 39 (2002); M. Greiner, O. Mandel, T. Rom, *et al.*, Physica B (Amsterdam) **329–333**, 11 (2003).
6. N. V. Morrow, S. K. Dutta, and G. Raithel, Phys. Rev. Lett. **88**, 093003 (2002).
7. S. van der Meer, Rev. Mod. Phys. **57**, 689 (1985).
8. M. G. Raizen, J. Koga, B. Sundaram, *et al.*, Phys. Rev. A **58**, 4757 (1998).
9. I. Sh. Averbukh and Y. Prior, Phys. Rev. Lett. **94**, 153002 (2005).
10. M. A. Neumark, Dokl. Akad. Nauk SSSR **41**, 359 (1943); K. Kraus, *States, Effects and Operations: Fundamental Notions of Quantum Theory* (Springer, Berlin, 1983), Lect. Notes Phys., Vol. 190.

JETP Letters, Vol. 82, No. 8, 2005, pp. 487–491. From Pis'ma v Zhurnal Éksperimental'noĭ i Teoreticheskoĭ Fiziki, Vol. 82, No. 8, 2005, pp. 544–548.

Mesoscopic Wave Turbulence¶

V. E. Zakharov[a, b, c], A. O. Korotkevich[a], A. N. Pushkarev[a, c], and A. I. Dyachenko[a]

[a] *Landau Institute for Theoretical Physics, Russian Academy of Sciences, Moscow, 119334 Russia*
e-mail: kao@landau.ac.ru

[b] *Department of Mathematics, University of Arizona, Tucson, AZ 85721, USA*

[c] *Waves and Solitons LLC, Gilbert, AZ 85233, USA*

Received August 17, 2005

We report results of simulation of wave turbulence. Both inverse and direct cascades are observed. The definition of "mesoscopic turbulence" is given. This is a regime when the number of modes in a system involved in turbulence is high enough to qualitatively simulate most of the processes but significantly smaller than the threshold, which gives us quantitative agreement with the statistical description, such as the kinetic equation. Such a regime takes place in numerical simulation, in essentially finite systems, etc. © *2005 Pleiades Publishing, Inc.*

PACS numbers: 02.60.Cb, 47.11.+j, 47.27.Eq, 47.35.+i

The theory of wave turbulence is developed for infinitely large systems. In weakly nonlinear dispersive media, the turbulence is described by a kinetic equation for squared wave amplitudes (weak turbulence). However, all real systems are finite. Computer simulation of wave turbulence can also be performed only in finite systems (typically, in a box with periodic boundary conditions). It is important to know how strong discreteness of a system impacts the physical picture of wave turbulence.

Let a turbulence be realized in a Q-dimensional cube with side L. Then, wave vectors form a cubic lattice with the lattice constant $\Delta k = 2\pi/L$. Suppose that four-wave resonant conditions are dominating. Exact resonances satisfy the equations

$$\mathbf{k} + \mathbf{k}_1 - \mathbf{k}_2 - \mathbf{k}_3 = 0, \quad (1)$$

$$\Delta = \omega(k) + \omega(k_1) - \omega(k_2) - \omega(k_3) = 0. \quad (2)$$

In an infinite medium, Eqs. (1) and (2) define hypersurface dimension $3Q - 1$ in $4Q$-dimensional space $\mathbf{k}$, $\mathbf{k}_1$, $\mathbf{k}_2$, $\mathbf{k}_3$. In a finite system, (1) and (2) are Diophantine equations, which might have or have no exact solutions. The Diophantine equations for four-wave resonant processes are not studied yet. For three-wave resonant processes, they are studied for Rossby waves on the β plane [1].

However, not only exact resonances are important. Individual harmonics in the wave ensemble fluctuate with inverse time $\Gamma_{\mathbf{k}}$, dependent on their wavenumbers. Suppose that all $\Gamma_{\mathbf{k}_i}$ for waves composing a resonant quartet are of the same order of magnitude $\Gamma_{\mathbf{k}_i} \sim \Gamma$. Then, resonant equation (2) has to be satisfied up to accuracy $\Delta \sim \Gamma$, and the resonant surface is blurred into the layer of thickness $\delta k/k \simeq \Gamma_k/\omega_k$. This thickness should be compared with the lattice constant Δk. Three different cases are possible:

(1) $\delta k \gg \Delta k$. In this case, the resonant layer is thick enough to hold many approximate resonant quartets on a unit of resonant surface square. These resonances are dense, and the theory is close to the classical weak turbulent theory in infinite media. The weak turbulent theory offers recipes for calculation of Γ_k. The weak-turbulent Γ_k are the smallest among all the given by theoretical models. To be sure that the case is realized, one has to use weak-turbulent formulas for Γ_k.

(2) $\delta k < \Delta k$. This is the opposite case. Resonances are rarefied, and the system consists of a discrete set of weakly interacting oscillators. A typical regime in this situation is the "frozen turbulence" [2–4], which is actually a system of KAM tori accomplished with a weak Arnold's diffusion.

(3) The intermediate case $\delta k \simeq \Delta k$ can be called "mesoscopic turbulence." The density of approximate resonances is high enough to provide the energy transport along the spectrum but low enough to guarantee "equal rights" for all the harmonics, which is a necessary condition for the applicability of the weak turbulent theory.

In this article, we report results of our numerical experiments on modeling of turbulence of gravity waves on the surface of deep ideal incompressible fluid. The motivation for this work was numerical justification of the Hasselmann kinetic equation. The result is discovery of the mesoscopic turbulence. The fluid motion is potential and described by the shape of surface $\eta(\mathbf{r}, t)$ and the velocity potential $\psi(\mathbf{r}, t)$ evaluated

¶The text was submitted by the authors in English.

on the surface. These variables satisfy the canonical equations [5]

$$\frac{\partial \eta}{\partial t} = \frac{\delta H}{\delta \psi}, \quad \frac{\partial \psi}{\partial t} = -\frac{\delta H}{\delta \eta}, \tag{3}$$

Hamiltonian H is represented by the first three terms in expansion of powers of nonlinearity $\nabla\eta$:

$$\begin{aligned} H &= H_0 + H_1 + H_2 + \ldots, \\ H_0 &= \frac{1}{2}\int (g\eta^2 + \psi\hat{k}\psi)dxdy, \\ H_1 &= \frac{1}{2}\int \eta[|\nabla\psi|^2 - (\hat{k}\psi)^2]dxdy, \\ H_2 &= \frac{1}{2}\int \eta(\hat{k}\psi)[\hat{k}(\eta(\hat{k}\psi)) + \eta\nabla^2\psi]dxdy. \end{aligned} \tag{4}$$

Thereafter, we put the gravity acceleration equal to $g = 1$. Here, $\hat{k}$ is a linear integral operator ($\hat{k} = \sqrt{-\nabla^2}$), such that, in k space, it corresponds to multiplication of Fourier harmonics $\left(\psi_{\mathbf{k}} = \frac{1}{2\pi}\int \psi_{\mathbf{r}} e^{i\mathbf{kr}}dxdy\right)$ by $\sqrt{k_x^2 + k_y^2}$. For gravity waves, this reduced Hamiltonian describes four-wave interaction. Then, dynamical equations (3) acquire the form

$$\begin{aligned} \dot{\eta} &= \hat{k}\psi - (\nabla(\eta\nabla\psi)) - \hat{k}[\eta\hat{k}\psi] \\ &+ \hat{k}(\eta\hat{k}[\eta\hat{k}\psi]) + \frac{1}{2}\nabla^2[\eta^2\hat{k}\psi] + \frac{1}{2}\hat{k}[\eta^2\nabla^2\psi], \\ \dot{\psi} &= -g\eta - \frac{1}{2}[(\nabla\psi)^2 - (\hat{k}\psi)^2] \\ &- [\hat{k}\psi]\hat{k}[\eta\hat{k}\psi] - [\eta\hat{k}\psi]\nabla^2\psi. \end{aligned} \tag{5}$$

Let us introduce the canonical variables $a_{\mathbf{k}}$ as shown below:

$$a_{\mathbf{k}} = \sqrt{\frac{\omega_k}{2k}}\eta_{\mathbf{k}} + i\sqrt{\frac{k}{2\omega_k}}\psi_{\mathbf{k}}, \tag{6}$$

where $\omega_k = \sqrt{gk}$. In these so-called normal variables, equations (3) take the form

$$\frac{\partial a_{\mathbf{k}}}{\partial t} = -i\frac{\delta H}{\delta a_{\mathbf{k}}^*}. \tag{7}$$

The physical meaning of these variables is quite clear: $|a_{\mathbf{k}}|^2$ is an action spectral density, or $|a_{\mathbf{k}}|^2\Delta k^2$ is a number of particles with the particular wavenumber $\mathbf{k}$.

We solved equations (5) numerically in a box $2\pi \times 2\pi$ using a spectral code on a rectangular grid with double periodic boundary conditions. The implicit energy-preserving scheme is similar to that used in [6–8] was implemented. We studied the evolution of freely propagating waves (swell) in the absence of wind in the spirit of paper [9]. Different grids (512×512, 256×1024, 256×2048) with different initial data were tried. In all the cases, we observed mesoscopic wave turbulence. The most spectacular results are achieved on the grid 256×2048.

As initial conditions, we used a Gauss-shaped distribution on a long axis of the wavenumbers plane

$$\begin{cases} |a_{\mathbf{k}}| = A_i \exp\left(-\frac{1}{2}\frac{|\mathbf{k} - \mathbf{k}_0|^2}{D_i^2}\right), & |\mathbf{k} - \mathbf{k}_0| \le 2D_i, \\ |a_{\mathbf{k}}| = 10^{-12}, & |\mathbf{k} - \mathbf{k}_0| > 2D_i, \end{cases} \tag{8}$$

$$A_i = 5 \times 10^{-6}, \quad D_i = 30, \quad \mathbf{k}_0 = (0; 150).$$

The initial phases of all the harmonics were random. The average steepness is $\mu = \langle|\nabla\eta|\rangle \simeq 0.115$. To stabilize the computations in the high-frequency region [10], we introduced artificial damping, mimicking viscosity at small scales, and an artificial smoothing term to the equation for the surface evolution

$$\begin{aligned} \frac{\partial \psi_{\mathbf{k}}}{\partial t} &\longrightarrow \frac{\partial \psi_{\mathbf{k}}}{\partial t} + \gamma_k \psi_{\mathbf{k}}, \\ \frac{\partial \eta_{\mathbf{k}}}{\partial t} &\longrightarrow \frac{\partial \eta_{\mathbf{k}}}{\partial t} + \gamma_k \eta_{\mathbf{k}}, \\ \gamma_k &= \begin{cases} 0, & k < k_d, \\ -\gamma(k - k_d)^2, & k \ge k_d, \end{cases} \end{aligned} \tag{9}$$

$$k_d = 512, \quad \gamma = 2 \times 10^4, \quad \tau = 3.1 \times 10^{-4}.$$

With the time step τ, these calculations took about two months on an AMD Athlon 64 3500+ computer. During this time, we reached 1500 periods of the wave in the initial spectral maximum.

The process of waves evolution can be separated in two steps. On the first stage (about fifty initial wave periods), we observe fast loss of energy and wave action. This effect can be explained by formation of "slave" harmonics taking their part of motion constants. The initially smooth spectrum becomes very rough. The spectral maximum demonstrates a fast downshift.

In the second stage, the downshift continues but all the processes slow down. Plots of the energy, wave action, mean frequency, and mean steepness are presented in Figs. 1–4.

One can see a clear tendency to downshift of the spectral maximum corresponding to inverse cascade; however, this process is more slow than predicted by weak turbulence theory. The self-similar downshift in this theory gives [11, 12]

$$\omega \sim t^{-1/11}.$$

In our experiments,

$$\omega \sim t^{-\alpha},$$

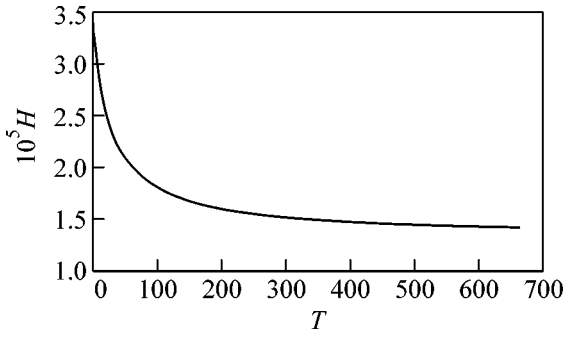

Fig. 1. Total energy of the system.

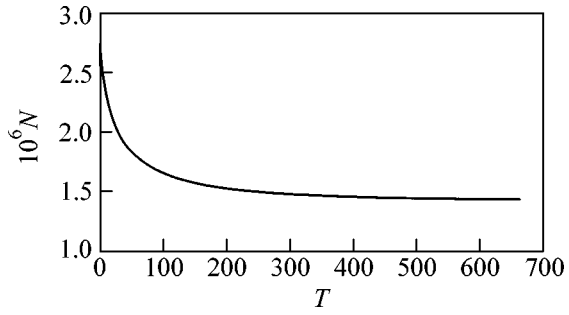

Fig. 2. Total action of the system.

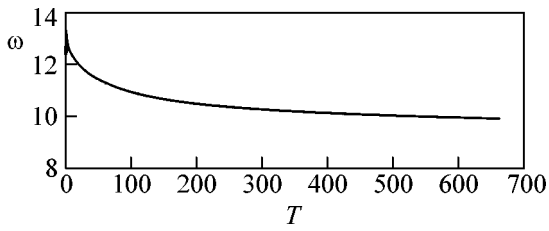

Fig. 3. Frequency of the spectral maximum.

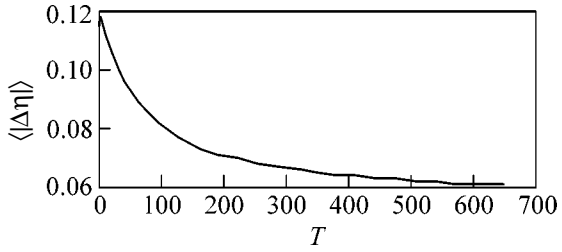

Fig. 4. Mean steepness of fluid surface.

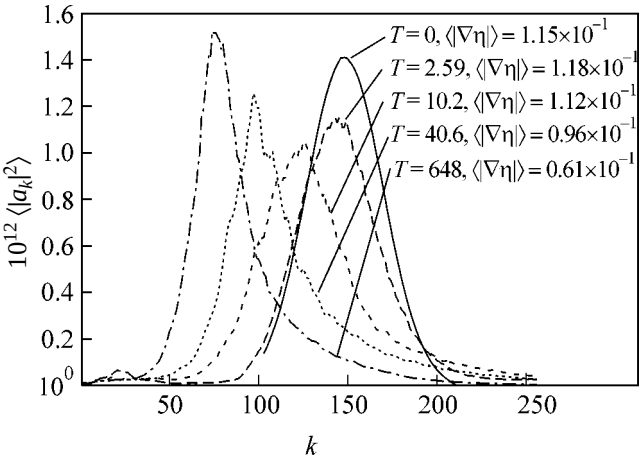

Fig. 5. Averaged with angle spectra. Downshift of spectral maximum is clearly observable.

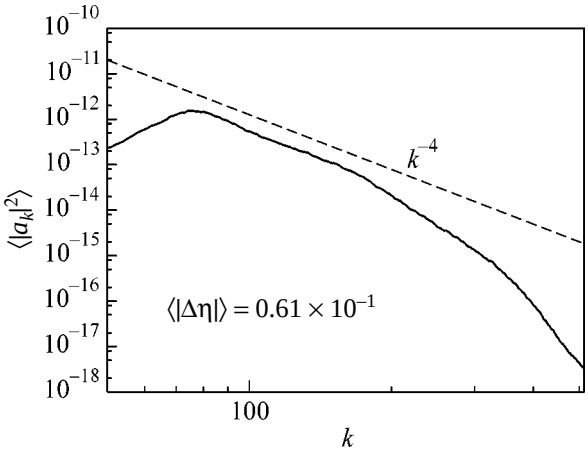

Fig. 6. Tails of angle-averaged spectrum in double logarithmic scale. $T = 648 = 1263T_0$. Powerlike tail and front slope are close to predicted by weak turbulent theory.

where α decreases with time from 1/16 to 1/20. Evolution of angle-averaged spectra $N_k = \int_0^{2\pi} |a_{\mathbf{k}}|^2 kdkd\vartheta$ is presented in Fig. 5. Their tails (Fig. 6) are Zakharov–Filonenko weak-turbulent Kolmogorov spectra [13] corresponding to direct cascade

$$\langle |a_k|^2 \rangle \sim 1/k^4. \qquad (10)$$

This result is robust; it was observed in similar calculations [7–9].

Two-dimensional spectra in the initial and in the last moments of the calculations are presented in Fig. 7. One can see formation of small-intensity "jets" posed on the Phillips resonant curve [14]

$$2\omega(\mathbf{k}_0) = \omega(\mathbf{k}_0 + \mathbf{k}) + \omega(\mathbf{k}_0 - \mathbf{k}). \qquad (11)$$

The spectra are very rough and sharp. The slice of spectra along the line (0; k_y) at the end of the computations is presented in Fig. 8. Evolution of squared wave

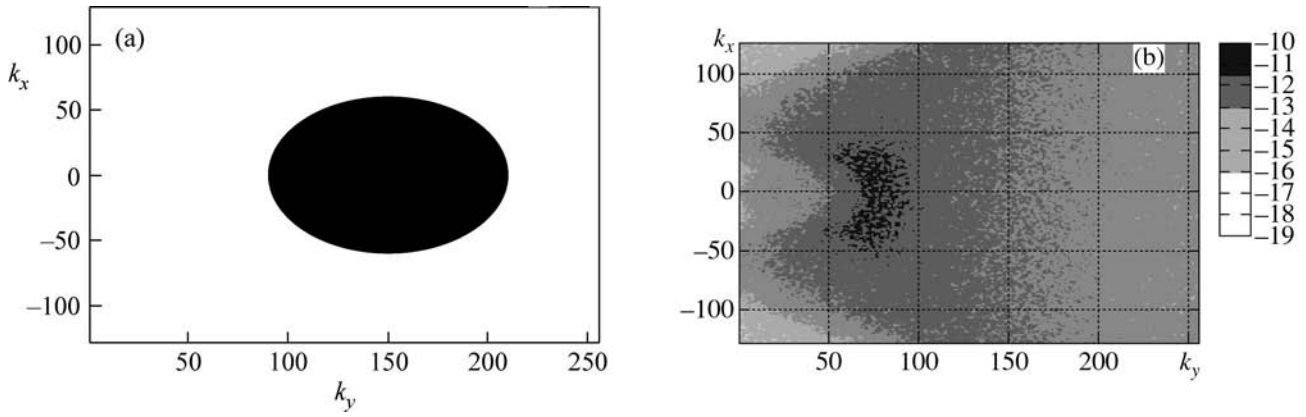

Fig. 7. (a) Level lines of logarithm of initial spectra distribution. $T = 0$. (b) Level lines of logarithm of spectra distribution at $T = 648 = 1263T_0$.

amplitudes for a cluster of neighboring harmonics is presented in Fig. 9.

Results presented in Fig. 9 show that what we modeled is mesoscopic turbulence. Indeed, the characteristic time of the amplitude evolution in the figure is a hundred or more of their periods; thus, Γ/ω_k is comparable with $\Delta k/k$. In the same figure, we can see the most remarkable features of such turbulence.

The weak turbulence in the first approximation obeys the Gaussian statistics. The neighboring harmonics are uncorrelated and statistically independent ($\langle a_k a^*_{k+1} \rangle = 0$). However, their averaged characteristics are close to each other. This is a "democratic society." On the contrary, mesoscopic turbulence is an "oligarchic society." The Phillips curve (11) has a genus of 2. After Faltings' proof [15] of Mordell's hypothesis [16], we know that the number of solutions of the Diophantine equation

$$\Delta = 2(n^2 + m^2)^{1/4} - [(n+x)^2 + (m+y)^2]^{1/4} - [(n-x)^2 + (m-y)^2]^{1/4} = 0 \quad (12)$$

is at most finite and most probably, except for a few trivial solutions, equals zero. The same statement is very plausible for more general resonances. Approximate integer solutions in the case

$$|\Delta| < \epsilon$$

do exist, but their number fast tends to zero at $\epsilon \longrightarrow 0$. Classification of these solutions is a hard problem of number theory. These solutions compose the "elite society" of the harmonics, which play the most active role in the mesoscopic turbulence. Almost all the inverse cascade of wave action is realized within mem-

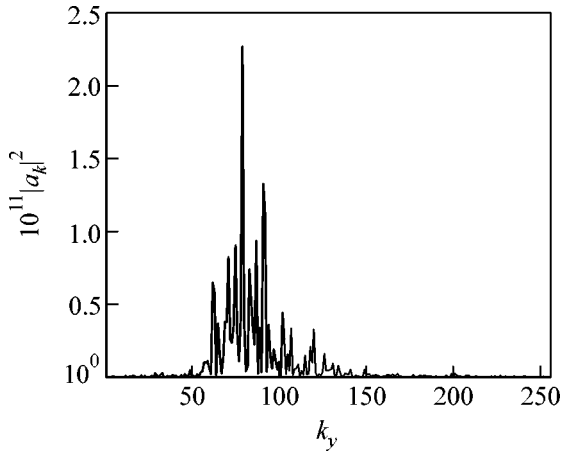

Fig. 8. Slice of spectrum on axis $(0; k_y)$ at $T = 648 = 1263T_0$.

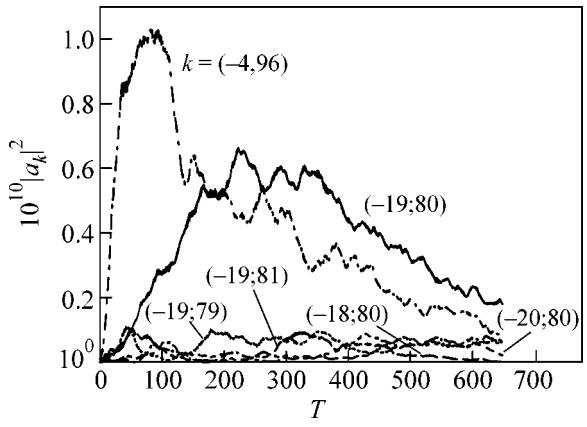

Fig. 9. Evolution of some cluster of harmonics and a distant large harmonic.

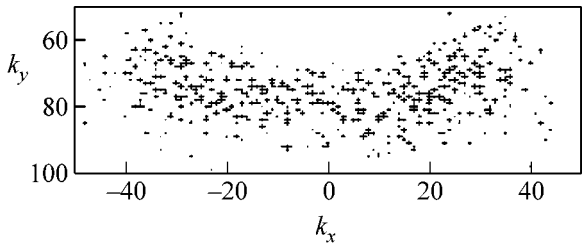

Fig. 10. Harmonics with square modulus exceeding level 10^{-11} at $T = 648 = 1263T_0$.

bers of this "privileged club." The distribution of the harmonics exceeding the reference level $|a_k|^2 = 10^{-11}$ at the moment $t = 1200T_0$ is presented in Fig. 10. The number of such harmonics is not more than 600, while the total number of harmonics involved into the turbulence is of the order of 10^4.

Note that a situation with direct cascade is different. As far as the coupling coefficient for gravity waves grow as fast as k^3 with the wave number, for short waves, Γ_k/ω_k easily exceeds $\Delta k/k$, and the conditions of the applicability of the weak turbulent theory for short waves are satisfied.

Note also that the mesoscopic turbulence is not a numerical artifact. Simple estimations show that, for gravity waves, it is realized in some conditions in basins of a moderate size, like small lakes as well as in experimental wave tanks. It is also common for long internal waves in the ocean and for inertial gravity waves in the atmosphere, for plasma waves in tokamaks, etc.

This work was supported by the Russian Foundation for Basic Research (project no. 03-01-00289), the program "Nonlinear Dynamics and Solitons" of the Presidium of the Russian Academy of Sciences, the "Leading Scientific Schools of Russia" grant, the ONR (grant no. N00014-03-1-0648), the US Army Corps of Engineers, the RDT & E Program no. W912HZ-04-P-0172, and by the DACA (grant no. 42-00-C0044). We use this opportunity to gratefully acknowledge the support of these foundations.

We also want to thank the creators of the open-source fast Fourier transform library FFTW [17] for this fast, portable, and completely free piece of software.

REFERENCES

1. G. Reznik, L. Piterbarg, and E. Kartashova, Dyn. Atmos. Oceans **18**, 235 (1993).
2. A. N. Pushkarev and V. E. Zakharov, Physica D (Amsterdam) **155**, 98 (1999).
3. A. N. Pushkarev, Eur. J. Mech. B/Fluids **18**, 345 (1999).
4. C. Connaughton, S. Nazarenko, and A. Pushkarev, Phys. Rev. E **63**, 046306 (2001).
5. V. E. Zakharov, J. Appl. Mech. Tech. Phys. **2**, 190 (1968).
6. A. I. Dyachenko, A. O. Korotkevich, and V. E. Zakharov, Pis'ma Zh. Éksp. Teor. Fiz. **77**, 572 (2003) [JETP Lett. **77**, 477 (2003)]; physics/0308100.
7. A. I. Dyachenko, A. O. Korotkevich, and V. E. Zakharov, Pis'ma Zh. Éksp. Teor. Fiz. **77**, 649 (2003) [JETP Lett. **77**, 546 (2003)]; physics/0308101.
8. A. I. Dyachenko, A. O. Korotkevich, and V. E. Zakharov, Phys. Rev. Lett. **92**, 134501 (2004); physics/0308099.
9. M. Onorato, A. R. Osborne, M. Serio, *et al.*, Phys. Rev. Lett. **89**, 144501 (2002); nlin.CD/0201017.
10. P. M. Lushnikov and V. E. Zakharov, Physica D (Amsterdam) **203**, 9 (2005); nlin.PS/0410054.
11. V. E. Zakharov, PhD Thesis (Budker Inst. for Nuclear Physics, Novosibirsk, USSR, 1966).
12. V. E. Zakharov and M. M. Zaslavskii, Izv. Akad. Nauk SSSR, Fiz. Atmos. Okeana **18**, 747 (1982).
13. V. E. Zakharov and N. N. Filonenko, J. Appl. Mech. Tech. Phys. **4**, 506 (1967).
14. O. M. Phillips, J. Fluid Mech. **107**, 465 (1981).
15. G. Faltings, Invent. Math. **73**, 349 (1983); Invent. Math. **75**, 381(E) (1984).
16. L. J. Mordell, Proc. Cambridge Philos. Soc. **21**, 179 (1922).
17. M. Frigo and S. G. Johnson, in *Proceedings of 23rd International Conference on Acoustics, Speech, and Signal Processing, ICASSP-1998* (1998), Vol. 3, p. 1381; http://fftw.org.

JETP Letters, Vol. 82, No. 8, 2005, pp. 492–497. Translated from Pis'ma v Zhurnal Éksperimental'noĭ i Teoreticheskoĭ Fiziki, Vol. 82, No. 8, 2005, pp. 549–555.

Experimental Study of Heat Transfer Processes for Macroparticles in a Dusty Plasma

V. E. Fortov, O. S. Vaulina, O. F. Petrov, I. A. Shakhova, A. V. Gavrikov, and Yu. V. Khrustalyov*

Institute of High Energy Densities, Russian Academy of Sciences, ul. Izhorskaya 13/19, Moscow, 125412 Russia

** e-mail: iushenka@yandex.ru*

Received April 14, 2005; in final form, September 7, 2005

The results of the experimental study of heat transfer processes in liquid dusty structures are reported. The experiments have been carried out for aluminum oxide particles in an rf discharge plasma. The thermal conductivity and thermal diffusivity of the dusty plasma component have been determined by analyzing the steady and unsteady heat transfer processes. The temperature dependence has been obtained for these quantities, which is in qualitative agreement with numerical simulation results for a simple one-atomic fluid. © *2005 Pleiades Publishing, Inc.*

PACS numbers: 52.25.–b, 82.70.Db

The physical properties of nonideal dissipative systems are of considerable interest in various areas of science and engineering (hydrodynamics, plasma physics, medicine, the physics and chemistry of polymers, etc.) [1–5]. The main difficulty in studying these systems is the absence of the consistent theory of fluids that could explain their thermodynamic properties, describe the heat and mass transfer processes in a wide region of the parameters of a liquid matter state, etc. A laboratory dusty plasma is a good experimental model for studying the properties of nonideal systems [5–8]. This plasma constitutes a partially ionized gas with charged particles of the condensed phase (macroparticles). Such particles can be recorded by a video camera, which allows investigations of various physical processes at the kinetic level and direct measurements of the transfer coefficients (such as the diffusivity D, the thermal conductivity χ, and the viscosity η) for nonideal systems.

Most numerical investigations of dusty plasma are based on the screened Coulomb potential model $U = (eZ)^2\exp(-r/\lambda)/r$, where r is the interparticle distance, λ is the screening length, and eZ is the charge. Two dimensionless parameters determining the transport processes in such systems were found in [9–11] for $\kappa = r_d/\lambda < 6$, where $r_d = n_d^{-1/3}$ is the mean distance between particles with concentration n_d. These two parameters are the effective nonideality parameter

$$\Gamma^* = (Ze)^2\{(1 + \kappa + \kappa^2/2)\exp(-\kappa)\}/Tr_d,$$

which determines the form of the pair correlation function from $\Gamma^* \sim 1$ to the crystallization point $\Gamma^* = \Gamma^*_c \cong 102$, and the scaling parameter $\xi \equiv \omega^*/\nu_{fr}$, where $\omega^* = eZ\{(1 + \kappa + \kappa^2/2)\exp(-\kappa)/r_d^3\pi M\}^{1/2}$ is the characteristic frequency of the collisions between charged particles, ν_{fr} is the effective frequency of the collisions of charged particles with the surrounding-gas neutrals, M is the mass of a particle, and T is its kinetic temperature (in energy units) characterizing the energy of its chaotic (thermal) motion. It is worth noting that the kinetic temperature of dust particles in the laboratory gas-discharge plasma may be much higher than both the temperature of its surface (determined by neutrals of the surrounding gas) and the temperature of the electron component (~1–5 eV) [12–16]. This relation takes place due to spatial or time fluctuations in the dusty-plasma parameters [13–15] (e.g., charges of macroparticles), as well as due to the development of various plasma–dust instabilities in the electric fields of gas-discharge chambers [16, 17].

In this paper, we describe the experiments concerning heat transfer processes in liquid dusty structures and present the results of the measurement of the thermal conductivity and thermal diffusivity $\theta = \chi/\rho c_p$, where $\rho = Mn_d$, and c_p is the specific heat at the constant pressure P. These coefficients are compared with the available numerical data.

The experiments were conducted in the plasma of a capacitance rf discharge plasma in argon ($P \approx 20$ Pa) with Al_2O_3 particles 3–5 μm in diameter (mean radius $a_d \approx 2$ μm and density $\rho_d \approx 2.4$ g cm^{-3}). The layout of the experiment is given in Fig. 1a. For diagnostics, particles of the dust cloud were illuminated by an He–Ne laser and were recorded by a video camera (with a speed of 50 fps). The coordinates and trajectories of the particles were determined by processing the video recording.

0021-3640/05/8208-0492$26.00

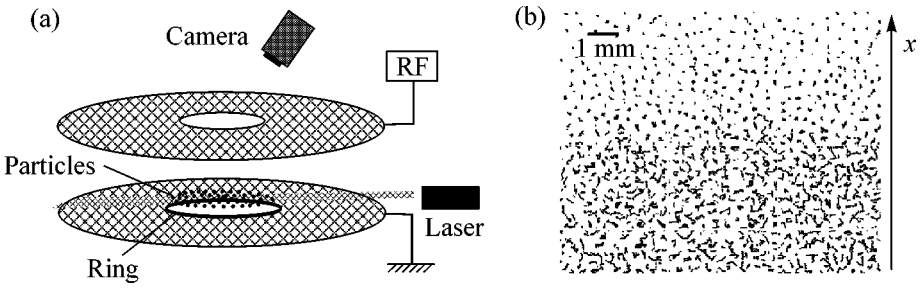

Fig. 1. (a) Layout of the experiment and (b) the fragment of the video recording of the dusty structure in the equilibrium two-phase state, where trajectories of individual particles for time $t = 0.25$ s are shown.

Under the experimental conditions, the dust cloud first constituted an equilibrium liquid structure consisting of 13–15 dust layers with a diameter of about 3.5 cm. Owing to small change in the working parameters of the discharge (increase in power or decrease in P), one of the edges of the cloud was rapidly heated. (The cause of such an asymmetric perturbation was the geometric inhomogeneity of the trap.) In 12–13 s, thermal perturbation propagated through the structure, which then came to a new steady two-phase state with a distinct interface between the low- and high-temperature regions (see Fig. 1b). The characteristics of the dusty structure under investigation remained almost unchanged during the further observation (~300 s).

The perturbation propagation front was flat; i.e., the perturbation propagated in the direction that is denoted as **x**. We emphasize that the method of the direct visualization of dust particles allows the detection of any changes in their translational degrees of freedom. Analysis of the measured velocity spectrum of dust particles did not reveal any convective motion of the medium under investigation (this spectrum was close to the Maxwellian spectrum) in both the steady case and unsteady regime, as well as any heat transfer (temperature gradients or particle drift) in other directions.

To analyze the characteristics of the medium in the process of the propagation of the thermal perturbation, a frame of the video recording was divided into several rectangular sections with the width $\delta x \approx 0.175$ cm. The pattern of the propagation of the thermal perturbation front that is obtained by averaging the temperature of particles in these sections is shown in Figs. 2 and 3. It is easy to see that the boundaries of the heated region expand for about 8 s after the thermal perturbation. Then, the velocity of the front decreases sharply and the kinetic energy of the particles undergoes new perturbation, which is probably attributed to the "collision" of the thermal front with the region containing the internal sources (drains) of heat. In a further 4–5 s, the dusty system reached a new equilibrium state and constituted

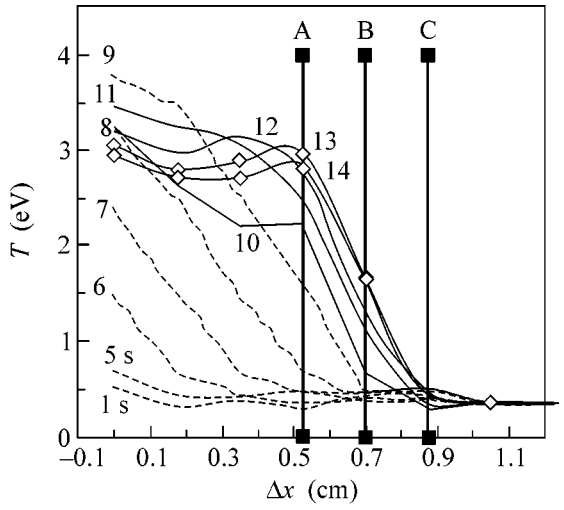

Fig. 2. Spatial distribution of thermal perturbation at various observation times (numbers on the line is time in seconds); $\Delta x = m\delta x$, where m is the number of analyzed regions with width δx; and the regions, where χ is measured in the steady state are indicated by the vertical straight lines.

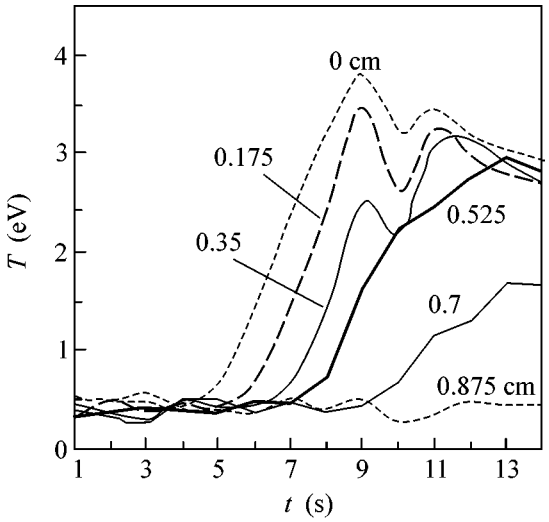

Fig. 3. Time dependence of the temperature of macroparticles in various regions Δx of the dusty structure.

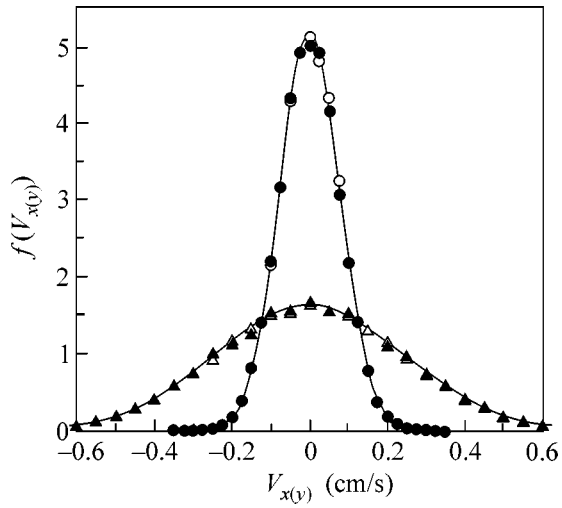

Fig. 4. Velocity spectrum of macroparticles in (▲, △) high- and (●, ○) low-temperature phases: (▲, ●) $f(V_x)$ and (△, ○) $f(V_y)$. The solid lines are the Maxwellian distributions with the half-width corresponding to the measured particle temperatures $T = 3$ and 0.3 eV, respectively.

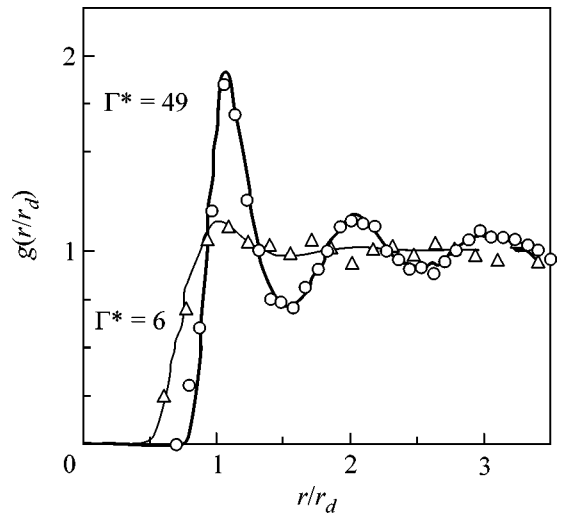

Fig. 5. Experimental correlation functions $g(r/r_d)$ for (△) high- and (○) low-temperature phases. The solid lines are the numerical simulations for various parameters Γ*.

a two-phase liquid medium with a distinct interface between the low- and high-temperature phases that was located at a distance of 2–2.5 cm from the place of the origination of the thermal perturbation.

To analyze the temperature of the dusty component, measurements of the velocity spectrum of the macroparticles (see Fig. 4) were used, whereas the mean interparticle distance r_d and the parameter Γ* were determined using the form of the pair correlation function (see Fig. 5). The friction coefficient in the free-molecular approximation was equal to $\nu_{fr} \approx 35$ s^{-1} (for $a_d \approx 2$ μm) [18]. The parameters of the high-temperature phase were $T \approx 3$ eV, $r_d \approx 400$ μm, $\Gamma^* \approx 6$, and $\omega^* = \{T\Gamma^*/M\pi r_d^2\}^{1/2} \approx 8.5$ s^{-1}. The characteristics of the low-temperature phase were close to the respective parameters of the unperturbed system: $T \approx 0.3$ eV, $r_d \approx 500$ μm, $\Gamma^* \approx 49$, and $\omega^* \approx 6.8$ s^{-1}. It is worth noting that the nonuniform (and strongly anisotropic) temperature distribution of dust particles in the plasma is observed quite often [12–14]. This phenomenon can be explained by the nonlinear spatial change in the macroparticle charges that ensures the formation of internal sources (drains) of heat in the dusty structure.

A preliminary estimate of the thermal diffusivity θ for the experimental conditions can be obtained from the solution of the problem of the temperature equalization in the layer whose one edge has a given temperature and two other edges are thermally isolated: $\theta = L^2/3\pi^2\tau$, where L is the characteristic length in the heat-propagation direction and τ is the time of the temperature equalization [19]. For this case, taking into account the experimental values $L \approx 2$–3 cm and $\tau \approx 12$–14 s, we obtain $\theta \approx 0.01$–0.016 cm^2/s.

To determine the thermal conductivity χ in the steady dusty structure ($t > 13$ s), the thermal flux density **q** and temperature gradient ∇T were measured at the interface (see Fig. 3). The thermal conductivity was determined from the Fourier equation

$$\mathbf{q} = -\chi \nabla T/k_B. \quad (1)$$

Here, k_B is the Boltzmann constant, $\mathbf{q} = 0.5[\int \mathbf{V}\, MV^2 dN]/[S\delta x]$ is the heat flux transferred by particles with velocity **V** through the area S of the substance layer with thickness δx, and N is the number of particles in the layer. In the absence of oscillations and rotation of particles, assuming that their energy is uniformly distributed over degrees of freedom, the heat flux density propagating in the given direction **x** can be determined as $q \approx 1.5\rho(\langle V_x^3\rangle_+ - \langle V_x^3\rangle_-)$, where $1.5\rho\langle V_x^3\rangle_{+(-)}$ is the amount of heat transferred along (+) and against (–) the flux direction. In this case, the coefficient χ is represented as

$$\chi \approx 1.5 n_d \delta x k_B (\langle V_x^3\rangle_+ - \langle V_x^3\rangle_-)(\langle V_x^2\rangle_+ - \langle V_x^2\rangle_-)^{-1}. \quad (2)$$

The thermal conductivity measured for the entire region A–C with width $2\delta x \approx 0.35$ cm and separately for the section A–B and B–C (see Fig. 2) is presented in the table as a function of the average temperature in these sections. The same table presents the parameter Γ*, which was obtained by simple scaling of its value for the high-temperature region.

The thermal diffusivity θ is measured for unsteady conditions by analyzing the motion of the thermal perturbation front for times $t \le 8$ s in the sections of the structure with $\Delta x \le 0.525$ cm. Since the temperature of

the dust particles in the steady state in the region under consideration (for $\Delta x \le 0.525$ cm) remained almost constant, $T \approx 3 \pm 0.15$ eV, we assumed that the effect of the internal sources could be disregarded. In this case, the heat transfer equation in the immovable medium can be represented in the form

$$c_p \rho \partial T/\partial t = \mathrm{div}(\chi \nabla T). \quad (3)$$

If finite heat Q_0 is focused at the initial time in the $x = 0$ plane of the extended system with the uniform temperature distribution $T_0 = \mathrm{const}$, the solution of Eq. (3) for the thermal diffusivity given by the function $\theta(T) = aT^n$ (where a is a certain constant and $n > 0$) can be written in the form [19]

$$T \approx C_Q \{at\}^{-1/(2+n)} f(\zeta) + T_0, \quad (4)$$

where $C_Q = C_Q(Q_0) \equiv \mathrm{const}$, $f(\zeta) = n(\zeta_0^2 - \zeta^2)/2(2+n)$, $\zeta = x(Q_0^n at)^{-1/(2+n)}$, and $\zeta_0^{2+n} = (2+n)^{1+n} 2^{1-n} \Gamma^n(0.5 + 1/n)/n\pi^{n/2}\Gamma^n(1/n)$. In this case, for $n \ll 1$, one can assume that

$$\partial T/\partial t \approx T[x^2/4\theta(T)t - 0.5]/t. \quad (5)$$

This expression was used for the empirical approximation of the experimental data for $\partial T/\partial t$ in various regions of the cloud (at $x = x_0 + \Delta x$) at times with close T values. The procedure of determination by means of the best agreement between analytical and experimental results is illustrated in Fig. 6, which shows values of x^2/θ obtained from Eq. (5) and the data of measurements of $\partial T/\partial t$ and T, along with the approximation curves. As a result, the distance $x_0 \cong 1$ cm from the "plane," where the perturbation occurs, as well as the thermal diffusivity as a function $\theta(T)$, was obtained (see table). We emphasize that the quantity θ in the temperature range under consideration varies from 0.01 to 0.016 cm^2/s, which agrees well with the results of the above preliminary estimate of the thermal diffusivity $\theta \approx 0.01$–0.016 cm^2/s using the time of temperature equalization in the layer.

Since the thermal conductivity of the dusty component in the plasma is yet unknown, in order to compare χ and θ (obtained in independent measurements), the specific heat c_P was taken to be equal to the specific heat of the ideal gas $c_P = 2.5k_B/M$. The choice of c_P is based on the available numerical data, which show that, for classical one-atomic fluids and for numerous pair potentials, the specific heat differs only slightly from the value for the ideal gas. Moreover, the transfer coefficients are in good agreement with the known approximate solutions of the kinetic equation if the mean free path of interacting particles colliding with each other is comparable with or larger than the mean interparticle distance (range $\Gamma^* < 30$–40) [4, 18].

The corresponding "missing" coefficients $\theta = 2\chi/\{5n_d k_B\}$ and $\chi = 2.5 n_d k_B \theta$ for $c_P = 2.5k_B/M$ are given in the table. It is easy to see that these values differ from the results of their direct measurements by approximately 35%, which exceeds the random measurement error (~5–10%, see table). Thus, the differences found are associated with the systematic measurement error. Disregarding any other systematic errors and assuming that the resulting difference is determined by the incorrect choice of c_P, one can find its "true" value from the results of the presented measurements as $c_P = \chi/\rho\theta \approx 1.85$. However, the systematic measurement errors can be associated with a number of other factors, in particular, with the insufficient justification of the assumption on the insignificant effect of internal sources on the heat

Coefficients θ and χ for the steady and unsteady states of the dusty structure

T, eV	Γ^*	$\chi \times 10^{14}$, erg/(s cm K)	$\theta \times 10^2$, cm^2/s
Stationary state			
2.7	6.7	2.39 ± 0.2	1.1
1.68	10.7	2.16 ± 0.2	1.0
1.3	13	1.93 ± 0.2	0.89
Unsteady state			
0.7	25.8	2.59	1.2 ± 0.17
1.49	12.1	2.59	1.2 ± 0.13
2.45	7.35	2.8	1.3 ± 0.06
3.325	5.4	3.13	1.45 ± 0.05
3.8	4.7	3.45	1.6 ± 0.06

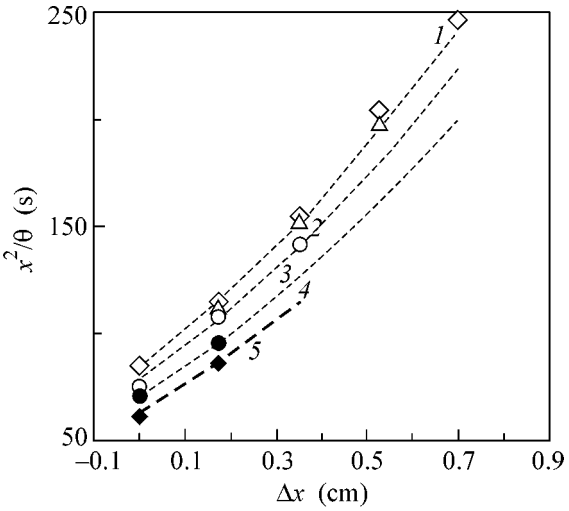

Fig. 6. (Points) Experimental values of x^2/θ for various regions of the dusty structure Δx that are obtained by measuring $\partial T/\partial t$ and T for various temperatures, along with (dashed lines) the approximation curves for $x_0 \cong 1$ cm and for (*1*, ◇) $T \cong 0.7$ eV and $\theta \cong 0.012$ cm^2/s, (*2*, △) $T \cong 1.49$ eV and $\theta \cong 0.012$ cm^2/s, (*3*, ○) $T \cong 2.45$ eV and $\theta \cong 0.013$ cm^2/s, (*4*, ●) $T \cong 3.33$ eV and $\theta \cong 0.0145$ cm^2/s, and (*5*, ◆) $T \cong 3.8$ eV and $\theta \cong 0.016$ cm^2/s.

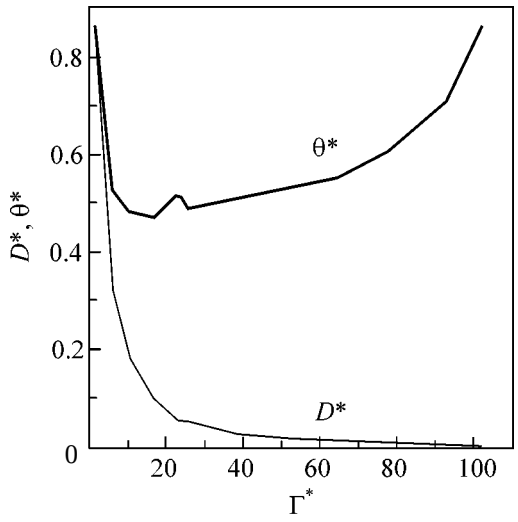

Fig. 7. Normalized coefficients D^* and θ^* vs. Γ^* for dispersion systems ($\nu_{fr} = 0$) with the screened Coulomb potential.

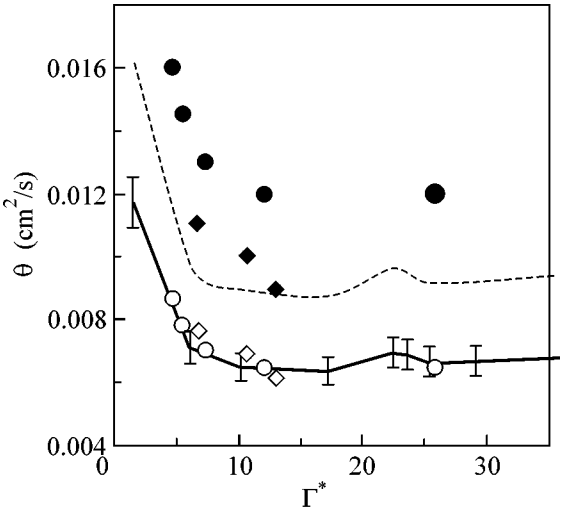

Fig. 8. Coefficient θ vs. Γ^* as obtained (solid line) from the simulation results ($\nu_{fr} = 0$) for dispersion systems and from experimental data for (◆) steady and (●) unsteady dusty structure, as well as (◇) $\theta/1.45$ and (○) $\theta/1.95$ for the steady and unsteady cases, respectively. The dashed line is calculated for $\xi = 0.36$.

transfer processes when solving heat conduction equation (3) or with the fact that $\theta(T) \propto T^n$ with $n \approx 0.2$ under the experimental conditions and, correspondingly, when the criterion $n \ll 1$ is invalid.

Let us compare the resulting heat transfer coefficients with the results of the numerical simulation of the transport processes in a simple one-atomic fluid. Such a simulation for systems with numerous isotropic interaction potentials shows that the diffusion coefficient D and viscosity η of simple fluids are related to each other by the Stokes formula $\eta \cong T/8.1 r_d D$ [4, 11] and the relation between the thermal diffusivity and diffusion coefficient may be represented as [4]

$$\theta \cong \frac{1.5 k_B}{M c_P} r_d V_t \left(\frac{0.6 r_d V_t}{D}\right)^{5/8}, \qquad (6)$$

where $V_t = (T/M)^{1/2}$. The basic difference of the properties of simple fluids and plasma–dust systems is associated with the presence of the dissipation of dust particle energy due to their collisions with a neutral gas. For slightly dissipative systems ($\nu_{fr} \ll \omega^*$, $\xi \longrightarrow \infty$), the results of dynamic simulation for microparticles and simple fluids coincide with each other. The normalized diffusion coefficient $D^*(\Gamma^*) = D/\omega^* r_d^2$ for slightly dissipative systems ($\xi \longrightarrow \infty$) with the screened potential is shown in Fig. 7 [9, 11, 20]. To take into account dissipation, the presented diffusion coefficient should be reduced by a factor of $1 + \xi^{-1}$ [11, 20]. Figure 7 also shows the normalized thermal diffusivity $\theta^* = \theta/\omega^* r_d^2$) determined from the data of the simulation of particle diffusion by using Eq. (6) with $c_P = 2.5 k_B/M$. The comparison of the measurements of the thermal diffusivity with the numerical simulation data is given in Fig. 8. It is easily seen that the temperature dependence of the measured coefficients is in qualitative agreement with the numerical results. The quantitative differences of the presented data can be attributed to the energy dissociation processes of macroparticles. Taking into account that $D \propto 1/(1 + \xi^{-1})$, the heat transfer coefficients in dissipative systems should be larger than the value for the dispersion case by a factor of $(1 + \xi^{-1})^{5/8}$ [see Eq. (6)], which is equal to 3–4 under the experimental conditions. However, the observed differences are equal to half this value (see Fig. 8). The calculation results for dissipative systems under the conditions close to the experimental conditions (for $\xi = 0.36$) are shown by the dashed line in Fig. 8.

We briefly analyze possible heat transfer mechanisms in the reported experiments. As is known, heat transfer can be attributed not only to heat exchange (due to heat conduction or convection) caused by temperature gradients but also to inhomogeneities in other physical quantities such as concentration gradients (thermal diffusion) or external perturbations of force fields. We emphasize that the method of the direct visualization of dust particles allows the detection of any changes in their translational degrees of freedom. Analysis of the measured velocity spectrum of dust particles did not reveal any convective or other regular motion of the medium under investigation (this spectrum was close to the Maxwellian spectrum) in both the steady case and the unsteady regime, as well as any heat transfer (temperature gradients or particle drift) in other directions. For this reason, we conclude that the convection and thermal diffusion mechanisms are absent in the reported experiments.

Since the dusty component under investigation is an open subsystem of the entire complex plasma–dust system, the processes of perturbation in the temperature of dust particles can be determined by the presence of perturbations in the surrounding plasma component (electrons and ions). In turn, this can initiate perturbation in mean electric fields in the system under consideration, as well as in local electric fields determining the interaction between dust particles. The appearance of an uncompensated regular component of the electric field would induce an additional (uncompensated) force producing the translational motion of particles (we remind that this motion is not detected). If the heat transfer process (for the dusty component) occurs through heat conduction, the presence of local perturbations in other charged components of the plasma determines the potential energy of the interaction between dust particles (their charges and potential type), which, in turn, determines the equalization rate and gradients of the temperature of the dusty component (i.e., thermal diffusivity and thermal conductivity). Thus, the observed differences between the numerical and experimental results can likely be attributed not only to the presence of dissipation but also to the inconsistency of the numerical model under consideration, which implies the presence of the screened Coulomb potential, to the experimental conditions.

Thus, we carried out direct experiments allowing detailed kinetic analysis of the heat conduction processes in liquid dusty structures. The heat transfer coefficients for the dusty component in the plasma were measured by two independent methods: first, the thermal conductivity χ was determined by analyzing the steady heat transfer and, second, the thermal diffusivity θ was determined by analyzing the unsteady process. The quantity θ was additionally estimated by solving the problem of the equalization of temperature in the layer. All three independent methods of analyzing the experimental data are in good agreement with each other. Thus, the temperature gradients and the propagation of thermal perturbation that were observed in the reported experiments were likely caused by the heat conduction mechanism in the dusty component of the plasma.

The experimental data on the temperature dependence of the heat transfer coefficients were presented for liquid dusty structures in the plasma. In contrast to ideal gases [where $\theta(T) \propto T^{0.5}$], this dependence qualitatively agrees with the results of the simulation of heat transfer for simple fluids. The quantitative difference of the measurements from the numerical calculations can be attributed to the energy losses of dust particles due to their collisions with the neutrals of the surrounding gas, as well as to the inconsistency of the numerical model under consideration, which implies the presence of the screened Coulomb potential of the interaction between the dust particles, to the experimental conditions. The comparison of the thermal diffusivity for plasma–dust structures with the heat transfer coefficients of real one-atomic fluids shows that the measured θ value is more than one order of magnitude larger than the value for liquid dielectrics (such as condensed inert gases) and more than one order of magnitude less than the θ value for most liquid metals (by a factor of 20 to 100). Liquid mercury has the most close thermal diffusivity ($\theta \approx 0.04$ cm^2/s).

This study was supported in part by the Russian Foundation for Basic Research (project no. 04-02-16362), the U.S. Civilian Research and Development Foundation (grant no. RU-P2-2593-MO-04), the Presidium of the Russian Academy of Sciences, and the Foundation for Support of Russian Science.

REFERENCES

1. Ya. I. Frenkel', *Kinetic Theory of Liquids* (Nauka, Leningrad, 1975; Clarendon, Oxford, 1946).
2. *Photon Correlation and Light Beating Spectroscopy*, Ed. by H. Z. Cummins and E. R. Pike (Plenum, New York, 1974).
3. N. K. Ailawadi, Phys. Rep. **57**, 241 (1980).
4. N. H. March and M. P. Tosi, *Introduction to Liquid State Physics* (World Sci., Singapore, 1995).
5. H. M. Thomas and G. E. Morfill, Nature **379**, 806 (1996).
6. V. E. Fortov, O. S. Vaulina, O. F. Petrov, *et al.*, Phys. Rev. Lett. **90**, 245005 (2003).
7. V. E. Fortov, O. S. Vaulina, O. F. Petrov, *et al.*, Zh. Éksp. Teor. Fiz. **123**, 798 (2003) [JETP **96**, 704 (2003)].
8. O. S. Vaulina, O. F. Petrov, V. E. Fortov, *et al.*, Phys. Rev. Lett. **93**, 035004 (2004).
9. O. S. Vaulina and S. V. Vladimirov, Plasma Phys. **9**, 835 (2002).
10. O. S. Vaulina, S. V. Vladimirov, O. F. Petrov, *et al.*, Phys. Rev. Lett. **88**, 245002 (2002).
11. O. S. Vaulina and O. F. Petrov, JETP **99**, 510 (2004).
12. V. I. Molotkov, A. P. Nefedov, V. M. Torchinskiĭ, *et al.*, Zh. Éksp. Teor. Fiz. **116**, 902 (1999) [JETP **89**, 477 (1999)].
13. V. V. Zhakhovskii, V. I. Molotkov, A. P. Nefedov, *et al.*, JETP Lett. **66**, 419 (1997).
14. O. S. Vaulina, A. A. Samaryan, B. James, *et al.*, Zh. Éksp. Teor. Fiz. **123**, 1179 (2003) [JETP **96**, 1037 (2003)].
15. O. S. Vaulina, S. A. Khrapak, O. F. Petrov, *et al.*, Phys. Rev. E **60**, 5959 (1999).
16. O. S. Vaulina, A. A. Samarian, O. F. Petrov, *et al.*, Plasma Phys. Rep. **30**, 652 (2004).
17. S. V. Vladimirov, S. A. Maiorov, and N. F. Cramer, Phys. Rev. E **63**, 045401 (2001).
18. E. M. Lifshitz and L. P. Pitaevskiĭ, *Physical Kinetics* (Nauka, Moscow, 1979; Pergamon, Oxford, 1981).
19. L. D. Landau and E. M. Lifshitz, *Course of Theoretical Physics*, Vol. 6: *Fluid Mechanics*, 3rd ed. (Nauka, Moscow, 1986; Pergamon, New York, 1987).
20. H. Ohta and S. Hamaguchi, Phys. Plasmas **7**, 4506 (2000).

Translated by R. Tyapaev

JETP Letters, Vol. 82, No. 8, 2005, pp. 498–503. From Pis'ma v Zhurnal Éksperimental'noĭ i Teoreticheskoĭ Fiziki, Vol. 82, No. 8, 2005, pp. 556–561.

Trapping of an Electron in the Transmission through Two Quantum Dots Coupled by a Wire¶

A. F. Sadreev[a, b], E. N. Bulgakov[a], and I. Rotter[c]

[a] *Institute of Physics, Russian Academy of Sciences, Krasnoyarsk, 660036 Russia*

[b] *Department of Physics and Measurement Technology, Linköping University, S-58183 Linköping, Sweden*

[c] *Max-Planck-Institut für Physik komplexer Systeme, D-01187 Dresden, Germany*

e-mail: almsa@ifm.liu.se, almas@tnp.krasn.ru, ben@tnp.krasn.ru, rotter@mpipks-dresden.mpg.de

Received September 20, 2005

We consider single-channel transmission through a double quantum dot that consists of two identical single dots coupled by a wire. The numerical solution for the scattering wave function shows that the resonance width of a few of the states may vanish when the width (or length) of the wire and the energy of the incident particle each take a certain value. In such a case, a particle is trapped inside the wire as the numerical visualization of the scattering wave function shows. To understand these numerical results, we explore a simple model with a small number of states, which allows us to consider the problem analytically. If the eigenenergies of the closed system cross the energies of the transmission zeroes, the wire effectively decouples from the rest of the system and traps the particle. © *2005 Pleiades Publishing, Inc.*

PACS numbers: 03.75.Fi, 05.30.Jp, 67.57.Fg

Dramatic changes of the widths of resonance states may arise by resonance trapping: at strong coupling, a few resonance states of the system align with the channels and become short-lived, while the remaining ones decouple more or less strongly from the continuum of decay channels. This effect, which was first found in nuclear reactions [1], has been observed meanwhile in many different systems [2]. In atoms, it may appear as population trapping in laser-induced continuum structures [3]. In microwave cavities, it is studied theoretically [4] and experimentally [5]. Resonance trapping is caused by the existence of singular points in the complex energy plane [6].

In the transmission through microwave cavities or quantum dots (QDs), an additional parameter for varying the widths of the resonance states is involved. The transmission is determined by the manner the leads are attached to them, and the widths of the resonance states can be changed even without changing the coupling strength between the system and lead [7]. In a double QD, an internal wire couples the two single dots. The coupling and the wire's energy can be controlled. This allows us to even stabilize the system at certain parameter values without varying the coupling strength to the environment [8], at least in the one-channel case. On the one hand, the position of the transmission zeroes through such a system is determined by the spectroscopic properties of the single dots since the leads are attached only to them. On the other hand, the transmission is resonant in any case and related to the spectroscopic properties of the double QD as a whole. These two conflicting facts cause some nontrivial constraint on the system in order to fulfill the unitarity of the *S*-matrix [8]. As a consequence, the widths of the resonance states may be strongly parameter-dependent, and some of them may even *vanish* at certain parameter values. Such a case presents a novel bound state that corresponds to the confinement of an electron in the internal wire as we will show in the following.

The relation between transmission zeroes and resonance states with vanishing width has been studied also by other authors. Firstly, a drastic narrowing of the resonant peak was shown by Shahbazyan and Raikh in a junction of two resonant impurities [9]. In [10], an antibonding state is found to be totally decoupled from the leads and to give rise to a "ghost" Fano peak with zero width in the system of two coupled QDs. According to [11], a dynamic confinement of electrons in time-dependent quantum structures may appear due to the coherent interaction between two Fano resonances. The system studied is a double-well structure in which the electrons are confined in the region between the two wells at some special values of the energy of the incident particle and the length of the region between the wells. It is the aim of the present study to show that a similar phenomenon appears in the system of identical QDs connected by a wire. Localization of electrons in the wire takes place in this system without time-periodic perturbation, as we will show by considering the wave functions of the resonance states with vanishing width.

¶ The text was submitted by the authors in English.

The split gate in the middle of a double QD allows us to control, e.g., the width W of the wire that connects the two single QDs [12–14]. Using the exact correspondence between the quantum-mechanical description of the single-electron transmission through a QD and the transmission of planar electromagnetic waves through a microwave billiard [15], it is convenient to control the length L of the connecting waveguide. In any case, considering the wire as a stripe with the width W and the length L, we present the wire as a third quantum subsystem with the energies $\varepsilon_w \sim m^2W^{-2} + n^2L^{-2}$, where m and n are the quantum numbers of the wire. These modes appear in addition to the eigenenergies $\varepsilon_i \propto R^{-2}$ of the single QDs, where R is the characteristic scale of the single dot. If $L, W \ll R$ and $\varepsilon_w \gg \varepsilon_i$, the role of the wire as a third quantum subsystem is not relevant because the coupling between the dots is of tunneling type. However, for the case $\varepsilon_w \sim \varepsilon_i$, the wire degrees of freedom are important. In this case, the quantum system consists, indeed, of two quantum subsystems coupled by a third quantum subsystem that has its own energy spectrum. In the following, we present the theory for the one-channel case of this system. It is not restricted to the description of double billiards but can be applied also to the transmission through a system consisting of two scattering centers that are connected by a waveguide. Such a system might be, e.g., waveguides with two bends [16–18].

In order to vary smoothly the width of the wire in the numerical computation, we apply an auxiliary potential

$$V(x, y) = V_0\{1 + 0.5[\tanh(C(y - W/2)) - \tanh(C(y + W/2))]\} \quad (1)$$

to squeeze the wire in a similar manner as in a real double QD system [12–14]. In computations, we take $V_0 = 100$, $C = 17$. The transmission probability, presented in the log scale in Fig. 1, clearly shows transmission zeroes appearing at certain energies independently of the width W of the stripe (for details, see the discussion in [8]). The most interesting features appear, however, at the points where the eigenenergies of the double QD system cross the transmission zeroes (two points are marked by open circles in Fig. 1).

Originally, the spectroscopic values such as the positions in energy of states are defined for the discrete eigenstates of Hermitian Hamiltonian H_B that describes the closed quantum system. When embedded into the continuum of scattering states, the discrete eigenstates of the closed system turn over into resonance states with a finite lifetime. The effective Hamiltonian H_{eff} of the open quantum system contains H_B as well as an additional term [2] that describes the coupling of the resonance states to the common environment,

$$H_{\text{eff}} = H_B + \sum_C V_{BC}\frac{1}{E^+ - H_C}V_{CB}. \quad (2)$$

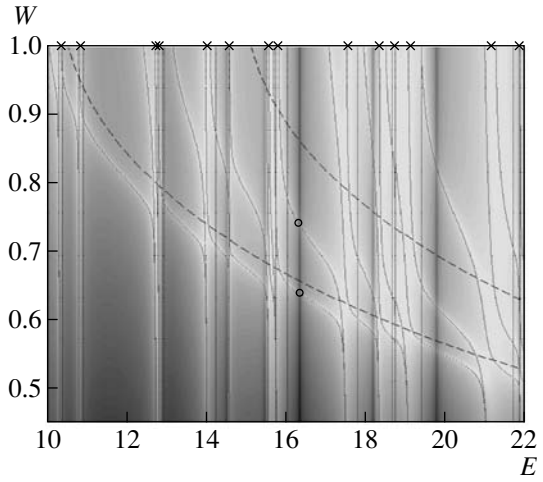

Fig. 1. The probability $\ln(T(E, W))$ for the transmission through the double QD shown in Fig. 3 versus energy and width of the wire. The eigenenergies of each single QD are marked by crosses. The eigenenergies of the wire are shown by dashed curves, and those of the closed double QD system, by thin dotted curves. In the present calculation, the eigenenergies of the closed system are almost the same as the eigenenergies of the open system. The radius of the QD in units of the width d of the input and output leads is $3d$. The length of the wire is $2.5d$. The size of all diaphragms is $0.6d$.

Here, V_{BC} and V_{CB} stand for the coupling matrix elements between the eigenstates of H_B and the environment that may consist of different continua C, e.g., the scattering waves propagating in the left and right leads attached to the closed system. The concept of the effective Hamiltonian appeared first in Feshbach's papers [19] and, independently, in Livshitz's study of open quantum system [20]. H_{eff} is non-Hermitian, its eigenvalues z_k and eigenfunctions are complex and contain the "external" interaction of the resonance states via the continuum. The complex eigenvalues of the effective Hamiltonian determine the positions and widths of the resonance states. They are energy-dependent functions, since the non-Hermitian effective Hamilton operator (2) depends on energy. Nevertheless, spectroscopic values for resonance states can be defined also for the resonance states [2, 21] by solving the fixed-point equations

$$E_k = \text{Re}(z_k)\big|_{E = E_k} \quad (3)$$

and defining

$$\Gamma_k = 2\text{Im}(z_k)\big|_{E = E_k}. \quad (4)$$

The values E_k and Γ_k characterize a resonance state whose position in energy is E_k and whose decay width is Γ_k. These values coincide approximately with the poles of the S matrix.

The effective Hamiltonian H_{eff} appears in the derivation of the S matrix [2, 21]. Calculations performed

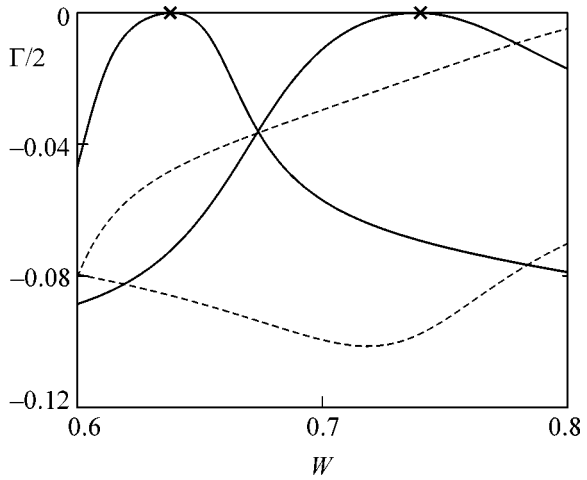

Fig. 2. The imaginary part Γ_k of the first four eigenvalues z_λ as a function of W for $E = 16.36$. The first two Γ_k which vanish at $W = 0.638$ and $W = 0.74$ are shown by the solid curves. Corresponding points are marked by crosses. They exactly correspond to points shown in Fig. 1 by open circles.

with H_{eff} correspond therefore to calculations on the basis of the S matrix, but they contain additionally a unique definition of the spectroscopic values [21]. Explicitly in the tight-binding approach, H_{eff} is given in [22, 23]. The results of a numerical computation for the system consisting of two quantum dots coupled by a wire are shown in Fig. 2 for the imaginary parts of four complex eigenvalues z_k. The points marked by crosses in Fig. 3 are found by self-consistent solution of Eqs. (3) and (4). They exactly correspond to the points shown in Fig. 1.

The numerically computed scattering wave functions (Fig. 3) demonstrate that, at these points, the electrons are localized inside the wire that connects the two single QDs. This effect appears, of course, only in the open double-dot system. In the closed system, a localization in the wire will never occur.

In order to understand this mechanism of electron confinement, we use the periodicity of the transmission picture (Fig. 1), which allows us to restrict the investigation to the transmission properties of a simple model with only a few states in each single QD [8].

The Hamiltonian of the closed system consists of three parts: two parts describe the two single QDs, and a third one is related to the wire. The Hamiltonian of minimal dimension, which can cause a zero in the transmission through a single QD, is two [8]. Then, the total Hamiltonian, which can explain the characteristic features of Figs. 1 and 2, has the following matrix form:

$$H_B = \begin{pmatrix} \varepsilon_1 & 0 & u & 0 & 0 \\ 0 & \varepsilon_2 & u & 0 & 0 \\ u & u & \varepsilon_w & u & u \\ 0 & 0 & u & \varepsilon_2 & 0 \\ 0 & 0 & u & 0 & \varepsilon_1 \end{pmatrix}. \quad (5)$$

For simplicity, it is assumed here that the two single QDs are identical and that all the coupling constants u between the wire and the single QDs are the same. The Hamiltonian (5) differs from those used in the literature [10, 24, 25] for the description of a double QD by taking explicitly into account the wire as a third subsystem. The eigenenergies ε_w of the wire depend on at least two values: on the width W and the length L. Without loss of generality, we can consider the energy ε_w to be the parameter by which the system can be controlled.

The knowledge of the eigenstates of the closed quantum system allows us to formulate the S-matrix

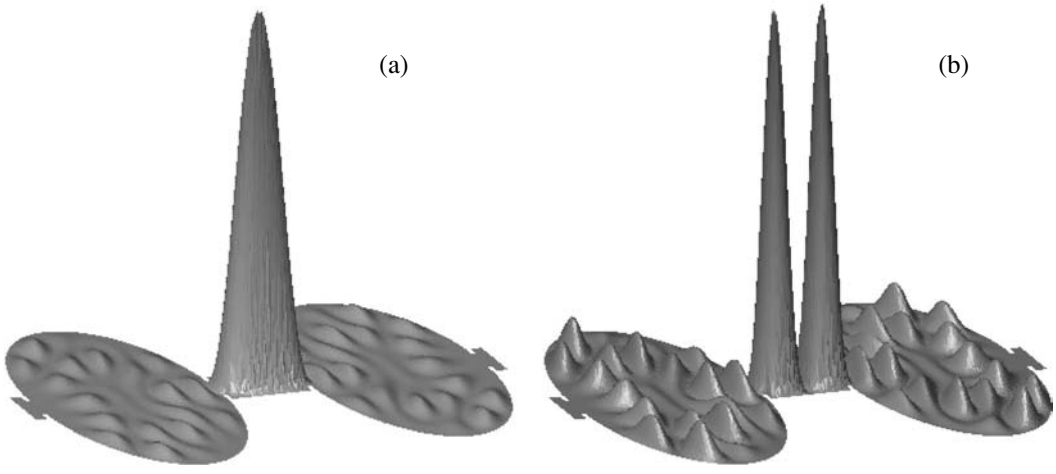

Fig. 3. The density probability for the transmission through the double QD for the two cases shown in Fig. 1 by open circles: (a) $E = 16.36$, $W = 0.638$; (b) $E = 16.36$, $W = 0.74$.

and the effective Hamiltonian in the manner described in [23, 26] in order to consider the transmission through the system. Let E_m and $|m\rangle$ with $m = 1, \ldots, 5$ denote the five eigenenergies and eigenstates of (5). The amplitudes $\langle j = 1, 2|m\rangle$ describe the left billiard, $\langle j = 3|m\rangle$ the wire, and $\langle j = 4, 5|m\rangle$ the right billiard. Similar to [10], we assume that the left lead is coupled to both states ($j = 1, 2$) of the left billiard with the same strength v. Correspondingly, the right lead is coupled to both states ($j = 4, 5$) of the right billiard with the same strength v. Then, the coupling matrix elements between the closed system and the two leads L and R can be written as

$$\langle E, C|V|m\rangle = v\sqrt{\frac{\sin k}{2\pi}}V_C(m), \tag{6}$$

where $C = L, R$, $V_L(m) = v\sum_{j=1,2}\langle j|m\rangle$, $V_R(m) = v\sum_{j=4,5}\langle j|m\rangle$. The factor $\sqrt{\sin k}$ in (6) results from the one-dimensional leads [8, 23]. The matrix elements of the effective Hamiltonian are [8, 23, 26]

$$\langle m|H_{\text{eff}}|n\rangle = E_m\delta_{mn} - (V_L(m)V_L(n) + V_R(m)V_R(n))e^{ik}. \tag{7}$$

Using the S-matrix formalism [2, 23, 26], the amplitude for the transmission through the system reads [23]

$$t = -2\pi i\sum_{\lambda}\frac{\langle L|V|\lambda)(\lambda|V|R\rangle}{E - z_\lambda}. \tag{8}$$

Figure 4a closely reproduces a fragment of the total picture (Fig. 1), including the appearance of transmission zeroes. According to Fig. 4b, the decay widths of the eigenstates 2 and 4 of the effective Hamiltonian are independent of the wire's energy ε_w, while those of the other states depend on it. The state 3, lying in the middle of the spectrum, crosses the transmission zero at

$$\varepsilon_w = \varepsilon_b = \frac{\varepsilon_1 + \varepsilon_2}{2}. \tag{9}$$

At this energy, we have from (5) the following eigenenergies

$$E_{1,5} = \varepsilon_b \pm \eta, \quad E_2 = \varepsilon_1, \quad E_3 = \varepsilon_b, \quad E_4 = \varepsilon_2 \tag{10}$$

and eigenstates

$$\langle 1| = \frac{\sqrt{2}u}{\eta}\left(\frac{u}{\eta - \Delta\varepsilon}, \frac{u}{\eta + \Delta\varepsilon}, -1, \frac{u}{\eta + \Delta\varepsilon}, \frac{u}{\eta - \Delta\varepsilon}\right),$$

$$\langle 2| = \frac{1}{\sqrt{2}}(1, 0, 0, 0, -1),$$

$$\langle 3| = \frac{u}{\eta}\left(1, -1, \frac{\Delta\varepsilon}{u}, -1, 1\right), \tag{11}$$

$$\langle 4| = \frac{1}{\sqrt{2}}(0, 1, 0, -1, 0),$$

$$\langle 5| = \frac{\sqrt{2}u}{\eta}\left(\frac{u}{\eta + \Delta\varepsilon}, \frac{u}{\eta - \Delta\varepsilon}, 1, \frac{u}{\eta - \Delta\varepsilon}, \frac{u}{\eta + \Delta\varepsilon}\right),$$

where $\eta^2 = \Delta\varepsilon^2 + 4u^2$, $\Delta\varepsilon = (\varepsilon_2 - \varepsilon_1)/2$. Substituting (11) into (6), we obtain

$$\langle m|V|E, C = L, R\rangle = v\sqrt{\frac{\sin k}{8\pi}}(1 \pm 1 \quad 0 \pm 1 \quad 1) \tag{12}$$

for the elements of the coupling matrix. One can see that, under condition (9), the wire decouples from the rest of the system. Substitution of (12) into (2) shows

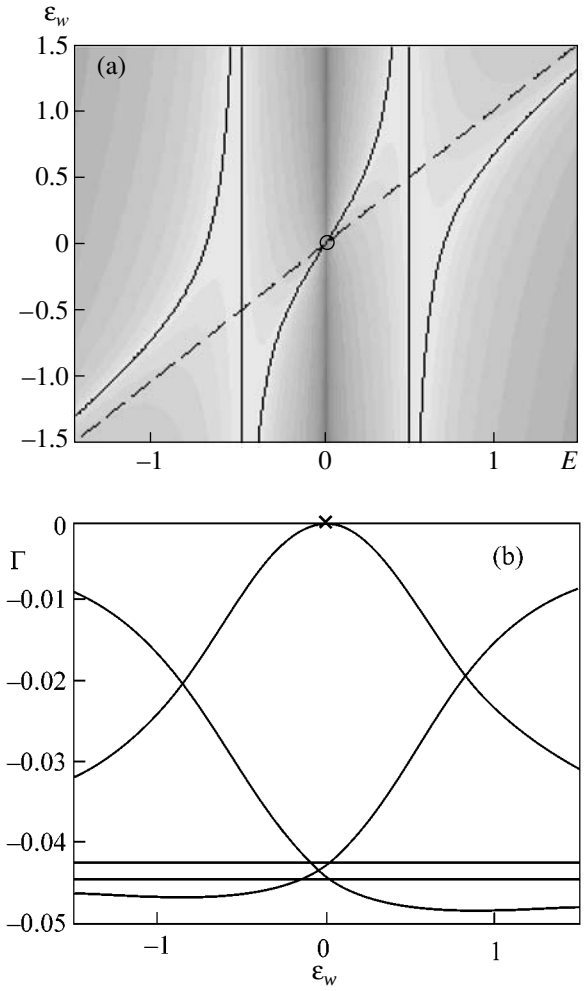

Fig. 4. (a) The transmission through a system with two identical QDs that are connected by a wire versus incident energy E and energy of the wire ε_w. The eigenenergies of (5) are shown by solid curves, and the energy ε_w of the wire is shown by the dashed curve. The QDs have energies $\varepsilon_{1,2} = \pm 1/2$. $v = 1/2$, $u = 1/4$. (b) The imaginary part of the five eigenvalues z_λ of the effective Hamiltonian (2) as a function of ε_w for $E = 0.5$ (at $E = 0$, the widths of the two short-lived states are equal). One of imaginary parts is equal to zero at $\varepsilon_w = \varepsilon_b = 0$ for all energies E marked by cross.

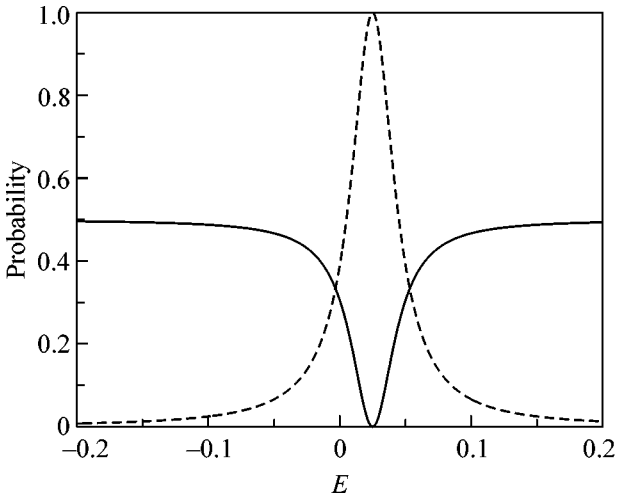

Fig. 5. The probabilities for the electron to be in the wire (dashed curve) and in the right and left QD (full curve) as a function of the wire's energy. $\varepsilon_{1,2} = \pm 1/2$, $v = 1/2$, $E = 0.02$, $u = 0.2$.

that, at $\varepsilon_w = \varepsilon_b$, the effective Hamiltonian matrix 5×5 decomposes as $H_{\text{eff}} = H_1 \oplus E_3 \oplus H_2$, where

$$H_1 = \begin{pmatrix} E_1 + \Gamma & \Gamma \\ \Gamma & E_5 + \Gamma \end{pmatrix}; \quad H_2 = \begin{pmatrix} E_2 + \Gamma & \Gamma \\ \Gamma & E_4 + \Gamma \end{pmatrix}, \tag{13}$$

and $\Gamma = -v^2\exp(ik)/2$. Obviously, the imaginary part of the third eigenvalue of H_{eff} is zero, i.e., the width of the third eigenstate vanishes at $\varepsilon_w = \varepsilon_b$. According to formula (105) of [23], the scattering wave function can be decomposed in the set of eigenfunctions of H_{eff},

$$\psi = \sum_{\lambda,\, C = L,\, R} \frac{V_\lambda(E, C)}{E^+ - z_\lambda}\psi_\lambda, \tag{14}$$

where the $V_\lambda(E, C)$ are the coupling matrix elements between the leads C and the *open* double QD described by the eigenstates ψ_λ of H_{eff}. Since the eigenvalue z_3 is real, $V_3(E, C) \longrightarrow 0$ if $E \longrightarrow z_3 = E_3 = \varepsilon_b$. Therefore, a particle moving from the left (right) lead to the left (right) billiard is fully reflected. That means the wire is decoupled from the reservoirs and the electrons are trapped inside the wire. According to (8), the contributions from $\lambda = 1$ and 5 as well as those from $\lambda = 2$ and 4 to the transmission cancel each other at $E = \varepsilon_b$ due to the symmetry in relation to ε_b, while the contribution from $\lambda = 3$ vanishes. As a consequence, an electron will not be transmitted at the energy $E = \varepsilon_b$. The probability for the electron to be in the left QD is $\sum_{j=1,2}|\psi(j)|^2$ and in the right one $\sum_{j=4,5}|\psi(j)|^2$. For the case of time reversal symmetry (both leads are equivalent), these probabilities coincide (Fig. 5, full curve). The probability for the electron to be in the wire is given by $|\psi(3)|^2$ (Fig. 5, dashed curve). A localization of the electron in the wire takes place when $\varepsilon_w = \varepsilon_b$.

The physical reason of the localization of electrons inside the wire in the one-channel case is flux conservation expressed by the unitarity of the *S*-matrix. A full localization takes place only when the two single QDs are identical and both leads are equivalent. The effect exists also when the two single dots are slightly different from one another and (or) time reversal symmetry is broken. It is, however, somewhat reduced in such a case. These features are similar to those observed in laser-induced continuum structures in atoms, which are called population trapping [3]. The mechanism by which the resonance states with vanishing width are created is, however, different in the two cases.

The electron localization in the transmission through a system with two identical QDs can be seen also in the generalized Fabry–Perot approach [11]. We ignore the evanescent modes in the wire, the total transmission amplitude in the single-channel case can be easily calculated as a geometrical sum over all the individual transmitted and reflected elementary processes. This gives the simple expression

$$T = \frac{t_1^2}{1 - r_1^2\exp(2iqL)} \tag{15}$$

for the transmission probability, where t_1 and r_1 are the complex amplitudes of the transmission and reflection for a single quantum billiard, and q is the wave number of the connecting waveguide related to the energy of the single-channel transmission by $E = q^2 + \pi^2/W^2$. The bound states are defined by the zeroes of the denominator in T, i.e., by $\sin(\phi(E) + q(E)L) = 0$, where $\phi(E) = \arg(r1)$. One obtains, therefore, a quantization rule for the particle trapped in the one-dimensional box of length L. In fact, Fig. 3 shows the first two of these bound states in the wire. However, exponentially small evanescent modes in the internal wire slightly violate formula (15).

In conclusion, controlling the eigenenergies of the wire that connects the two single QDs of a double QD, by means of the gate voltage, the widths of the resonance states of the double QD system and the transmission through this system can be manipulated. When the width of one of the resonance states vanishes, the electrons are trapped in the wire and the transmission is zero. This effect might be used for quantum information storage.

We are grateful to K.N. Pichugin for many fruitful discussions and to P.A. Mello for a critical reading of the manuscript. A.F.S. also thanks K.-F. Berggren for discussions. This work was supported by the Russian

Foundation for Basic Research (project no. 05-02-97713 “Enisey”).

REFERENCES

1. P. Kleinwächter and I. Rotter, Phys. Rev. C **32**, 1742 (1985); I. Rotter, Rep. Prog. Phys. **54**, 635 (1991).
2. J. Okołowicz, M. Płoszajczak, and I. Rotter, Phys. Rep. **374**, 271 (2003).
3. A. I. Magunov, I. Rotter, and S. I. Strakhova, J. Phys. B **32**, 1669 (1999); J. Phys. B **34**, 29 (2001).
4. E. Persson, K. Pichugin, I. Rotter, and P. Seba, Phys. Rev. E **58**, 8001 (1998); P. Seba, I. Rotter, M. Müller, *et al.*, Phys. Rev. E **61**, 66 (2000); I. Rotter, E. Persson, K. Pichugin, and P. Seba, Phys. Rev. E **62**, 450 (2000).
5. E. Persson, I. Rotter, H. J. Stöckmann, and M. Barth, Phys. Rev. Lett. **85**, 2478 (2000); H. J. Stöckmann *et al.*, Phys. Rev. E **65**, 066 211 (2002).
6. I. Rotter and A. F. Sadreev, Phys. Rev. E **71**, 036227 (2005).
7. R. G. Nazmitdinov, K. N. Pichugin, I. Rotter, and P. Seba, Phys. Rev. E **64**, 056214 (2001); Phys. Rev. B **66**, 085322 (2002).
8. I. Rotter and A. F. Sadreev, Phys. Rev. E **71**, 046204 (2005).
9. V. Shahbazyan and M. E. Raikh, Phys. Rev. B **49**, 17123 (1994).
10. M. L. Ladron de Guevara, F. Claro, and P. A. Orellana, Phys. Rev. B **67**, 195335 (2003).
11. C. S. Kim and A. M. Satanin, Phys. Rev. B **58**, 15 389 (1998).
12. N. C. van der Vaart *et al.*, Phys. Rev. Lett. **74**, 4702 (1995).
13. F. R. Waugh *et al.*, Phys. Rev. Lett. **75**, 705 (1995).
14. J. C. Chen, A. M. Chang, and M. R. Melloch, Phys. Rev. Lett. **92**, 176801 (2004).
15. H.-J. Stöckmann, *Quantum Chaos: An Introduction* (Cambridge Univ. Press, Cambridge, 1999).
16. K.-F. Berggren and Zh.-L. Ji, Phys. Rev. B **47**, 6390 (1993).
17. K. Vacek, A. Okiji, and H. Kasai, Phys. Rev. B **47**, 3695 (1993).
18. J. P. Carini *et al.*, Phys. Rev. B **55**, 9842 (1997).
19. H. Feshbach, Ann. Phys. (N.Y.) **5**, 357 (1958); Ann. Phys. (N.Y.) **19**, 287 (1962).
20. M. S. Livshits, Sov. Phys. JETP **4**, 91 (1957).
21. I. Rotter, Rep. Prog. Phys. **54**, 635 (1991).
22. S. Datta, *Electronic Transport in Mesoscopic Systems* (Cambridge Univ. Press, Cambridge, 1995).
23. A. F. Sadreev and I. Rotter, J. Phys. A **36**, 11413 (2003).
24. M. N. Kiselev, K. A. Kikoin, and L. W. Molenkamp, JETP Lett. **77**, 366 (2003).
25. T.-S. Kim and S. Hershfield, Phys. Rev. B **67**, 235330 (2003).
26. F. M. Dittes, Phys. Rep. **339**, 215 (2000).

JETP Letters, Vol. 82, No. 8, 2005, pp. 504–508. Translated from Pis'ma v Zhurnal Éksperimental'noĭ i Teoreticheskoĭ Fiziki, Vol. 82, No. 8, 2005, pp. 562–566.

Giant Photoplastic Effect in Vitreous Semiconductors near the Rigidity Percolation Transition

M. L. Trunov[a, *], V. S. Bilanich[a], S. N. Dub[b], and R. S. Shmegera[b]

[a] *Uzhgorod National University, Uzhgorod, 88000 Ukraine*

** e-mail: stm@tn.uz.ua*

[b] *Bakul Institute for Superhard Materials, National Academy of Sciences of Ukraine, Kiev, 04074 Ukraine*

Received August 11, 2005

The negative giant photoplastic effect (giant photosoftening) has been experimentally observed in the As–Se system when films obtained by thermal evaporation of $As_{20}Se_{80}$ chalcogenide glass are irradiated by light from the region of the fundamental absorption edge. Correlation has been found between the photoplastic effect and rigidity percolation transition in the As–Se chalcogenide glass matrix. Such a correlation is not revealed when light irradiation changes the optical properties of these glass films. It has been shown that a nonlinear (non-Hookian) mechanism of the formation of the strain response is realized in the films subjected to the combined action of light and external mechanical loading. © *2005 Pleiades Publishing, Inc.*

PACS numbers: 61.43.Fs, 63.50.+x, 78.35.+c

The negative photoplastic effect was observed previously [1–3] in As–S(Se) vitreous semiconductor films irradiated by light from the region of the absorption edge. A macroscopic model of this phenomenon was based on the assumption of the athermal decrease in the viscosity of the films during irradiation to 10^{12}–10^{13} P, which is close to the viscosity of vitreous semiconductors near their softening temperature T_g. This assumption was directly corroborated in experiment [2].

Further observations of a manifestation of the negative photoplastic effect at low temperatures in amorphous selenium (optical melting [4]), photoinduced fluidity [5], which was discovered when vitreous semiconductor fibers were irradiated by slightly-absorbed light, as well as the presence of the temperature hindering of the negative photoplastic effect [5, 6], show that the law found in [1, 2] is universal and common. Further theoretical [7, 8] and experimental [9–12] investigations support the assumption that the negative photoplastic effect is caused by specific molecular structures such as $As_4S_4(Se_4)$ and/or $As_4S_3(Se_3)$. It is essential that the presence of these structural units is responsible for the known effect of light-induced changes in the optical constants in chalcogenide glasses and films based on them. The concentration of such structural units are maximal in compositions close to the stoichiometric compounds $As_{40}S_{60}$ and $As_{40}Se_{60}$, as well as in nonstoichiometric compounds with arsenic excess ($As_{44}S_{66}$ and $As_{50}Se_{50}$). Thus, investigations of the physical properties of As–S(Se) amorphous materials show that the maximum photoinduced changes in the structure must be observed in stoichiometric compositions and compositions with arsenic excess [4–12]. Moreover, one-to-one correlation must exist between photoinduced changes in the optical and elastoplastic properties.

At the same time, Mandelstam–Brillouin scattering investigations with Ge–Se glasses [13] indicate that specific atomic configurations (clusters) with broken bonds play a significant role: a change in their concentration causes the rigidity percolation transition in the system of defects of the chalcogenide glass matrix [14]. Near such a concentration transition, the maximum changes in the elastoplastic properties of films irradiated by light, i.e., the maximum negative photoplastic effects, should be expected. This approach is likely universal and can be applied to chalcogenide glasses in other systems, for which the rigidity-percolation theory is developed, including As–Se glasses [15].

In this work, it is shown that in amorphous films obtained by thermal evaporation of As–Se chalcogenide glasses, the negative photoplastic effect is observed whose magnitude significantly depends on the concentration of chalcogen atoms. The giant photosoftening (the giant negative photoplastic effect) is reached in films with the selenium concentration near 80 at %, whereas the photoinduced changes in the optical constants in such films are minimal. This behavior indicates that there is correlation between the negative photoplastic effect and the threshold of the rigidity percolation transition in vitreous semiconductors. At the same time, there is no correlation with the known phenomenon of photostructural transformations in chalcogenide glasses that give rise to changes in their optical characteristics.

The photomechanical response of films to the irradiation by light from the region of the absorption edge was studied by the method of nanoindentation of sam-

ples on a Nanoindenter II (MTS Systems) nanohardness meter. The instrument is equipped with a sharp indenter (a three-sided diamond Berkovich pyramid with a vertex angle of 65.3° and a tip curvature radius of about 200 nm) and allows investigation of samples with various loading application schemes. The basic characteristics of the instrument and the nanohardness test procedure were described in [16, 17]. The nanohardness H and Young's modulus E were determined by the Oliver–Pharr method [18] in terms of the indented-region depth using the indenter penetration diagram obtained during the test. In order to accumulate statistics and to estimate the reproducibility of the results, tests were carried out with three samples obtained in one technological deposition cycle. The measurement accuracies in our experiments did not exceed 0.01 GPa and 0.5 GPa for the nanohardness and Young's modulus, respectively.

We used the scheme of applying a load in the form of a rectangular pulse. In contrast to the load scheme commonly accepted for nanoindentation [16], after the unloading of a sample, the nanohardness meter operated in the regime of the viscoelastic recovery of the indented region. Each nanoindentation test consisted of four time segments: the loading segment (2 s), the segment of the exposition of the indenter at the maximum loading (60 s), the unloading segment (2 s), and the segment of the indented-region recovery (60 s) (line *1* in Fig. 1). The maximum load in each cycle was equal to 2 mN. During the experiment, several pricks (test cycles) of a sample were performed at the same test parameters and with the lateral displacement of the indenter after each test. Thus, a new test cycle was conducted in the following (clean) film section. The distance between sections was equal to 25 ± 0.5 μm. The total area of the tested section was much less than the area of the laser spot (2 mm^2) that was further focused on the sample. Each sample was subjected to five test cycles: two cycles in darkness (before and after irradiation) and three cycles during light irradiation, which allowed investigation of the dynamics of the elastoplastic properties of films in nanocontacts upon irradiation.

We tested films obtained by thermal evaporation of As_xSe_{100-x} chalcogenide glass (with x = 0, 10, 20, 30, 40, and 50 at %) on K-8 glass substrates. This material was chosen because As–Se glasses have the minimum concentration dependence of the gap width as compared to other binary chalcogenide glasses (in particular, As–S and Ge–Se systems) [19]. This choice excludes the necessity of the choice of the radiation source for each composition and the fundamental resonance absorption of light is ensured upon irradiation by light with a wavelength of 630–690 nm.

The film thickness in the deposition process was controlled by the interference method and was equal to 2 μm. To reduce the effect of relaxation processes upon the stabilization of the structure, freshly deposited films were kept in darkness for three months. The irradiation

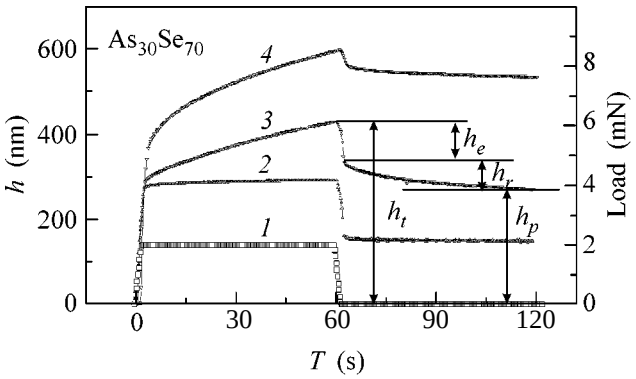

Fig. 1. Time dependence of the indenter penetration depth in nanoindentation of $As_{30}Se_{70}$ films (*2*) in darkness and in the (*3*) second and (*4*) third cycles of tests upon continuous light irradiation, along with the (*1*) loading application scheme in the test process.

was carried out by means of a 650-nm solid state laser whose radiation energy (E = 1.90 eV) is close to the gap width of the films under investigation ($E_g \approx$ 1.78–1.90 eV at absorption $\alpha = 10^3$ cm^{-1}), and the radiation power did not exceed 20 mW/cm^2.

Figure 1 shows the characteristic time dependences of the penetration depth of the Berkovich indenter for an $As_{30}Se_{70}$ film. Qualitatively similar dependences were observed for films of other compositions.

By analogy with investigations of the retarded elasticity in glasses by the strain relaxation method [20], the total penetration depth h_t of the indenter at the unloading time can be represented as the sum $h_t = h_e + h_r + h_p$ of the elastic h_e, the relaxation h_r, and the plastic h_p components (see line *3* in Fig. 1).

As is seen in Fig. 1, the indenter penetration depth in the nanoindentation of the film in darkness varies only slightly during the indenter exposition to loading and the recovery of the indented region is primarily determined by the elastic component h_e at the step unloading (line *2* in Fig. 1). Upon irradiation, the ratios of the components h_e, h_r, and h_p, as well as h_t, sharply change. The dynamics of these changes are correlated with the previously obtained results for variation in the micro- and nanohardness of the As–Se films during irradiation [21–25]. In particular, when loading is combined with the simultaneous irradiation of the sample (line *3* in Fig. 1), a sharp increase in the indenter penetration depth, as well as a pronounced viscoelastic increase in the indented-region depth, is observed. Unloading is accompanied by a step decrease in the indented-region depth by h_e and by a further recovery of the indented region due to the h_r component.

The results obtained in the next nanoindentation cycle (line *4* in Fig. 1) represent the dynamics of the photoinduced redistribution of the components h_e, h_r, and h_p, which depends on the chemical composition of

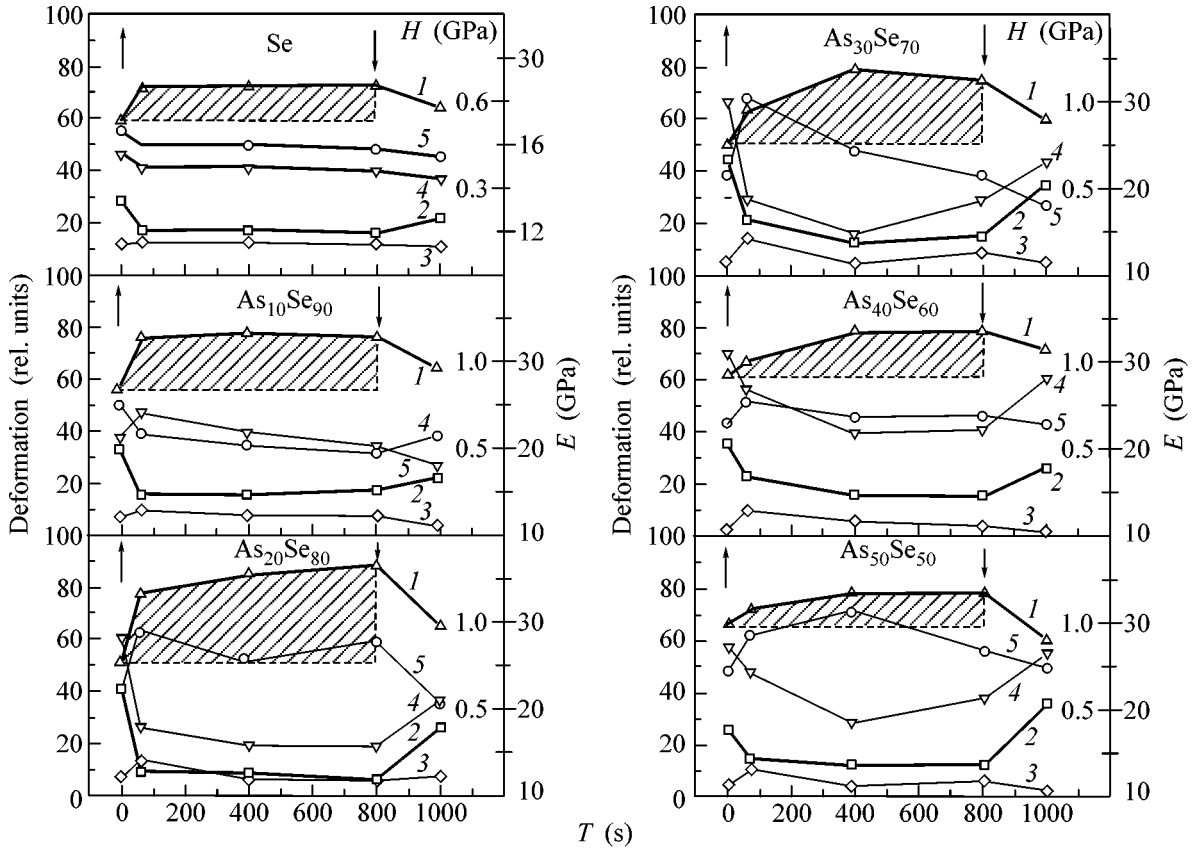

Fig. 2. Dynamics of the photomechanical response of As_xSe_{100-x} films upon indentation: the (*1*) plastic h_p, (*2*) elastic h_e, and (*3*) viscous h_r components of the total strain of the films, (*4*) nanohardness (*H*), and (*5*) Young's modulus (*E*). The area of the shaded region is proportional to dynamical variations ΔW in the energy absorbed by a sample in nanoindentation cycles upon light irradiation. The times of the appearance and disappearance of light irradiation are shown by ↑ and ↓, respectively.

the samples under investigation. This dependence, as well as the changes in the nanohardness and the Young's modulus upon light irradiation for all the test cycles, is shown in Fig. 2. The strain components are determined using the indenter unloading curve for each test cycle (see line *3* in Fig. 1). It is seen that dynamical changes are observed not only for the (line *1*) h_p, (line *2*) h_e, and (line *3*) h_r components but also for (line *4*) the nanohardness *H* and (line *5*) the Young's modulus *E*. A light-induced change in the mechanical parameters of the films indicates that the films become more compliant and plastic; maximum changes occur in the $As_{20}Se_{80}$ film. At the initial stage of irradiation, a step increase in the (line *1* in Fig. 2) plastic component and (line *5*) Young's modulus, as well as a simultaneous decrease in the (line *2*) elastic component and (line *4*) nanohardness, are observed. In particular, the plastic component h_p increases by 30% at the initial time, whereas the nanohardness is halved. Figure 2 also shows that, for the same loading on the indenter, change is observed in (line *2*) the elastic strain component h_e upon unloading, which testifies to the non-Hookian character of the film deformation process upon irradiation. The estimate of resistance to plastic deformation obtained using the parameter $K = H^3/E^2$ [26] shows that the $As_{20}Se_{80}$ film becomes 20 times more plastic at the initial irradiation stage than before irradiation. However, for films of other compositions, this factor is much lower; e.g., it varies from 1.5 to 5 for $As_{10}Se_{90}$ and $As_{40}Se_{60}$, respectively.

Using the data obtained in all the test cycles, one can obtain the concentration dependence of the parameters of the photoplastic effect in As_xSe_{100-x}. It is known [27] that the energy *W* absorbed by a sample per loading cycle in nanoindentation is determined by the loop area of the loading–unloading cycle in the force–displacement diagram. The main parameter determining this energy is h_p. Taking into account that radiation-induced change in the relaxation component depends only slightly on the composition (line *3* in Fig. 2), the dynamical variations in the energy ΔW absorbed in the As_xSe_{100-x} films subjected to nanoindentation during irradiation are primarily determined by the redistribution of the h_p and h_e components (because $h_r < h_e < h_p$) and, therefore, are proportional to the area ΔS under the $h_p(t)$ curve (the shaded region in Fig. 2). As one of the

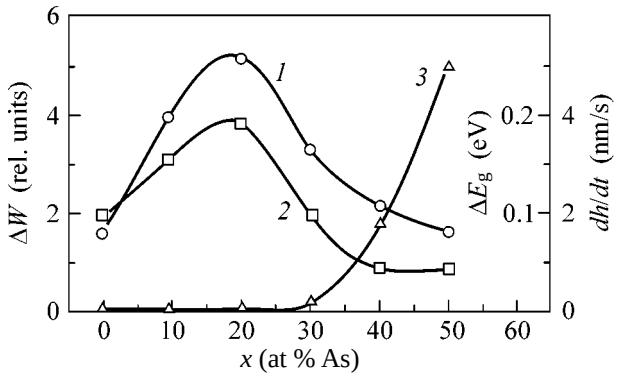

Fig. 3. Concentration dependences of (*1*) the absorbed energy increment ΔW, (*2*) the initial variation rate dh_p/dt for the plastic component of the photomechanical response in the photoplastic effect, and (*3*) photoinduced variation in the gap width for As_xSe_{100-x} films (according to [28]).

parameters of the photoplastic effect, one can also use the photomechanical response of a material that determines its sensitivity to radiation and constitutes the rate of radiation-induced structural changes. This quantity is equal to the variation rate dh_p/dt of the plastic component and can be determined in the first two test cycles, i.e., the dark cycle and first cycle of the sample irradiation.

Figure 3 shows the concentration dependences of (line *1*) $\Delta S(x)$ and (line *2*) $dh_p/dt(x)$. According to the above data, both parameters exhibit a peak near a selenium atom concentration of 80 at %, which points to giant changes in the mechanical compliance of the light-irradiated material and to a significant increase in the energy absorbed in the film of this composition in the nanoindentation process. In particular, the plastic strain rate in $As_{20}Se_{80}$ films is five times higher than that in amorphous selenium and in $As_{40}Se_{60}$. Similarly, the maximum of the absorbed energy per nanoindentation cycle is also observed in the $As_{20}Se_{80}$ film and is two or three times higher than the corresponding values for amorphous selenium and arsenic triselenide films. At the same time, light-induced changes in the optical properties of $As_{20}Se_{80}$ films are almost absent (line *3* in Fig. 3). The above data unambiguously indicate that the photoplastic effect in these materials depends on their structure and on the presence of certain structural elements.

The giant photoplastic effect found in this work can be analyzed in the framework of rigidity percolation theory. The dependence of the interaction character and the cohesion degree in the amorphous matrix for As_xSe_{100-x} glasses on the coordination number z makes it possible to separate three elastic phases [14]: floppy ($z < 2.29$), intermediate ($2.29 < z < 2.37$), and rigid ($z > 2.37$). The effective coordination number for covalent bonds in Se ($z = 2$) and $As_{20}Se_{80}$ ($z = 2.20$) is lower than the hardness percolation threshold ($z = 2.29$), whereas $z = 2.4$ for the structure-forming matrix in the stoichiometric composition $As_{40}Se_{60}$. This indicates that the structure-forming matrix in arsenic triselenide is topologically rigid, whereas the structure of $As_{20}Se_{80}$ glass is relatively soft and free of internal stresses. Thus, the maximum photomechanical response to light irradiation is expected in bulk glasses of the compositions for which the coordination number z corresponds to the transition from the floppy phase to the intermediate one, i.e., $z \approx 2.29$.

At the same time, it is worth noting that such argumentations are completely valid for bulk glasses and can so far be applied to films with certain qualifications before the unambiguous experimental corroborations of the existence of such phases in film samples. Indeed, it is known that the structure of the films differs from the initial glass despite the good agreement of the chemical composition for the objects of our investigation [29]. Possibly owing to this circumstance, the maximum of the negative photoplastic effect is reached in $As_{20}Se_{80}$ films, whereas the percolation transition from the floppy phase to the intermediate one for bulk glasses is observed in $As_{29}Se_{71}$ glass [15].

REFERENCES

1. M. L. Trunov and A. G. Anchugin, Pis'ma Zh. Tekh. Fiz. **18** (1), 37 (1992) [Sov. Tech. Phys. Lett. **18**, 14 (1992)].
2. M. L. Trunov and A. G. Anchugin, Pis'ma Zh. Tekh. Fiz. **18** (5), 78 (1992) [Sov. Tech. Phys. Lett. **18**, 158 (1992)].
3. M. L. Trunov, J. Non-Cryst. Solids **192–193**, 431 (1995).
4. H. Oyanagi, A. Kolobov, and K. Tanaka, Phase Transit. **00**, 1 (2000).
5. H. Hisakuni and K. Tanaka, Science **270**, 974 (1995).
6. D. Th. Kastrissios, G. N. Papatheodorou, and S. N. Yannopoulos, Phys. Rev. B **64**, 214203 (2001).
7. H. Fritzsche, Solid State Commun. **99**, 153 (1996).
8. J. Li and D. A. Drabold, Phys. Rev. Lett. **85**, 2785 (2000).
9. K. Tanaka, C. R. Chimie **5**, 805 (2002).
10. D. Th. Kastrissios, G. N. Papatheodorou, and S. N. Yannopoulos, Phys. Rev. B **65**, 165211 (2002).
11. S. N. Yannopoulos, Phys. Rev. B **68**, 064206 (2003).
12. S. N. Yannopoulos, in *Photo-induced Metastability in Amorphous Semiconductors*, Ed. by A. V. Kolobov (Wiley–VCH, Berlin, 2003), pp. 119–137.
13. J. Gump, I. Finkler, H. Xia, *et al.*, Phys. Rev. Lett. **92**, 245501 (2004).
14. S. Mamedov, D. G. Georgiev, Tao Qu, and P. Boolchand, J. Phys.: Condens. Matter **15**, S2397 (2003).
15. D. G. Georgiev, P. Boolchand, and M. Micoulaut, Phys. Rev. B **62**, R9228 (2000).
16. N. G. Olson, C. Leung, and X. Wang, Exp. Tech. **12**, 51 (2002).
17. S. N. Dub and N. V. Novikov, Sverkhtverd. Mater., No. 6, 16 (2004).
18. W. C. Oliver and G. M. Pharr, J. Mater. Res. **7**, 1564 (1992).

19. R. A. Street, R. J. Nemanich, and G. A. N. Conell, Phys. Rev. B **18**, 6915 (1978).
20. S. Suzuki, M. Takahashi, and T. Kobayashi, J. Non-Cryst. Solids **46**, 163 (1981).
21. M. L. Trunov and V. S. Bilanich, J. Optoelectron. Adv. Mater. **5**, 1085 (2003).
22. M. L. Trunov and V. S. Bilanich, Thin Solid Films **459**, 228 (2004).
23. M. L. Trunov, Pis'ma Zh. Tekh. Fiz. **30** (20), 49 (2004) [Tech. Phys. Lett. **30**, 865 (2004)].
24. M. L. Trunov, S. N. Dub, and R. S. Shmegera, J. Optoelectron. Adv. Mater. **7**, 619 (2005).
25. M. L. Trunov, S. N. Dub, and R. S. Shmegera, Pis'ma Zh. Tekh. Fiz. **31** (13), 31 (2005) [Tech. Phys. Lett. **31**, 551 (2005)].
26. A. Leyland and A. Matthews, Wear **1**, 246 (2000).
27. Yu. I. Golovin and A. I. Tyurin, Priroda (Moscow), No. 4, 60 (2003).
28. K. Schwartz, *The Physics of Optical Recording* (Springer, Berlin, 1993), p. 445.
29. V. I. Mikla, A. A. Baganich, A. P. Sokolov, and A. P. Shebanin, Phys. Status Solidi B **175**, 281 (1993).

Translated by R. Tyapaev

JETP Letters, Vol. 82, No. 8, 2005, pp. 509–514. Translated from Pis'ma v Zhurnal Éksperimental'noĭ i Teoreticheskoĭ Fiziki, Vol. 82, No. 8, 2005, pp. 567–572.

Magnetic Susceptibility of Tungsten Carbide: Relaxation and Impurity Effects

A. S. Kurlov, S. Z. Nazarova, and A. I. Gusev

Institute of Solid State Chemistry, Ural Division, Russian Academy of Sciences, ul. Pervomaĭskaya 91, Yekaterinburg, 620219 Russia

e-mail: gusev@ihim.uran.ru

Received August 22, 2005

The magnetic susceptibility χ of coarse-grained WC and nanocrystalline n-WC tungsten carbides has been studied in a temperature range of 300–1250 K. The dependence $\chi(T)$ for coarse-grained WC carbide has no singularities. A stable particle size of about 55 nm remains in the n-WC nanopowder after annealing at 300–1200 K, whereas the relaxation of microstrains occurs at 550–920 K. The dependence $\chi(T)$ for nanocrystalline n-WC carbide in a range of 550–920 K exhibits features associated with the annealing of microstrains, which reduces the contribution of orbital paramagnetism to the susceptibility of n-WC carbide and initiates the precipitation of small iron and cobalt impurities in the form of superparamagnetic particles. *© 2005 Pleiades Publishing, Inc.*

PACS numbers: 61.46.+w, 75.75.+a, 81.07.–b, 81.40.Rs

In recent years, condensed substances in the nanocrystalline state have been actively studied, because a decrease in the sizes of structural elements (particles, crystallites, and grains) below a certain threshold value can result in a noticeable change in the properties of the substances [1–3]. Such effects are clearly observed when the size of grains is less than 10 nm. Owing to the large area of interfaces, nanocrystalline substances are contaminated by impurities. The effect of impurities on the properties of nanocrystalline substances can be stronger than the effect of the small size of grains. As was shown in [3–5], after verification, many unordinary results that were obtained for nanocrystalline substances and initially attributed to size effects appeared to be due to the contamination of the objects under investigation by oxygen and hydrogen, as well as by ferromagnetic and other impurities. In this work, the magnetic susceptibility χ of coarse-grained and nanocrystalline tungsten carbide WC was studied *in situ* in a wide temperature range.

The published data on the magnetic properties of nanocrystalline tungsten carbide are absent. There is only one work [6] devoted to the magnetic susceptibility χ of coarse-grained tungsten carbide. According to that work, the susceptibility of WC carbide measured in a field of 3.6 kG at temperatures of 293, 513, and 723 K is equal to 0.07×10^{-6}, 0.06×10^{-6}, and 0.02×10^{-6} cm^3 g^{-1}, respectively.

In this work, the magnetic susceptibility of the coarse-grained tungsten carbide powder is measured in order to exclude any effects caused by the small size of particles. For measurements, we used a hexagonal WC carbide powder that was washed in hydrochloric acid and did not contain ferromagnetic impurities. The size of the agglomerated particles of the WC powder, which was determined by the Fischer method, was 4–9 μm.

To detect the direct or indirect effect of the small size of the particles on the magnetic susceptibility of tungsten carbide, we studied the n-WC nanopowder. The nanopowder was synthesized by the plasmachemical method from WO_3 and C_3H_8 propane at a temperature of 3300–3800 K in hydrogen plasma with additional annealing in an argon atmosphere at 1100–1300 K. The mean size of the nanopowder particles was equal to about 50 nm. According to the spectral analysis data, the content of Fe, Co, and Ni in the coarse-grained WC carbide was less than 0.00001 wt %, and the n-WC nanocrystalline carbide contains 0.02 wt % Fe, 0.002 wt % Co, and less than 0.0001 wt % Ni. The content of each rare-earth ferromagnetic metal (Gd, Dy, Tb, Ho, Er, and Tm) in the WC and n-WC carbides did not exceed 0.000005 wt %.

The WC powders were tested in structure and phase composition by the x-ray diffraction method in the step scanning regime using a DRON-UM1 diffractometer with the Bragg–Brentano geometry in Cu$K\alpha_{1,2}$ radiation. To accurately determine the position, width, and intensity, the diffraction reflections were described by the pseudo-Voigt function. The size of the nanopowder particles was determined using scanning electron microscopy and from the broadening of the diffraction reflections. To quantitatively estimate the broadening, the instrumental resolution function of the diffractometer $\mathrm{FWHM}_R(2\theta) = \sqrt{u\tan^2\theta + v\cot\theta + w}$, where u = 0.0041, v = –0.0020, and w = 0.0093, was determined

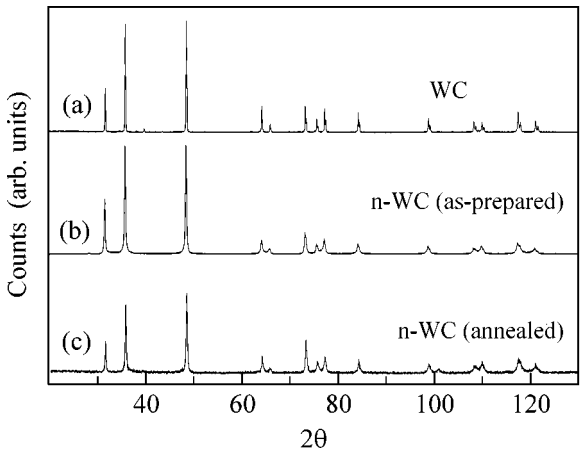

Fig. 1. X-ray patterns of tungsten carbide powders (Cu$K\alpha_{1,2}$ radiation): (a) coarse-grained powder, (b) as-prepared nanopowder, and (c) nanopowder after the complete cycle of the measurement of magnetic susceptibility. All powders contain only hexagonal (space group $P\bar{6}m2$) WC carbide, but the diffraction reflections of nanopowders are significantly broadened.

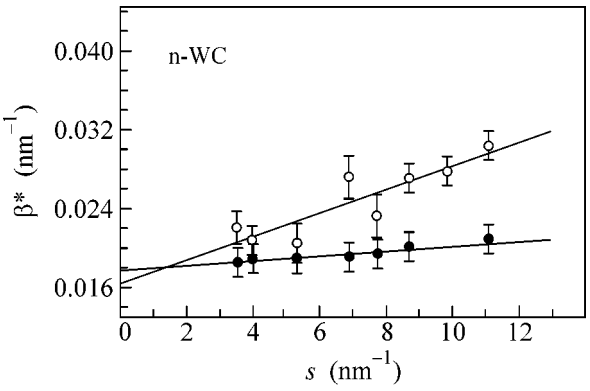

Fig. 2. Reduced broadening $\beta^*(2\theta) = [\beta(2\theta)\cos\theta]/\lambda$ of the diffraction reflections vs. the scattering-vector magnitude $s = (2\sin\theta)/\lambda$ for (○) the as-prepared (before the measurement of magnetic susceptibility χ) n-WC nanopowder and (●) the nanopowder annealed when measuring susceptibility. From these dependences, the mean particle size D and microstress ε are estimated as $D = 55 \pm 10$ nm and $\varepsilon = 0.03 \pm 0.005\%$ for the as-prepared powder and $D = 55 \pm 10$ nm and $\varepsilon = 0.006 \pm 0.002\%$ for the annealed powder. The mean size D of coherent-scattering regions in n-WC nanodisperse carbide remains unchanged after annealing at 300–1200 K, whereas the microstress value ε decreases almost to zero.

in a special diffraction experiment with lanthanum hexaboride LaB_6 (NIST Standard Reference Powder 660a) with a cubic lattice constant $a_{cub} = 415.69162 \pm 0.00097$ pm. The broadening $\beta(2\theta) \equiv 2\beta(\theta)$ is quantitatively determined as $\beta(2\theta) = \sqrt{\mathrm{FWHM}_{exp}^2 - \mathrm{FWHM}_R^2}$ by comparing the experimental width of the diffraction reflections of WC carbide with the instrumental resolution function of the diffractometer.

The magnetic susceptibility χ was measured by the Faraday method on a Domenicalli balance that has a sensitivity of no worse than 0.5×10^{-8} cm^3 g^{-1} and is intended for studying weak para- and diamagnetic materials. The measurements were conducted in a vacuum of 10^{-3} Pa at a temperature of 300 to 1250 K in magnetic fields of 7.2, 8.0, and 8.8 kG.

Figure 1 shows the x-ray diffraction patterns of coarse-grained and nanodisperse (as-prepared and annealed when measuring susceptibility) tungsten carbides. All powders contain only hexagonal (space group $P\bar{6}m2$) WC carbide with the unit cell parameters $a = 0.29060$ nm and $c = 0.28375$ nm, but the reflections of nanopowders are broadened (Figs. 1b, 1c).

The diffraction reflections were analyzed taking into account the size and the strain broadening [3] and the mean size D of the coherent-scattering regions was determined by the Williamson–Hall method [7, 8] from the dependence of the reduced broadening $\beta^*(2\theta) = [\beta(2\theta)\cos\theta]/\lambda$ on the scattering vector magnitude $s = (2\sin\theta)/\lambda$ as $D = 1/\beta^*(2\theta)$ at $\theta = 0$. The quantitative analysis of the broadening of the diffraction reflections (Fig. 2) shows that the mean size of the coherent-scattering regions in the n-WC nanopowder is equal to 55 ± 10 nm and does not change during annealing when measuring χ in the range of 300–1250 K. However, microstrains ε are relaxed due to annealing and they decrease from $0.03 \pm 0.005\%$ to $0.006 \pm 0.002\%$. The broadening of the diffraction reflections from the coarse-grained WC carbide is absent.

The measurements of the magnetic susceptibility χ of the coarse-grained WC powder (Fig. 3, line *1*) show that WC carbide is a weak paramagnetic material with a susceptibility of $\chi(300) \approx 0.058 \times 10^{-6}$ cm^3 g^{-1} (11.4×10^{-6} cm^3 mol^{-1}). The susceptibility $\chi(T)$ of WC carbide has no singularities in the range of 300–1250 K and is described by the function $\chi(T) = \chi(0) + BT^2$ characteristic of Pauli paramagnetism, where $\chi(0) \approx 0.0565 \times 10^{-6}$ cm^3 g^{-1} and $B \approx 1.30 \times 10^{-14}$ cm^3 g^{-1} K^{-2}.

According to [9, 10], the magnetic susceptibility of tungsten carbide, which is an electron conductor, can be represented as

$$\chi(T) = \chi_p^-(T) + \chi_d^- + \chi_{vv\,orb} + \chi_{pW}^+ + \chi_{dW}^+ + \chi_{pC}^+ + \chi_{dC}^+, \quad (1)$$

where χ_p^- is the Pauli paramagnetism of conduction electrons; $\chi_d^- = -(m_0/m^*)^2\chi_p^-(0)/3$ is the Landau diamagnetism (m_0 is the free-electron mass and m^* is the effective mass), which is proportional to the Pauli paramagnetism $\chi_p^-(0)$ at 0 K; $\chi_{vv\,orb}$ is the Van Vleck orbital paramagnetism; and χ_p^+ and χ_d^+ are the para- and diamagnetisms of ion cores ($\chi_{pW}^+ = \chi_{pC}^+ = 0$ and $\chi_{dW}^+ = -1.3 \times 10^{-6}$ cm^3/atom and $\chi_{dC}^+ = -0.15 \times 10^{-6}$ cm^3/atom

[11] for W^{6+} and C^{4+}, respectively). Among all the terms of Eq. (1), only the Pauli paramagnetism depends on temperature [12]:

$$\chi_p^-(T) = 2N_A\mu_{eff}^2 N(E_F) + \frac{\pi^2 k_B^2}{3} N_A \mu_{eff}^2 \left\{ N''(E_F) - \frac{[N'(E_F)]^2}{N(E_F)} \right\} T^2. \quad (2)$$

Here, $N'(E_F) \equiv [dN(E)/dE]|_{E=E_F}$ and $N''(E_F) \equiv [d^2N(E)/dE^2]|_{E=E_F}$ are the first and second energy derivatives of the density $N(E)$ of electronic states at $E = E_F$, and $\mu_{eff} = p\mu_B$ is the effective magnetic moment, where p is the number of Bohr magnetons μ_B. According to Eq. (2), the Pauli paramagnetism $\chi_p^-(0) = 2N_A\mu_B^2 p^2 N(E_F)$ at 0 K depends only on the density of the electronic states at the Fermi level $N(E_F)$, and the temperature susceptibility coefficient is given by the expression

$$B = (\pi^2 k_B^2 N_A \mu_{eff}^2/3)\{N''(E_F) - [N'(E_F)]^2/N(E_F)\} \equiv (\pi^2 k_B^2 N_A \mu_B^2 p^2/3) b, \quad (3)$$

where $b = N''(E_F) - [N'(E_F)]^2/N(E_F)$.

According to the calculations of the electron energy spectrum of hexagonal tungsten carbide [13, 14], the Fermi level is located near the minimum of the curve $N(E)$ and the density of states at the Fermi level $N(E_F)$ is low and equal to 0.3–0.4 eV^{-1} per unit cell. In the calculated curves $N(E)$ [13, 14] of WC carbide, the position of the Fermi level is such that the first derivative $N'(E_F)$ is negative and the second derivative $N''(E_F)$ is positive. For this reason, the temperature coefficient B may be positive or negative in dependence on the specific values of $N(E_F)$, $N'(E_F)$, and $N''(E_F)$. The numerical differentiation of the curve $N(E)$ [13] near the Fermi energy yields $N(E_F) \approx 0.33$ eV^{-1}, $N'(E_F) \approx -1.20$ eV^{-2}, and $N''(E_F) \approx 6.10$ eV^{-3}. Therefore, $b = 1.74 \pm 0.06$ eV^{-3} that agrees with the positive coefficient B of the susceptibility of WC carbide that follows from experiment.

Taking into account the experimental coefficient $B \approx 2.55 \times 10^{-12}$ cm^3 mol^{-1} K^{-2} and $b = 1.74$ eV^{-3}, from Eq. (3) we obtain $p = [3B/\pi^2 k_B^2 N_A \mu_B^2 b]^{1/2} \approx 1.36 \pm 0.06$. For $p = 1.36$ and $N(E_F) \approx 0.33$ eV^{-1}, $\chi_p^-(0) = (39.6 \pm 2.0) \times 10^{-6}$ cm^3 mol^{-1}, and the contribution of the Pauli paramagnetism to the susceptibility of WC carbide is $\chi_p^-(T) = (39.6 + 2.55 \times 10^{-6} T^2 \pm 2.0) \times 10^{-6}$ cm^3 mol^{-1}. If $m^* = m_0$, $\chi_d^- = -\chi_p^-(0)/3 = -13.2 \times 10^{-6}$ cm^3 mol^{-1}. The sum $\chi_p^-(300) + \chi_d^- + \chi_{pW}^+ + \chi_{dW}^+ + \chi_{pC}^+ + \chi_{dC}^+ = (13.4 \pm 2.0) \times 10^{-6}$ cm^3 mol^{-1} within the calculation error coincides with the measured susceptibility $\chi(300) = (11.4 \pm 1.0) \times 10^{-6}$ cm^3 mol^{-1} of coarse-grained WC carbide. Therefore, the orbital paramagnetic contribution $\chi_{vv\,orb}$ is close to zero in coarse-grained WC carbide.

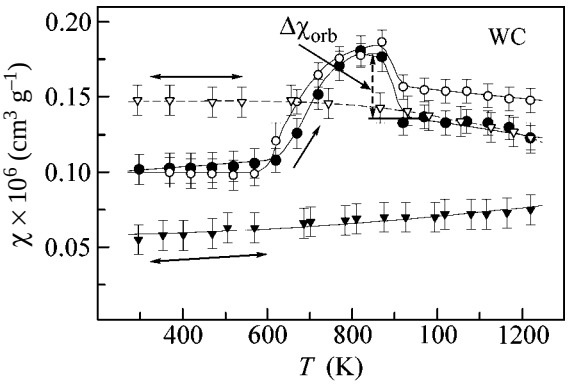

Fig. 3. Magnetic susceptibility of tungsten carbide in a field of $H = 8800$ G: (▼) the temperature dependence of the susceptibility $\chi_{WC}(T)$ of pure coarse-grained WC carbide, (●) the temperature dependence of the susceptibility $\chi_{n-WC}(T)$ of n-WC nanocrystalline carbide, (○) the annealing dependence of the susceptibility $\chi(300, T)$ of n-WC carbide, (▽) the temperature dependence of the susceptibility $\chi_{n-WC}^{(ann)}(T)$ of n-WC carbide annealed when measuring susceptibility, and $\Delta\chi_{orb} \approx 0.04 \times 10^{-6}$ cm^3 g^{-1} is the contribution from the Van Vleck orbital paramagnetism to the susceptibility of the as-prepared n-WC nanocrystalline carbide. The direction of variation in temperature when measuring χ is shown by arrows.

Let us discuss the susceptibility of nanocrystalline tungsten carbide. The measurements of the magnetic susceptibility χ of the n-WC nanopowder were carried out as follows: heating from 300 K to the annealing temperature T, 1-h aging at this temperature and the measurement of the susceptibility $\chi(T)$ at the end of the annealing, cooling from the annealing temperature T to 300 K and the measurement of the susceptibility $\chi(300, T)$ at 300 K, heating to the next annealing temperature, etc. The average temperature step was equal to 50 K.

Figure 3 shows the typical temperature dependence of the magnetic susceptibility χ of the n-WC nanopowder. The susceptibility χ of the nanopowder is higher than the susceptibility of pure coarse-grained WC carbide. In contrast to the smooth dependence $\chi(T)$ for coarse-grained WC carbide, the susceptibility curve for the n-WC nanopowder exhibits noticeable features. In the temperature, $\chi(T)$, and annealing, $\chi(300, T)$, curves for n-WC carbide, the susceptibility begins to sharply increase at T = 550–600 K, reaches a maximum at ~820–870 K, then the susceptibilities $\chi(T)$ and $\chi(300, T)$ of n-WC carbide decrease noticeably at 870–920 K, and the susceptibilities $\chi(T)$ and $\chi(300, T)$ decrease slightly as the temperature further increases from 920–930 K to 1220 K. The susceptibility $\chi(T)$ measured at $T > 600$ K is less than the susceptibility $\chi(300, T)$ measured at 300 K after the cooling of the carbide from temperature T, whereas the susceptibilities $\chi(T)$ and

$\chi(300, T)$ in a range of 300–600 K coincide within the measurement errors (Fig. 3). When n-WC carbide is cooled from 1220 K to 300 K and then is repeatedly heated to 1200 K, the susceptibility varies monotonically without any singularities along line *4* (Fig. 3).

According to diffraction data, the size of the coherent-scattering regions remains almost unchanged when measuring χ, whereas the microstrains decrease almost to zero. It might be thought that relaxation annealing of microstrains is responsible for the features observed on the susceptibility curve. Are these features associated with the magnetic properties and electronic structure of tungsten carbide or they are caused by impurities? A large difference between the absolute values of the susceptibilities χ of (line *1*) pure coarse-grained and (line *4*) annealed nanocrystalline tungsten carbides indicates that the impurity paramagnetic contribution to the susceptibility of annealed n-WC carbide is significant. We emphasize that the susceptibility of the as-prepared (before the measurement of χ) n-WC carbide is higher than the value of coarse-grained WC carbide even at 300 K.

Spectral analysis shows that small iron and cobalt impurities are present in n-WC carbide. The measurements did not reveal any magnetic-field dependence of the susceptibility χ of the as-prepared nanocrystalline carbide. Therefore, Fe and Co impurities are present in the as-prepared n-WC carbide not in the ferromagnetic state. This is possible if these impurities are dissolved in n-WC carbide. Indeed, in this case, they make an additional paramagnetic rather than ferromagnetic contribution to the susceptibility. The precipitation of impurities in the form of superparamagnetic particles also makes a paramagnetic contribution, but this contribution for $T < T_C$ (T_C is the Curie temperature) is larger than the contribution from the same amount of dissolved impurities.

Let us discuss the following qualitative explanation of the susceptibility of n-WC carbide. In as-prepared n-WC carbide, there are microstrains responsible for an additional positive contribution $\Delta\chi_{orb}$ of the Van Vleck orbital paramagnetism to the susceptibility and, moreover, Fe and Co impurities are dissolved in the carbide matrix. Therefore, the susceptibility of n-WC carbide is higher than the susceptibility of pure coarse-grained WC carbide. The deformation action initiates the precipitation of dissolved metallic impurities: for example, the precipitation of Fe particles from a solution in copper was observed in [15, 16]. It can be assumed that the annealing of microstrains, which begins in n-WC carbide at 570–600 K, initiates the precipitation of Fe and Co impurities in the form of small superparamagnetic particles. As the temperature increases from 600 to 800–820 K, the number and volume of the superparamagnetic particles increase and this increase is accompanied by an increase in the susceptibility to maximum. The precipitation of superparamagnetic particles stops at ~820 K, but the annealing of microstrains continues to ~920 K. A decrease in χ in the range of 820–920 K is not an impurity effect and is directly associated with n-WC carbide, namely, with a decrease in the orbital paramagnetism $\chi_{vv\,orb}$. Indeed, the relaxation of microstrains that occurs at 820–920 K reduces distortions of the local symmetry of the atomic environment and the strain distortions of the symmetric electron shells of ion cores, which leads to the disappearance of the contribution from the orbital paramagnetism $\Delta\chi_{orb} \approx 0.04 \times 10^{-6}$ cm^3 g^{-1} and to a decrease in the susceptibility. For $T > 920$ K, when microstrains in n-WC carbide are absent, a decrease in χ is caused only by the temperature dependence of the impurity superparamagnetism.

Taking into account the above discussion, the difference $\Delta\chi(T) = (\chi_{n\text{–}WC}(T) - \Delta\chi_{orb}) - \chi_{WC}(T)$ between the susceptibilities of the as-prepared nanocrystalline n-WC carbide (● in Fig. 3) and the coarse-grained WC carbide (▼ in Fig. 3) in the range of 300–570 K corresponds to the paramagnetic susceptibility $\chi^{(m)}_{p\text{–}imp}(T)$ of the dissolved Fe and Co impurities; i.e., $\Delta\chi(T) = \chi^{(m)}_{p\text{–}imp}(T)$. The magnetization of a dissolved impurity is described by the dependence characteristic of Curie paramagnetic materials. Changing magnetization M to susceptibility χ, we represent the paramagnetic contribution from impurities (per unit mass) at the temperature T in the magnetic field H in the form

$$\chi^{(m)}_{p\text{–}imp}(T) = \sum_i \frac{n_i \mu_{eff}}{\rho_{M_i} H} L\left(\frac{\mu_{eff\,i} H}{k_B T}\right), \qquad (4)$$

where n_i is the number of atoms of the ith impurity per unit volume, $L(x) = [\coth(x) - 1/x]$ is the Langevin function, $\mu_{eff\,i} = p_i \mu_B$ is the effective magnetic moment of the ith impurity atom, and ρ_{M_i} is the density of the ith impurity metal. If the relative mass content of the ith impurity is equal to c_i and $c \ll 1$, its relative volume content is given as $c_{Vi} \approx c_i \rho_{WC}/\rho_{M_i}$ and $n_i = c_{Vi} N_A \rho_{M_i}/A_{M_i} = c_i N_A \rho_{WC}/A_{M_i}$ (A_{M_i} is the atomic mass of the ith impurity and $\rho_{WC} = 15.8$ g cm^{-3} is the density of WC carbide). Since $\chi^{(m)}_{p\text{–}imp}(T) = (\chi_{n\text{–}WC}(T) - \Delta\chi_{orb}) - \chi_{WC}(T)$ and $n_i = c_i N_A \rho_{WC}/A_{M_i}$, it follows from Eq. (4) that the difference between the susceptibilities of the as-prepared n-WC carbide and coarse-grained WC carbide in a range of 300–570 K can be represented as

$$(\chi_{n\text{–}WC}(T) - \Delta\chi_{orb}) - \chi_{WC}(T) = \frac{\rho_{WC} N_A \mu_B}{H} \times \left[\frac{c_{Fe} p_{Fe}}{\rho_{Fe} A_{Fe}} L\left(\frac{p_{Fe}\mu_B H}{k_B T}\right) + \frac{c_{Co} p_{Co}}{\rho_{Co} A_{Co}} L\left(\frac{p_{Co}\mu_B H}{k_B T}\right)\right], \qquad (5)$$

where $p_{Fe} = 2.22$ [17], $\rho_{Fe} = 7.86$ g cm^{-3}, $A_{Fe} = 55.85$, $p_{Co} = 1.72$ [17], $\rho_{Co} = 8.9$ g cm^{-3}, and $A_{Co} = 58.93$. Function (5) satisfactorily approximates the experimental

data for $\chi_{\text{p–imp}}^{(m)}(T)$ (Fig. 4a) at the parameters $c_{\text{Fe}} = (3.6 \pm 0.5) \times 10^{-5}$ (~0.003–0.004 wt %) and $c_{\text{Co}} = (7.3 \pm 0.5) \times 10^{-5}$ (~0.007–0.008 wt %), which are in satisfactory agreement with the spectral analysis.

If the jump in the dependence $\chi(T)$ for n-WC carbide at 600–820 K is attributed to the precipitation of impurity superparamagnetic particles, the experimental contribution $\chi_{\text{sp}}^{(m)}(T)$ from the superparamagnetic phase to the susceptibility is equal to the difference between the susceptibility $\chi_{\text{n–WC}}^{(\text{ann})}(T)$ of annealed n-WC carbide (▽ in Fig. 3) and the susceptibility $\chi_{\text{WC}}(T)$ of coarse-grained WC carbide (▼ in Fig. 3); i.e., $\chi_{\text{sp}}^{(m)}(T) = \chi_{\text{n–WC}}^{(\text{ann})}(T) - \chi_{\text{WC}}(T)$. At the same time, the superparamagnetic contribution (per unit mass) at temperature T in the magnetic field H is expressed as

$$\chi_{\text{sp}}^{(m)}(T) = \sum_i \frac{n_{\text{sp}\,i}\mu_{\text{sp}\,i}}{\rho_{\text{M}_i} H} L\left(\frac{\mu_{\text{sp}\,i} H}{k_{\text{B}} T}\right), \qquad (6)$$

where $n_{\text{sp}\,i}$ is the number of the ith superparamagnetic particles per unit volume and L is the Langevin function. If the magnetic moment $\mu_{\text{sp}\,i}$ of a superparamagnetic particle is independent of temperature, then $\mu_{\text{sp}\,i} = V_{\text{sp}}^{(i)} M_{\text{sp}}^{(i)}(T)$, where $V_{\text{sp}}^{(i)}$ is the volume of the ith superparamagnetic particle. The saturation magnetization of the ith ferromagnetic at temperature T is determined as

$$M_{\text{s}}^{(i)}(T) = M_{\text{s}}^{(i)}(0) \tanh\left(\frac{M_{\text{s}}^{(i)}(T) T_{\text{C}}^{(i)}}{M_{\text{s}}^{(i)}(0) T}\right),$$

where $M_{\text{s}}^{(i)}(0)$ is the saturation magnetization at 0 K and $T_{\text{C}}^{(i)}$ is the Curie temperature of the ith ferromagnetic material ($M_{\text{s}}^{\text{Fe}}(0) = 1740$ G, $T_{\text{C}}^{\text{Fe}} = 1043$ K and $M_{\text{s}}^{\text{Co}}(0) = 1400$ G, $T_{\text{C}}^{\text{Co}} = 1403$ K for crystalline iron and cobalt, respectively [12, 17]).

Since $\chi_{\text{sp}}^{(m)}(T) \equiv \chi_{\text{sp Co}}^{(m)}(T) + \chi_{\text{sp Fe}}^{(m)}(T) = \chi_{\text{n–WC}}^{(\text{ann})}(T) - \chi_{\text{WC}}(T)$ and taking into account Eq. (6), we obtain

$$\chi_{\text{n–WC}}^{(\text{ann})}(T) - \chi_{\text{WC}}(T) = \sum_i \frac{n_{\text{sp}\,i} V_{\text{sp}}^{(i)} M_{\text{s}}^{(i)}(T)}{\rho_{\text{M}_i} H} L\left(\frac{V_{\text{sp}}^{(i)} M_{\text{s}}^{(i)}(T) H}{k_{\text{B}} T}\right). \qquad (7)$$

For the case under consideration, the summation in Eq. (7) is performed over two substances, Fe and Co. The approximation of the experimental dependence $\chi_{\text{n–WC}}^{(\text{ann})}(T) - \chi_{\text{WC}}(T)$ by function (7) makes it possible to determine the contributions from each of the superparamagnetic phases to the impurity susceptibility (Fig. 4b)

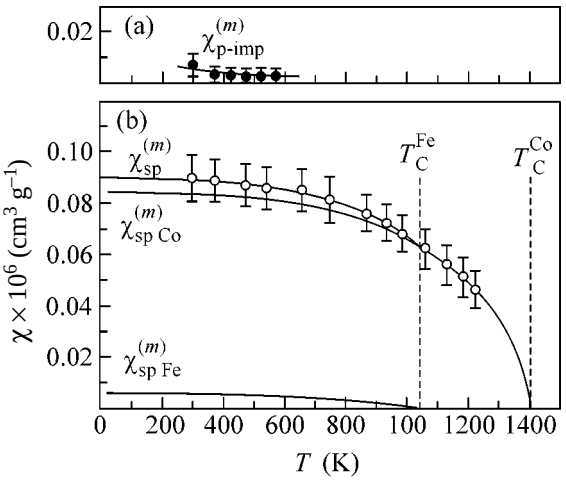

Fig. 4. Temperature dependences of the mass magnetic susceptibility χ of the iron and cobalt impurity phases in the n-WC nanopowder: (a) experimental magnetic susceptibility $\chi_{\text{p–imp}}^{(m)}(T) = (\chi_{\text{n–WC}}(T) - \Delta\chi_{\text{orb}}) - \chi_{\text{WC}}(T)$ of dissolved Fe and Co is described by function (5) with $c_{\text{Fe}} = 0.000036$ and $c_{\text{Co}} = 0.000073$ and (b) experimental contribution $\chi_{\text{sp}}^{(m)}(T) \equiv \chi_{\text{sp Co}}^{(m)}(T) + \chi_{\text{sp Fe}}^{(m)}(T) = \chi_{\text{n–WC}}^{(\text{ann})}(T) - \chi_{\text{WC}}(T)$ of superparamagnetic Fe and Co impurity phases to the susceptibility of n-WC carbide is well approximated by function (7). The vertical dashed straight lines are the Curie temperatures of iron $T_{\text{C}}^{\text{Fe}} = 1043$ K and cobalt $T_{\text{C}}^{\text{Co}} = 1403$ K. The solid lines are approximations.

and to estimate the volumes $V_{\text{sp}}^{\text{Fe}}$ and $V_{\text{sp}}^{\text{Co}}$ of iron and cobalt superparamagnetic particles as 4.0×10^{-20} and 4.0×10^{-19} cm^3, respectively, which correspond to the linear dimensions of the respective particles 3.4 and 7.4 nm, respectively. The numbers of superparamagnetic iron and cobalt particles per unit volume are $n_{\text{sp Co}} = (1.2 \pm 0.2) \times 10^{13}$ and $n_{\text{sp Fe}} = (5.9 \pm 1.0) \times 10^{12}$.

The reported calculations are estimating, because they ignore the solvability of Fe and Co in tungsten carbide.

Thus, hexagonal tungsten carbide WC in the coarse-grained and nanocrystalline states is a weak paramagnetic material at 300–1250 K. The size of the particles in the n-WC nanopowder remains unchanged during annealing in the temperature range from 300 to 1200 K, whereas the complete relaxation of microstrains occurs at 600–900 K. The features manifested in the temperature dependence of the magnetic susceptibility of nanocrystalline tungsten carbide are associated with the relaxation annealing of microstrains, which reduces the contribution of the orbital paramagnetism to the susceptibility of n-WC carbide and initiates the precipitation of iron and cobalt impurities in the form of superparamagnetic particles. The direct effect of the small size of the particles of nanocrystalline tungsten carbide on its magnetic susceptibility has not been revealed.

We are grateful to V.A. Moldaver for assistance in the synthesis of the n-WC nanopowder and to A.A. Rempel for stimulating discussions. This work was supported by the Russian Foundation for Basic Research (project no. 03-03-32031a).

REFERENCES

1. *Nanomaterials: Synthesis, Properties and Applications*, Ed. by A. S. Edelstein and R. C. Cammarata (The Johns Hopkins Univ., Baltimor, 1998).
2. H. Gleiter, Acta Mater. **48**, 1 (2000).
3. A. I. Gusev and A. A. Rempel, *Nanocrystalline Materials* (Cambridge Int. Sci., Cambridge, 2004).
4. A. I. Gusev, Usp. Fiz. Nauk **168**, 55 (1998) [Phys. Usp. **41**, 49 (1998)].
5. A. I. Gusev and A. A. Rempel, *Nanocrystalline Materials* (Fizmatlit, Moscow, 2000) [in Russian].
6. W. Klemm and W. Schüth, Z. Anorg. Allg. Chem. **201**, 24 (1931).
7. W. H. Hall, Proc. Phys. Soc. London, Sect. A **62**, 741 (1949).
8. G. K. Williamson and W. H. Hall, Acta Metall. **1**, 22 (1953).
9. A. I. Gusev, A. A. Rempel, and A. A. Magerl, *Disorder and Order in Strongly Nonstoichiometric Compounds. Transition Metal Carbides, Nitrides and Oxides* (Springer, Berlin, 2001).
10. A. I. Gusev and S. Z. Nazarova, Usp. Fiz. Nauk **175**, 681 (2005) [Phys. Usp. **48**, 651 (2005)].
11. P. W. Selwood, *Magnetochemistry*, 2nd ed. (Interscience, New York, 1956; Inostrannaya Literatura, Moscow, 1958).
12. S. V. Vonsovskiĭ, *Magnetism* (Nauka, Moscow, 1971; Wiley, New York, 1974).
13. L. F. Mattheiss and D. R. Hamann, Phys. Rev. B **30**, 1731 (1984).
14. Y. Liu, R. M. Wentzcovitch, and M. L. Cohen, Phys. Rev. B **38**, 9483 (1988).
15. G. Tammann and W. Oelsen, Z. Anorg. Chem. **186**, 257 (1930).
16. A. A. Rempel, S. Z. Nazarova, and A. I. Gusev, J. Nanopart. Res. **1**, 485 (1999).
17. C. Kittel, *Introduction to Solid State Physics*, 7th ed. (Wiley, New York, 1996; Nauka, Moscow, 1978).

Translated by R. Tyapaev

JETP Letters, Vol. 82, No. 8, 2005, pp. 515–520. Translated from Pis'ma v Zhurnal Éksperimental'noĭ i Teoreticheskoĭ Fiziki, Vol. 82, No. 8, 2005, pp. 573–579.

Mössbauer Spectra of the Quadrupole Hyperfine Structure in the Presence of the Rotation of the Principal Axis of the Electric Field Gradient Tensor

M. A. Chuev

Institute of Physics and Technology, Russian Academy of Sciences, Moscow, 117218 Russia

Received August 24, 2005

It is found that the rotation of the principal axis of the electric field gradient tensor about a certain axis radically changes the shape of the Mössbauer spectra of the quadrupole hyperfine structure. This change may be a manifestation of a qualitatively different physical origin of rotational dynamics in liquids. In particular, the absorption spectra of ^{57}Fe nuclei may contain the triplet, quartet, and octet of lines instead of the standard quadrupole doublet. Simple analytical expressions derived for a number of limiting cases describe the spectra in terms of the effective quadrupole coupling constant and the rotational splitting constant for the main lines. The observed features of the formation of quadrupole hyperfine structure spectra must be taken into account in analysis of experimental Mössbauer spectra in liquids. © *2005 Pleiades Publishing, Inc.*

PACS numbers: 33.45.+x, 61.43.–j, 76.80.+y, 78.30.Cp

Analysis of most experimental Mössbauer absorption spectra is based on the static hyperfine structure, when the positions and intensities of spectral lines are described by the magnetic hyperfine interaction in a static hyperfine magnetic field $\mathbf{H}_{\rm hf}$ at the nucleus and the quadrupole hyperfine interaction in the presence of an electric-field gradient (EFG) at the nucleus. For example, in the case of the ^{57}Fe isotope, which is widely used in Mössbauer spectroscopy, field $\mathbf{H}_{\rm hf}$ splits the levels of the ground state of the nucleus with spin $I_{\rm g} = 1/2$ into two sublevels with different spin projections $m_{\rm g}$ onto the direction of $\mathbf{H}_{\rm hf}$, while the excited state with energy $E_0 = 14.4$ keV and spin $I_{\rm e} = 3/2$ is split into four sublevels with different spin projections $m_{\rm e}$ in complete agreement with the energies of the Zeeman interaction of the nuclear magnetic moments with $\mathbf{H}_{\rm hf}$,

$$\hat{H}^{(\rm g,\,e)} = -g_{\rm g,\,e}\mu_N \mathbf{H}_{\rm hf}\hat{\mathbf{I}}^{(\rm g,\,e)}, \qquad (1)$$

where μ_N is the nuclear magneton and $g_{\rm g,\,e}$ and $\hat{\mathbf{I}}^{(\rm g,\,e)}$ are the nuclear g factors and nuclear spins for the ground and excited states, respectively.

In the case of the quadrupole hyperfine interaction between the quadrupole nuclear moment Q and the electric-field gradient at the ^{57}Fe nucleus, its ground state remains degenerate, while the excited state splits into two sublevels, which are degenerate in the spin projection $|m_{\rm e}|$ in accordance with the Hamiltonian

$$\hat{H}^{(\rm e)} = q\left[\hat{I}_z^2 - \frac{1}{3}I(I+1) + \frac{\eta}{3}(\hat{I}_x^2 - \hat{I}_y^2)\right], \qquad (2)$$

where the quadrupole interaction constant is given by

$$q = \frac{3eQV_{zz}}{4I(2I-1)}, \qquad (3a)$$

the asymmetry parameter is defined as

$$\eta = \frac{V_{xx} - V_{yy}}{V_{zz}}, \qquad (3b)$$

and V_{ii} are the principal values of the EFG tensor ($|V_{xx}| \le |V_{yy}| \le |V_{zz}|$). In expression (2), the indices of the excited state for the nuclear spin are omitted.

The transitions that may occur between the split sublevels of the nucleus in the excited and ground states are observed in the absorption spectra as a series of lines, whose positions and intensities are completely determined by Hamiltonians (1) and (2), as well as by the multipolarity of the transition from the ground state of the nucleus to the excited state. In the case of ^{57}Fe nuclei, magnetic dipole radiation of the $M1$ type takes place; the spectrum of the magnetic hyperfine structure consists of six lines (the so-called magnetic sextet), while the spectrum of the quadrupole hyperfine structure consists of two lines (the quadrupole doublet). Accordingly, experimental spectra are usually represented in the form of a combination of magnetic sextets and quadrupole doublets, whose parameters precisely determine the physical characteristics of a given material.

If the experimental spectra do not fit this scheme of analysis, more complex models are used for describing the so-called relaxation effects in which the magnitude and direction of $\mathbf{H}_{\rm hf}$ and/or the parameters of the EFG tensor vary randomly with time [1, 2]. As a rule, spectra

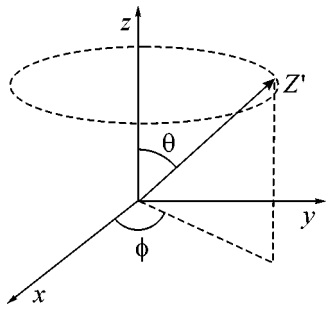

Fig. 1. Model with the rotating principal axis of the electric field gradient tensor.

lines are broadened or the hyperfine structure collapses into a single line (or into a quadrupole doublet in the case of a magnetic hyperfine structure) depending on the relaxation rate (temperature). Deviations from such an evolution in the form of the Mössbauer spectra were observed only in special cases of relaxation processes (e.g., in paramagnets, ferroliquids, or magnetic nanoparticles [3]).

The recently developed theory of the Mössbauer spectra of a magnetic hyperfine structure in a rotating field $\mathbf{H}_{\rm hf}$ has demonstrated an astonishingly nontrivial dependence of the shape of the absorption spectra on model parameters, which radically differ from the static spectra of the hyperfine structure [4]. In particular, it was shown in [4] that the standard magnetic sextet of lines for ^{57}Fe nuclei may be transformed as a result of rotation into an effective magnetic "doublet" of lines. This theory was developed for obtaining an alternative description of the Mössbauer spectra for systems of magnetic nanoparticles, in which rotation of $\mathbf{H}_{\rm hf}$ due to the rotation of the magnetic moment of a particle in the magnetic anisotropy field also takes place along with random variations.

In this connection, the interest in solving an abstract problem of calculation of absorption spectra in the presence of the quadrupole hyperfine interaction with the EFG principal axis rotating about a certain axis naturally arises. This interest is also closely related to a real physical problem of rotational dynamics in liquids, glasses, ferroliquids, and other "soft" systems ("liquids"), which has been intensely studied for many years using various methods including Mössbauer spectroscopy [5] as well as the recently developed method of perturbed angular correlations of synchrotron radiation (PACSR) [6], which is allied to Mössbauer spectroscopy in the physics of the phenomena being studied. The present study is devoted precisely to the solution of this problem.

In this paper, we consider only an axisymmetric quadrupole interaction for *M*1 transitions between the excited and ground nuclear states with spins $I_{\rm e} = 3/2 \longrightarrow I_{\rm g} = 1/2$, a random distribution of orientations of molecular axes, and an unpolarized source of gamma radiation.

Thus, let us consider a molecule freely rotating in a liquid (e.g., about one of the principal axes of its inertia tensor). In the general case, the principal axis *z*' of the EFG tensor forms a certain angle θ with the rotational axis (Fig. 1). The rotation of the molecule in this case induces the rotation of the EFG principal axis about the *z* axis at a certain frequency Ω, i.e., with a time-invariable rate of variation in the azimuth angle ϕ:

$$\phi(t) = \Omega t. \tag{4}$$

Let us choose the *z* axis as the quantization axis; then Hamiltonian (2) for the axisymmetric ($\eta = 0$) quadrupole hyperfine interaction can be written in the molecular system of coordinates in the form

$$\hat{H}^{(\rm e)}(t) = q\Bigg[\frac{3\cos^2\theta - 1}{2}\Big(\hat{I}_z^2 - \frac{1}{3}I(I+1)\Big) + \frac{\sin^2\theta}{4}(\hat{I}_+^2 e^{-2i\Omega t} + \hat{I}_-^2 e^{2i\Omega t}) + \frac{\sin\theta\cos\theta}{2}((\hat{I}_z\hat{I}_+ + \hat{I}_+\hat{I}_z)e^{-i\Omega t} + (\hat{I}_z\hat{I}_- + \hat{I}_-\hat{I}_z)e^{i\Omega t})\Bigg]. \tag{5}$$

To derive the formulas describing the absorption spectrum in this model, we can use the results obtained in [7, 8], where a theory of the Mössbauer spectra was developed for a periodically varying $\mathbf{H}_{\rm hf}(t)$ along an arbitrary trajectory. The following expression was derived for the absorption cross section of a gamma quantum by a nucleus in the case when the value of $\mathbf{H}_{\rm hf}(t)$ periodically varies with time along an arbitrary deterministic trajectory [7]:

$$\sigma(\omega) = \frac{2}{\Gamma_0 T_{\rm hf}}{\rm Re} \times \int_0^{T_{\rm hf}} dt_0 \int_{t_0}^{\infty} {\rm Tr}\Bigg\{\hat{V}^+\Bigg[\hat{T}\exp\Bigg\{\int_{t_0}^{t} i[(\omega + i\Gamma_0/2)\hat{\mathbf{I}} - \hat{\mathbf{L}}_{\hat{H}}(t')]dt'\Bigg\}\Bigg]\hat{V}\Bigg\}dt. \tag{6}$$

Here, ω is the spectral frequency, Γ_0 is the level width of the excited state of the nucleus, $T_{\rm hf}$ is the period of variation of $\mathbf{H}_{\rm hf}$, $\hat{V}$ is the operator of interaction between a gamma quantum and the nucleus, $\hat{T}$ is the chronological ordering operator, $\hat{\mathbf{I}}$ is the unit operator, and the Liouville superoperator $\hat{\mathbf{L}}_{\hat{H}}(t)$ is determined by the time-dependent Hamiltonians $\hat{H}^{(\rm g)}$ and $\hat{H}^{(\rm e)}$ [9]:

$$(\hat{\mathbf{L}}_{\hat{H}})_{m_{\rm e}m_{\rm g}m'_{\rm e}m'_{\rm g}} = \hat{H}^{(\rm e)}_{m_{\rm e}m'_{\rm e}}\delta_{m_{\rm g}m'_{\rm g}} - \hat{H}^{(\rm g)}_{m_{\rm g}m'_{\rm g}}\delta_{m_{\rm e}m'_{\rm e}}. \tag{7}$$

The absorption spectra of nanomagnetic alloys exposed to an external rf field [7, 8] were calculated on the basis of formula (6) and its modifications.

It is easily seen that expressions (6) and (7) can also be used for describing the Mössbauer spectra for arbitrary hyperfine interactions varying periodically with time along an arbitrary deterministic trajectory. For example, in the case of the quadrupole hyperfine interaction given by Eq. (5) with a degenerate ground state of the nucleus, a random distribution of orientations of molecular axes, and the unpolarized source of gamma radiation considered here, expression (6) for the absorption spectrum assumes the simple form

$$\sigma(\omega) = \frac{\sigma_0\Gamma_0}{2T_r(2I_e+1)}\mathrm{Re} \times \int_0^{T_r} dt_0 \int_{t_0}^{\infty} dt \mathrm{Tr}\{e^{i\tilde{\omega}(t-t_0)}\hat{G}^{(e)}(t_0,t)\}, \quad (8)$$

where σ_0 is the resonance absorption cross section, $T_r = 2\pi/\Omega$ is the period of rotation, $\tilde{\omega} = \omega + i\Gamma_0/2$, and

$$\hat{G}^{(e)}(t_0,t) = \hat{T}\exp\left\{-i\int_{t_0}^{t} dt'\hat{H}^{(e)}(t')\right\} \quad (9)$$

is the conventional evolution operator.

Expressions (8) and (9) is significantly simplified in the coordinate system rotating at frequency Ω about the z axis. Such a transition corresponds to unitary transformations using the elementary operators of rotation about the z axis,

$$\hat{U}(t) = e^{-i\Omega\hat{I}_z t}, \quad (10)$$

which can be employed for integrating the evolution operator (9) with respect to time:

$$\hat{G}^{(e)}(t_0,t) = \hat{U}^{+}(t_0)e^{-i(t-t_0)\hat{\tilde{H}}^{(e)}}\hat{U}(t). \quad (11)$$

Here, $\hat{\tilde{H}}^{(e)}$ is the time-independent Hamiltonian of the quadrupole interaction in the excited state of the nucleus in the rotating system of coordinates:

$$\hat{\tilde{H}}^{(e)} = \hat{H}^{(e)}(0) - \Omega\hat{I}_z. \quad (12)$$

Using expression (11), we can easily prove that formula (8) in the present case is reduced to the following simple analytical expression for the absorption cross section

$$\sigma(\omega) = -\frac{\sigma_0\Gamma_0}{2(2I_e+1)} \times \mathrm{Im}\sum_{m_e\tilde{m}_e}\frac{|\langle m_e|\tilde{m}_e\rangle|^2}{\omega - \tilde{\lambda}_{\tilde{m}_e} - \Omega m_e + i\Gamma_0/2}, \quad (13)$$

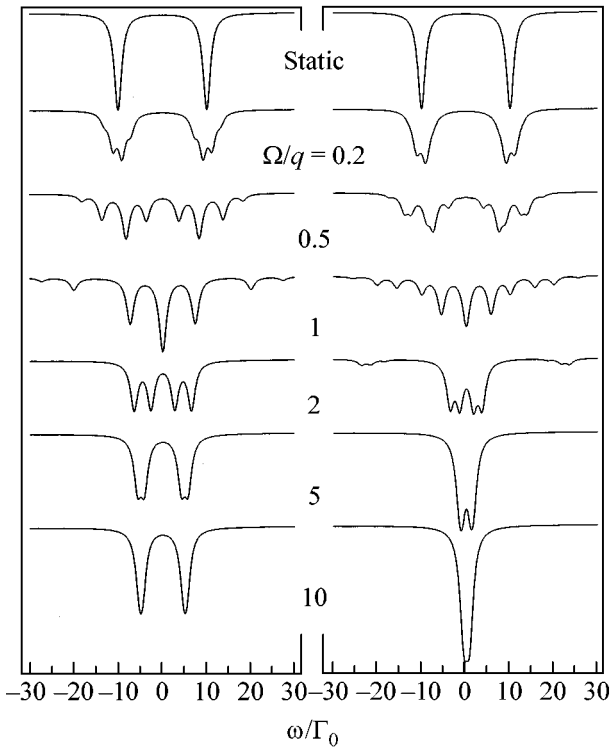

Fig. 2. Mössbauer absorption spectra in the case of the rotation of the principal axis of the electric field gradient tensor at angle θ = (left) 90° and (right) 54.7° for various ratios Ω/q. Here and below, $q = 10\Gamma_0$; the spectra are calculated for the $M1$ transitions $I_e = 3/2 \longrightarrow I_g = 1/2$ and a random distribution of the orientations of molecular axes and the unpolarized source of gamma radiation.

where $\tilde{\lambda}_{\tilde{m}_e}$ are eigenvalues of Hamiltonian (12), $\tilde{m}_e$ are the projections of the spin onto the $\tilde{z}$ axis, for which operator (12) is a diagonal operator, and m_e are the projections of the nuclear spin onto the z axis. Formula (13) shows that the absorption spectrum in this case is represented by a superposition of natural Lorentzian lines; however, in contrast to a static quadrupole doublet, this spectrum generally contains 16 lines whose intensities are determined by mutual orientation of the z and $\tilde{z}$ axes.

Using formula (13), we can easily perform specific calculation of absorption spectra depending on the model parameters q, Ω, and θ. Figure 2 shows the typical Mössbauer spectra for different orientations of the EFG principal axis (θ = 90° and 54.7°) as functions of the rotational frequency Ω. The static spectrum contains the standard quadrupole doublet represented by the superposition of two natural Lorentzian lines:

$$\sigma(\omega) = -\frac{\sigma\Gamma_0}{4}\mathrm{Im}\left(\frac{1}{\omega - q + i\frac{\Gamma_0}{2}} + \frac{1}{\omega + q + i\frac{\Gamma_0}{2}}\right). \quad (14)$$

Upon an increase in the rotational frequency, the Mössbauer spectra are transformed in a specific manner; the nontrivial pattern of line splitting in the spectrum is obviously determined by the eigenvalues $\tilde{\lambda}_{\tilde{m}_e}$ of Hamiltonian (12) and by rotational satellites in accordance with expression (13). It should be noted that the formal structure of Hamiltonian (12) is typical for describing the combined magnetic and quadrupole hyperfine interaction, which is well known in Mössbauer spectroscopy. In our case, the rotational frequency vector Ω directed along the z axis plays the role of $\mathbf{H}_{hf}$.

Consequently, at low rotational frequencies ($\Omega \ll q$), the quadrupole term in Hamiltonian (12) makes the main contribution to the absorption spectrum; the hyperfine structure of the spectrum is strongly blurred in this case by rotational satellites in complete analogy with perturbation of the quadrupole interaction by a weak field $\mathbf{H}_{hf}$. At the same time, line splitting of the static doublet is clearly seen in the case of rotation in the plane ($\theta = 90°$), while the splitting structure is visually indistinguishable in the case of rotation at the "magic" angle $\theta = 54.7°$.

In the limit of high rotational frequencies ($\Omega \gg q$), the spectra also contain a doublet of lines, but with effectively smaller splitting. It is easily seen that the effective quadrupole interaction constant $\bar{q}$ tends asymptotically to a quite natural limit, which is determined by complete averaging of the off-diagonal elements of initial Hamiltonian (5) to zero,

$$\bar{q} = \alpha(\theta)q, \tag{15a}$$

where

$$\alpha(\theta) = (1 + 3\cos 2\theta)/4. \tag{15b}$$

It should be noted that the effective constant $\bar{q}$ is equal to $-q/2$ for rotation in the plane ($\theta = 90°$) and is zero for rotation at the magic angle $\theta = 54.7°$. However, the shape of the Mössbauer spectrum in this limiting case is determined by expression (14), in which $\bar{q}$ should be substituted for q.

As rotational frequency Ω decreases from the high-frequency limit, clearly manifested splitting of each line in the effective doublet begins being manifested in the spectra. Finally, in the intermediate range of rotational frequencies ($\Omega \approx q$), a complex transformation of the Mössbauer spectra is observed. It follows from expressions (12) and (13) that such a form of the spectra is determined not only by the main components, but also by all satellites whose intensities are determined by the mutual orientations of the z and $\tilde{z}$ axes.

To clarify the physical origin of such a qualitative transformation of the Mössbauer spectra upon rotation of the EFG principal axis, we analyze the simplest case of rotation in the plane ($\theta = 90°$). It is seen from formula (5) that the effective time-independent Hamiltonian (12) is reduced in this case to a block diagonal matrix with two identical 2×2 blocks whose eigenvalues

$$\tilde{\lambda}_{\tilde{m}_e} = \begin{cases} -\dfrac{\Omega}{2} \pm \sqrt{q^2 + q\Omega + \Omega^2} \\ \dfrac{\Omega}{2} \pm \sqrt{q^2 - q\Omega + \Omega^2} \end{cases}, \tag{16}$$

can be easily determined and used for obtaining the corresponding eigenvectors $|\tilde{m}_e\rangle$.

Let us now consider the limiting case of rapid ($\Omega \gg q$) rotation. It follows from expression (12) that the $\tilde{z}$ axis in this case deviates from the z axis only slightly. For this reason, the absorption spectrum consists of four main lines with indices $\tilde{m}_e = m_e$ and low-intensity satellites that can be ignored in the first approximation. In this case, expression (13) is simplified so that the absorption spectrum becomes a superposition of four natural Lorentzian lines, whose positions in the spectra are determined by the effective quadrupole interaction constant $\bar{q}$ and rotational splitting δ:

$$\sigma(\omega) = -\frac{\sigma_0\Gamma_0}{8}\mathrm{Im}\left(\frac{1}{\omega - (\bar{q} - \delta) + i(\Gamma_0/2)}\right.$$
$$+ \frac{1}{\omega - (\bar{q} + \delta) + i(\Gamma_0/2)} + \frac{1}{\omega + (\bar{q} - \delta) + i(\Gamma_0/2)} \tag{17}$$
$$\left. + \frac{1}{\omega + (\bar{q} + \delta) + i(\Gamma_0/2)}\right).$$

Using expression (16), we can easily obtain the following estimates accurate to the terms quadratic in (q/Ω):

$$\bar{q} = q/2, \tag{18a}$$

$$\delta = 3q^2/8\Omega. \tag{18b}$$

An analogous simple analysis based on formula (16) cannot be carried out in the case where the principal axis of the electric-field gradient rotates at an arbitrary angle θ to the rotational axis. In this case, we must find the eigenvalues of time-independent Hamiltonian (12) by solving the fourth-degree dispersion equation

$$\tilde{\lambda}^4 - 2\left(q^2 + \frac{5}{4}\Omega^2\right)\tilde{\lambda}^2 - 4\alpha(\theta)q\Omega^2\tilde{\lambda}$$
$$+ q^4 - \frac{1 + 4\alpha(\theta)}{2}q^2\Omega^2 + \frac{9}{16}\Omega^4 = 0, \tag{19}$$

where $\alpha(\theta)$ is defined by formula (15b). We can in principle write the general analytical solution to this equation, but it is rather cumbersome and it would be much more interesting to consider again the limiting case of rapid rotation ($\Omega \gg q$). In this limit, the absorption spectrum is a superposition of four natural Lorentzian lines; however, in contrast to expression (17), splitting

of the main lines of the doublet with effective constant $\bar{q}$ becomes asymmetric,

$$\sigma(\omega) = -\frac{\sigma_0\Gamma_0}{8}\mathrm{Im}\left(\frac{1}{\omega-(\bar{q}-\delta_1)+i(\Gamma_0/2)}\right.$$
$$+\frac{1}{\omega-(\bar{q}+\delta_1)+i(\Gamma_0/2)}+\frac{1}{\omega+(\bar{q}-\delta_2)+i(\Gamma_0/2)} \quad (20)$$
$$\left.+\frac{1}{\omega+(\bar{q}+\delta_2)+i(\Gamma_0/2)}\right)$$

with different values of rotational splitting δ_1 and δ_2 for arbitrary rotational angles θ. In the limit of rapid rotation, we can obtain the following expressions by solving Eq. (19) to within the terms quadratic in (q/Ω):

$$\bar{q} = \alpha(\theta)q, \quad (21a)$$

$$\delta_1 = \frac{5+2\alpha(\theta)-7\alpha^2(\theta)}{6}\frac{q^2}{\Omega}, \quad (21b)$$

$$\delta_2 = \frac{1+2\alpha(\theta)-3\alpha^2(\theta)}{2}\frac{q^2}{\Omega}. \quad (21c)$$

It is easily seen that, in the case of rotation in the plane, we have $\alpha(90°) = -1/2$ and formulas (21) can be reduced to formulas (18) with $\delta_1 = \delta_2 = \delta$, while absorption spectra (20) can be reduced to expression (17). For rotation at the magic angle, we have $\alpha(54.7°) = 0$ and $\bar{q} = 0$, but the absorption spectrum is still determined by expressions (20) and consists of four lines whose positions are defined by rotational splittings $\pm\delta_1$ and $\pm\delta_2$. It should also be noted that, in the case of "rotation" at zero angle, $\alpha(0) = 1$ and expressions (21) lead to quite natural results $\bar{q} = q$ and $\delta_1 = \delta_2 = 0$ (i.e., vanishing of all rotational effects and static spectrum (14)).

Figure 3 shows the dependence of the positions of the main lines in the absorption spectrum on angle θ in the limit of rapid rotation of the EFG principal axis. It is seen in the figure that, in addition to the typical spectral parameters for the above-mentioned values of angle θ, we can single out five points on this curve, at which the spectrum consists of three and not four lines. The four values of angle θ for which a triplet of lines is observed lie in the neighborhood of the magic angle and are determined by the obvious relations

$$2\bar{q} = \pm(\delta_1 \pm \delta_2), \quad (22a)$$

while the fifth value is determined by the condition

$$\delta_2 = 0. \quad (22b)$$

The latter condition is satisfied for the angle $\theta = 70.5°$, for which $\alpha(70.5°) = -1/3$. Figure 4 shows the dependence of the shape of the spectrum on angle θ, which demonstrates the above-mentioned features of the formation of a quadrupole hyperfine structure upon rapid rotation of the principal axis of the electric-field gradient. Direct comparison shows that simple formulas (17), (18), and (20)–(22) successfully describe the shape of the spectra shown in Fig. 2 (lower spectra) and Fig. 4.

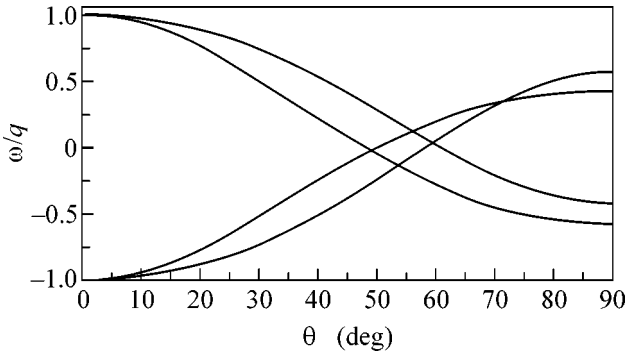

Fig. 3. Position of the main lines in the absorption spectrum vs. angle θ in the regime of the rapid rotation of the principal axis of the electric field gradient ($\Omega/q = 5$).

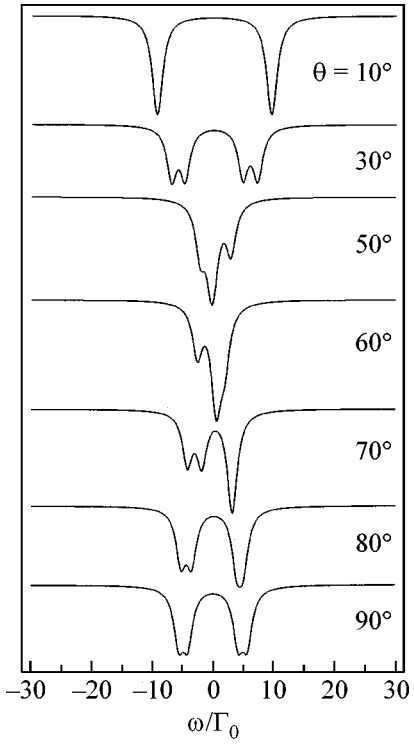

Fig. 4. Mössbauer absorption spectra in the case of the rapid rotation ($\Omega/q = 5$) of the principal axis of the electric field gradient at various angles θ.

Another limiting case in this problem is slow rotation ($\Omega \ll q$) of the EFG principal axis. In analogy with the rapid rotation limit, we can easily find the solution to dispersion equation (21) to within the terms linear in (Ω/q) for slow rotation also:

$$\tilde{\lambda} = \begin{cases} q \pm \dfrac{\sqrt{3(1+2\alpha(\theta))}}{2}\Omega \\ -q \pm \dfrac{\sqrt{3-2\alpha(\theta)}}{2}\Omega. \end{cases} \quad (23)$$

However, in contrast to the previous limiting case, the quantization $\tilde{z}$ axis for operator $\hat{\tilde{H}}^{(e)}$ now forms a certain finite angle with the z axis for any value of angle θ in accordance with formula (12). As a result, all rotational satellites make a significant contribution to absorption spectrum (13), which becomes strongly blurred.

Nevertheless, we can find at least one more simple solution for the absorption spectrum in the case of slow ($\Omega \ll q$) rotation of the EFG principal axis in the plane ($\theta = 90°$). It was noted above that the time-independent Hamiltonian (12) in the rotating system of coordinates is reduced in this case to a block diagonal matrix with two identical 2×2 blocks, which allows us to simplify the general expression (13) for the absorption spectrum. Using simple algebraic transformations, we can prove that the absorption spectrum in this limit consists of eight lines forming two groups of four lines in the vicinity of the two lines of the original static doublet (14),

$$\sigma(\omega) = -\frac{\sigma_0\Gamma_0}{4}\mathrm{Im}\sum_{m_e} A_{m_e}\left(\frac{1}{\omega - (q + m_e\Omega) + i\frac{\Gamma_0}{2}} + \frac{1}{\omega + (q + m_e\Omega) + i\frac{\Gamma_0}{2}}\right), \quad (24)$$

where

$$A_{m_e} = \frac{3}{8|m_e|}\left(1 - m_e\frac{\Omega}{q}\right) \quad (25)$$

are the intensities of the satellites to within the terms linear in (q/Ω). Simple formulas (24) and (25) correctly describe the shape of the Mössbauer spectrum shown in Fig. 2 for $\Omega/q = 0.2$ (left).

Thus, allowance for rotation of the principal axis of the EFG tensor leads to a specific transformation of the Mössbauer spectra, in which a qualitatively different origin of rotations in liquids can be manifested. It should be emphasized that all the peculiarities predicted above can be observed in the spectra only if the stochastic processes are slower than the deterministic rotational motion (i.e., when the relaxation rate is smaller than the characteristic frequency of rotation). However, even if the features of the formation of a quadrupole hyperfine structure predicted above are not manifested in experimental spectra clearly due to the superposition of partial components corresponding to different temporal trajectories of the molecular angular momentum or due to relaxation effects, traces of the predicted specific forms might be manifested in the spectra and should be taken into account in analysis of these spectra.

Preliminary investigations show that the above results can be effectively used in the new PACSR method implemented at the ID18 ESRF station in Grenoble; this method is extremely perspective for broadening the range of materials in which the hyperfine interaction can be studied [6]. The results of these investigations will be reported later.

This study was supported by the Russian Foundation for Basic Research (project no. 05-02-16297) and the European Synchrotron Radiation Facility (contract no. ESRF-074-2005). I am sincerely grateful to A.I. Chumakov, I. Sergeev, and R. Rüffer who work at the ESRF for fruitful discussions, which in fact stimulated this work.

REFERENCES

1. H. H. Wickman, in *Mössbauer Effect Methodology*, Ed. by I. J. Gruverman (Plenum, New York, 1966), Vol. 2; M. Blume, Phys. Rev. **174**, 351 (1968); A. M. Afanas'ev and V. D. Gorobchenko, Zh. Éksp. Teor. Fiz. **66**, 1406 (1974) [Sov. Phys. JETP **39**, 690 (1974)].
2. S. Dattagupta and M. Blume, Phys. Rev. B **10**, 4540 (1974); S. Dattagupta, Phys. Rev. B **12**, 47 (1975); S. Dattagupta and M. Blume, Phys. Rev. B **14**, 480 (1976).
3. A. M. Afanas'ev, S. S. Yakimov, V. M. Cherepanov, *et al.*, Zh. Éksp. Teor. Fiz. **89**, 182 (1985) [Sov. Phys. JETP **62**, 104 (1985)]; A. M. Afanas'ev, P. V. Hendriksen, and S. Mørup, Hyperfine Interact. **88**, 35 (1994); A. M. Afanas'ev and M. A. Chuev, Pis'ma Zh. Éksp. Teor. Fiz. **74**, 112 (2001) [JETP Lett. **74**, 107 (2001)]; M. A. Chuev, O. Hupe, A. M. Afanas'ev, *et al.*, Pis'ma Zh. Éksp. Teor. Fiz. **76**, 656 (2002) [JETP Lett. **76**, 558 (2002)].
4. A. M. Afanas'ev and M. A. Chuev, Pis'ma Zh. Éksp. Teor. Fiz. **77**, 489 (2003) [JETP Lett. **77**, 415 (2003)]; Dokl. Akad. Nauk **390**, 750 (2003) [Dokl. Phys. **48**, 277 (2003)]; J. Phys.: Condens. Matter **15**, 4827 (2003).
5. P. P. Craig and N. Sutin, Phys. Rev. Lett. **11**, 460 (1963); A. Abras and J. G. Mullen, Phys. Rev. A **6**, 2343 (1972); S. L. Ruby, J. C. Love, P. A. Flinn, and B. J. Zabransky, Appl. Phys. Lett. **27**, 320 (1975); D. C. Champeney, E. S. M. Higgy, and R. G. Ross, J. Phys. C: Solid State Phys. **8**, 507 (1975); A. Vasquez and P. A. Flinn, J. Chem. Phys. **72**, 1958 (1980); G. U. Nienhaus, H. Frauenfelder, and F. Parak, Phys. Rev. B **43**, 3345 (1991); I. Chang, H. Hartmann, Yu. Krupyanskii, *et al.*, Chem. Phys. **212**, 221 (1996); A. Gahl, M. Hillberg, F. J. Litterst, *et al.*, J. Phys.: Condens. Matter **10**, 961 (1998).
6. I. Sergueev, U. van Bürck, A. I. Chumakov, *et al.*, Annu. Rep. TUM Phys.-Dep. E **13**, 39 (2001); S. Dattagupta, Radiat. Phys. Chem. **70**, 511 (2004); I. Sergueev, U. van Bürck, A. I. Chumakov, *et al.*, Phys. Rev. B (2005) (in press).
7. A. M. Afanas'ev, M. A. Chuev, and J. Hesse, Zh. Éksp. Teor. Fiz. **113**, 1799 (1998) [JETP **86**, 983 (1998)].
8. A. M. Afanas'ev, M. A. Chuev, and J. Hesse, Phys. Rev. B **56**, 5489 (1997); Zh. Éksp. Teor. Fiz. **116**, 1001 (1999) [JETP **89**, 533 (1999)].
9. R. Zwanzig, Physica (Amsterdam) **30**, 1109 (1964).

Translated by N. Wadhwa

JETP Letters, Vol. 82, No. 8, 2005, pp. 521–525. Translated from Pis'ma v Zhurnal Éksperimental'noĭ i Teoreticheskoĭ Fiziki, Vol. 82, No. 8, 2005, pp. 580–584.

Delocalization of Excitations in Disordered Media with Dipole Transfer

F. S. Dzheparov

Institute of Theoretical and Experimental Physics, Moscow, 117218 Russia

e-mail: dzheparov@itep.ru

Received August 25, 2005

The migration of excitations over a system of impurity centers due to dipole–dipole interactions is studied. A numerical and analytical study of the probability of finding an excitation on the center of its primary localization is carried out for the main models describing the kinetics of spin systems and systems of localized excitons. The results obtained are characterized by a uniformly high accuracy over the entire range of times available for experimental investigations. It is revealed that the preasymptotic effects are in qualitative agreement with theoretical predictions but are quantitatively twice as large as those. © *2005 Pleiades Publishing, Inc.*

PACS numbers: 05.40.–a, 76.20.+q, 76.60.Es, 78.47.+p

1. The transfer of localized excitations over a system of fixed impurity centers (donors) randomly distributed over crystal lattice sites is described by the kinetic equation

$$\dot{p}_{ij} = -\sum_m (\nu_{mi} p_{ij} - \nu_{im} p_{mj}) = -(Ap)_{ij}, \quad p_{ij}(t=0) = \delta_{ij}, \tag{1}$$

where $p_{ij}(t)$ is the probability of finding an excitation at an instant t on the ith donor if it was initially on donor j and the summation is performed over all the donors. In standard models of dipole–dipole transfer, it is usually assumed that the rates of transitions at $i \neq j$ have the form

$$\nu_{ij} = \nu_0 r_0^6 / r_{ij}^6 \tag{2}$$

for the transfer of localized electronic excitations caused by electric dipole transitions [1–3] and

$$\nu_{ij} = \xi_i w_{ij}, \quad w_{ij} = \frac{\nu_0 r_0^6}{r_{ij}^6}(1 - 3\cos^2\theta_{ij})^2 \tag{3}$$

for spin systems when transitions are initiated by magnetic dipole–dipole interactions [4, 5] and $\nu_{jj} = 0$. Here, $\mathbf{r}_{ij} = \mathbf{x}_i - \mathbf{x}_j$, $\mathbf{x}_j$ is the position of the jth donor, θ_{ij} is the angle between $\mathbf{r}_{ij}$ and the external constant magnetic field $\mathbf{H}_0$, and r_0 is the distance between the nearest donors. The parameter ξ_i in Eq. (3) reflects the difference in donor spins. In the model ^{8}Li–^{6}Li spin system discussed below, $\xi_i = 1 + \delta_{i0}(\xi - 1)$ and $\xi = I(I+1)/[S(S+1)]$, where $I = 2$ and $S = 1$ are the spins of ^{8}Li and ^{6}Li nuclei, respectively [4, 5]. In this case, the primarily polarized nucleus is β-active ^{8}Li, which is assumed to be placed at the origin of coordinates at the site $\mathbf{r}_0 = 0$, and the initial condition has the form $p_{i0}(t = 0) = \delta_{i0}$.

Experimentally measurable values are usually expressed using the propagator

$$P_{\mathbf{xy}}(t) = \langle \hat{P}_{\mathbf{xy}}(t) \rangle_c, \tag{4}$$

which equals the probability of finding an excitation at the lattice site $\mathbf{x}$ if it was initially localized at the site $\mathbf{y}$. Here $\langle \ldots \rangle_c$ designates averaging over the spatial distribution of donors. The unaveraged propagator $\tilde{P}_{\mathbf{xy}}(t)$ obeys the equation [6]

$$\frac{d}{dt}\tilde{P}_{\mathbf{xy}}(t) = -\sum_{\mathbf{z}} (n_{\mathbf{z}} \nu_{\mathbf{zx}} \tilde{P}_{\mathbf{xy}}(t) - n_{\mathbf{x}} \nu_{\mathbf{xz}} \tilde{P}_{\mathbf{zy}}(t)) = -(\tilde{A}\tilde{P})_{\mathbf{xy}}, \quad \tilde{P}_{\mathbf{xy}}(t=0) = \frac{n_{\mathbf{y}}}{c}\delta_{\mathbf{xy}}, \tag{5}$$

where $n_{\mathbf{x}}$ is the occupation number: $n_{\mathbf{x}} = 1(0)$ if the site $\mathbf{x}$ is occupied (or not) with a donor, the concentration $c = \langle n_{\mathbf{x}} \rangle_c$, and $\nu_{\mathbf{xz}} = \nu_{ij}(\mathbf{x}_i = \mathbf{x}, \mathbf{x}_j = \mathbf{z})$. From here on, the occupations of different sites are considered independent. The equivalence of Eqs. (1) and (5) is evident if (i) to take into account that, according to Eq. (5), transfer is possible only onto sites occupied with donors and, therefore, $\tilde{P}_{\mathbf{xy}}(t) = 0$ in empty sites and (ii) to retain only terms with occupied sites in Eq. (5) (for the ^{8}Li–^{6}Li system, the β-active ^{8}Li nucleus is located at $\mathbf{y} = 0$). The normalization of $\tilde{P}_{\mathbf{xy}}(t)$ is such that $\sum_{\mathbf{x}} P_{\mathbf{xy}}(t) = 1$.

System of equations (1) is among the simplest ones; however, the great number of particles participating in the process and the necessity of averaging over their possible spatial positions lead on the whole to such a complicated problem that series expansions of observables in terms of the donor concentration [5–8] still remains the only reliable way of its analytical investigation. Among the most important analytical results is the proof of the fact that the propagator in the continuous medium limit (when $c \longrightarrow 0$, but the variation $\Delta P_{\mathbf{xy}}(t) = P_{\mathbf{xy}}(t) - P_{\mathbf{xy}}(0)$ is finite) takes the form [6, 5]

$$P_{00}(t) = f(\beta t), \quad P_{\mathbf{r}\neq 0}(t) = cg(r/\bar{r}, \beta t). \qquad (6)$$

Here, the functions f and g depend on coordinates, time, and concentration only through arguments indicated in Eq. (6); the Forster parameter β is determined by the relation $\langle \exp(\sum n_{\mathbf{z}} \nu_{\mathbf{zx}} t)\rangle_c = \exp(-(\beta t)^{\alpha})$; and the mean distance between donors $\bar{r} = (\Omega/c)^{1/3}$, where Ω is the unit cell volume. For dipole transfer in a three-dimensional system, $\alpha = 1/2$. In the case of an arbitrary multipole order (when $\nu_{ij} \propto r_{ij}^{-s}$) and transfer over a d-dimensional medium, $\alpha = d/s$, and $\bar{r} = (\Omega/c)^{1/d}$. From Eqs. (6), it follows that the expansion in terms of concentration is in fact performed in terms of degrees of the parameter $(\beta t)^{\alpha}$, which is not small at large t. In the continuous medium limit, arbitrarily small distances between donors are allowed; therefore, the operator $\tilde{A}$ in Eq. (5) becomes unbounded. The mathematical investigation of the problems is so complicated that the question of whether the long-time asymptotic behavior has a diffusive character has had no analytical answer so far. Essential arguments in favor of this hypothesis were obtained in [9–11], where a numerical and analytical investigation of both the problem of three-dimensional dipole transfer and the asymptotically exactly solvable model [12] of random jumps with long-range dipole interaction was performed within a unified algorithm. In these works, the diffusion coefficient for the isotropic transfer model (Eq. (2)) [10] and the diffusion tensor for magnetic dipole transfer (Eq. (3)) [11] were calculated at an arbitrary concentration.

The autocorrelation function $P_{00}(t)$ is one of the most important observable quantities. It is accessible to direct measurements by β-NMR spectroscopy [4, 13], fluorescence depolarization experiments [14], and time-resolved narrow-line laser spectroscopy [15]. Here, it is necessary to note that the measurements in β-NMR spectroscopy are performed for the ^{8}Li–^{6}Li spin system in cubic LiF crystals. In this system, the process is initiated by the primarily polarized β-active ^{8}Li nucleus and the observation is carried out by the asymmetry of the β radiation of these nuclei. It is essential that the g factors of the ^{8}Li and ^{6}Li nuclei coincide with an accuracy of 0.57%. In this work, we restricted ourselves to the case of such a low magnetic field ($150 \le H_0 \le 200$ G) that its effect on w_{j0} can be neglected.

To predict the results of experimental studies at impurity concentrations $c < 0.1$, the equation proposed in [16] on the basis of a semiphenomenological theory (see, also, [5]) was used

$$P_{00}(t) = F(t) = \exp(-\sqrt{\beta t}) + \xi \frac{1-\exp(-\sqrt{\beta t})}{(\mu\beta(t+\tau))^{3/2}}\left(1 + \frac{\varphi}{\sqrt{\mu\beta(t+\tau)}}\right), \qquad (7)$$

where, for the ^{8}Li–^{6}Li system,

$$\beta = \frac{256}{243}\pi^3 c^2 \nu_0 \frac{r_0^6}{\Omega^2}, \quad \xi = 3, \quad \varphi = 2.09, \quad \mu\beta\tau = 5.11, \qquad (8)$$

and, for the isotropic model,

$$\beta = \frac{16}{9}\pi^3 c^2 \nu_0 \frac{r_0^6}{\Omega^2}, \quad \xi = 1, \quad \varphi = 1.93, \quad \mu\beta\tau = 3.61. \qquad (9)$$

The parameter μ is determined by the principal values of the diffusion tensor D_{α}

$$(\mu\beta)^{-3/2} = (\Omega/c)\prod_{\alpha=1}^{3}(4\pi D_{\alpha})^{-1/2}. \qquad (10)$$

If the exact values of D_{α} are used, Eq. (8) must be accurate up to the terms $\sim(\beta t)^{1/2}$ at $\beta t \lesssim 1$, up to the terms $\sim(\beta t)^{-2}$ at large βt, and qualitatively accurate in the intermediate region.

In the course of investigations, it was revealed that Eq. (8) does not contradict to the experiment on magnetic dipole transfer at $\beta t \le 15$ [4, 13]. However, as statistics was accumulated, the most recent measurements by the research team from the Institute of Theoretical and Experimental Physics [17, 18] showed that Eq. (8) should be corrected at $\beta t \sim 25$. The simplest form of this correction is

$$P_{00}(t) = F(t)G(t), \qquad (11)$$

$$G(t) = G_{\exp}(t) = \left(1 - \frac{\left(\frac{1}{8} + \alpha\right)\beta t - u(\beta t)^2}{(1 + \nu\beta t)^3}\right). \qquad (12)$$

Here, $F(t)$ is determined in Eq. (7), $\alpha = \alpha(H_0)$ has been calculated in [5], Table 2, and $\alpha = 0.013$ for the low magnetic fields under consideration, and u and ν are parameters that are to be determined experimentally. Equation (12) is accurate up to the terms $\propto\beta t$ at small βt and up to the terms $\sim(\beta t)^{-2}$ at large βt. The dependence given by Eq. (12) with parameters $u = 0.054(3)$ and $\nu = 0.111(6)$ obtained experimentally is presented in Fig. 1.

Table 1. Isotropic model

c	c_1	a	b	d_0	d_1	f_0	f_1	f_2
0.01	0.2022	50.61	4.06	0.06711	0.001804	0.2357	0.02794	0.008377
0.1	0.2920	51.59	4.389	0.06002	0.001	−0.1103	0.1106	0.004183

Table 2. Identical spins

c	c_1	a	b	d_0	d_1	f_0	f_1	f_2
0.01	0.4392	28.70	6.790	−0.0869	0.194	8.43	−1.438	0.15
0.1	0.7074	36.47	6.55	−0.09843	0.08744	−0.7844	0.7158	0.00894

The correcting factor $G(t)$ enhances reoscillation predicted by Eq. (8), which was found experimentally for exciton delocalization [15].

The method of numerical and analytical simulation of random walks in disordered media developed in [10] was modified in this work for the full calculation of $P_{00}(t)$ on the basis of Eqs. (1)–(3) at arbitrary times, and equations describing the $G(t)$ correction with an error $\delta \lesssim 0.01$ were obtained for transfer over identical donors and with $\delta \lesssim 0.05$ for the ^{8}Li–^{6}Li system.

2. In the initial model, donors are randomly scattered over the sites of an infinite crystal. The foundation of the method [10] is the replacement of this infinite random medium by a (super)crystal formed by translations of a large unit (super)cell with the basis $\mathbf{R}_\alpha = N_g \mathbf{e}_\alpha$ cut from the initial crystal with basis vectors $\mathbf{e}_\alpha$. Here, the integer $N_g \gg 1$, and $\alpha = 1, 2, 3$. $N_d = cN_g^3 \sim 1000$ donors are scattered over the supercell sites. Now, the generator A from Eq. (1) is periodic with respect to a translation by any of the edges $\mathbf{R}_\alpha$ of the supercell

$$A_{ij}(\{\mathbf{x}_i \longrightarrow \mathbf{x}_i + \mathbf{R}_\alpha\}, \{\mathbf{x}_j \longrightarrow \mathbf{x}_j + \mathbf{R}_\alpha\}) = A_{ij}. \quad (13)$$

By virtue of the Bloch theorem, the eigenfunctions $f_n(j)$ of the operator A have the form

$$f_n(j) \equiv f_{\mu,\mathbf{k}}(j) = \exp(i\mathbf{k}\mathbf{x}_j)\phi_{\mu,\mathbf{k}}(j), \quad |\mathbf{k}\mathbf{R}_\alpha| \le \pi. \quad (14)$$

Here, the periodic functions $\phi_{\mu,\mathbf{k}}(j, \{\mathbf{x}_m\}) = \phi_{\mu,\mathbf{k}}(j, \{\mathbf{x}_m \longrightarrow \mathbf{x}_m + \mathbf{R}_\alpha\})$ are eigenfunctions for the operator

$$A_{ij}(\mathbf{k}) = \sum_{l_\alpha} A_{ij}(\{\mathbf{x}_j \longrightarrow \mathbf{x}_j + l_\alpha \mathbf{R}_\alpha\}) e^{-i\mathbf{k}(\mathbf{x}_i - \mathbf{x}_j - l_\alpha \mathbf{R}_\alpha)}, \quad (15)$$

where $0 \le i, j \le N_d - 1$ and the summation is performed over all the integer l_α.

Correspondingly, the propagator assumes the representation

$$P_{00}(t) = \int_B \frac{d^3k}{V_B} \langle (\exp(-A(\mathbf{k})t))_{00} \rangle_c, \quad (16)$$

$$P_{\mathbf{x}0}(t) = c \int_B \frac{d^3k}{V_B} \exp(i\mathbf{k}\mathbf{x}) \times \langle (\exp(-A(\mathbf{k}, \mathbf{x}_1 = \mathbf{x})t))_{10} \rangle_c. \quad (17)$$

Here, the integration region (the Brillouin zone for the superlattice) is determined by Eq. (14) and its volume $V_B = (2\pi)^3/(N_g^3 \Omega)$. For identical donors, Eq. (16) is simplified to the form

$$P_{00}(t) = P_{\mathbf{y}\mathbf{y}}(t) = \int_B \frac{d^3k}{V_B} \frac{1}{N_d} \left\langle \sum_{j=0}^{N_d - 1} (e^{-A(k)t})_{jj} \right\rangle_c = \int_B \frac{d^3k}{V_B} \frac{1}{N_d} \langle \mathrm{Tr}\{\exp(-A(\mathbf{k})t)\} \rangle_c. \quad (18)$$

This relation provides a considerably faster (by a factor of N_d) accumulation of statistics for averaging over

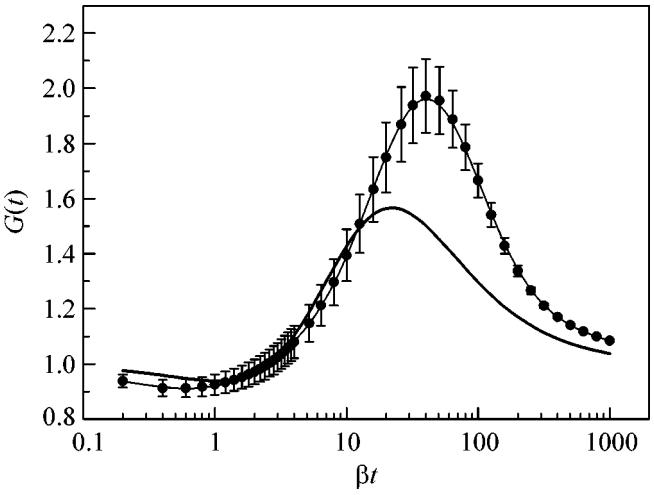

Fig. 1. Numerical simulation results for (thin line with statistical error bars) the functions $G(t)$ and (thick line) $G_{\exp}(t)$ given by Eq. (12) with the parameters $u = 0.054$ and $\nu = 0.111$ obtained experimentally [18] for concentration $c = 0.1$.

Table 3. ^{8}Li–^{6}Li system

c	c_1	a	b	d_0	d_1	f_0	f_1	f_2
0.01	1.06	49.73	11.39	–0.4103	0.005118	3.247	–0.229	0.01888
0.1	0.7098	40.59	6.121	–3.616	2.283	1.568	1.603	0.1093

donor configurations in comparison with Eq. (16). However, this approach is applicable only for systems that are translationally invariant in the mean. A similar approach was used previously in [9–11] for the calculation of the diffusion tensor.

Equations (16) and (18) were used for the calculation of P_{00}, and both the diagonal element $(\exp(-A(\mathbf{k})t))_{00}$ and the trace $\mathrm{Tr}\{\exp(-A(\mathbf{k})t)\}$ were determined by a numerical diagonalization of the operator $A(\mathbf{k})$. In this work, we restricted ourselves by the case of a face-centered cubic lattice. For the ^{8}Li–^{6}Li system (in accordance with the experiment), the $\mathbf{H}_0 \parallel [111]$ magnetic field orientation was used.

Note that, in the case of the ^{8}Li–^{6}Li system, the method used here has a systematic error due to the fact that one spin ^{8}Li resides in each cell of the superlattice, while this spin is only one for the entire crystal in the initial system. However, this error is manifested only at long times when $P_{00}(t) \lesssim \xi/N_d$ and the relative error has the same order of magnitude $\delta P_{00}/P_{00} \lesssim \xi/N_d$. Within the accuracy of our calculations, this error is negligibly small.

3. Numerical analysis was performed at $c \le 0.1$ for $G(t) = P_{00}(t)/F(t)$. The parameter μ from F in Eq. (10) was calculated from the relation

$$D_\alpha = \frac{1}{6}\kappa_\alpha \beta \bar{r}^2 \tag{19}$$

and equations

$$\begin{aligned}\kappa_\alpha &= \kappa = 0.2895 \\ &+ (0.0066 + 0.132c - 0.09c^2)(1-c)\end{aligned} \tag{20}$$

for isotropic transfer [10] or

$$\begin{aligned}\kappa_\perp &= 0.2765 + 0.135c + 0.653c^2 \\ &- 1.32c^3 + 0.6193c^4, \\ \kappa_\parallel &= 0.5116 + 0.421c - 0.455c^2 \\ &- 0.22c^3 + 0.2825c^4\end{aligned} \tag{21}$$

for the magnetic dipole case [11]. Here, the symbols $\parallel$ and $\perp$ correspond to the parallel and orthogonal directions with respect to the field $\mathbf{H}_0$.

The main calculations were performed at the number of donors $N_d \approx 1000$ and $\beta t \le 1000$. The change from $N_d = 60$ to $N_d = 1000$ lead to no more than a 10% change in the values of $G(t)$ and to no more than a 15% change in the position of the maximum coordinate $x_{\max} = \beta t_{\max}$. The changes in $G(t)$ upon passing from $N_d = 1000$ to $N_d = 4000$ are negligibly small.

In all cases, the results were reasonably described by the relation $G(x) = G_a(x)$ at

$$\begin{aligned}G_a(x) &= 1 + c_1 \exp\left(-\frac{1}{2}\left(\left(\ln\frac{h^2 + x^2}{h^2 + a^2}\right)/\ln b\right)^2\right) \\ &- \frac{gx - d_0 x^{3/2} - d_1 x^2}{(1 + f_0 x^{1/2} + f_1 x + f_2 x^{3/2})^2},\end{aligned} \tag{22}$$

where $x = \beta t$ and $h = 0.01$. The parameter g in this equation was calculated by the first (known to $\propto c^2$) terms of the concentration expansion ([8] for the isotropic model and [6, 7, 5] for magnetic dipole transfer). In the case of spin models, both delocalization in the ^{8}Li–^{6}Li system and transfer over identical spins were considered. In the isotropic model, $g = 0.097$; for identical spins, $g = 0.10$; and, for the ^{8}Li–^{6}Li system, $g = 1/8 + \alpha = 0.138$.

The available statistics is not sufficient for determining the concentration dependence of parameters in Eq. (22); therefore, below, in Tables 1–3, the results of calculations are given for two concentrations $c = 0.01$ and $c = 0.1$.

Equation (22) with parameters from Tables 1–3 approximates almost all our results with an error no higher than 2%. An exclusion is provided by the region $\beta t \le 1$ for the isotropic model at $c = 0.1$ (see Fig. 2). Evidently, the reason for this discrepancy is in the fact that, instead of the relation

$$P_{00} = 1 - (\beta t/(\xi + 1))^{1/2} + O(\beta t) \tag{23}$$

(which forms the basis of the continuous medium approximation and the construction of Eq. (8)), the general representation

$$P_{00} = 1 - \frac{c}{\xi + 1}\sum_{\mathbf{x}}(1 - e^{-(\xi+1)W_{\mathbf{x}0}t}) + O(c^2), \tag{24}$$

should be used, where $\xi = 1$ and $W_{\mathbf{x}0} = \nu_{\mathbf{x}0}$ for the isotropic model, $\xi = 1$ and $W_{\mathbf{x}0} = w_{\mathbf{x}0}$ for identical spins, and $\xi = 3$ and $W_{\mathbf{x}0} = w_{\mathbf{x}0}$ for the ^{8}Li–^{6}Li system. The statistical accuracy of the results for the ^{8}Li–^{6}Li system is still no better than 5% as it is seen in Fig. 2 (in the maximum region). The plots for transfer over identical spins look similarly: at the maximum, $G_{\max} = 1.65$–1.9, and the maximum itself is located at $\beta t \approx 40$–50.

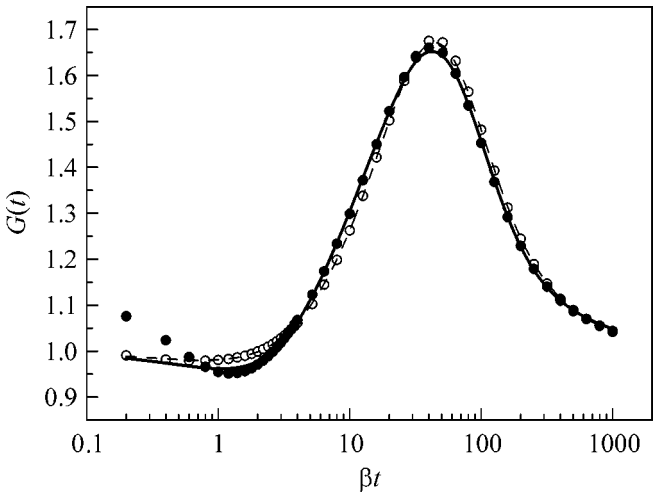

Fig. 2. Numerical simulation results for the function $G(t)$ for the isotropic model at c = (open points) 0.01 and (closed points) 0.1 along with (dashed and solid lines, respectively) the approximating functions $G_a(t)$. At c = 0.01, the rms deviation between $G(t)$ and $G_a(t)$ is much less than the computational error (1%).

4. The main result of this work is in the fact that the problem of the configurational averaging of the solution to kinetic equations (1)–(3) received a full numerical solution. This part of the problem of dipole transfer in disordered systems was considered as the most problematic one up to the present day. In particular, it is associated with quite nontrivial problems of the field theory [10]. The further experimental studies will mainly give information on the degree of validity of Eqs. (1)–(3) themselves.

This work was supported by the Russian Foundation for Basic Research, project no. 03-02-17126, and by the Council of the President of the Russian Federation for Support of Young Scientists and Leading Scientific Schools, project no. NSh-1907.2003.2.

REFERENCES

1. O. K. Alimov, M. Kh. Ashurov, T. T. Basiev, *et al.*, Tr. Inst. Obshch. Fiz. Akad. Nauk SSSR **9**, 50 (1987).
2. P. T. Rieger, S. P. Palese, and R. J. D. Miller, Chem. Phys. **221**, 85 (1997).
3. E. N. Bodunov, M. N. Berberan-Santos, E. J. Nunes Pereira, and J. M. G. Martinho, Chem. Phys. **259**, 49 (2000).
4. Yu. G. Abov, M. I. Bulgakov, S. P. Borovlev, *et al.*, Zh. Éksp. Teor. Fiz. **99**, 962 (1991) [Sov. Phys. JETP **72**, 534 (1991)].
5. F. S. Dzheparov, Zh. Éksp. Teor. Fiz. **99**, 982 (1991) [Sov. Phys. JETP **72**, 546 (1991)].
6. F. S. Dzheparov and A. A. Lundin, Zh. Éksp. Teor. Fiz. **75**, 1017 (1978) [Sov. Phys. JETP **48**, 514 (1978)].
7. F. S. Dzheparov, V. S. Smelov, and V. E. Shestopal, Pis'ma Zh. Éksp. Teor. Fiz. **32**, 51 (1980) [JETP Lett. **32**, 47 (1980)].
8. C. R. Gochanour, H. C. Andersen, and M. D. Fayer, J. Chem. Phys. **70**, 4254 (1979).
9. F. S. Dzheparov, D. V. L'vov, K. N. Nechaev, and V. E. Shestopal, Pis'ma Zh. Éksp. Teor. Fiz. **62**, 639 (1995) [JETP Lett. **62**, 662 (1995)].
10. F. S. Dzheparov, D. V. L'vov, and V. E. Shestopal, Zh. Éksp. Teor. Fiz. **114**, 2166 (1998) [JETP **87**, 1179 (1998)].
11. F. S. Dzheparov, D. V. Lvov, and V. E. Shestopal, in *Nanoscale Properties of Condensed Matter Probed by Resonance Phenomena* (Kazan, 2004), Abstract PS23, J. Supercond. (2005) (in press).
12. F. S. Dzheparov and V. E. Shestopal, Teor. Mat. Fiz. **94**, 496 (1993).
13. F. S. Dzheparov, A. D. Gul'ko, P. Heitjans, *et al.*, Physica B (Amsterdam) **297**, 288 (2001).
14. C. R. Gochanour and M. D. Fayer, J. Phys. Chem. **85**, 1989 (1981).
15. V. P. Gapontsev, F. S. Dzheparov, N. S. Platonov, and V. E. Shestopal, Pis'ma Zh. Éksp. Teor. Fiz. **41**, 460 (1985) [JETP Lett. **41**, 561 (1985)].
16. F. S. Dzheparov, Radiospektroskopiya **13**, 135 (1980).
17. F. S. Dzheparov and A. D. Gul'ko, in *Modern Problems of Nuclear Physics and Physics and Chemistry of Condensed Matter* (Akademprint, Moscow, 2004), pp. 65–71.
18. A. D. Gul'ko, O. N. Ermakov, S. V. Stepanov, and S. S. Trostin, in *Nanoscale Properties of Condensed Matter Probed by Resonance Phenomena* (Kazan, 2004), Abstract PS58, J. Supercond. (2005) (in press).

Translated by A. Bagatur'yants

JETP Letters, Vol. 82, No. 8, 2005, pp. 526–531. Translated from Pis'ma v Zhurnal Éksperimental'noĭ i Teoreticheskoĭ Fiziki, Vol. 82, No. 8, 2005, pp. 585–590.

Coulomb Oscillations of the Current through Spin-Nondegenerate *p* States of InAs Quantum Dots

Yu. N. Khanin[a], E. E. Vdovin[a], S. V. Dubonos[a], A. Levin[b], L. Eaves[b], and M. Henini[b]

[a] *Institute of Microelectronics Technology and High Purity Materials, Russian Academy of Sciences, Chernogolovka, Moscow region, 142432 Russia*

e-mail: vdovin@ipmt-hpm.ac.ru

[b] *The School of Physics and Astronomy, University of Nottingham, Nottingham NG7 2RD, United Kingdom*

Received September 5, 2005; in final form, September 15, 2005

The electron transport is studied in split-gate structures fabricated on the basis of a modulation-doped heterostructure that contains a single quantum well and self-assembled InAs quantum dots near the 2D electron gas regions. The current passing through the channel with a denumerable set of InAs quantum dots is found to exhibit Coulomb oscillations as a function of the gate voltage. The oscillations are associated with the excited *p* states of InAs quantum dots, which are characterized by opposite spins and caused by lifting of the spin degeneracy of the *p* state due to the Coulomb interaction. The Coulomb oscillations of the current are observed up to a temperature of ~20 K. The Coulomb energy is found to be ΔE_c = 12.5 meV, which agrees well with the theoretical estimates for the *p* states of quantum dots in the structures under study. © *2005 Pleiades Publishing, Inc.*

PACS numbers: 73.23.Hk, 73.40.Gk

The interest in studying the properties of different types of quantum dots (QDs) is primarily motivated by the possibility to obtain basic information on the new physical phenomena and processes, such as spin effects [1–3] and Coulomb interactions between electrons (within zero-dimensional objects or between electrons in the QDs and in the electrodes) [4, 5]. In addition, semiconductor QDs seem to be very promising from the viewpoint of designing new optoelectronic and nanoelectronic devices, such as single-electron transistors, memory cells, single-photon detectors, and sources of radiation; the electron spin states of QDs are candidates for quantum bits [5–8].

Today, the most promising objects of investigation are self-assembled QDs formed in the process of growth of epitaxial InAs layers by the Stranski–Krastanov method in the GaAs or AlAs host lattice. This is related to the simplicity of their fabrication, as compared to the QDs bounded electrostatically or laterally by etching, and to the possibility of obtaining smaller geometrical dimensions. The small characteristic dimensions of InAs QDs lead to a considerable increase in the energy gaps between dimensional quantization levels and in the Coulomb energy of the electron–electron interaction within the system, which enhances the influence of these effects on the electron and optical properties of the QDs. In addition, the ultrasmall size of self-assembled QDs provides a possibility for the manifestation of Coulomb and spin effects [3] in low-dimensional objects at higher temperatures, beyond the millikelvin range.

Earlier, the electron transport through an ensemble of self-assembled QDs was usually studied by capacity [9, 10] and resonance tunnel spectroscopy [11–17]. However, the interpretation of the experiments for systems containing relatively large numbers of QDs (~10^2–10^6) was difficult and did not allow one to study the properties of an individual QD. From this point of view, it is of interest to study the transport through a single QD (or a denumerable set of QDs), because these studies may give detailed information on both electron and spin properties of QDs, as well as on the Coulomb interaction between electrons localized within individual QDs and electrons in the contacts. The objects most suitable for such experiments are structures with QDs localized in the gap of the split gate, which are prototypes of single-electron transistors. However, despite the fundamental simplicity of this approach, only few publications reporting on its successful implementation can be found in the literature [17–19]. The main problem in studying the lateral transport through an InAs QD is that its ground state lies deep in the band gap of GaAs and, hence, a careful adjustment of the parameters of the heterostructure and the design of the gate system is necessary. In [17], the transport in a structure with QDs and a one-dimensional channel formed using an atomic-force microscope was studied. On the background of a strong current through this channel, different sets of conductivity features (from 2 to 5 features)

were detected, which were ascribed by the authors to the states of different QDs. In [18], Coulomb oscillations of conductivity were observed in the tunneling through localized states (electron pools containing about 20 electrons) induced by the presence of InAs QDs in the gap of the split gate. The authors determined the Coulomb interaction energy E_C = 2–3 meV, which corresponded to the dimensions far greater than those of the self-assembled InAs QDs. In [19], two *s* states of QDs were observed in the channel as a result of the spin splitting of the ground state due to the Coulomb interaction.

In this paper, we report on the observation of clearly pronounced Coulomb oscillations of the current passing through a denumerable set of InAs QDs (1 to 3 QDs) in the channel of a split-gate transistor as a function of the gate voltage. These oscillations were associated with the excited states of InAs QDs. The first four of the experimentally detected oscillations were caused by the electron tunneling through the *p* states of InAs QDs that were spin-nondegenerate due to the Coulomb interaction. The Coulomb oscillations of the current were observed up to a temperature of ~20 K. We determined the Coulomb energy as ΔE_C = 12.5 meV. This value fits the theoretical estimates for QDs with a diameter of ~22 nm, which coincides with the characteristic lateral dimension of InAs QDs in our experimental structures.

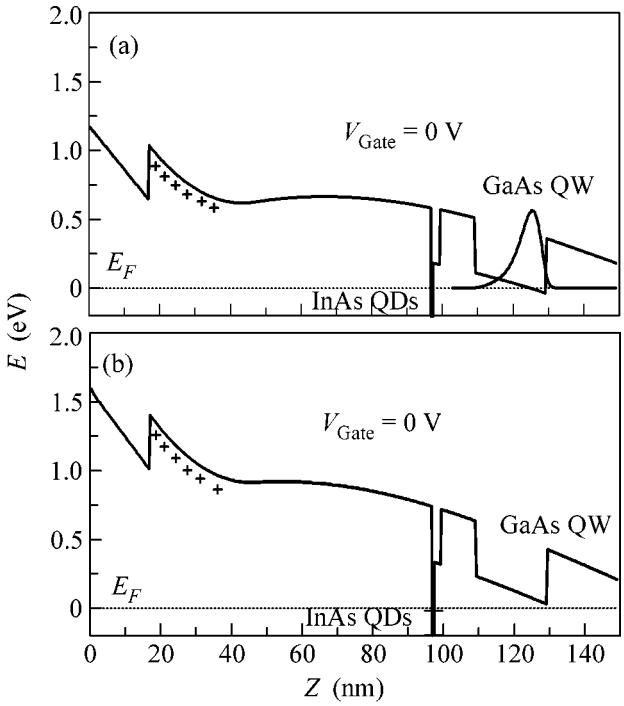

Fig. 1. Calculated potential profile of the active part of the experimental structure at (a) zero and (b) negative gate voltage.

The electron transport was studied in split-gate structures fabricated on the basis of a modulation doped heterostructure with a single 20-nm-wide GaAs quantum well, in which self-assembled InAs QDs were embedded near the 2D electron gas regions. The distance between the layer of self-assembled InAs QDs and the GaAs quantum well was 10 nm. The heterostructure was grown by molecular beam epitaxy on a substrate with the (100) surface orientation. The self-assembled InAs QDs were formed in the process of the growth of strained InAs epitaxial layers by the Stranski–Krastanov method. The characteristic diameter of QDs, their height, and the surface concentration were determined by scanning tunneling spectroscopy of samples grown under the same conditions as the experimental samples and were found to be ~20 nm, 3 nm, and 1×10^{11} cm^{-2}, respectively. The mobility and concentration of the 2D electron gas in the structure under study were determined by Hall measurements at 4.2 K and amounted to 2×10^4 cm^2/V s and $n = 1.2 \times 10^{11}$ cm^{-2}, respectively. The calculated bottom profile of the conduction band of the heterostructure is shown in Fig. 1. In the absence of gate voltage (Fig. 1a), electrons are in both self-assembled InAs QDs and GaAs quantum well. Applying a negative voltage, it is possible to create the conditions at which only the InAs QDs lie below the Fermi energy level while no electrons are present in the GaAs quantum well (Fig. 1b). Thus, because of the electrostatic depletion, a tunnel barrier arises in the split-gate region between the 2D contacts, and the current through the structure is predominantly determined by the tunneling through the InAs QDs localized in the region of this barrier (Fig. 2c). The tunnel transparency of such a structure and the energy of the QD states with respect to the Fermi energy in the contacts may be varied by both varying the gate voltage V_g and applying a source–drain voltage V_{SD}. In the case when the energy gap of dimensional quantization ΔE_N (because of the similarity between a QD and an atom, ΔE_N is often interpreted as the distance between the *s*, *p*, and *d* states of the QD) is much greater than the Coulomb interaction energy ΔE_C, a peak of current should occur each time when the Fermi energy of the emitter coincides with a spin-nondegenerate energy level of the QD; i.e., in such a situation, the Coulomb interaction lifts the spin degeneracy of the QD states, and the spectroscopy of all the E_N states with opposite spins is possible [3]. By contrast, in the case of $\Delta E_C \gg \Delta E_N$, equidistant peaks determined by ΔE_C will predominate in the experimental records while the information on the dimensional quantization levels will be lost.

Figure 2 shows the (a) electron microscope image of the active part of the experimental structure, (b) its schematic representation, and (c) the schematic diagram of the tunneling transport through the InAs QDs in the channel of the transistor. To fabricate an AuNi split gate, we used electron lithography; the width of the gate in its narrowest part was about 0.2 μm, and the width of the gap varied from 0.5 to 0.3 μm for different

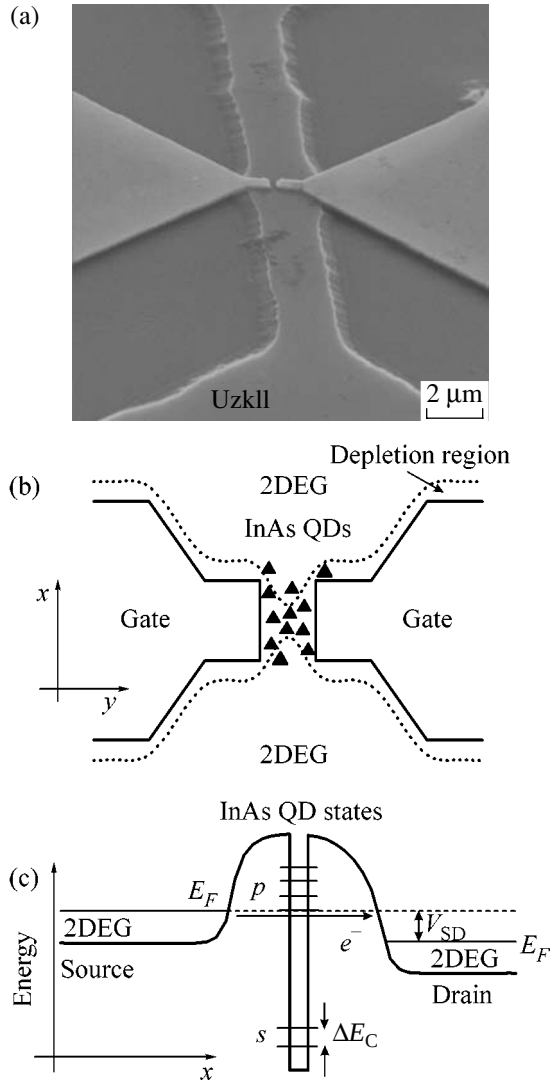

Fig. 2. (a) Electron microscope image of the active part of the experimental structure, (b) its schematic representation, and (c) the schematic diagram of the tunneling transport through the InAs quantum dots (QDs) in the channel of the transistor.

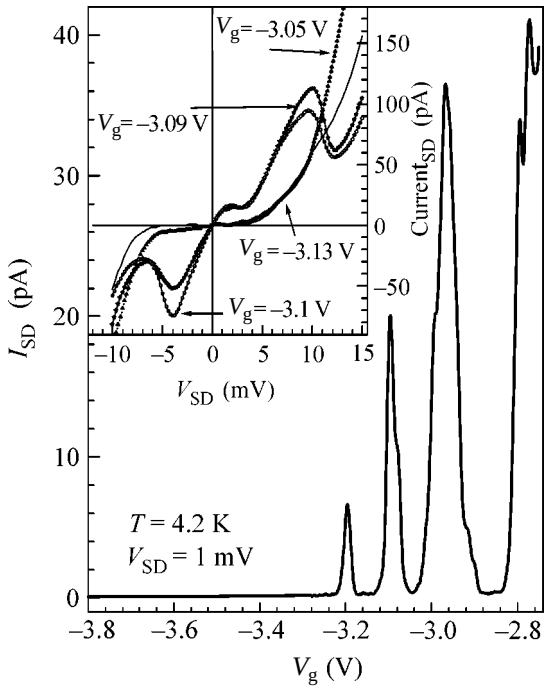

Fig. 3. (a) The $I_{SD}(V_g)$ dependence of the experimental sample at a bias voltage of V_{SD} = 1 mV at T = 4.2 K. The inset shows the $I_{SD}(V_{SD})$ dependences for various gate voltages V_g.

samples. The ohmic contacts were made by a sequential deposition of AuGe/Ni/Au layers with a subsequent annealing at T = 400°C. To fabricate a mesa structure with a width of 2–5 μm, a standard photolithographic technique with chemical etching was used. The application of a negative voltage to the gate reduces the active (transparent for tunneling) part of the device. When the density of QDs in the gap of the split gate is 1×10^{11} cm^{-2}, the number of QDs in this region may reach 50; however, in the presence of a relatively large gate voltage V_g = –3 V, the tunneling occurs through only one QD or a small number of QDs. Hence, owing to the Coulomb blockade, such a device is equivalent to a single-electron transistor. In our experiments, we carried out dc measurements of the $I_{SD}(V_g)$ and $I_{SD}(V_{SD})$ dependences at T = 4.2–30 K.

Figure 3a shows the $I_{SD}(V_g)$ dependence for an experimental sample with a split gate gap width of 0.3 μm at T = 4.2 K. The dependence was obtained as a result of cooling the sample and illuminating it with a short pulse of IR radiation from an IR diode. As one can see from this figure, the $I_{SD}(V_g)$ dependence exhibits sharp peaks of current beginning from V_g = –3.2 V; the first four peaks are caused by the Coulomb resonances of the tunneling current passing through the channel with nondegenerate excited p states of InAs QDs with opposite spins. Such an identification (as is shown below) is confirmed by the value of the Coulomb energy ΔE_C obtained from the processing of experimental data: this value precisely corresponds to the p states of InAs QDs with a size of ~22 nm. Note that we detected no resonances associated with the s states of InAs QDs, which can be explained by the large depth (~0.5 eV) at which these states lie under the bottom of the conduction band of GaAs and by the impossibility of their detection under the conditions of our experiment. Additional evidence in favor of the interpretation of our experiment and the failure to detect the s states is given by the self-consistent calculation of the potential profile of the heterostructure (see Fig. 1). The experimental $I_{SD}(V_g)$ curves are time-independent and reproducible in detail in repeated measurements; however, they are modified by thermal cycling. In the measure-

ments sequentially repeated after heating to room temperature, the $I_{SD}(V_g)$ dependences exhibit similar sets of resonance features and differ only in the shift of the tunneling threshold of V_g, as well as in the fine structure of the oscillations. The modification of the dependences in sequential cooling–illumination cycles is presumably related to random charging–discharging of the denumerable set of QDs in the channel formed by the split gate. As it will be seen from the temperature measurements described below, almost all the experimental peaks in the $I_{SD}(V_g)$ characteristic represent packets of resonances corresponding to the tunneling through similar excited states of different QDs with close in energies, and the width of the peaks is determined by the bias voltage V_{SD}. An exception is the first resonance at $V_g \sim -3.2$ V. In this case, the resonance feature is presumably caused by the tunneling through the lower excited *p* state of a single QD that is most efficient for tunneling, and the width of the peak of the current at $V_{SD} \longrightarrow 0$ is determined by the broadening Γ of this energy state. An increase in the current at $V_g > -2.8$ V is caused by the fact that, as the magnitude of the negative voltage V_g decreases, the depletion region in the gap also decreases and the number of QDs involved in the transport process increases. This situation leads to aperiodic oscillations of the current (the corresponding part of the $I_{SD}(V_g)$ dependence is not considered in the present paper), which are caused by the contributions of the progressively increasing number of excited QD states possessing different energies because of their different positions in the potential profile of the channel. Such chaotic oscillations were observed, e.g., in a short-channel GaAs field-effect transistor [20] or in a quasi-one-dimensional system fabricated on the basis of a field-effect transistor on the *n*-Si surface [21].

The inset in Fig. 3 shows $I_{SD}(V_{SD})$ dependences for a sample with a split-gate gap width of 0.3 μm at T = 4.2 K for different values of V_g. At $V_g = -3.09$ and −3.1 V, the dependence exhibits a pronounced resonance feature with a region of negative differential conductivity, which, in these coordinates, is associated with the resonance process corresponding to the second peak in the $I_{SD}(V_{SD})$ curve shown in Fig. 3. The width of the experimental resonance in the $I_{SD}(V_{SD})$ dependence is determined by the Fermi energy of the emitter; i.e., the beginning of the resonance corresponds to the coincidence of the QD energy with the Fermi energy of the emitter, while the end of the resonance corresponds to the coincidence with the bottom of the conduction band of the two-dimensional subband of the emitter. Setting the factor of conversion from bias voltage V_{SD} to energy equal to 2 (i.e., assuming that the QD is in the middle of the tunnel barrier), we obtain that the Fermi energy of the emitter is approximately equal to 5 meV, which agrees well with the value obtained from analyzing the Shubnikov–de Haas oscillations observed in the given heterostructure in the Hall geometry.

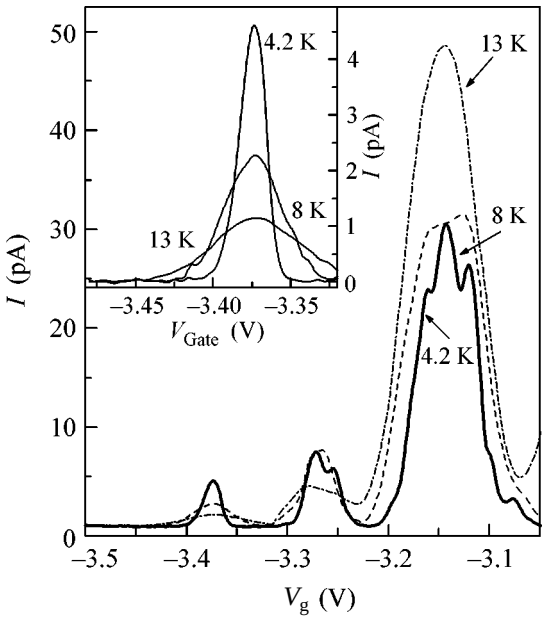

Fig. 4. Dependences of the current I_{SD} through the structure on the gate voltage V_g for three temperatures: 4.2, 8, and 13 K (the solid, dashed, and dot-and-dash curves, respectively) at a bias voltage of V_{SD} = 1 mV. The inset shows the modification of the first peak with increasing temperature.

To determine the factor α of conversion from the gate voltage V_g to the energy scale, we measured the $I_{SD}(V_g)$ dependences at different temperatures (Fig. 4) with the bias voltage V_{SD} = 1 mV. It should be noted that the Coulomb oscillations of the tunneling current through InAs QDs were observed by us up to a temperature of ~20 K, but the peak amplitudes varied in different ways with increasing temperature. The amplitudes of the first two resonances near the tunneling threshold, which corresponded to the tunneling through the energy states of a single QD, decreased with increasing temperature mainly because of the temperature spread of the Fermi distribution in the emitter. By contrast, the amplitudes of the subsequent resonances, which corresponded to the tunneling through several dots, increased. The latter result can be explained as follows: as the temperature grows, additional tunnel channels with close energies become included in the transport process, the amplitudes of integral Coulomb oscillations (starting from the third one in Fig. 4) increase, and this increase begins to exceed the effect of the temperature spread. In view of the aforesaid, to obtain the value of α, the broadening of the first experimental peak should be analyzed.

Preliminarily, in order to exclude error in determining α due to the effect V_{SD} on the width of the experimental Coulomb resonance, it is necessary to discuss the $I_{SD}(V_g)$ dependences obtained for different values of V_{SD}. Figure 5a shows the $I_{SD}(V_g)$ characteristics for V_{SD} from 0.5 to 4 mV at T = 4.2 K. As one can see from

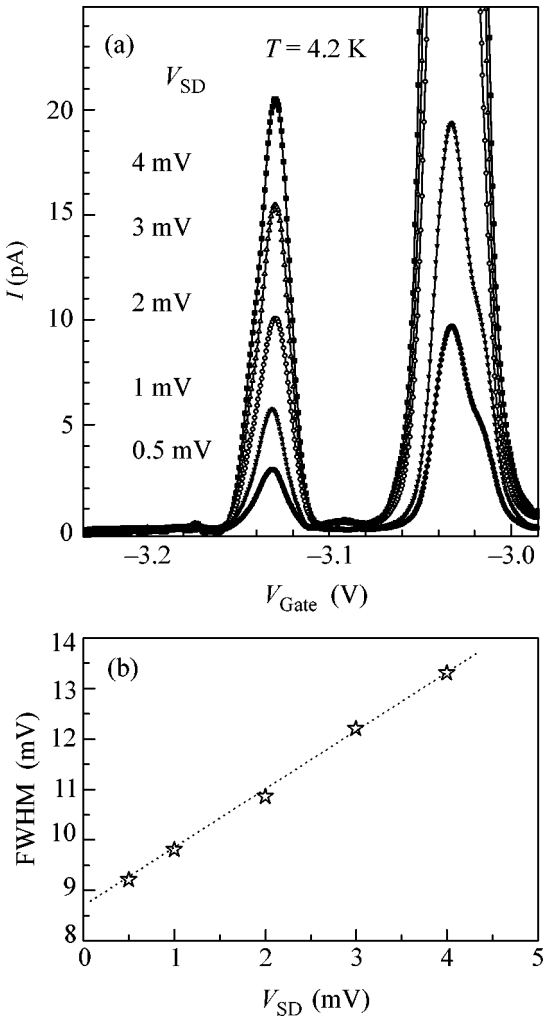

Fig. 5. (a) Current I_{SD} through the structure vs. the gate voltage V_g at T = 4.2 K for various bias voltages V_{SD} from 0.5 to 4 mV and (b) the FWHM of the first experimental peak on the bias voltage V_{SD}.

Fig. 5b, the dependence of the FWHM of the first experimental feature on voltage V_{SD} is linear, which evidently confirms the model proposed above for the resonance feature formation in the $I_{SD}(V_g)$ transport characteristics. A similar behavior of the width of the first resonance feature versus V_{SD} was observed for all of the samples studied. In addition, Fig. 5b shows that the studies of the $I_{SD}(V_g)$ dependence at V_{SD} = 1 mV, which were represented in Fig. 4, give only a small error (~10%) in the determination of the FWHM and, hence, in α. Extending the dependence of the FWHM on V_{SD} to V_{SD} = 0, we obtain the upper boundary for the width of the experimental feature at T = 4.2 K: ~9 mV. Assuming that, at relatively high temperatures in the limit $V_{SD} \longrightarrow 0$, the FWHM is mainly determined by the temperature spread of the Fermi distribution of the emitter, i.e., FWHM ~ 3.5kT [22] (at T = 4.2 K, 3.5kT ~ 1.16 meV), we obtain $\alpha \approx 8$ mV/meV. Close values of the factor α were obtained for the curves measured at the temperatures of 8 and 13 K. As a result, from the experimental dependences of the Coulomb oscillations of the tunneling current, we determined the value of the Coulomb energy $\Delta E_C = \delta V_g/\alpha$, where δV_g ~ 100 mV is the distance between the peaks in the $I_{SD}(V_g)$ dependence. The resulting value ΔE_C = 12.5 meV agrees well with the theoretical estimates of the Coulomb energy for the *p* states of QDs with a diameter of ~22 nm [9, 17], which coincides with the characteristic lateral size of InAs QDs in our experimental structures.

Thus, in this paper, we presented the results of studying the electron transport in split-gate structures fabricated on the basis of modulation doped heterostructure with a single quantum well, in which self-assembled InAs quantum dots were embedded near the 2D electron gas regions. Up to a temperature of ~20 K, we observed clearly pronounced Coulomb oscillations of the current passing through a denumerable set of InAs QDs in the channel of the transistor as a function of the gate voltage. The oscillations are associated with the excited *p* states of InAs QDs with opposite spins, which are caused by lifting of spin degeneracy due to the Coulomb interaction. We determined the value of the Coulomb energy ΔE_C = 12.5 meV. This value agrees well with the theoretical estimates for the *p* states of QDs with a diameter of ~22 nm, which coincides with the characteristic lateral size of InAs QDs in the experimental structures.

We are grateful to V.V. Belov, L.G. Maĭstrenko, and R.N. Vydumkina for technical assistance and to S.V. Morozov for the interest in our work and for useful discussions. This work was supported in part by the Russian Foundation for Basic Research (project nos. 03-02-17693 and 04-02-16869), the Branch of Information Technologies and Computer Systems, the Russian Academy of Sciences (the program "Setting up Computations with the Use of New Physical Principles"), the Engineering and Physical Sciences Research Council (EPSRC, United Kingdom), and the SANDiE (Self-Assembled Semiconductor Nanostructures for new Devices in Photonics and Electronics) Network of Excellence (contract no. NMP4-CN-2004-500101).

REFERENCES

1. K. Ono and S. Tarucha, Phys. Rev. Lett. **92**, 256803 (2004).
2. R. Hanson, B. Witkamp, L. M. K. Vandersypen, *et al.*, Phys. Rev. Lett. **91**, 196802 (2003).
3. L. P. Kouwenhoven, D. G. Austing, and S. Tarucha, Rep. Prog. Phys. **64**, 701 (2001).
4. D. Goldhaber-Gordon, H. Shtrikman, D. Mahalu, *et al.*, Nature **391**, 156 (1998).
5. C. Balocco, A. M. Song, and M. Missous, Appl. Phys. Lett. **85**, 5911 (2004).
6. J. C. Blakesley, P. See, A. J. Shields, *et al.*, Phys. Rev. Lett. **94**, 067401 (2005).

7. B. E. Kardynal, A. J. Shields, M. P. O'Sullivan, *et al.*, Meas. Sci. Technol. **13**, 1721 (2002).
8. T. Kodera, W. G. van der Wiel, K. Ono, *et al.*, Physica E (Amsterdam) **22**, 518 (2004).
9. B. T. Miller, W. Hansen, S. Manus, *et al.*, Phys. Rev. B **56**, 6764 (1997).
10. K. H. Schmidt, G. Medeiros-Ribeiro, M. Oestreich, *et al.*, Phys. Rev. B **54**, 11346 (1996).
11. I. E. Itskevich, T. Ihn, A. Thornton, *et al.*, Phys. Rev. B **54**, 16401 (1996).
12. M. Narihiro, G. Yusa, Y. Nakamura, *et al.*, Appl. Phys. Lett. **70**, 105 (1997).
13. A. S. G. Thornton, T. Ihn, P. C. Main, *et al.*, Appl. Phys. Lett. **73**, 354 (1998).
14. E. E. Vdovin, A. Levin, A. Patane, *et al.*, Science **290**, 122 (2000).
15. I. Hapke-Wurst, U. Zeitler, H. Frahm, *et al.*, Phys. Rev. B **62**, 12621 (2000).
16. Yu. N. Khanin and E. E. Vdovin, Pis'ma Zh. Éksp. Teor. Fiz. **81**, 330 (2005) [JETP Lett. **81**, 267 (2005)].
17. K. H. Schmidt, M. Versen, C. Bock, *et al.*, Physica E (Amsterdam) **7**, 425 (2000); K. H. Schmidt, M. Versen, U. Kunze, *et al.*, Phys. Rev. B **62**, 15 879 (2000).
18. G. H. Kim, J. T. Nichols, S. I. Khondaker, *et al.*, Phys. Rev. B **61**, 10910 (2000).
19. N. Horiguchi, T. Futatsugi, Y. Nakata, and N. Yokoyama, Appl. Phys. Lett. **70**, 2294 (1997).
20. A. B. Fowler, A. Harstein, and R. A. Webb, Phys. Rev. Lett. **48**, 196 (1982).
21. A. K. Savchenko, V. V. Kuznetsov, A. Woolfe, *et al.*, Phys. Rev. B **52**, R17021 (1995).
22. C. W. J. Beenakker, Phys. Rev. B **44**, 1646 (1991).

Translated by E. Golyamina

JETP Letters, Vol. 82, No. 8, 2005, pp. 532–538. Translated from Pis'ma v Zhurnal Éksperimental'noĭ i Teoreticheskoĭ Fiziki, Vol. 82, No. 8, 2005, pp. 591–597.

EPR Study of Exchange Interactions of Manganese Ions in a $CdGeAs_2$ Matrix

S. V. Gudenko[a], B. A. Aronzon[a, c], and V. A. Ivanov[b]

[a] *Russian Research Centre Kurchatov Institute, pl. Kurchatova 1, Moscow, 123182 Russia*
e-mail: gudenko@imp.kiae.ru
[b] *Kurnakov Institute of General and Inorganic Chemistry, Russian Academy of Sciences, Leninskiĭ pr. 31, Moscow, 117907 Russia*
[c] *Institute of Theoretical and Applied Electrodynamics, Russian Academy of Sciences, Izhorskaya ul. 13/19, Moscow, 127412 Russia*

Received September 9, 2005

The results of an EPR study of the $CdGeAs_2$ compound doped with 6 at % Mn are reported. The experimental data are analyzed under the assumption that magnetic centers of the following two types are formed in the system: Mn_{Cd}, Mn ions that replace Cd^{2+} and have spin $S = 5/2$, and Mn_{Ge}, Mn ions that replace Ge^{4+} and form the $Mn^{2+} + 2p$ complex with two "heavy" holes with spin $S = 1/2$. The absence of signals from isolated centers and the Lorentzian shape of an absorption curve suggest a strong exchange narrowing of the spectrum and the extension of an isotropic exchange interaction involving Mn_{Ge} to distances much longer than the lattice parameter. It is found that the exchange interaction between $Mn^{2+} + 2p$ complexes is ferromagnetic, and it is stronger than the characteristic superexchange interaction involving Mn_{Cd} centers by three to four orders of magnitude. The form of the temperature dependence of susceptibility obtained by the double integration of spectra is indicative of the formation of nanoscale regions, which weakly interact with each other, with ferromagnetically ordered $Mn^{2+} + 2p$ complexes at ~250 K. © *2005 Pleiades Publishing, Inc.*

PACS numbers: 73.61.Le, 75.30.–m, 75.50.Pp, 76.30.–v, 85.75.–d

1. INTRODUCTION

Dilute magnetic semiconductors based on $A^{III}B^{V}$ and $A^{II}B^{IV}C_2^{V}$ matrices are the most promising families of materials for spintronics [1, 2]. This is due to the possibility of doping diamond-like matrices with transition metals (TMs = Mn, Fe, Cr, etc.) over a wide range, the high mobility of hole-type carriers, the high Curie temperatures, and the manufacturability of these materials as high-quality single crystals and films. Depending on the degree of doping, transition elements in a $A^{II}B^{IV}C_2^{V}$ matrix can occupy the positions of both Group II and Group IV elements in various proportions. For example, Zhao *et al.* [3] calculated that, upon the substitution of Mn^{2+} ions with spin $S_2 = 5/2$ for bivalent Cd and Zn in $CdGeP_2$ and $ZnGeP_2$ matrices, the ground state of the resulting compounds is antiferromagnetic. However, Medvedkin *et al.* [4, 5] experimentally found the reverse: under optimum doping conditions, the materials were found to be ferromagnets with high critical temperatures (320 and 350 K, respectively). The conceivable mechanisms of the appearance of ferromagnetic exchange in $A^{III}B^{V}$ dilute magnetic semiconductors have been considered [6–9]. It was found that ferromagnetism in *p*-type dilute magnetic semiconductors is due to a so-called kinematic exchange mechanism, which occurs by virtual transitions of *d* electrons between transition metal ions through unoccupied valence and impurity states near the top of the valence band. The application of the developed ideas to compounds based on $A^{II}B^{IV}C_2^{V}$ matrices demonstrated that the kinematic exchange occurs between $TM^{2+} + 2p$ complexes, which consist of a transition element at the position of a Group IV element and two "heavy" holes of the valence band. Because of the antiferromagnetic character of the exchange interaction of spin $S_2 = 5/2$ of the *d* electrons of TM^{2+} with the angular momentum of holes $S_p + S_p = 3/2 + 3/2 = 3$, the complex has the resulting spin $S_1 = 1/2$. Thus, ternary *p*-type dilute magnetic semiconductors based on $A^{II}B^{IV}C_2^{V}$ matrices should consist of two magnetic subsystems relatively weakly bound to one another: (1) the $TM^{2+} + 2p$ complexes at the positions of Group IV elements, which interact with each other by kinematic exchange, and (2) the local spins of TM^{2+} at the positions of Group II elements, which hypothetically interact with each other in an antiferromagnetic manner.

In this work, we studied the magnetic properties of the ternary compound $CdGeAs_2$ doped with manganese ($c = 6$ at %) using EPR spectroscopy because the form of the observed spectra was found highly sensitive to the character and intensity of exchange interactions. Previously [10], a procedure was developed for the syn-

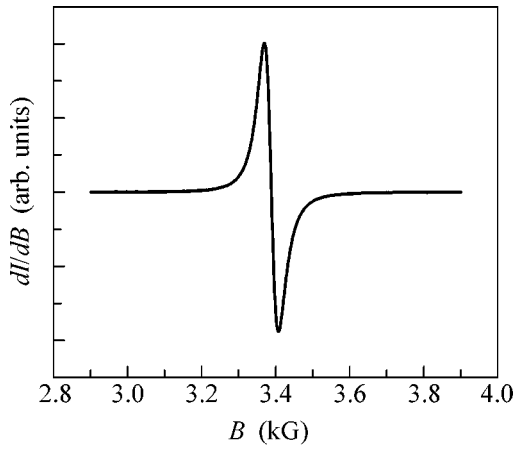

Fig. 1. EPR spectrum of Mn ions in a ground single crystal of $CdGeAs_2$: Mn 6 at % at $T = 290$ K and the frequency $\nu \cong 9.46$ GHz.

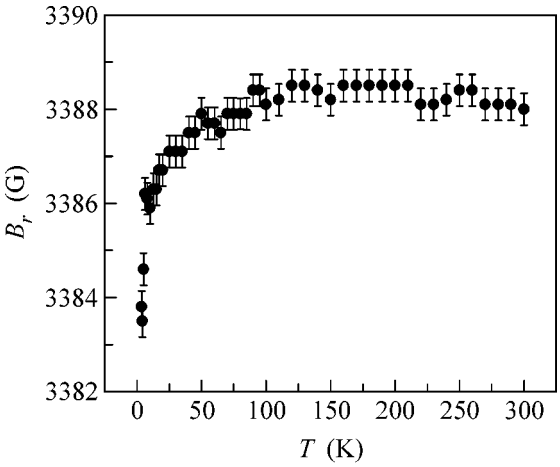

Fig. 2. Temperature dependence of the resonance field intensity in a ground single crystal of $CdGeAs_2$: Mn 6 at %.

thesis samples of this compound with manganese concentrations up to the boundary of a homogeneity region (≈34 at % Mn) and the magnetic and conducting properties of these samples were examined. It was found that the samples exhibited ferromagnetic properties at manganese concentrations higher than 6 at %; for example, the transition temperature was about 355 K for 18 and 34 at % Mn. The samples with lower manganese concentrations remained paramagnetic down to helium temperatures. The structurally and chemically similar chalcopyrite $ZnGeP_2$ with $c \approx 2$ at % Mn, which was studied by EPR spectroscopy, clearly exhibited fine and hyperfine structures due to isolated Mn^{2+} centers and $Mn^{2+} + p$ complexes. However, the concentration of manganese was found insufficient for the manifestation of interimpurity interactions in full measure [11]. We found experimentally that interimpurity interactions at a manganese concentration of about 6 at % resulted in dramatic changes in the EPR spectra. However, they were not adequately intense for causing the disappearance of an EPR signal due to a total phase transition to a magnetically ordered phase over the temperature range being studied. This allowed us to study the character of interimpurity exchange interactions, to evaluate their intensities, and to draw conclusions on the magnetic phase state of the system.

2. EXPERIMENTAL PROCEDURE

A single-crystal specimen of $CdGeAs_2$ doped with $c = 6$ at % Mn was grown by the directional crystallization from a melt using the vertical Bridgman technique. The single-phase composition of the specimen was controlled by x-ray powder diffraction analysis, which demonstrated the absence of ferromagnetic phases like Mn–As. The x-ray diffraction analysis of the sample under study showed that Mn atoms replaced both isovalent Cd^{2+} positions and the positions of tetravalent Ge^{4+} with approximately equal probabilities [10]. The Hall effect and thermoelectric power were measured in the single crystal. These measurements demonstrated that the specimen exhibited activation *p*-type conductivity with an activation energy of 175 MeV; the concentration and mobility of free charge carriers at room temperature were equal to 6.5×10^{15} cm^{-3} and 160 $cm^2\ s^{-1}\ V^{-1}$, respectively. Under these conditions, the penetration depth of an electromagnetic field with a frequency of ≈10 GHz was as small as fractions of a millimeter; that is, it was comparable to or even smaller than the size of the test single crystal. In this context, the EPR measurements were performed in both a single-crystal sample and a powder sample prepared by grinding a single crystal. The characteristic particle size of the powder was a few microns. To perform an experiment, the powder was placed in a quartz ampoule and then fixed in it with paraffin. Powdering was used for avoiding distortions in the EPR line shapes and susceptibility data because of the displacement of a high-frequency field from the sample with increasing temperature and, correspondingly, specific conductivity. A typical sample mass was 15–20 mg.

The EPR spectra were recorded on a Bruker ESP-300 spectrometer equipped with an Oxford Instruments helium flow cryostat. The first-order derivative of an absorption signal was measured. The measurements were performed at the frequency $\nu \cong 9.46$ GHz over a temperature range from 4 to 300 K.

3. RESULTS

Figures 1–4 show the experimental results. Figure 1 shows a spectrum at $T = 290$ K as an example. The absorption line shape for a powder sample was adequately described by a Lorentzian curve over the entire range of test temperatures. The peak ratio of the second-order derivative was close to 4. (Remember that

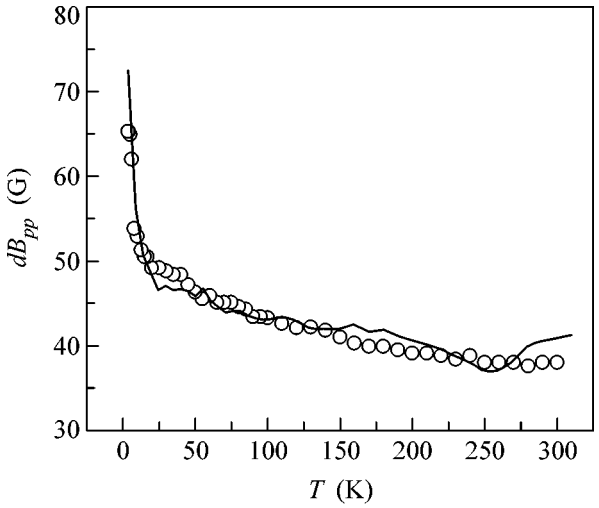

Fig. 3. Temperature dependence of the linewidth dB_{pp} in a ground single crystal of $CdGeAs_2$: Mn 6 at %: (○) experimental points (the accuracy of measurements is approximately equal to the size of a circle). The solid curve is plotted using Eq. (20) with the parameters G = 174 K and dB_0 = 20.5 G.

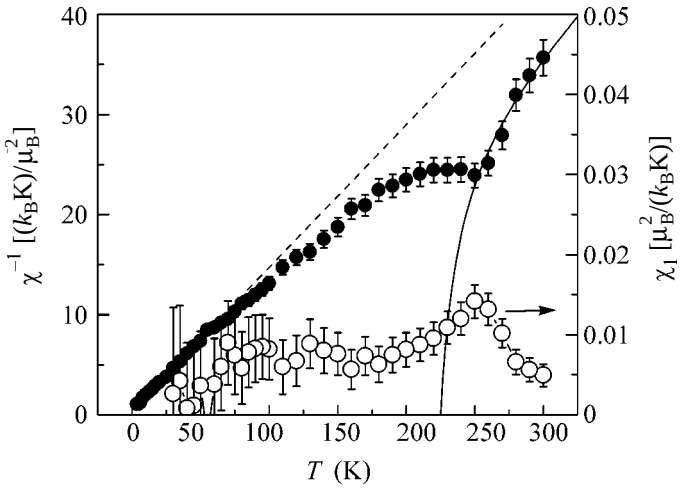

Fig. 4. Temperature dependence of (○) the inverse magnetic susceptibility χ^{-1} (per manganese ion) of a ground single crystal of $CdGeAs_2$: Mn 6 at %, (●) the susceptibility χ_1 of Mn_{Ge} centers, and (dashed curve) the inverse magnetic susceptibility χ_2^{-1} of Mn_{Cd} centers; the solid curve was plotted using Eq. (7) with the parameters x = 0.4, Θ_1 = 255 K, and Θ_2 = –3 K.

this ratio is equal to 2.24 or exactly 4 for a Gaussian or Lorentzian, respectively.) The line for a single-crystal sample also exhibited a near-Lorentzian shape; however, at temperatures higher than ≈200 K, it became not fully symmetrical and took features of a Dyson curve [12]. This was a circumstance that stimulated us to perform experiments with a powder sample, for which the penetration depth of a microwave field exceeds the characteristic particle size of the powder.

Figure 2 shows data on the resonance field B_r in a powder sample. The line position depended on temperature only slightly and corresponded to the spectroscopic splitting factor $g_{exp} = 1.994 \pm 0.001$. Only in the region below 20 K, the resonance field decreased by approximately 5 G, which corresponded to an increase in the g factor by $\Delta g_{exp} \approx 0.003$. The dependence of the resonance field intensity on the magnetic field orientation with respect to the crystallographic axes of a single-crystal sample was weak: the spread of the fields was no higher than a few gausses.

As the temperature was decreased, a monotonic increase in the line width was observed over the entire temperature range from ≈38 G at 300 K to ≈65 G at 5 K (see Fig. 3). To characterize the width, the distance dB_{pp} between the first-order derivative peaks along the field was chosen. In this case, as with the resonance field intensity, a change in the line width depending on the magnetic field orientation with respect to the crystallographic axes was also weak, and it did not exceed 1–2 G.

The magnetic susceptibility χ was obtained by double integration of the experimentally measured spectra. Figure 4 shows data on the inverse magnetic susceptibility χ^{-1} (henceforth, the value of χ per manganese ion in the units of $\mu_B^2/(k_B\,\mathrm{K})$ is used, where μ_B is the Bohr magneton, and k_B is the Boltzmann constant). It can be seen that its temperature dependence is noticeably different from the conventional Curie–Weiss law $\chi = C/(T - \Theta)$ and exhibits special features. As compared to the region of $T < 200$ K, the region of $T > 250$ K is characterized by a much higher temperature Θ but a much lower constant C.

4. DISCUSSION

In accordance with the concepts formulated in the Introduction, let us consider that two types of magnetic impurity centers are formed in the system under consideration. These are the Mn ions that occupy the places of Cd (Mn_{Cd}) and occur in a bivalent ($3d^5$)S state with the orbital angular momentum $L = 0$ and the resulting spin $S_2 = 5/2$ and the Mn ions that occupy the positions of tetravalent Ge^{4+} (Mn_{Ge}) and form the $Mn^{2+} + 2p$ complex with two heavy holes of the valence band with the resulting spin $S_1 = 1/2$. The Mn_{Cd} centers can participate in superexchange interactions with both one another and the Mn_{Ge} centers; ferromagnetic kinematic exchange is the predominant type of interactions between the Mn_{Ge} centers.

An axial deviation of the symmetry of a crystalline environment from purely cubic for ions with spin $S_2 = 5/2 > 1/2$ must result in the fine splitting of the spectrum

into five components. For example, for Mn ions in the structurally similar chalcopyrite $ZnGeP_2$: Mn (≈2 at %) [11], the magnitude of splitting between adjacent components was as high as 170 G, which corresponds to the crystal field constant $D \cong 10^{-2}k_B$ K for an interaction of the type

$$H_{CF} = -DS_z^2. \quad (1)$$

Moreover, each of the fine structure components was split into six hyperfine structure lines because of the interaction

$$H_{HF} = A\mathbf{SI} \quad (2)$$

with the ^{55}Mn nuclear moment $I = 5/2$. The constant $A \cong (0.7–0.8) \times 10^{-2}k_B$ K [13] is comparable with the value of D. Assuming that approximately a half of Mn ions substitute for Cd positions and occur in a state with spin $S_2 = 5/2$, we can readily estimate the second spectral moment due to dipole–dipole interaction $\hbar^2 M_{2dd} \approx 3 \times 10^{-5}(k_B\text{K})^2$ ($\hbar$ is Planck's constant) and the corresponding line broadening $dB_{ppdd} \approx 80–100$ G. However, we found experimentally (see Fig. 1) that neither fine and hyperfine structures nor dipole–dipole line broadening was observed in the test samples. Along with the Lorentzian line shape, this is indicative of a strong exchange narrowing of the spectrum. The absence of two different lines due to Mn_{Ge} and Mn_{Cd} centers also suggests that bottleneck conditions are fulfilled, that is, the spin–lattice relaxation rates are much lower than characteristic exchange frequencies [14].

Exchange interactions in the system under study can be represented in the following form:

$$H_{11} = -\sum_{i<j} J_{(11)ij}\mathbf{S}_{1i}\mathbf{S}_{1j}, \quad (3)$$

between the spins of Mn_{Ge};

$$H_{22} = -\sum_{i<j} J_{(22)ij}\mathbf{S}_{2i}\mathbf{S}_{2j}, \quad (4)$$

between the spins of Mn_{Cd};

$$H_{12} = -\sum_{i,j} J_{(12)ij}\mathbf{S}_{1i}\mathbf{S}_{2j}, \quad (5)$$

between the spins of Mn_{Ge} and Mn_{Cd}.

The summation in Eqs. (3)–(5) is over all of the possible pairs of interacting Mn ions; the subscripts 1 and 2 refer to Mn_{Ge} and Mn_{Cd} centers, respectively. In accordance with published data [6–9], let us consider that the characteristic constant of kinematic exchange (3) far exceeds the constants of interactions (4) and (5), that is,

$$J_{(11)} \gg |J_{(12)}| \approx |J_{(22)}|. \quad (6)$$

In this case, the magnetic susceptibility of the system in terms of the mean-field theory is taken as

$$\chi \cong \chi_1 + \chi_2 \cong \frac{xC_1}{T-\Theta_1} + \frac{(1-x)C_2}{T-\Theta_2}, \quad (7)$$

where x is the relative fraction of Mn_{Ge}; $C_1 = g_1^2 S_1(S_1 + 1)\mu_B^2/3k_B$ and $C_2 = g_2^2 S_2(S_2 + 1)\mu_B^2/3k_B$ are the Curie constants; and Θ_1 and Θ_2 are the Curie–Weiss temperatures such that $\Theta_1 \gg |\Theta_2|$. In accordance with the experimental data on the line position (see Fig. 2), the g-factor values can be considered to be $g_1 \cong g_2 \cong g_{exp} \cong 2$. The values of $x \cong 0.4$, $\Theta_1 \cong 225$ K, and $\Theta_2 \approx -3$ K can be estimated by an approximation of the experimental data on magnetic susceptibility in the region at $T > 250$ K using Eq. (7) (see Fig. 4).

Using the well-known relationship for the Curie–Weiss temperature [15]

$$\Theta = \frac{S(S+1)}{3k_B}\sum_j J_{ij} \quad (8)$$

and assuming that $J_{(11)ij} \neq 0$ only for z_{11} neighboring Ge sites, that is, $\sum_j J_{(11)ij} = cxz_{11}J_{(11)}$, we can estimate the averaged value

$$J_{(11)} = \langle J_{(11)ij}\rangle = 3k_B\Theta_1/cxz_{11}S_1(S_1+1) \cong 166k_B\Theta_1/z_{11} \cong 3.75\times 10^4 k_B\text{K}/z_{11}. \quad (9)$$

It can be seen that the value of $J_{(11)}$ is great: on the assumption that the interaction extends for $z_{11} \approx 300–1000$ Ge sites (see below), the value of $J_{(11)}/k_B$ can range from several tens to one hundred Kelvins or more.

As the temperature was decreased below $T \approx \Theta_1$, the temperature dependence of susceptibility dramatically changed. A redistribution of Mn ions between Cd and Ge sites with decreasing temperature is unlikely. Changes in the values of S_2 and C_2 are also unlikely because of a weak interaction between Mn_{Cd} ions. By this is meant that a Curie–Weiss approximation with the previous (high-temperature) parameters can be used for describing the temperature dependence of χ_2. On the other hand, the signs of ferromagnetic ordering would be expected to appear in the Mn_{Ge} system in this temperature region. Ignoring the interaction between Mn_{Ge} and Mn_{Cd} subsystems in view of expression (6), we can evaluate the susceptibility χ_1 under these conditions by subtracting the value of χ_2 from the experimentally measured total susceptibility χ. The temperature dependence of χ_1 thus obtained is also shown in Fig. 4. The curve exhibits a maximum at $T \cong 250$ K, and $\chi_1 \ll \chi_2$ at this point. As the temperature was decreased below 100–150 K, this inequality further enhanced: even by taking into account the measurement error, the

susceptibility values differed by one order of magnitude or more in this region. The shape of the $\chi_1(T)$ curve is similar to the temperature dependence of susceptibility in an antiferromagnet; however, the positive Curie–Weiss temperature Θ_1 in the high-temperature region precludes this possibility. Caprara *et al.* [16] demonstrated that the spatial concentration fluctuations of a magnetic impurity, which occur both statistically and as a consequence of intrinsic defects (for example, formed during the process of crystal growth), can result (with exchange interaction that rapidly decreases with distance) in the appearance of a local ferromagnetic order in nanoscale regions (ferromagnetic clusters) with decreasing temperature. In our case, the regions with an increased concentration of Mn_{Ge} centers can be formed due to an increase in the binding energy with decreasing distance between impurities because of an increase in the hopping integral for t_2 wave functions of *d* electrons through itinerant holes. The absolute value of the magnetic moment per Mn_{Ge} center at a maximum of the susceptibility χ_1 is $\mu_1 = \chi_1 B_r/x \cong 8.5 \times 10^{-3}\mu_B$, that is, no higher than a hundredth of a maximally possible value. By this is meant that the directions of magnetic moments in the regions under consideration are almost chaotically distributed in space. White [17] demonstrated that, in the case of the formation of magnetically ordered regions with the resulting spin $NS_1 > 1/2$ (N is an integer number), the low susceptibility of the system at temperatures lower than a critical value can be due to an anisotropy of interaction with crystal fields like (1).

To evaluate the exchange interaction constants (3)–(5) from experimentally measured Curie–Weiss temperatures and exchange-narrowed line widths, we should know, at least approximately, the numbers of neighboring sites (z_{11}, z_{12}, and z_{22}) occupied by Mn ions at which exchange interaction should be taken into consideration, that is, for which $J_{ij} \neq 0$. Taking into account the interactions between only nearest neighbors for our structure, we obtain $z_{11}^{(N)} = z_{22}^{(N)} = 4$ and $z_{12}^{(N)} = 8$ [10]. In this case, the probability that the Mn ion under consideration is isolated, that is, is not involved in interactions (3)–(5), is equal to $w^{(N)} \cong (1-c)^{4+8} \cong 0.5$. By this is meant that the EPR spectrum would necessarily exhibit fine and hyperfine structures, dipole–dipole broadening, and other peculiarities inherent in the spectrum of isolated Mn_{Cd} and Mn_{Ge} centers. However, as we can see, this is not observed. Consequently, the exchange interaction binds not only nearest neighbors. The sensitivity of measurements allowed us to state that the fraction of isolated centers was no higher than $\approx 10^{-3}$. Therefore, we can estimate the lowest values of z_{11} and z_{12}. Ignoring interaction (4), one can arrive at the inequality $(1-cx)^{z_{12}(z_{11})} \leq 10^{-3}$; therefore, for $x \cong 0.4$, we obtain $z_{11}\,(z_{12}) \geq 300$. In our opinion, this can be due to a large size of the hole orbits of Mn_{Ge} centers. The hole-orbit size can be evaluated from the well-known relation

$$R_h \approx R_B \varepsilon \frac{m_e}{m^*}, \tag{10}$$

where R_B is the Bohr radius, ε is the dielectric constant, m^* is the effective mass of holes, and m_e is the free electron mass. For typical values of $\varepsilon \approx 18$ and $m^* \approx (0.3–0.4)m_e$ [2, 18], this gives $R_h \approx$ (23–30) Å. The volume per formula unit for $CdGeAs_2$ is $V_\mu \cong 100$ Å^3 [10]. Assuming that ions with overlapping electron shells participate in exchange interaction, we can readily estimate the values of $z_{12} \approx z_{11} \approx 4\pi R_h^3/3V_\mu \approx 500–1000 > 300$, which are consistent with values estimated previously based on the assumption that the fraction of isolated centers is small. (This range (300–1000) of z_{11} was used above for estimating the value of $J_{(11)}$.) It can be seen that

$$z_{11}, z_{12} \gg z_{22} \approx z_{22}^{(N)} = 4. \tag{11}$$

Note that the number of occupied centers that really participate in the interaction, for example, $cxz_{11} \cong 7–24$, is comparable with the characteristic number of nearest neighbors in the simplest lattices.

Huber *et al.* [19] demonstrated that, ignoring spin–lattice relaxation, the temperature dependence of the exchange-narrowed linewidth is expressed by the equation

$$dB_{pp}(T) = \frac{\chi_0(T)}{\chi(T)} dB_{pp}(\infty). \tag{12}$$

Here, $\chi_0(T) = C/T = [xC_1 + (1-x)C_2]/T$ is the susceptibility of noninteracting ions; $\chi(T) = \chi_{exp}(T)$ is the experimentally observed susceptibility; $dB_{pp}(\infty)$ is the exchange-narrowed line width at the high-temperature limit, that is, under conditions where the majority of Hamiltonian eigenvalues for exchange interactions between spins under consideration (in our case, these are interactions (3)–(5)) are much smaller than k_BT. Under bottleneck conditions, a contribution from various ions to the line width in the case of single-ion broadening mechanisms is proportional to the partial susceptibility [14]:

$$dB_{pp}(\infty) \cong \frac{\hbar}{g\mu_B} \times \left[\frac{xC_1}{C}\alpha^{(1)}\frac{M_2^{(1)}}{\omega_{ex(1)}} + \frac{(1-x)C_2}{C}\alpha^{(2)}\frac{M_2^{(2)}}{\omega_{ex(2)}}\right], \tag{13}$$

where $M_2^{(i)}$ and $\omega_{ex(i)}$ are the second spectral moment and the exchange frequency for ith ions, respectively; $\alpha^{(1)} \approx \alpha^{(2)} \approx 1$ are coefficients. The characteristic exchange frequencies $\omega_{ex(i)}$ can be approximately eval-

uated in terms of the sums of squares of exchange integrals for a given center [20, 21]:

$$\hbar^2\omega_{ex(1)}^2 \approx S_1(S_1+1)\left(\sum_j J_{(11)ij}^2 + \sum_j J_{(12)ij}^2\right), \quad (14)$$

$$\hbar^2\omega_{ex(2)}^2 \approx S_2(S_2+1)\left(\sum_j J_{(22)ij}^2 + \sum_j J_{(12)ij}^2\right). \quad (15)$$

With consideration for relationships (6) and (11), expressions (14) and (15) for exchange frequencies take the forms

$$\hbar^2\omega_{ex(1)}^2 \approx S_1(S_1+1)cxz_{11}J_{(11)}^2, \quad (14a)$$

$$\hbar^2\omega_{ex(2)}^2 \approx S_2(S_2+1)cxz_{12}J_{(12)}^2, \quad (15a)$$

respectively, where $J_{(11)}^2$ and $J_{(12)}^2$ denote the rms values of exchange integrals over all of the neighbors that participate in the interaction. By virtue of relationships (6) and (11),

$$\omega_{ex(1)} \gg \omega_{ex(2)}. \quad (16)$$

The contribution to the second moment due to hyperfine interaction (2) is determined by the well-known expression

$$\hbar^2 M_{2HF} \cong \frac{1}{3}I(I+1)A^2 \approx (1.5\text{–}1.9)\times 10^{-4}(k_B\text{K})^2, \quad (17)$$

where the above value of constant A was taken. It is well known that hyperfine interaction constants depend on the state of the ion only slightly; therefore, it is believed that $M_{2HF}^{(1)} \cong M_{2HF}^{(2)}$. The contribution to the second moment due to the uniaxial anisotropy of a crystal field of type (1) can be evaluated for a chaotic spread of the crystallite axes of a powdered sample using the relation [19]

$$\hbar^2 M_{2CF} \approx \frac{1}{2}\left[S(S+1) - \frac{3}{4}\right]D^2. \quad (18)$$

This contribution was absent from Mn_{Ge} centers with $S_1 = 1/2$. For Mn_{Cd} ions with $S_2 = 5/2$, the value of $\hbar^2 M_{2CF}^{(2)} \approx 4\times 10^{-4}(k_B\text{K})^2$ was estimated on the assumption that the crystal field constant is close to that obtained by Baranov *et al.* [11]. It can be seen that, first, the contributions of M_{2HF} and $M_{2CF}^{(2)}$ are comparable and, second, these contributions are considerably (by an order of magnitude) higher than the contribution of dipole–dipole interaction to the second moment. Thus, the assumption of a single-ion mechanism of line broadening is properly justified.

In expression (13) for the line width $dB_{pp}(\infty)$, $x \approx 1 - x$, $C_1 \ll C_2$, $\omega_{ex(1)} \gg \omega_{ex(2)}$, $\alpha^{(1)} \approx \alpha^{(2)}$, and $M_2^{(2)} = M_{2CF}^{(2)} + M_{2HF} > M_2^{(1)} = M_{2HF}$; whence it follows that the first term within the square brackets can be ignored with a good accuracy. With consideration for expressions (15a), (17), and (18), Eq. (12) for the temperature dependence of line width is rearranged to the form

$$dB_{pp}(T) \cong \frac{\alpha^{(2)}}{g\mu_B}\frac{(1-x)C_2}{T\chi_{exp}(T)}\frac{\hbar^2(M_{2CF}^{(2)} + M_{2HF}^{(2)})}{\sqrt{S_2(S_2+1)cxz_{12}}|J_{(12)}|} \approx \frac{3.4\times 10^5}{T\chi_{exp}(T)}\frac{1.3D^2 + A^2}{k_B\sqrt{z_{12}}|J_{(12)}|}\ (\text{G}). \quad (19)$$

In accordance with derived expression (19), the experimental data on the line width were approximated by the function of other experimental quantities (susceptibility and temperature)

$$dB_{pp}(T) = \frac{G}{T\chi_{exp}(T)} + dB_0, \quad (20)$$

where the term $dB_0 \cong$ const describes line broadening caused by all of the other mechanisms that were not taken into account in our model. The best fit was observed at $G = 174$ K and $dB_0 = 20.5$ G (see Fig. 3). It can be seen that curves are consistent with each other at these parameters. Now, with the use of expression (19), the estimated number z_{12}, and the above values of D and A, we can readily obtain the characteristic exchange constant $|J_{(12)}| \approx (1.5\text{–}2.5)\times 10^{-2}k_B$K. As expected, this value is much lower (by three or four orders of magnitude) than $J_{(11)}$.

5. CONCLUSIONS

The experimental study of a $CdGeAs_2$ based dilute magnetic semiconductor demonstrated that exchange interactions play an important role in the formation of the EPR spectrum of Mn impurity centers at a concentration of 6 at % or higher. The intensity and degree of long-range interactions in the system under study were found sufficient for the involvement of almost all centers in the formation of an exchange-narrowed line. This resulted in the absence of any signs of fine and hyperfine structures and dipole–dipole broadening from the observed spectrum. An analysis of the temperature dependence of the line width and susceptibility was performed based on the assumption that two types of manganese ions, which replaced the positions of cadmium (Mn_{Cd}) and germanium (Mn_{Ge}), are formed in the system. The behavior of the temperature dependence of the susceptibility considered in the framework of mean-field theory allowed us to evaluate the relative fractions of Mn_{Cd} and Mn_{Ge} centers (0.6 and 0.4, respectively), and the characteristic value of the Mn_{Ge}–Mn_{Ge} exchange interaction $J_{(11)} \approx (30\text{–}120)k_B$ K. It is likely that a maximum in the temperature dependence of the susceptibility of Mn_{Ge} centers suggests the formation of a local ferromagnetic order in nanoscale regions (mag-

netic nanoclusters) at $T \approx 250$ K. The experimental data on the line width and susceptibility were found related by Eq. (20); the Mn_{Ge}–Mn_{Cd} exchange interaction value of $|J_{(12)}| \approx (1.5–2.5) \times 10^{-2} k_B$ K $\ll J_{(11)}$ can be estimated from the parameters of this equation. The absence of signals due to isolated manganese ions suggests that the exchange interaction radius is much greater than the lattice parameter. This is consistent with the interaction radius estimated on the assumption of the overlapping of the hole orbits of Mn_{Ge} centers of size $R_h \approx (23–30)$ Å.

Experimental results supported the hypothesis that a strong indirect ferromagnetic exchange interaction between transition ions in a semiconductor matrix with a relatively low concentration of free carriers can occur under certain conditions. These results count in favor of the kinematic exchange interaction proposed previously [6–9] to describe the magnetic properties of dilute magnetic semiconductors.

We are grateful to S.F. Marenkin and S.G. Mikhaĭlov for providing us with the single crystal. This work was supported by the Russian Foundation for Basic Research (project nos. 04-02-19964, 05-02-17666, and 05-02-17021).

REFERENCES

1. H. Ohno, Science **291**, 840 (2001).
2. V. A. Ivanov, T. G. Aminov, V. M. Novotortsev, and V. T. Kalinnikov, Izv. Ross. Akad. Nauk, Ser. Khim., No. 11, 2255 (2004) [Russ. Chem. Bull. **53**, 2357 (2004)].
3. Y. H. Zhao, W. T. Geng, A. J. Freeman, and T. Oguchi, Phys. Rev. B **63**, 201202 (2001).
4. G. A. Medvedkin, T. Ishibashi, T. Nishi, *et al.*, Jpn. J. Appl. Phys. **39**, L949 (2000).
5. G. A. Medvedkin, K. Hirose, T. Ishibashi, and K. Hiyata, J. Cryst. Growth **236**, 609 (2002).
6. P. M. Krstajić, F. M. Peeters, V. A. Ivanov, *et al.*, Phys. Rev. B **70**, 195215 (2004).
7. V. A. Ivanov, P. M. Krstajić, F. M. Peeters, *et al.*, Physica B (Amsterdam) **329**, 1282 (2003).
8. P. M. Krstajić, V. A. Ivanov, F. M. Peeters, *et al.*, Europhys. Lett. **61**, 235 (2003).
9. V. Fleurov, K. Kikoin, V. A. Ivanov, *et al.*, J. Magn. Magn. Mater. **272–276**, 1967 (2004).
10. V. M. Novotortsev, V. T. Kalinnikov, L. I. Koroleva, *et al.*, Zh. Neorg. Khim. **50**, 592 (2005) [Russ. J. Inorg. Chem. **50**, 492 (2005)].
11. P. G. Baranov, S. I. Goloshchapov, G. A. Medvedkin, and V. G. Voevodin, Pis'ma Zh. Éksp. Teor. Fiz. **77**, 686 (2003) [JETP Lett. **77**, 582 (2003)].
12. F. J. Dyson, Phys. Rev. **98**, 349 (1955).
13. S. A. Al'tshuller and B. M. Kozyrev, *Electron Paramagnetic Resonance in Compounds of Transition Elements* (Nauka, Moscow, 1972; Halsted, New York, 1975).
14. S. E. Barnes, Adv. Phys. **30**, 801 (1981).
15. S. V. Vonsovskiĭ, *Magnetism* (Nauka, Moscow, 1971; Wiley, New York, 1974).
16. S. Caprara, V. V. Tugushev, and N. K. Chumakov, JETP **101**, 305 (2005).
17. R. M. White, *Quantum Theory of Magnetism* (Springer, Berlin, 1983; Mir, Moscow, 1985).
18. G. D. Holah, A. Miller, W. D. Dunnett, and G. W. Iseler, Solid State Commun. **23**, 75 (1977).
19. D. L. Huber, G. Alejandro, A. Caneiro, *et al.*, Phys. Rev. B **60**, 12 155 (1999).
20. J. E. Gulley and V. Jaccarino, Phys. Rev. B **6**, 58 (1972).
21. J. E. Gulley, D. Hone, D. J. Scalapino, and B. G. Silbernagel, Phys. Rev. B **1**, 1020 (1970).

Translated by V. Makhlyarchuk

JETP Letters, Vol. 82, No. 8, 2005, pp. 539–543. From Pis'ma v Zhurnal Éksperimental'noĭ i Teoreticheskoĭ Fiziki, Vol. 82, No. 8, 2005, pp. 598–602.

Experimental Investigation of the Edge States Structure at Fractional Filling Factors¶

E. V. Deviatov[a, *], V. T. Dolgopolov[a], A. Lorke[b], W. Wegscheider[c], and A. D. Wieck[d]

[a] *Institute of Solid State Physics, Russian Academy of Sciences, Chernogolovka, Moscow region, 142432 Russia*
**e-mail: dev@issp.ac.ru*

[b] *Laboratorium für Festkörperphysik, Universität Duisburg–Essen, Lotharstr. 1, D-47048 Duisburg, Germany*

[c] *Institut für Angewandte und Experimentelle Physik, Universität Regensburg, 93040 Regensburg, Germany*

[d] *Lehrstuhl für Angewandte Festkörperphysik, Ruhr-Universität Bochum, Universitätsstrasse 150, D-44780 Bochum, Germany*

Received September 22, 2005

We experimentally study the electron transport between edge states in the fractional quantum Hall effect regime. We find an anomalous increase of the transport across the 2/3 incompressible fractional stripe in comparison with the theoretical predictions for the smooth edge potential profile. We interpret our results as a first experimental demonstration of the intrinsic structure of the incompressible stripes arising at the sample edge in the fractional quantum Hall effect regime. © *2005 Pleiades Publishing, Inc.*

PACS numbers: 71.30.+h, 73.40.Qv

The concept of the edge states (ESs) was first introduced by Halperin [1] to describe the transport phenomena in two-dimensional (2D) systems in the integer quantum Hall effect regime. ES, arising at the intersections of distinct Landau levels with a Fermi level, can be introduced for both sharp [2] and smooth [3] edge potential profiles. Experimentally, the existence of ES was proved not only in transport experiments along the sample edge (for a review, see [4]) but also across it [5–7].

This single-electron description is not applicable to the fractional quantum Hall effect, which is fundamentally a many-body phenomenon [8]. The electron system forms a many-body ground state below the Fermi level and an excited state above it. A set of compressible stripes, separated by the incompressible regions with fractional fillings, is expected to exist at the sample edge for the case of the smooth edge potential [9]. One-dimensional chiral Luttinger liquid states are predicted theoretically for the opposite case of the sharp potential jump at the sample edge [10, 11]. The ES structure in the later case was found to be determined by the hierarchical structure [12] of the bulk ground state [10, 11]. The transport along the sample edge, however, is not sensitive to the form of the edge potential but only to the filling factor in the bulk. It can be described by modified Buttiker formulas [9, 10] in good agreement with experiments [13] in Hall-bar geometry with cross gates. For this reason, these experiments cannot be used to distinguish between the proposed models. In real experiments, the strength of the potential profile cannot be regarded as infinitely large, so the model of the smooth edge potential seems to be more realistic. On the other hand, experiments on tunneling into the fractional edge demonstrate the complicated structure of the edge excitation spectrum [14, 15], which is expected for the sharp edge [11]. This controversial situation demands the investigation of the fractional ES structure for real samples.

It was shown theoretically [16] that, after smoothening the sharp edge potential, a transition takes place and new branches of ESs appear. For example, the edge that had one right-moving ES before the transition has two right-moving ESs and one left-moving ES after it. The same prediction about the edge reconstruction with smoothing the edge potential was made using the composite-fermion language [17]. Experimentally, the edge reconstruction picture can be verified by studying the electron transport across the sample edge in the quasi-Corbino geometry, because this experiment was shown to be very sensitive to the ES structure [18].

Here, we experimentally study the electron transport between different ES in the fractional quantum Hall effect regime. We find an anomalous increase of the transport, at some filling factors, in comparison with the prediction of the simple Beenakker model [9] of fractional ES. We interpret our results as the first experimental demonstration of the intrinsic structure of the incompressible stripes arising at the reconstructed sample edge in the fractional quantum Hall effect regime in accordance with the model of Wen and Chamon [16].

Our samples are fabricated from two molecular beam epitaxial-grown GaAs/AlGaAs heterostructures

¶ The text was submitted by the authors in English.

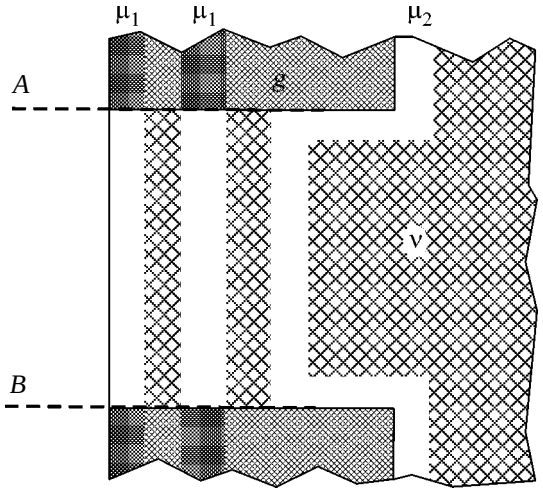

Fig. 1. Schematic diagram of the gate-gap region in the pseudo-Corbino sample geometry. The dark area represents the Schottky-gate. The hatched area indicates incompressible regions in the sample. In a quantizing magnetic field at total filling factor ν, one set of the edge states (the number is equal to the filling factor under the gate, g; $g < \nu$) is propagating under the gate along the etched edge of the sample and carry the electrochemical potentials μ_1. The other edge states (their number is $\nu - g$) are going along the gate edge and carry electrochemical potentials μ_2. In the gate-gap region, both sets of the edge states are running in parallel, leading to the current across the incompressible region between them, if $\mu_1 \neq \mu_2$.

with different carrier concentrations and mobilities. One of them (*A*) contains a two-dimensional electron gas (2DEG) located 210 nm below the surface. The mobility at 4 K is 1.93×10^6 cm^2/(V s), and the carrier density is 1.61×10^{11} cm^{-2}. For heterostructure *B*, the corresponding parameters are 150 nm, 1.83×10^6 cm^2/(V s), and 8.49×10^{10} cm^{-2}.

The measurements are performed in the quasi-Corbino sample geometry [5, 6]. In this geometry, a sample has two nonconnected etched mesa edges (the inner and the outer ones, as Corbino disks) with independent ohmic contacts at every edge. ES originating from one mesa edge are redirected to the other mesa edge by using the split-gate technique. As a result, ES from independent ohmic contacts run together along the outer etched edge of the sample in the gate-gap region as depicted in Fig. 1. The gate-gap width (*AB*) is 5 μm for samples from wafer *A* and 0.5 μm for ones from wafer *B*. The available fractional filling factors and the electron concentration in the ungated region were obtained from the usual magnetoresistance measurements. Also, magnetocapacitance measurements were performed to characterize the electron system under the gate. The contact resistance at low temperatures is about 100 Ω per contact, as was determined from two-point magnetoresistance measurements. The temperature of the experiment is 80 mK; the magnetic field is up to 14 T.

We studied the *I–V* characteristics of the gate-gap region by applying dc voltage between the outer and the inner ohmic contacts and by measuring the dc current that appeared. In the integer quantum Hall effect regime, the dissipative conductance component is close to zero in the 2DEG. For this reason, the measuring current is the current between two groups of independently-contacted ES in the gate-gap (see Fig. 1). If the equilibration length for the transport between them is smaller than the gate-gap width, we can expect a full equilibration in the gate-gap and a linear *I–V* trace. In the opposite regime, charge transfer does not change the chemical potentials of the ES significantly, and the applied voltage V directly affects the value of the potential barrier between the ES, thus, leading to its disappearance at some positive voltage $V_{th} > 0$ (because of the negative electron charge). The zero potential barrier means zero equilibration length between the ES. Thus, in spite of the strongly nonlinear *I–V* trace in this case, a positive branch above V_{th} has to be linear as in the opposite regime. It was experimentally established [5, 6] that V_{th} and the slope of the linear part of the positive branch are universal characteristics reflecting the potential barrier value between ES and the redistribution of the electrochemical potential imbalance between them. They coincide with the theoretical values (the spectral gap and the equilibrium redistribution obtained from Buttiker formulas [2]) with a possible 10% deviation. This 10% deviation is connected to the potential disorder at the sample edge and is a constant for the given sample. It does not depend on the cooling procedure and other occasional parameters.

Typical *I–V* curves in the integer quantum Hall effect regime are shown in Fig. 2 for the filling factor combination $\nu = 2$, $g = 1$. The *I–V* traces reflect the electron transport between two spin-split edge states, because, at $\nu = 2$, two spin-split energy levels are filled in the bulk. The equilibration length in this case can reach a millimeter [19], which is much higher than the gate-gap width for both samples *A* and *B*. Every experimental *I–V* trace is strongly nonlinear with the linear part on the positive branch. Tilting the sample plane with respect to the magnetic field allows us to introduce an in-plane field component, keeping the filling factor by adjusting the value of the total field. As can be seen from Fig. 2, in-plane field affects affect the linear part of *I–V* only by increasing the V_{th} value, leaving the slope to be nonaffected. We can conclude for our samples that the in-plane magnetic field does not change the equilibrium mixing of ES in the integer quantum Hall effect regime.

Examples of the *I–V* curves for fractional fillings are shown in Fig. 3 for $\nu = 2/3$, $g = 1/3$. As it can be seen from the inset to the figure, the *I–V* curve is strongly nonlinear at the lowest temperature of 30 mK for the sample *B* with the smallest gate-gap width 0.5 μm (also, nonlinear *I–V*'s for fractional fillings were reported in [20]). By increasing the temperature and the

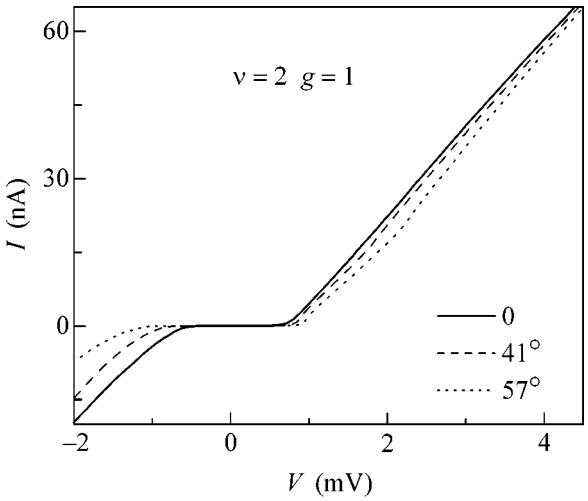

Fig. 2. *I–V* curves for the sample *A* for filling factors ν = 2 and $g = 1$ at different tilt angles: θ = 0 (solid line), θ = 41° (dashed line), θ = 57° (dotted line). Experimental slope of the positive branch is constant and equals to $2.2h/e^2$, the equilibrium Buttiker value is $2h/e^2$. Perpendicular magnetic field equals to 3.34 T, gate voltage $V_g = -268$ mV.

gate-gap width (80 mK and 5 μm for sample *A*), the equilibration length between the fractional ES can be made smaller than the gate-gap width, thus, leading to the fully linear *I–V* (see the main part of Fig. 3). In this letter, we focus our attention on the analysis of the linear *I–V* curves at fractional filling factors.

The most intriguing results are obtained for the following filling factor combinations: ν = 1, $g = 1/3$ and ν = 1, $g = 2/3$. In Fig. 4, the experimental slopes of the linear *I–V* curves are shown in dependence on the sample tilt angle in the magnetic field. The slopes for ν = 1, $g = 1/3$ behave as in the integer case: they are practically independent of the in-plane field. The experimental values for ν = 1, $g = 2/3$ differ significantly from the ones for ν = 1, $g = 1/3$ in the normal field and approach them with increasing the in-plane field component (see Fig. 4). It can also be seen from the inset in Fig. 4, where the original *I–V* curves for different tilt angles are shown for the filling factor combination ν = 1, $g = 2/3$. Let us stress that curves *I–V* are well reproducible.

Because the gate-gap region in our quasi-Corbino geometry is formed electrostatically by using the split-gate, it is obvious to use the Beenakker model [9] of fractional ES in the smooth edge profile to describe the experiment. In this model, the edge potential is supposed to be smooth enough to introduce the local filling factor ν_c. At the sample edge, it is monotonically changing from the bulk value ν = 1 to zero. Incompressible stripes are formed around fractional local filling factors $\nu_c = 2/3$ and 1/3. Buttiker formulas can easily be generalized to this situation [9]:

$$I_\alpha = \frac{e}{h}\nu_\alpha\mu_\alpha - \frac{e}{h}\sum_\beta T_{\alpha\beta}\mu_\beta,$$

where I_α is the current in the ES α corresponding to the fractional filling factor ν_α and connected to a contact

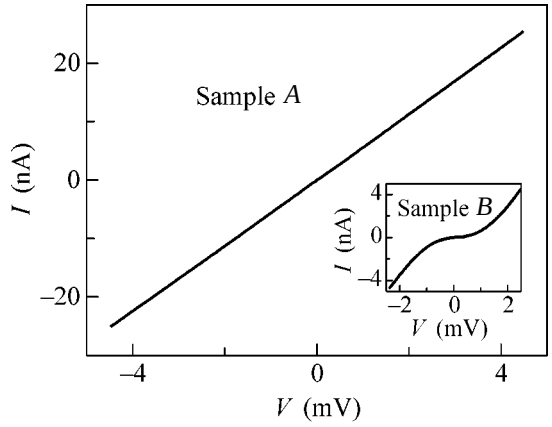

Fig. 3. *I–V* curves for the samples *A* (main field) and *B* (inset) for filling factors ν = 2/3 and $g = 1/3$. Magnetic field equals to 10 T for the sample *A* and to 4.85 T for the sample *B*. The gate-gap width and the temperature of the experiment are different for both samples: 5 μm and 80 mK for the sample *A* and 0.5 μm and 30 mK for the sample *B*. The experimental slope of the linear *I–V* curve is $6.8h/e^2$, the equilibrium Buttiker value is $6h/e^2$.

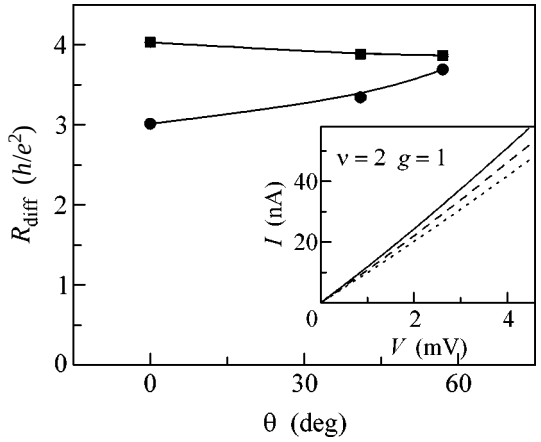

Fig. 4. Experimental slopes of linear *I–V* curves for the sample *A* for filling factor combinations ν = 1 and $g = 1/3$ (squares) and ν = 1 and $g = 2/3$ (circles) as functions of tilt angle. Error bars are within the symbol size. The equilibrium Buttiker value is $4.5h/e^2$ for both filling factor combinations. The normal magnetic field is constant and equals to 6.68 T. Inset shows the original *I–V* curves for filling factors ν = 1 and $g = 2/3$ at different tilt angles: θ = 0 (solid line), θ = 41° (dashed line), θ = 57° (dotted line). *I–V* curves are independent of the cooling cycle and well reproducible.

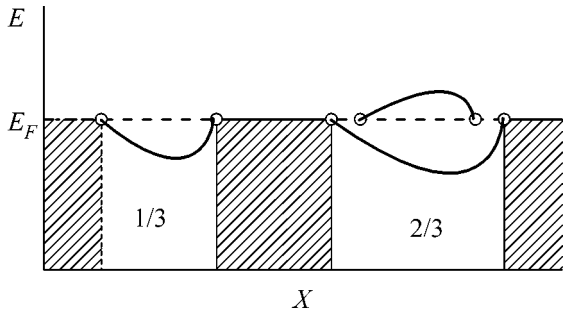

Fig. 5. Schematic energy diagram of the sample edge in the fractional quantum Hall effect regime. Hatched regions represent compressible stripes with electrons at the Fermi level. In the incompressible "puddles" between them, the energy of the fractional ground state is sketched (it is asymmetric because of the edge potential). It is a simple Laughlin fractional ground state for the puddle with 1/3 local filling factor. The ground state for the 2/3 local filling is more complicated: it is electron ground state for the filling factor 1 and hole fractional for the filling factor 1/3. It leads to the two counterpropagating branches of ES per edge of this puddle. ES are denoted by open circles.

with electrochemical potential μ_α; e and h are the electron charge and the Planck constant, respectively; and $T_{\alpha\beta}$ are the Buttiker coefficients for the transmission from contact β to contact α.

This formula can easily be applied to our experimental geometry, while the only difference from the integer case is the presence of constant weight coefficients ν_α. Slopes of the linear *I–V* curves can be calculated under the assumption of full equilibration between all the ES in the gate-gap:

$$R_{\text{diff}} = \frac{h}{e^2}\frac{\nu}{g(\nu - g)}.$$

Correspondingly, we can expect that, as for integer ES, (i) the linear curve *I–V* means the full equilibration between ES in the gate-gap; (ii) the experimental slopes should coincide with the calculated ones within 10%, as was discussed above; (iii) these slopes should be independent of the in-plane magnetic field component, as presented in Fig. 2. Moreover, we can expect from the calculations that slopes *I–V* for the filling factor combinations $\nu = 1$, $g = 1/3$ and $\nu = 1$, $g = 2/3$ will coincide exactly. In the experiment, however, the former filling factor combination (as well as $\nu = 2/3$, $g = 1/3$) behaves as described, while the *I–V* slope for $\nu = 1$, $g = 2/3$ is 1.5 times smaller than the theoretical value, approaching the values for $\nu = 1$, $g = 1/3$ with increasing the in-plane field component. Thus, we can conclude that electron transport at $\nu = 1$, $g = 2/3$ is anomalously enhanced in comparison with the equilibrium electrochemical potential redistribution, while, at $\nu = 1$, $g = 1/3$, it is about the theoretical value. For these two filling factor combinations, the filling factor in the gate-gap $\nu = 1$ is the same as well as the other parameters of the sample edge (the potential profile, disorder, etc.). The only difference is the incompressible stripe, which separates the ES from the inner and outer contacts in the gate-gap: it corresponds to $\nu_c = 2/3$ for $\nu = 1$, $g = 2/3$ and to $\nu_c = 1/3$ for $\nu = 1$, $g = 1/3$.

This behavior cannot be explained within the model of Beenakker, where the local filling factor $\nu_c = 2/3$ has no difference from any other one. On the other hand, 2/3 has a very special character in the model of sharp edge potential profile of MacDonald [10]. Here, $\nu = 2/3$ is regarded as the electron ground state of the filling factor 1 and the Laughlin hole fractional one with the positive fractional charge 1/3. Both ones make their contributions into the ES formation, thus, leading to two counter propagating ES at one edge: the outer integer for electrons and the inner fractional for holes. This model cannot be directly applied to our experiment, because the electrostatical edges in any case are not sharp and even etched ones are very doubtful. It was predicted [16, 17] that, while smoothing the edge profile, edge reconstruction occurs and quantum Hall "puddles" form with local fractional filling factors (see Fig. 5). Each boundary of the fractional quantum Hall puddle still can be regarded as a sharp boundary of the quantum Hall system with a particular fractional filling factor. This leads to the formation of a number of counterpropagating fractional ES at every sample edge. Of course, the net current along the edge is still dependent on the bulk filling factor only, so in our experiment, the detailed structure of the ES is important only in the gate-gap, where the charge transfer across the edge occurs. Also, the etched edge seems to be sharp enough to apply this model of reconstructed ES.

Let us consider the filling factor combination $\nu = 1$, $g = 2/3$. At low temperatures, the bulk of the sample is in the incompressible state at filling factor $\nu = 1$ in the ungated region and at $g = 2/3$ under the gate. Approaching the etched edge, incompressible "puddles" of lower fractional fillings are formed (see Fig. 5). In the gate-gap, they correspond to $\nu_c = 2/3$; 1/3, while only $g_c = 1/3$ is present under the gate. It is clear that an incompressible puddle with $\nu_c = 2/3$ in the gate-gap is directly connected to the incompressible state $g = 2/3$ under the gate, while the puddles $\nu_c = 1/3$ and $g_c = 1/3$ form the incompressible stripe along the etched edge as is shown in Fig. 1. It means that the picture of compressible and incompressible states, presented in Fig. 1, still survive in the fractional quantum Hall regime, but the structure of the ES is very different. Fractional ES are formed at the edges of every incompressible puddle. The current across the sample edge can flow only by tunneling between these ES through the incompressible regions and by diffusion in the compressible ones. At the filling factor combination $\nu = 1$, $g = 2/3$, the tunneling in the gate-gap takes place across the 2/3 incompressible puddle (see Figs. 1, 5). As it is described above, fractional ES at every edge of the puddle with $\nu_c = 2/3$ are the

counterpropagating electron integer ES with current $\mu_\alpha \frac{e}{h}$ and the hole fractional with current $-\frac{1}{3}\mu_\alpha \frac{e}{h}$, thus, leading to the sum current $\frac{2}{3}\mu_\alpha \frac{e}{h}$ per one edge (see Fig. 5). Because of the complex nature of the ES for $\nu_c = 2/3$, they are not far away from each other, and we can expect that only these ES are mixing their electrochemical potentials in the gate-gap. A simple calculation gives in this case the resistance of $3h/e^2$. It is 1.5 times smaller than it would be if all the ES in the gate-gap mixed their electrochemical potentials and is in fact observed in the experiment in normal magnetic fields (see Fig. 4). The in-plane magnetic field increases the fractional gaps (it was verified for our samples by the usual magnetocapacitance spectroscopy) transforming fractional quantum Hall puddles into stripes of significant width. It makes the proposed mechanism ineffective, and the only way is to mix the electrochemical potentials of all the ES in the present gate-gap, as in the Beenakker model. As a result, the differential resistance increases to the value of $9/2\ h/e^2$. About the other fillings under consideration, $\nu = 1$, $g = 1/3$ and $\nu = 2/3$, $g = 1/3$; tunneling should occur between the ES in the $\nu_c = 1/3$ quantum Hall puddle. There is no complex ES structure in this case and the ES are far away from each other. The proposed mechanism is ineffective and mixing between all the existing ES in the gate-gap takes place at any in-plane field, as we observe in the experiment (see Figs. 3, 4).

As a result, we studied the electron transport across the sample edge in the fractional quantum Hall effect regime in the quasi-Corbino sample geometry. At the filling factor combination $\nu = 1$, $g = 2/3$, we observe an anomalous increasing of the current in comparison with the prediction of the simple Beenakker model [9] of fractional ES. We interpret our results as a first experimental demonstration of the intrinsic structure of the incompressible stripes arising at the reconstructed sample edge in the fractional quantum Hall effect regime in accordance with the model of Wen and Chamon [16].

We wish to thank D.E. Feldman for fruitful discussions and A.A. Shashkin for help during the experiment. We gratefully acknowledge financial support from the Russian Foundation for Basic Research, the Russian Academy of Sciences, the program "State Support for Leading Scientific Schools," Deutsche Forschungsgemeinschaft, and SPP "Quantum Hall Systems" (grant no. LO 705/1-2). E.V.D. acknowledges support from the Russian Science Support Foundation.

REFERENCES

1. B. I. Halperin, Phys. Rev. B **25**, 2185 (1982).
2. M. Büttiker, Phys. Rev. B **38**, 9375 (1988).
3. D. B. Chklovskii, B. I. Shklovskii, and L. I. Glazman, Phys. Rev. B **46**, 4026 (1992).
4. R. J. Haug, Semicond. Sci. Technol. **8**, 131 (1993).
5. A. Würtz, R. Wildfeuer, A. Lorke, *et al.*, Phys. Rev. B **65**, 075303 (2002).
6. E. V. Deviatov, V. T. Dolgopolov, and A. Wurtz, JETP Lett. **79**, 504 (2004).
7. E. V. Deviatov, A. Wurtz, A. Lorke, *et al.*, Phys. Rev. B **69**, 115330 (2004).
8. R. B. Laughlin, Phys. Rev. Lett. **50**, 1395 (1983).
9. C. W. J. Beenakker, Phys. Rev. Lett. **64**, 216 (1990).
10. A. H. MacDonald, Phys. Rev. Lett. **64**, 220 (1990).
11. Xiao-Gang Wen, Phys. Rev. B **41**, 12838 (1990).
12. F. D. M. Haldane, Phys. Rev. Lett. **51**, 605 (1983); B. I. Halperin, Phys. Rev. Lett. **52**, 1583 (1984).
13. D. A. Syphers and P. J. Stiles, Phys. Rev. B **32**, 6620 (1985); R. J. Haug, A. H. MacDonald, P. Streda, and K. von Klitzing, Phys. Rev. Lett. **61**, 2797 (1988); S. Washburn, A. B. Fowler, H. Schmid, and O. Kem, Phys. Rev. Lett. **61**, 2801 (1988); S. Komijama, H. Hira, S. Sasoand, and S. Yiyamizu, Phys. Rev. B **40**, 5176 (1989).
14. A. M. Chang, L. N. Pfeiffer, and K. W. West, Phys. Rev. Lett. **77**, 2538 (1996).
15. F. P. Milliken, C. P. Umbach, and R. A. Webb, Solid State Commun. **97**, 309 (1995).
16. C. de C. Chamon and X. G. Wen, Phys. Rev. B **49**, 8227 (1994).
17. D. B. Chklovskii, Phys. Rev. B **51**, 9895 (1995).
18. E. V. Deviatov, V. T. Dolgopolov, A. Wurtz, *et al.*, Phys. Rev. B **72**, 041305(R) (2005).
19. G. Müller, D. Weiss, A. V. Khaetskii, *et al.*, Phys. Rev. B **45**, 3932 (1992).
20. A. Wurtz, E. V. Deviatov, A. Lorke, *et al.*, Physica E (Amsterdam) **22**, 177 (2004).

JETP Letters, Vol. 82, No. 8, 2005, pp. 544–548. From Pis'ma v Zhurnal Éksperimental'noĭ i Teoreticheskoĭ Fiziki, Vol. 82, No. 8, 2005, pp. 603–607.

Universal Statistics of the Local Green's Function in Wave Chaotic Systems with Absorption¶

D. V. Savin[a], H.-J. Sommers[a], and Y. V. Fyodorov[b, c]

[a] *Fachbereich Physik, Universität Duisburg–Essen, 45117 Essen, Germany*

[b] *School of Mathematical Sciences, University of Nottingham, Nottingham NG7 2RD, United Kingdom*

[c] *Petersburg Nuclear Physics Institute, Russian Academy of Sciences, Gatchina, 188300 Russia*

Received September 19, 2005

We establish a general relation between the statistics of the local Green's function for systems with chaotic wave scattering and uniform energy loss (absorption) and the two-point correlator of its resolvents for the same system without absorption. Within the random matrix approach, this kind of a fluctuation dissipation relation allows us to derive the explicit analytic expression for the joint distribution function of the real and imaginary part of the local Green's function for all symmetry classes as well as at an arbitrary degree of time-reversal symmetry breaking in the system. The outstanding problem of orthogonal symmetry is further reduced to simple quadratures. The results can be applied, in particular, to the experimentally accessible impedance and reflection in a microwave cavity attached to a single-mode antenna. © *2005 Pleiades Publishing, Inc.*

PACS numbers: 05.45.Mt, 73.23.–b, 42.25.Bs

Statistical fluctuations of physical observables in quantum systems with underlying chaotic classical dynamics are the subject of a very active field of research in theoretical and experimental physics. A considerable progress was underpinned by revealing the apparent universality of the fluctuations in systems of very diverse microscopic nature, ranging from atomic nuclei and Rydberg atoms in strong external fields to complex molecules, quantum dots, and mesoscopic samples [1, 2]. This universality allows one to exploit the random matrix theory (RMT) as a powerful tool for a theoretical analysis of the generic statistical properties of such systems [3]. In many cases, the quantity, which is readily obtained experimentally, is the absorption spectrum for transitions from a given initial state to highly excited chaotic states at the energy E. Most frequently, the absorption spectra look practically continuous due to both inevitable level broadening and finite experimental resolution. Then, the relevant statistics are the distribution and the correlation functions of the absorption probability [4]. In the simplest situation of uniform level broadening Γ, the problem thus amounts to studying statistical properties of the resolvent (Green's function) operator $\hat{G}(E) \equiv (E + i\Gamma/2 - \hat{H})^{-1}$ associated with the random matrix $\hat{H}$, which replaces the actual chaotic Hamiltonian. In particular, the imaginary part of the diagonal entries of $\hat{G}(E)$ is well known in solid-state physics as the *local density of states* (LDoS), and, in this capacity, its statistics enjoyed many studies [4–8].

From the experimental point of view, the same universality, which makes the use of the RMT legitimate, provides one with an attractive possibility to employ simple model systems for analyzing generic statistics of the fluctuating quantities. Various billiards are nowadays proved to be an ideal playground for investigating a variety of quantum chaos phenomena (see [2] for a general discussion, as well as [9–13] for the current problem). They are usually realized as electromagnetic resonators in the form of two-dimensional cavities shaped to ensure the chaoticity of internal scattering and coupled to waveguides (antennas), which are used to inject microwaves into the system as well as to collect the output. In particular, it turns out that, for a single-mode antenna, the local Green's function $G(E)$ (i.e., a diagonal element of $\hat{G}$ taken at the port position) has the direct physical meaning of the electric impedance of the cavity which linearly relates voltages and currents at the antenna port (see [10] for a discussion). In this way, not only the imaginary part but also the real part of G turn out to be experimentally accessible quantities whose statistics are, therefore, of considerable interest. Inevitable energy losses (absorption) must be taken into account properly when describing the experiments theoretically [14, 15].

The majority of the experiments are performed in systems which are time-reversal invariant (the so-called orthogonal symmetry class of the RMT characterized by Dyson's symmetry index $\beta = 1$). However, nonperturbative analytical results are available presently only for systems with no time-reversal symmetry (TRS) ($\beta = 2$ or unitary symmetry class) derived by various methods in [5, 8], and for systems with spin–orbit scattering

¶ The text was submitted by the authors in English.

($\beta = 4$ or the symplectic symmetry class) [8]. An attempt [6] to provide an expression for the LDoS distribution for the $\beta = 1$ case cannot be considered as particularly successful, as the final expression was given in the form of an intractable fivefold integral. Very recently, a heuristic interpolation formula at $\beta = 1$ incorporating exactly the limiting cases of strong and weak absorption was suggested [8, 9] to describe reasonably well the available data at moderate absorption. Therefore, an exact analytical treatment of the $\beta = 1$ case remains a considerable theoretical challenge.

In this letter, we present a novel approach to the problem, which allows us to derive the joint distribution function of the real and imaginary parts of the local Green's function exactly at arbitrary absorption for the whole regime of the gradual TRS breaking between the $\beta = 1$ and $\beta = 2$ symmetry classes.

The Hamiltonian $\hat{H}$ of the chaotic system gives rise to N levels (eigenfrequencies) characterized locally in the relevant range of the energy E by the mean level spacing Δ. We consider, as usual, dimensionless quantities expressed in units of Δ, $K(E) \equiv (N\Delta/\pi)G(E)$, and define the distribution of interest as follows:

$$\mathcal{P}(u, v) = \langle \delta(u - \mathrm{Re}K)\delta(v + \mathrm{Im}K)\rangle. \qquad (1)$$

Angular brackets stand for the ensemble averaging. In such units, the mean LDoS $\langle v\rangle = 1$. The function $iK = Z$ has also the meaning of the normalized cavity impedance Z [10].

We start with establishing the general relation between the joint distribution function (1) at *finite* absorption (assumed to be uniform, $\Gamma > 0$) and the energy autocorrelation function

$$C_\Omega(z_-, z_+) = \left\langle \frac{1}{z_- - i0 - K_0(E - \Omega/2 - i0)} \times \frac{1}{z_+ + i0 - K_0(E + \Omega/2 + i0)} \right\rangle \qquad (2)$$

of the *resolvents* of the local Green's function K_0 at *zero* absorption ($\Gamma = 0$). Distribution (1) can be obtained from (2) by analytic continuation in Ω from a real to purely imaginary value $\Omega = i\Gamma$ as follows. $K_0(E)$ is an analytic function of the energy in the upper or lower half-plane and can be thus analytically continued to the complex values: $K_0(E \pm i\Gamma/2) \equiv u \mp iv$, $v > 0$. This allows us to then continue analytically the correlation function (2) from a pair of its real arguments to the complex conjugate one: $z_+ = (z_-)^* \equiv z' + iz''$, $z'' > 0$. As a result, function (2) acquires at $\Omega = i\Gamma$ the following form:

$$C(z', z'') \equiv C_{\Omega = i\Gamma}(z_-, z_+) = \left\langle \frac{1}{(z' - u)^2 + (z'' + v)^2} \right\rangle = \int_{-\infty}^{\infty} du \int_0^{\infty} dv \frac{\mathcal{P}(u, v)}{(z' - u)^2 + (z'' + v)^2}. \qquad (3)$$

The second line here is due to definition (1). To solve this equation for $\mathcal{P}(u, v)$, we perform first the Fourier transform (FT) $\hat{C}(k, z'') \equiv \int_{-\infty}^{\infty} dz' e^{ikz'} C(z', z'')$ with respect to z' that leads to

$$\hat{C}(k, z'') = \int_0^{\infty} dv \hat{\mathcal{P}}(k, v) \frac{\pi e^{-|k|(z'' + v)}}{z'' + v}, \qquad (4)$$

where $\hat{\mathcal{P}}(k, v)$ is the corresponding FT of $\mathcal{P}(u, v)$. Being derived at $z'' > 0$, Eq. (4) can be analytically continued to the whole complex z'' plane with a cut along negative Rez''. Calculating then the jump of $\hat{C}(k, z'')$ on the discontinuity line $z'' = -v$ ($v > 0$), we finally get the following expression:

$$\hat{\mathcal{P}}(k, v) = \frac{\Theta(v)}{2\pi^2 i}[\hat{C}(k, -v - i0) - \hat{C}(k, -v + i0)], \qquad (5)$$

with the Heaviside step function $\Theta(v)$. The inverse FT of (5) yields the desired distribution.

This relationship is one of our central results. It resembles (and reduces to) the well-known relation between the spectral density of states and the imaginary part of the corresponding resolvent operator when the case of one real variable is considered. In contrast, the case of the distribution function of two real variables requires us to deal with the two-point correlation function. Physically, the latter is a generalized susceptibility that describes a response of the system that allows one to treat (5) in the sense of a fluctuation dissipation relation: the left-hand side there stands for the *distribution* (of K) in the presence of dissipation/absorption, whereas the *correlator* (of resolvents of K) in the right-hand side accounts for fluctuations in the system, i.e., for arbitrary order correlations in the absence of absorption.

We proceed now with applications. The main advantage of the derived relation is that the correlator is a much easier object to calculate analytically than the distribution, and such a calculation for ideal systems at zero absorption has actually already been performed in many interesting cases. Let us consider the chaotic cavity mentioned already. In this case, an exact result for the correlation function (2) has been previously obtained by us in [16, 17]. Its analytic continuation to

complex $\Omega = i\Gamma$ can be represented generally as follows:

$$C(z', z'') = \frac{1}{z'^2 + (z''+1)^2} + \frac{1}{4}\left(\frac{\partial^2}{\partial z'^2} + \frac{\partial^2}{\partial z''^2}\right)\mathcal{F}(\tilde{x}), \quad (6)$$

where it is important that the function $\mathcal{F}(\tilde{x})$ depends on z' and z'' only via the scaling variable $\tilde{x} \equiv (z'^2 + z''^2 + 1)/2z'' > 1$. Its explicit form depends on the symmetry present (e.g., preserved or broken TRS), the following common structure being, however, generic:

$$\mathcal{F}(\tilde{x}) = \int_{-1}^{1} d\lambda_0 \int_{1}^{\infty} d\lambda_1 \int_{1}^{\infty} d\lambda_2 f(\{\lambda\}) e^{-\gamma(\lambda_1\lambda_2 - \lambda_0)/2} \times \left[\frac{(\tilde{x}+\lambda_0)^2}{(\tilde{x}+\lambda_1\lambda_2)^2 - (\lambda_1^2-1)(\lambda_2^2-1)}\right]^{1/2}. \quad (7)$$

Here, the dimensionless parameter $\gamma \equiv 2\pi\Gamma/\Delta$ (i.e., absorption width Γ in units of the mean level spacing Δ) accounts for the absorption strength. The *real* function $f(\{\lambda\})$ is the only symmetry-dependent term. In the crossover regime of gradually broken TRS, it can be represented explicitly as follows [17]:

$$f(\{\lambda\}) = \{(1-\lambda_0^2)(1+e^{-2Y}) - (\lambda_1^2-\lambda_2^2)(1-e^{-2Y}) + 4y^2\mathcal{R}[(1-\lambda_0^2)e^{-2Y} + \lambda_2^2(1-e^{-2Y})]\}\frac{e^{-2y^2(\lambda_2^2-1)}}{\mathcal{R}^2}, \quad (8)$$

with $\mathcal{R} = \lambda_0^2 + \lambda_1^2 + \lambda_2^2 - 2\lambda_0\lambda_1\lambda_2 - 1$ and $Y \equiv y^2(1-\lambda_0^2)$, where y denotes a crossover driving parameter. Physically, $y^2 \sim \delta E_y/\Delta$ is determined by the energy shift δE_y of energy levels due to a TRS breaking perturbation (e.g., a weak external magnetic field in the case of quantum dots). Such an effect is conventionally modeled within the framework of RMT by means of the "Pandey–Mehta" Hamiltonian [18], $\hat{H} = \hat{H}_S + i(y/\sqrt{N})\hat{H}_A$, with $\hat{H}_S$ ($\hat{H}_A$) being a random real symmetric (antisymmetric) matrix with independent Gaussian distributed entries. The limit $y \longrightarrow 0$ or ∞ corresponds to fully preserved or broken TRS, respectively.

Now, we apply relation (5) to Eq. (6) and then perform the inverse FT to get $\mathcal{P}(u, v)$. Relegating all technical details to a more extended publication, we emphasize the most important points. The nontrivial contribution to the distribution comes from the second ("connected") part of the correlation function (6), whereas the first ("disconnected") one is easily found to yield the singular contribution $\delta(u)\delta(v-1)$. A careful analysis shows that, due to specific $\tilde{x}$ dependence given by Eq. (7), the above-described procedure for the analytic continuation of the connected part of $\hat{C}(k, z'')$ is equivalent to continuing $\mathcal{F}(\tilde{x})$ analytically and taking the jump at $\tilde{x} = -x \pm i0$, with

$$x \equiv \frac{u^2 + v^2 + 1}{2v} > 1.$$

The nonzero imaginary part $F(x) = \mathrm{Im}\mathcal{F}(-x)$ is thus determined at given x by the integration region $\mathcal{B}_x = \{(\lambda_1, \lambda_2) | 1 \le \lambda_{1,2} < \infty, (\lambda_1\lambda_2 - x)^2 < (\lambda_1^2-1)(\lambda_2^2-1)\}$, where the square root in (7) attains pure imaginary values. Taking into account the identity $\partial^2 F(x)/\partial u^2 + \partial^2 F(x)/\partial v^2 = v^{-2}\frac{d}{dx}(x^2-1)\frac{d}{dx}F(x)$ valid for $x^2 \neq 1$, we arrive finally at

$$\mathcal{P}(u, v) = \frac{1}{4\pi^2 v^2}\frac{d}{dx}(x^2-1)\frac{dF(x)}{dx} \equiv \frac{1}{2\pi v^2}P_0(x). \quad (9)$$

This distribution is easily checked to be invariant under the change $iK \longrightarrow 1/iK$, meaning physically that the impedance and its inverse have one and the same distribution function.

Such a form of the distribution is completely generic, as all the symmetry-specific dependences were not essential for the above discussion. It can be shown [8] by exploiting the well-known relation $S = (1 - i\kappa K)/(1 + i\kappa K) \equiv \sqrt{r}\, e^{i\theta}$ between the scattering matrix S and the local Green's function (known as a K function in this context) that the representation given by the second equality in Eq. (9) is a consequence of the two following properties at the so-called *perfect coupling*, $\kappa = 1$ [19]: (i) the uniform distribution of the scattering phase $\theta \in (0, 2\pi)$ and (ii) the statistical independence of θ and the S matrix modulus. This also establishes a physical meaning of x by relating it to the *reflection coefficient* r, thus $P_0(x)$ is the normalized distribution of $x = (1 + r)/(1 - r)$. Remarkably, Eq. (9) relates the distribution of the local Green's function in the closed system to that of reflection in the perfectly open one.

Both these properties can be verified using the methods of [14] but only in the cases of preserved or completely broken TRS. Our approach proves it generally for the crossover regime at an arbitrary degree of TRS breaking. Taking into account our findings, we can bring the final result to the following form:

$$F(x) = \int_{-1}^{1} d\lambda_0 \int\int_{\mathcal{B}_x} d\lambda_1 d\lambda_2 f(\{\lambda\}) e^{-\gamma(\lambda_1\lambda_2 - \lambda_0)/2} \times \frac{(x-\lambda_0)}{[(\lambda_1^2-1)(\lambda_2^2-1) - (\lambda_1\lambda_2 - x)^2]^{1/2}}. \quad (10)$$

At arbitrary values of the crossover parameter y, the obtained result can be treated only numerically. Further analytical study is possible in the limiting cases of pure symmetries considered below.

The simplest case of unitary symmetry ($\beta = 2$) [20] is correctly reproduced from (10) as $y \longrightarrow \infty$. We find [21]

$$P_0(x) = \frac{\mathcal{N}_\beta}{2}[A(\alpha(x+1)/2)^{\beta/2} + B]e^{-\alpha(x+1)/2}, \quad (11)$$

where it is convenient for the subsequent use to introduce the absorption parameter $\alpha \equiv \gamma\beta/2$ scaled with the symmetry index β, the α-dependent constants being $A \equiv e^\alpha - 1$ and $B \equiv 1 + \alpha - e^\alpha$, and the normalization constant $\mathcal{N}_2 = 1$.

As to the case of orthogonal symmetry ($\beta = 1$), no general result was available in the literature. Expression (11) (with $\mathcal{N}_\beta = \alpha/(A\Gamma(\beta/2 + 1, \alpha) + Be^{-\alpha})$ and $\Gamma(\nu, \alpha) = \int_\alpha^\infty dt\, t^{\nu-1}e^{-t}$) was suggested in [8] (see also [9]) to be an appropriate interpolation formula at $\beta = 1$. It incorporates correctly both known limiting cases of weak or strong absorption, and a reasonable agreement with available numerical and experimental data was found in a broad range of the absorption strength. We proceed with providing an exact analytical treatment of this case which amounts to investigating (8) and (10) at $y = 0$. Fortunately, further simplifications are possible if one considers the integrated probability distribution

$$W(x) \equiv -\frac{x^2-1}{2\pi}\frac{dF(x)}{dx} = \int_x^\infty dx P_0(x), \quad (12)$$

which is a positive monotonically decaying function by definition. To this end, we note that it is useful to switch to the parametrization of [22] to carry out the threefold integration. The latter turns out to yield a sum of decoupled terms, and, after some algebra, we have been able to cast the result in the following final form:

$$W(x) = \frac{x+1}{4\pi}[f_1(w)g_2(w) + f_2(w)g_1(w) + h_1(w)j_2(w) + h_2(w)j_1(w)]_{w=(x-1)/2}, \quad (13)$$

with auxiliary functions defined as follows:

$$f_1(w) = \int_w^\infty dt \frac{\sqrt{t|t-w|}\,e^{-\gamma t/2}}{(1+t)^{3/2}}[1 - e^{-\gamma} + t^{-1}],$$

$$g_1(w) = \int_w^\infty dt \frac{1}{\sqrt{t|t-w|}}\frac{e^{-\gamma t/2}}{(1+t)^{3/2}},$$

$$h_1(w) = \int_w^\infty dt \frac{\sqrt{|t-w|}\,e^{-\gamma t/2}}{\sqrt{t(1+t)}}[\gamma + (1-e^{-\gamma})(\gamma t - 2)], \quad (14)$$

$$j_1(w) = \int_w^\infty dt \frac{1}{\sqrt{t|t-w|}}\frac{e^{-\gamma t/2}}{\sqrt{1+t}},$$

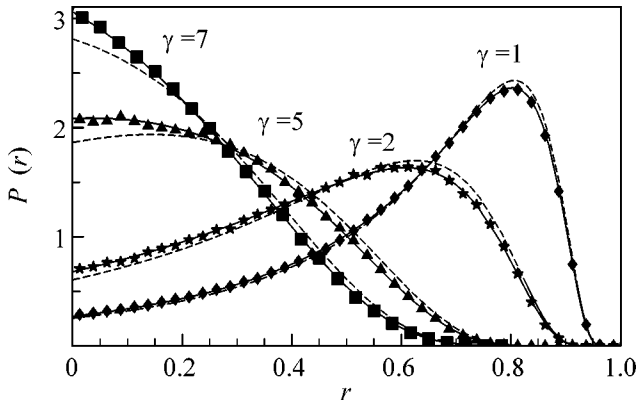

The reflection coefficient distribution in chaotic systems invariant under time reversal at perfect coupling is plotted at moderate values of the absorption strength $\gamma = 2\pi\Gamma/\Delta$, where systematic deviations between the exact result drawn from Eq. (13) (solid curves) and the interpolation expression (11) at $\beta = 1$ (dashed curves) are most noticeable. Symbols stand for numerics done for 10^3 realizations of 500×500 random GOE matrices.

their counterpart with the index 2 being given by the same expression save for the integration region $t \in [0, w]$ instead of $[w, \infty)$. For an illustration of our findings, the reflection distribution $P(r) = \frac{2}{(1-r)^2}P_0\left(\frac{1+r}{1-r}\right)$ is shown in the figure.

Finally, we mention that the general case of arbitrary transmission $T < 1$ can be mapped [23, 24] onto that of the perfect one considered so far. The scattering phase θ is then no longer uniformly distributed and gets statistically correlated with x. However, their joint distribution $P(x, \theta)$ can be found [8] to be again determined by $P_0(x)$ as follows:

$$P(x, \theta) = \frac{1}{2\pi}P_0(xg - \sqrt{(x^2-1)(g^2-1)}\cos\theta), \quad (15)$$

with $g \equiv 2/T - 1$. This equation provides us with further distributions of the phase and reflection coefficient, which were recently studied experimentally [9].

In summary, we provided a new approach to statistical properties of the local Green's function in quantum chaotic or disordered absorptive systems of any symmetry class. It would be highly interesting to extend the current experimental studies [11] of the crossover regime to check our findings. Although the validity of the explicit formulas given above is restricted to the completely ergodic ("zero-dimensional") case, it is actually possible to adopt the above method [25] to quasi-one- (or higher-) dimensional situations when Anderson localization effects already play an important role [7].

We thank V.V. Sokolov for useful comments. The work of D.V.S. and H.-J.S. was supported by Deutsche Forschungsgemeinschaft (grant no. SFB/TR) and the

work of Y.V.F. was supported by the Engineering and Physical Sciences Research Council (grant no. EP/C515056/1 "Random Matrices and Polynomials: A Tool to Understand Complexity").

REFERENCES

1. F. Haake, *Quantum Signatures of Chaos* (Springer, Berlin, 1991).
2. H.-J. Stöckmann, *Quantum Chaos: An Introduction* (Cambridge Univ. Press, Cambridge, 1999).
3. T. Guhr, A. Müller-Groeling, and H. A. Weidenmüller, Phys. Rep. **299**, 189 (1998).
4. Y. V. Fyodorov and Y. Alhassid, Phys. Rev. A **58**, R3375 (1998).
5. K. B. Efetov and V. N. Prigodin, Phys. Rev. Lett. **70**, 1315 (1993); C. W. J. Beenakker, Phys. Rev. B **50**, 15170 (1994); A. D. Mirlin and Y. V. Fyodorov, Europhys. Lett. **25**, 669 (1994); A. V. Andreev and B. D. Simons, Phys. Rev. Lett. **75**, 2304 (1995).
6. N. Taniguchi and V. N. Prigodin, Phys. Rev. B **54**, R14305 (1996).
7. A. D. Mirlin, Phys. Rep. **326**, 259 (2000).
8. Y. V. Fyodorov and D. V. Savin, JETP Lett. **80**, 725 (2004).
9. U. Kuhl *et al.*, Phys. Rev. Lett. **94**, 144101 (2005).
10. S. Hemmady *et al.*, Phys. Rev. Lett. **94**, 014102 (2005); X. Zheng, T. M. Antonsen, and E. Ott, cond-mat/0408327; cond-mat/0408317.
11. Y.-H. Kim *et al.*, Phys. Rev. Lett. **94**, 036804 (2005); S.-H. Chung *et al.*, Phys. Rev. Lett. **85**, 2482 (2000).
12. O. I. Lobkis, I. S. Rozhkov, and R. L. Weaver, Phys. Rev. Lett. **91**, 194101 (2003).
13. J. Barthélemy, O. Legrand, and F. Mortessagne, Phys. Rev. E **71**, 016205 (2005).
14. P. W. Brouwer and C. W. J. Beenakker, Phys. Rev. B **55**, 4695 (1997).
15. D. V. Savin and H.-J. Sommers, Phys. Rev. E **68**, 036211 (2003); Y. V. Fyodorov, JETP Lett. **78**, 250 (2003).
16. Y. V. Fyodorov and H.-J. Sommers, J. Math. Phys. **38**, 1918 (1997).
17. Y. V. Fyodorov, D. V. Savin, and H.-J. Sommers, Phys. Rev. E **55**, R4857 (1997).
18. A. Pandey and M. L. Mehta, Commun. Math. Phys. **16**, 2655 (1983); A. Altland *et al.*, Ann. Phys. (N.Y.) **219**, 148 (1992).
19. The coupling constant $\kappa > 0$ enters the S matrix statistics only through the so-called *transmission coefficient* $T \equiv 1 - |\langle S \rangle|^2$ ($= 4\kappa/(1+\kappa)^2$ at $E = 0$), referring $T = 1$ (0) to the perfectly open (closed) system; see, e.g., Refs. [16, 22] for details.
20. C. W. J. Beenakker and P. W. Brouwer, Physica E (Amsterdam) **9**, 463 (2001).
21. $4y^2\int_1^\infty d\lambda_2\lambda_2^2 e^{-2y^2(\lambda_2^2-1)} \longrightarrow 1$ as $y \longrightarrow \infty$, so that one can put $\lambda_2 = 1$ everywhere else in (10). As a result, the λ_1 integration in $F(x)$ shrinks to a point $\propto\delta(\lambda_1 - x)$, then the integration over λ_0 is easily performed to yield Eq. (11).
22. J. J. M. Verbaarschot, H. A. Weidenmüller, and M. R. Zirnbauer, Phys. Rep. **129**, 367 (1985).
23. P. A. Mello, P. Pereyra, and T. Seligman, Ann. Phys. (N.Y.) **161**, 254 (1985); P. W. Brouwer, Phys. Rev. B **51**, 16 878 (1995); The following map $S_{T=1} = (S - \sqrt{1-T})/(1 - \sqrt{1-T}S)$ relates the S matrices at perfect and arbitrary transmission thus the corresponding statistics as well; see also Ref. [9].
24. D. V. Savin, Y. V. Fyodorov, and H.-J. Sommers, Phys. Rev. E **63**, 035 202 (2001).
25. Y. V. Fyodorov, D. V. Savin, and H.-J. Sommers, cond-mat/0507016.